SANDIA REPORT SAND83-8225 • Unlimited Release • UC-13
Printed July 1983

Experimental Mixed Convection Heat Transfer From a Large, Vertical Surface in a Horizontal Flow

D. L. Siebers, R. G. Schwind, and R. J. Moffat

Prepared by
Sandia National Laboratories
Albuquerque, New Mexico 87185 and Livermore, California 94550
for the United States Department of Energy
under Contract DE-AC04-76DP00789

Issued by Sandia National Laboratories, operated for the United States Department of Energy by Sandia Corporation.

Printed in the United States of America
Available from
National Technical Information Service
5285 Port Royal Road
Springfield, VA 22161

NTIS price codes
Printed copy: A09
Microfiche copy: A01

SAND83-8225
Unlimited Release
Printed July 1983

UC-13

EXPERIMENTAL MIXED CONVECTION HEAT TRANSFER FROM A LARGE, VERTICAL SURFACE IN A HORIZONTAL FLOW

Dennis L. Siebers
Sandia National Laboratories
Livermore, CA 94550

Richard G. Schwind
Nielsen Engineering and Research, Inc.
Mountain View, CA 94043

Robert J. Moffat
Stanford University
Stanford, CA 94305

ABSTRACT

The convective heat transfer from and the boundary layer flow on a vertical, 3 *m* square surface parallel to a horizontal air flow were studied. The test conditions ranged from pure forced convection driven by a horizontal inertial force induced by the horizontal free-stream flow, to combined forced and free convection (i.e., mixed convection) driven by orthogonal forces, the horizontal inertial force and a vertical buoyant force generated by the heated vertical wall, to pure free convection driven by the vertical buoyant force. The emphasis of the study was on mixed convection. Surface temperatures and free-stream velocities ranged from 40 to 600 C and 0 to 6.0 m/s, respectively, resulting in Reynolds numbers (Re) and Grashof numbers (Gr) up to 2×10^6 and 2×10^{12}, respectively.

Convective heat transfer and boundary layer profiles of mean velocity, flow angle, and temperature were measured. The heat transfer results showed the range of conditions for which the heat transfer was characterized either as forced, mixed, or free convection. Correlations for mixed convection heat transfer and for variable properties free convection heat transfer were developed from the heat transfer results. The combined effects of free-stream velocity, buoyancy, and variable properties on the location of the transition from laminar to turbulent flow were also noted from the heat transfer results. The boundary layer profiles demonstrated the variation of mean velocity, flow angle, and temperature through the boundary layer for test conditions ranging from forced, to mixed, to free convection.

TABLE OF CONTENTS

TABLE OF CONTENTS (cont.)

LIST OF FIGURES

LIST OF FIGURES (cont.)

LIST OF FIGURES (cont.)

LIST OF FIGURES (cont.)

LIST OF FIGURES (cont.)

LIST OF FIGURES (cont.)

LIST OF TABLES

NOMENCLATURE

a	Constant defined locally in text or the radius of a cylinder
A	Area, m^2
A_c	Correction to the surface heat flux for thermal expansion in Eqn. (2-2)
b	Constant defined locally in text
B	Flow leaving the test surface, *degrees*
C	Constant defined locally in text
C_1	Constant used in Eqn. (4-20)
C_2	Constant used in Eqn. (4-21)
C_f	Skin friction coefficient, $\tau_w/(\rho U_\infty^2/2)$
c_p	Specific heat at constant pressure, J/kgC
E	Voltage drop across a heating strip, *volts*
g	Gravitational constant, 9.80 m/s^2
Gr_ℓ	Grashof number, $g\beta(T_w - T_\infty)\ell^3/\nu^2$
h	Heat transfer coefficient, W/m^2C
$\overline{h}$	Average heat transfer coefficient, W/m^2C
H	Height of test surface, 3.030 m
i	Enthalpy, kJ/kg
I	Current through a heating strip, *amps*
ID	Heat transfer test identification number
ID^*	Boundary profile identification number
if_{tx}	Enthalpy flux in x-direction, defined in Appendix F, kJ/ms
if_{ty}	Enthalpy flux in y-direction, defined in Appendix F, kJ/ms
k	Thermal conductivity, W/mC
K	Pressure gradient parameter, $\dfrac{\nu}{U_\infty^2}\dfrac{dU_\infty}{dX}$
ℓ	A general characteristic length
L	Length of test surface, 2.954 m
LH	Characteristic length, defined by Eqn. (4-5), m
mf_x	Mass flux deficit in the x-direction, defined in Appendix F, kg/ms
mf_y	Mass flux deficit in the y-direction, defined in Appendix F, kg/ms
Mf_{xx}	x-Momentum flux deficit in the x-direction, defined in Appendix F, kg/s^2
Mf_{xy}	y-Momentum flux deficit in the x-direction, defined in Appendix F, kg/s^2

Mf_{yx}	x-Momentum flux deficit in the y-direction, defined in Appendix F, kg/s^2
Mf_{yy}	y-Momentum flux deficit in the y-direction, defined in Appendix F, kg/s^2
Nu_ℓ	Nusselt number, $h\ell/k$
Nu'_ℓ	Modified Nusselt number for free convection, $Nu_\ell\left(\frac{T_w}{T_\infty}\right)^{-n}$
	$n = -0.14$ for turbulent flow and -0.04 for laminar flow
Pr	Prandtl number, ν/α
q	Heat flux, W/m^2
Q	Total velocity, $\sqrt{u^2+v^2}$
r	Resistivity, $ohm\ cm$
r'	Average resistivity of a heating strip, $ohm\ cm$
R_c	Correction to surface heat flux for resistance variation in Eqn. (2-2)
Re_ℓ	Reynolds number, $U_\infty \ell/\nu$
Re^*	Effective free convection Reynolds number defined in Eqn. (1-2)
Re^{**}	Effective mixed convection Reynolds number defined in Eqn. (1-3)
St	Stanton number, $h/\rho_\infty c_p U_\infty$
t	Time, s
t^+	Temperature in wall coordinates, $\rho c_p(T_w - T)\sqrt{\tau_w/\rho}/q_w$
T	Temperature, C
$\overline{T}$	Average temperature of a stainless steel heating strip, C
T'	Temperature of a heating strip which gives the average strip resistivity, C
T_{cold}	Temperature of the unheated stainless steel strips, C
T_f	Film temperature, $(T_w + T_\infty)/2$, C
u, U	Horizontal or x-direction velocity component, m/s
$\overline{u}$	Average horizontal velocity component of the constant-angle region, m/s
u^+	Horizontal velocity component in wall coordinates, $u/\sqrt{\tau_w/\rho}$
v, V	Vertical or y-direction velocity component, m/s
$\overline{v}$	Average vertical velocity component of the constant-angle region, m/s
V_g	Buoyant reference velocity, defined by Eqn. (4-16)
w	Normal (to test surface) or z-direction velocity component, m/s
W	Width of test section inlet, 1.12 m
x	Horizontal direction on test surface - measured from stagnation line, m

y	Vertical direction on test surface - measured from bottom edge of bottom heated strip, m
z	Direction normal to test surface, m
z^{+}	Distance normal to wall in wall coordinates, $z\sqrt{\tau_w/\rho}/\nu$

Greek

α	Thermal diffusivity, m^2/s, or coefficient of thermal expansion, C^{-1}
β	Flow angle with respect to a horizontal plane, *degrees* or volumetric expansion coefficient, C^{-1}
δ_x	x-Displacement thickness, defined in Eqn. (2-4), cm
δ_{xx}	x-Momentum thickness in the x-direction, defined in Eqn. (2-5), cm
	Thermal boundary layer thickness, defined in Eqn. (2-3), cm
ϵ	Emissivity
ϕ	Angle between gravitational vector and the free-stream flow, *degrees*,
μ	Dynamic viscosity, kg/ms
ν	Kinematic viscosity, m^2/s
θ	Dimensionless temperature, $(T_w - T)/(T_w - T_\infty)$
θ_i	Dimensionless enthalpy, $(i_w - i)/(i_w - i_\infty)$
τ	Shear stress
ρ	Density, kg/m^3

Subscripts

a	Radius
act	Undisturbed value
$b1$	Base temperature one on the fluid temperature thermocouple
$b2$	Base temperature two on the fluid temperature thermocouple
$cond$	Conduction heat transfer
$conv$	Convective heat transfer
cp	Constant properties
D	Diameter
ele	Electric power

NOMENCLATURE (cont.)

Subscripts (cont.)

f	Film temperature
fc	Forced convection
fr	Free convection
h	Hemispherical
H	Height
ℓ	General length scale
L	Length
n	Normal
max	Maximum value
$meas$	Measured value
mp	Measuring point
mx	Mixed convection
o	Origin of a streamline
Q	Test section inlet velocity (tunnel-Q)
r	Reference temperature
rad	Radiation heat transfer
$streak$	Angle of the wake of the probe
u	Velocity
w	Wall or surface
x_c	x-Transition location
y_c	y-Transition location
∞	Free-stream or ambient
Δ_{tx}	Enthalpy thickness in the x-direction
δ_{xx}	x-Momentum thickness in the x-direction

SUMMARY

Convection heat transfer from a large (2.95 m long by 3.02 m high), vertical, electrically heated surface parallel to a horizontal air flow was studied. The regimes of heat transfer studied ranged from pure forced, to mixed, to pure free convection. The primary emphasis was on mixed convection. The boundary layer flow on the vertical surface was three-dimensional with a horizontal velocity component resulting from a horizontal free-stream air flow and a vertical velocity component resulting from a vertical buoyant force. The buoyant force was caused by a density variation across the heated boundary layer. Very little information exists in the literature on this problem, which is important in solar central power applications. The information which does exist is primarily in the form of simplified laminar flow analyses.

The electric power dissipated ranged from 200 to 13,000 W/m^2, resulting in average surface temperatures in the 40 to 600 C range. The free-stream air velocities ranged from 0 to 6 m/s. These conditions resulted in Reynolds numbers (Re) based on the test surface length and Grashof numbers (Gr) based on the test surface height of 2×10^6 and 2×10^{12}, respectively. Convective heat transfer coefficients were measured at 105 locations on the test surface by an energy balance. Boundary layer mean velocity and mean flow angle profiles were measured with pressure type probes. Boundary layer mean temperature profiles were measured with a thermocouple. The three boundary layer profiles of velocity, temperature, and flow angle were taken simultaneously.

The heat transfer data showed several important points. First, the heat transfer changed smoothly from forced convection, to mixed, to free convection as the ratio of the buoyant force to the inertial force (Gr/Re^2) increased. The range of Gr/Re^2 over which the average heat transfer coefficient could be described as "mixed" was approximately between values of Gr/Re^2 equal to 0.7 and 10.0. The average heat transfer coefficient could be considered (to within 5%) pure forced convection for $Gr/Re^2 < 0.7$ and pure free convection for $Gr/Re^2 > 10.0$.

Second, for similar ratios of the buoyant force to the inertial force, the local distribution of the heat transfer coefficient on the test surface was the same.

Third, the distribution of the convection heat transfer coefficient in the turbulent flow regions resembled either pure forced convection (i.e., $h \sim x^{-0.2}$) or pure

free convection (i.e., a spatially uniform h). The change from a forced-convection-like dependence on x to a free-convection-like uniform h occurred over a very short distance. (This does not imply, however, that the local heat transfer coefficient was always given by either pure forced or pure free convection.)

Fourth, when there was free-stream air flow, forced convection always dominated the heat transfer near the vertical leading edge where the boundary layer was laminar.

Fifth, the measured average convection heat transfer coefficient, $\overline{h}_{mx}$, can be estimated to within $\pm 3\%$ on the average for all test conditions (mixed, forced, and free convection) by:

$$\overline{h}_{mx} = (\overline{h}_{fc}{}^{3.2} + \overline{h}_{fr}{}^{3.2})^{1/3.2}$$

The average forced convection term $\overline{h}_{fc}$ and the average free convection term $\overline{h}_{fr}$ are estimates of the average convective heat transfer coefficient made considering only a single mechanism for heat transfer using correlations for pure forced or pure free convection, respectively.

Sixth, a prediction method similar to that for the average heat transfer coefficient in the previous paragraph can be used to predict the local heat transfer coefficient to within $\pm 10\%$. The local method is based on estimates of the local forced and free convection heat transfer coefficients. The local method, however, does not predict the exact local variation in the heat transfer coefficient that was observed in the turbulent heat transfer regions.

Seventh, high temperature, turbulent, pure free convection heat transfer results supported the following (new) correlation for variable properties, turbulent, free convection from a vertical surface in air:

$$Nu_y = 0.098 Gr_y^{1/3} \left(\frac{T_w}{T_\infty} \right)^{-0.14}$$

All properties in the correlation are to be evaluated at the free-stream temperature. The laminar flow results indicate that there was very little effect of variable properties on laminar free convection from a vertical surface.

Finally, the heat transfer results showed that location of transition from laminar to turbulent flow was affected by the free-stream velocity, by buoyancy, and by variable properties.

The boundary layer velocity, flow angle, and temperature profiles revealed several points about the mixed convective boundary layer. First, the boundary layer flow angle profiles showed the inner region of the turbulent mixed convection boundary had a collateral region from the wall out to the location where $u/U_\infty = 0.71$ (the inner 5-7% of the boundary layer). Second, the flow angle within the collateral region was related to the test conditions and location on the test surface by a simple relationship deduced from momentum considerations. Third, flow angle profiles for laminar flow showed no such collateral region. Fourth, the tangent of the local flow angle in the outer region of the turbulent boundary layer was linearly dependent on the local dimensionless temperature. Fifth, there was evidence that some of the momentum added to the flow in the vertical direction by the buoyant force was transferred to the horizontal direction by turbulence. Finally, the boundary layer velocity and temperature profiles changed smoothly from forced-convection-like profiles to free-convection-like profiles as the local ratio of the buoyant force to the inertial force increased.

Chapter 1.

INTRODUCTION AND OVERVIEW

This work presents the results and interpretation of an experimental study of the convective heat transfer from, and the boundary layer flow on, a large (2.95 m long by 3.02 m high), vertical, heated, flat surface parallel to a horizontal flow of air. The driving forces on the boundary layer flow are a vertical buoyant force, caused by density variations across the boundary layer, and a horizontal inertia force, induced by the external flow. These forces are orthogonal to each other and parallel to the heat transfer surface. When the effects of both driving forces are of similar magnitude, the boundary layer flow is three-dimensional having both vertical and horizontal velocity components. The convective heat transfer from the surface is affected by both forces.

The conditions studied ranged from a flow dominated by the vertical buoyant force (a two-dimensional, free convection flow in the vertical direction) to a flow dominated by the horizontal inertia force (a two-dimensional, forced convection flow in the horizontal direction). Most of the data, however, were taken in the three-dimensional "mixed-convection" flow regime.

Interest in this problem stems from the desire to predict more accurately the heat losses from the receivers of large-scale solar central power plants. Plans for large-scale electric power generation using solar energy envision an array of heliostats focusing sunlight onto a receiver sitting atop a tower. The receiver heats a working fluid (air, water, molten salts, or liquid metals) which is subsequently used in a thermal power plant cycle. The receiver operates at a high temperature and loses energy by convection and radiation to the environment. This energy loss is important, since efficient absorption and transfer of solar energy to the working fluid is critical to the central receiver concept. Plant performance, plant capital cost, and the cost of the energy produced are significantly affected by receiver efficiency [1]. The receivers currently proposed for solar central power plants can be divided into two categories, "cavity" and "external", each having its own characteristic mechanism for energy losses. The present research is most directly related to the convective energy losses from external receivers.

Convective heat transfer from an external receiver is complicated from both fluid mechanic and heat transfer standpoints. A typical receiver of this type is a cylinder, 10 to 20 m in diameter as well as in height, supported on a tower. The surface is made of vertical tubes which are welded together to form a rough surface whose elements are perpendicular to the external flow and large compared to the boundary layer thickness. The surface temperature is between 500 and 650 C, and the system is expected to operate in winds of up to 10-15 m/s. The Reynolds number (based on cylinder diameter) and the Grashof number (based on cylinder height), two important descriptors in this problem, range up to 10^7 and 10^{15}, respectively. Under these conditions there will be a complex flowfield around the heated cylinder, as indicated in Fig. 1-1. The upstream side shows a stagnation line and regions of laminar and turbulent boundary layer with a transition zone between them. The boundary layer regions can be characterized as mixed convection flow with orthogonal driving forces, a vertical buoyant force and a horizontal inertia force. The aft side shows a separation zone and a wake flow. In addition, there are likely to be strong end effects on a cylinder with a small aspect ratio.

The situation offers many complications over pure forced convection heat transfer from a smooth flat surface: roughness, curvature, end effects, pressure gradients, separated flow, significant buoyant forces orthogonal to the free-stream flow, and variable properties effects. In addition, the sheer size of the receivers puts them in a range of Grashof and Reynolds numbers in which not even simple cases have been studied. Of these factors, the effects of buoyancy on forced convection (i.e., mixed convection), where the buoyant force and the free-stream flow are orthogonal, is one of the least understood. The effects of variable properties on mixed convection and free convection heat transfer, which occur at the high receiver operating temperatures, are also poorly understood. In light of these facts, the present experiment was designed to isolate mixed convection driven by orthogonal forces on a simple geometry (a smooth, vertical, flat surface) and to be operable at high temperatures so that the effects of variable properties could be included. Also, the experimental apparatus was made as large as practical, so that the Grashof and Reynolds ranges of the experiment were as close as possible to those of a full-scale receiver.

The remainder of this chapter is divided into six sections. The first section is a brief physical description of the problem being investigated. The second and third sections present literature surveys for mixed convection and variable properties free convection, respectively (no information was found on variable properties effects on mixed convection). The fourth section is a summary of the present knowledge of mixed convection and variable properties free convection, based on the literature surveys. The fifth section presents the objectives of the experiment, and the final section is a brief description of the experiment in terms of the operating ranges of various test parameters.

1.1 Physical Description of Problem

When air is forced horizontally over a heated vertical surface, as shown schematically in Fig. 1-2, the air in the boundary layer is heated and begins to rise as it moves downstream. This effect is caused by a vertical buoyant force, which is proportional to the difference between the local and the free-stream density (caused by the difference between the local and the free-stream temperature) times the gravitational constant. Since the air nearest the wall is the hottest, it has the largest buoyant force and rises at the sharpest angle relative to the horizontal free-stream air flow. Outward from the wall toward the free-stream, the flow angle approaches zero as the local density approaches the free-stream density. Downstream, the flow angle increases, since the air is being accelerated vertically by the buoyant force as it is carried downstream by the forced flow. As a result, the air near the wall follows a streamline which curves upward while the free-stream flow remains horizontal (Fig. 1-2). This flow pattern causes a skewed three-dimensional boundary layer on the test surface. Also shown in Fig. 1-2, is a peak in the velocity profile near the wall. This will occur when the vertical buoyant acceleration has sufficient time to act relative to the effects of the horizontal free-stream flow.

The overall increase in boundary layer flow angle over the test surface and the mode of heat transfer from the test surface depend on the test conditions. For the low-velocity and high-temperature tests, the flow angle increase will be very large and free convection heat transfer will dominate. For the high-velocity and low-temperature tests, the boundary layer flow will remain nearly horizontal and pure forced convection heat transfer will dominate. Between these extremes, there will be a three-dimensional boundary layer flow described in the previous paragraph, with mixed convection heat transfer occurring and flow angles varying as shown in Fig. 1-2.

1.2 Previous Research on Mixed Convection

This section presents a review of mixed convection. The review emphasizes mixed convection flows whose mean flow patterns are three-dimensional and proposed methods for estimating mixed convection heat transfer coefficients.

Mixed convection heat transfer studies can be broken into two classes of flows: those which result in two-dimensional mean flow patterns, and those which result in three-dimensional mean flow patterns. Two-dimensional mean flows result when the buoyant force and the free-stream flow are aligned (aiding or opposing) or when the buoyant force is normal to the surface on which a forced convection boundary layer is developing. An example of the first case is a vertical heated surface with a vertical free-stream flow. An example of the second, is a horizontal heated surface in a horizontal free-stream flow. Three-dimensional mixed convection mean flow patterns results when the buoyant force and free-stream flow are at some angle with each other and both are parallel to a surface on which the flow is developing. This is like the case being studied in this work, a vertical heated surface parallel to a horizontal free-stream flow.

The two-dimensional flows have been extensively reviewed by Jularia [2] and Evans [3], which should be consulted for details. To summarize these reviews, the two-dimensional works are primarily numerical, similarity, and perturbation solutions of various laminar flow problems, plus a few experimental works. The important mixed convection parameter was found to be $(Gr_\ell/Re_\ell^m)^n$, where the Grashof and Reynolds numbers are based on the same length scale. When the buoyant force and the free-stream flow were parallel to the surface, the value of m was found to be 2.0 and the value of n was found to be 1.0 and 0.5 for forced convection dominated flows and for free convection dominated flows, respectively. The heat transfer and skin friction varied smoothly from pure forced to pure free convection as Gr_ℓ/Re_ℓ^2 varied over some range of values, which defined the mixed convection zone. The mixed convection heat transfer zone was much smaller in terms of Gr_ℓ/Re_ℓ^2 than the mixed convection skin friction zone.

When the buoyant force was normal to a horizontal surface in a horizontal flow, m and n were found to be 2.5 and 1.0, respectively. For this situation, the buoyant force acted as a favorable or an adverse pressure gradient on the forced flow depending on the surface orientation, upward or downward facing, and the temperature boundary conditions.

The three-dimensional mixed convection work started with Young and Yang [4]. They studied the effects of both a small horizontal free-stream flow parallel to a vertical, heated surface and a variation of the surface temperature in the horizontal flow direction on laminar free convection on a vertical surface. The solution was in the form of a perturbation analysis. It showed that for small cross flows and a uniform surface temperature, the heat transfer could still be estimated by pure free convection correlations even though there was a horizontal velocity component in the boundary layer.

Recently, three more works have appeared dealing with vertical heated surfaces in horizontal flows. Eichhorn and Hasan [5] present a similarity solution for a Falkner-Skan type of forced flow over a heated wedge with the leading edge either vertical or horizontal. The vertical leading edge case is directly related to this work and was found to have a similarity solution for a free-stream velocity varying linearly in the horizontal direction and for a wall-to-free-stream temperature difference varying linearly in the vertical or free convection direction. For this case the mixed convection parameter was $(x/y)(Gr_y/4Re_x^2)^{1/4}$. As this parameter varied from zero to about two, the heat transfer varied smoothly from that for a pure forced convection stagnation flow to that for a pure free convection heat transfer flow with a linearly varying surface temperature in the vertical direction. The mixed convective heat transfer region occurred over a smaller range of the mixed convection parameter than the mixed convective skin friction region. The maximum deviation of the mixed convection heat transfer coefficient from the larger of the pure free or the pure forced convective heat transfer coefficients was 23%. The results showed that for a large horizontal distance (x), a large wall-to-free-stream temperature difference, a small free-stream velocity, or a small vertical distance (y), the flow was free convection dominated, and for the opposite trend in each parameter, the flow was forced convection dominated. This means the flow was dominated along the vertical stagnation line by forced convection and along the lower horizontal leading edge by free convection.

The second article was by Plumb [6] who solved much the same problem as Eichhorn and Hasan [5]. His similarity solution allowed the temperature and the velocity boundary conditions to vary in both the vertical and horizontal directions. One case for which he found a similarity solution was the same wedge flow case that was reported on by Eichhorn and Hassan [5], which is the case most closely related to the study in this work. The results of Plumb were identical to those of Eichhorn and Hasan for that special case. The mixed convection parameter was $(y/x)^2(Re_x^2/Gr_y)^{1/2}$, a constant times the inverse square of the one used by Eichhorn and Hasan [5].

The third related article to appear was by Evans [3]. His work involved a numerical, analytical, and experimental study of a vertical heated surface with a horizontal free-stream flow parallel to it, the exact case being reported on in this work, but for laminar flow only. Some important results were that forced convection dominated on the vertical forced convective leading edge and that free convection dominated on the horizontal free convection leading edge. The mixed convection parameter was of the form $(x/y)^2(Gr_x/Re_y^2)^{1/2}$, the same as Plumb [6]. Also, as noted previously in other works, there was a smooth transition from forced to free convection heat transfer and the mixed convection heat transfer region occupied a smaller range of the mixed convection parameter than did the mixed convection skin friction region.

Several works more directly related to the central receiver itself have also been carried out. These were for a vertical heated cylinder in a horizontal cross-flow. Oosthuizen and Leung [7] presented an experimental mean heat transfer study for Grashof numbers less than 10^9 based on cylinder height, Reynolds numbers less than 7000 based on cylinder diameter, and aspect ratios (height to diameter) of about ten. Their results indicated the pure forced convection and the pure free convection Nusselt numbers could be combined by the root-mean-square method to estimate the mixed convective Nusselt number. Oosthuizen and Taralis [8] presented numerical and experimental results and Oosthuizen [9] presented numerical results for the vertical cylinder in a cross-flow. In both these studies, although the agreement was only qualitative, it was shown that in the boundary layer zones the local heat transfer was dominated by forced convection at higher vertical positions on the cylinder and by free convection near the lower edge. Experimentally, it was shown in Ref. 8 that free convection effects were significant in the separated region of the cylinder. As with Ref. 7, these last two studies were for low Grashof and Reynolds numbers. The mixed convection parameter used was Gr_D/Re_D^2, where both the Grashof and Reynolds numbers were based on cylinder diameter.

Yao and Chen [10] studied a semi-infinite vertical cylinder in a cross flow. They conducted a perturbation analysis treating forced convection as the perturbing effect. The results demonstrated that free convection dominates on the lower edge of the cylinder, as did References [7-9]. The buoyancy parameter in this study was $Re_a/Gr_a^{1/2}$ where a is the radius of the cylinder.

A semi-infinite horizontal cylinder in a horizontal flow aligned with the axis of the cylinder was studied numerically by Yao, Catton, and McDonough [11] and analytically by Yao and Catton [12]. The results indicate the effects of buoyancy were to enhance the heat transfer along the bottom half of the cylinder and retard it on the top. Eventually, far downstream the flow was dominated by free convection. The mixed convection parameter for these studies was Gr_a/Re_a^2 where a is the radius of the cylinder.

The estimation of mixed convection heat transfer coefficients has been treated by only a few authors. McAdams [13] recommends using the larger of the pure free and the pure forced convection heat transfer coefficient estimates for a given problem as the mixed convection heat transfer coefficient. Van der Hegge Zijnen [14] recommends calculating a mixed convection heat transfer coefficient from a mixed convection Nusselt number. Effectively, the mixed convection Nusselt number is obtained by root-sum-squaring the pure free and forced convection Nusselt numbers for the problem. This was used by Oosthuizen and Leung [7] also. Hatton, et al. [15] and later Morgan [16] recommended finding an effective Reynolds number for mixed convection to be used in a pure forced convection correlation to estimate a heat transfer coefficient for mixed convection. The effective mixed convection Reynolds number is a vectorial addition of an effective free convection Reynolds number and the forced convection Reynolds number for the problem. The effective Reynolds number for free convection, Re^*, was defined as follows using the forced and free convection heat transfer relationships for the problem:

$$Nu_{fr} = a(GrPr)^m = b(Re^*)^n Pr^p \tag{1-1}$$

or

$$Re^* = (\frac{a}{b} Pr^{m-p} Gr^m)^{1/n} \tag{1-2}$$

The effective Reynolds number for mixed convection is given by

$$(Re^{**})^2 = (Re^*)^2 + 2(Re^*)(Re)cos\phi + (Re)^2 \tag{1-3}$$

The term Re is the forced convection Reynolds number and the angle ϕ is the angle between the gravitational vector and the free-stream flow. The mixed convection Nusselt number is then estimated from the pure forced convection correlation as follows:

$$Nu_{mx} = b(Re^{**})^n Pr^p \tag{1-4}$$

Another method of combining pure free and pure forced convection heat transfer coefficients to obtain a mixed convection estimate is based on a combining law proposed by Churchill and Usagi [17] to correlate data in the intermediate ranges between the two limiting solutions to a problem, one for the independent parameter aproaching zero and one for it approaching infinity. This method is recommended in Evans [3]. The correlation proposed is of the form:

$$F_s = (1 + G_s^a)^{1/a} \tag{1-5}$$

The term G_s is a ratio of the two asymptotic solutions to the problem, one for the parameter s approaching zero and one for s approaching infinity. The term F_s is a ratio of the solution for a given value of s to the asymptotic solution used in the denominator of G_s. The exponent a is chosen to best fit the data. For example, if Eqn. (1-5) was applied to the mixed convection heat transfer problem, it would look like

$$\frac{h_{mx}}{h_{fc}} = \left[1 + \left(\frac{h_{fr}}{h_{fc}}\right)^a\right]^{1/a} \tag{1-6}$$

or

$$\frac{h_{mx}}{h_{fr}} = \left[1 + \left(\frac{h_{fc}}{h_{fr}}\right)^a\right]^{1/a} \tag{1-7}$$

The term h_{fc}, h_{fr}, and h_{mx} are a forced convection heat transfer coefficient estimate based on the pure forced convection correlations, a free convection heat transfer coefficient estimate based on the pure free convection correlations, and the mixed convection heat transfer coefficient estimate, respectively.

Evans [3] recommends a value of 3.0 for a for laminar flow on a vertical heated surface with a horizontal flow of air parallel to it, the geometry being studied here. The recommendation of McAdams [13], discussed earlier, is equivalent to using an a of infinity in Eqns. (1-6) and (1-7). For parallel free-stream flow and buoyant forces, the recommendation of Sparrow [18] is an a of 3.25 and the recommendation of van der Hegge Zijnen [14] is equivalent to an a of 2.0.

1.3 Previous Research on Variable Properties Free Convection

The effects of variable properties on laminar natural convection in liquids have been reviewed in two recent articles [19,20]. Variable properties effects on laminar natural convection in gases have been examined experimentally and analytically by several authors [21-23,26]. The general consensus is that the effects of property variations for laminar natural convection are small in gases for the T_w/T_∞ range studied to date (0.25 to 4.0). Reference temperature methods, where properties in the constant properties correlation are evaluated at some specified temperature, are recommended by most authors to account for the small variable properties effects. One author, Hara [21], demonstrated analytically that when all properties were evaluated at T_∞, the following relationship would account for variable properties effects in air:

$$Nu = Nu_{cp}\left[1 - 0.055\left(\frac{T_w - T_\infty}{T_\infty}\right)\right] \tag{1-8}$$

For those authors recommending a reference temperature method, definitions for T_r ranged from a film temperature [23,26] to that given in Ref. 22:

$$T_r = T_w - 0.38(T_w - T_\infty) \tag{1-9}$$

In most reference temperature methods, β in the Grashof number is evaluated at T_∞. One exception is Clausing and Kempka [26], who recommend that β be evaluated at T_f. Their recommendation was based on experimental laminar heat transfer data obtained in nitrogen at cryogenic temperatures, where T_w/T_∞ ranged from 1.0 to 2.6.

Variable properties effects on turbulent natural convection in gases have also been examined by several authors [1,23,26]. The numerical predictions of Siebers [1] for natural convection from a vertical surface in the T_w/T_∞ range of 1.0 to 3.0 with T_∞ at 20 C showed that evaluating the properties in the constant properties correlation, including β, at T_f did not correlate the turbulent natural convection heat transfer predictions in terms of Nu and Gr. Pirovano et al. [23] correlated their turbulent natural convection experimental results in air over the T_w/T_∞ range from 1.0 to 1.5, with properties evaluated at a T_r heavily weighted toward T_∞ and with β evaluated at T_∞. Pirovano et al. [23] defined T_r as:

$$T_r = T_\infty + 0.2(T_w - T_\infty) \tag{1-10}$$

If Siebers [1] had used the recommendations of Pirovano et al. [23] to correlate his numerical predictions of turbulent natural convection heat transfer, the results, when expressed in terms of Nu and Gr, would have agreed closely with the experimental results of Pirovano et al. [23]. Clausing and Kempka [26] used properties evaluated at T_f with an additional large temperature-dependent correction to correlate their turbulent natural convection data obtained in nitrogen at cryogenic temperatures. They did note, however, that using T_∞ as the reference temperature at which to evaluate the properties significantly reduced the size of the temperature-dependent correction needed to correlate their data. Most basic heat transfer textbooks generally recommend using properties evaluated at a T_r given by Eqn. (1-9) or T_f with β to be evaluated either at T_∞ or at T_r to account for variable properties effects in both laminar and turbulent flow.

1.4 Present Knowledge of Mixed Convection and Variable Properties Free Convection

The literature survey in Section 1.2 demonstrated that the present knowledge of mixed convection is very limited. What is presently known about mixed convection is based largely on a few numerical, similarity, and perturbation solutions to laminar flow problems on various geometries. These works show that for laminar flow the heat transfer and skin friction vary smoothly from pure forced to pure free convection. The mixed convective heat transfer region in terms of the mixed convection parameter is smaller than the mixed convection skin friction region. Free convection dominates the free convection leading edge and forced convection dominates the forced convection leading edge. The mixed convection parameter for the laminar flow driven by orthogonal forces involves Gr_ℓ/Re_ℓ^2 and most likely an aspect ratio, as indicated in Refs. [3-6]. The heat transfer results of the most complete solution of the orthogonal driving force problem for laminar flow, the numerical solution of Evans [3], indicate that laminar mixed convection heat transfer can be estimated by an expression similar to Eqns. (1-6) or (1-7) with an a of 3.0. The laminar flow predictions of Evans [3] also show the flow angle in the three-dimensional boundary layer varies smoothly from the free-stream to the wall, reaching a maximum value at the wall.

No information currently exists in the literature on the turbulent mixed convection boundary layer driven by orthogonal buoyant and inertia forces, or on the transition from laminar to turbulent flow in that boundary layer. In addition, the methods recommended in the literature for estimating mixed convection heat transfer coefficients are very different and in some cases produce very different answers. There is not enough information available to say which, if any, of the methods are better for the turbulent flows.

The literature survey in Section 1.3 demonstrates that there are conflicting recommendations on how to account for the effects of variable properties in gases on turbulent natural convection heat transfer. These recommendations range from using a reference temperature method with a T_r weighted toward T_w (given by Eqn. (1-9)) and β evaluated either at T_r or T_∞ to a reference temperature method with a T_r weighted toward T_∞ (given by Eqn. (1-10)) and β evaluated at T_∞. Basic heat transfer textbooks generally recommend a reference temperature method with a T_r given by Eqn. (1-9) of T_f and β evaluated either at T_r or T_∞, but recent experimental and numerical works [1,23,26] point to a T_r weighted toward T_∞ with β evaluated at T_∞. The differences in these various recommendations are significant when there are large temperature differences across the boundary layer.

Laminar flow results generally indicate that evaluating all the properties in the constant properties correlation at T_f and β at T_∞ will account for variable properties effects on laminar free convection in gases. An exception to this recommendation is a recent experiment conducted in nitrogen at cryogenic temperatures by Clausing and Kempka [26]. Clausing and Kempka recommend evaluating β at T_f, along with the rest of the properties, to account for variable properties effects in laminar flow.

1.5 Objectives

The objective of this experiment is to study the convection heat transfer from, and the boundary layer flow on, a surface where the boundary layer flow is driven by orthogonal buoyant and inertia forces, the surface being a large, vertical surface which is parallel to a horizontal flow of air. The emphasis is on mixed convection driven by orthogonal buoyant and inertia forces, but the effects of variable properties on heat transfer from the surface are also studied. The mixed convection data from this experiment is the first available on turbulent mixed convection driven by orthogonal forces.

The information is being used: (1) to develop a basic understanding of mixed convection, (2) to support the development of a computer code to predict heat transfer in a three-dimensional, boundary layer (turbulent and laminar) driven by orthogonal forced and free convection forces (such a computer program is being developed under the direction of Professor Joel Ferziger at Stanford University), and (3) to help develop a simple method for estimating the convection heat transfer from an external type receiver, a method which includes the effects of mixed convection and variable properties on heat transfer.

In support of these tasks, the specific objectives of the experiment are:

1. To measure the rate of convective heat transfer from a flat, vertical, smooth, heat transfer surface under carefully controlled starting and boundary conditions in the Grashof and Reynolds number range of a near-full-scale receiver (near as practical).
2. To measure the mean boundary layer velocity, flow angle, and temperature profiles under the same conditions as number one above.
3. To locate the transition zone as a function of test conditions.
4. To design and construct the facility to accomplish the above objectives on one heat transfer surface, which will help ensure consistent results over widely varying test conditions.

1.6 The Experiment

A smooth, flat, vertical, surface, 2.95 m long by 3.02 m high, with a horizontal air flow over it was electrically heated to generate the three-dimensional boundary layer driven by orthogonal buoyant and inertia forces described in Section 1.1. The surface was located in one vertical wall of a wind tunnel and had negligible pressure gradients on it. The surface heat flux, which included convection and radiation from the front of the test surface and conduction through the back, was uniform. The surface heat flux ranged from 200 to 13,000 W/m^2, resulting in surface temperatures in the 40 to 600 C range. The free-stream air velocity ranged from 0 to 6 m/s. The boundary layer was initially laminar, but transitioned to turbulent flow. A stagnation line was established as the forced convection, or vertical, leading edge condition. The horizontal, or free convection, leading edge was defined as the horizontal line where heating started near the lower edge of the test surface.

Detailed measurements of the surface convective heat transfer coefficients were made along with boundary layer mean velocity, flow angle, and temperature profiles. The heat transfer coefficients were obtained through an energy balance which accounted for the electric power dissipated by the surface, conduction of energy through the back of the surface, and radiation from the front of the surface to the surroundings. The boundary layer flow angle and velocity profiles were measured with pressure probes while the temperature profiles were measured with a thermocouple.

Figure 1-3 compares the operating domain of the experiment in terms of the Grashof number and the Reynolds number squared to the region of existing data in the literature related to the problem being studied here. The operating domain is the region inside $Gr_H = 2 \times 10^{12}$ and $Re_L^2 = 2 \times 10^{12}$. It is subdivided into initial guesses at the free, mixed, and forced convection heat transfer zones. The zones are separated by lines of constant Gr_H/Re_L^2 equal to 10.0 and 0.1. The approximate region of existing data in the literature is the dark gray region. This region is composed mainly of pure free and pure forced convection information, but does include some limited laminar mixed convection information The mixed convection information in the literature is generally in the form of numerical, perturbation, or similarity solutions, as indicated in Section 1.2. The figure shows that this experiment adds greatly to the existing body of heat transfer information, particularly, in the area of turbulent mixed convection heat transfer. In addition (something not shown in Fig. 1.3), none of the high-Grashof number free convection data in the literature is at temperatures above 150 C. Thus there is little information on the effects of significant property variations at high temperatures on free convection heat transfer from a vertical surface. The free convection data from this experiment are the first turbulent, high-temperature free convection data available. They cover a temperature range from ambient to 520 C or a T_w/T_∞ range of 1 to about 3.

Thirty-seven distinct heat transfer cases were run. Five of the cases were for baseline purposes, three of which were low-temperature pure forced convection cases and two of which were low-temperature pure free convection cases. The baseline results were compared with existing data in the literature. Also, included in the heat transfer data are several replications of baseline tests, as well as other test conditions, that were conducted to check the repeatability of the experiment.

For eleven of the thirty-seven heat transfer cases above, plus one cold wall condition, boundary layer data sets were taken. A boundary layer data set consists of mean temperature, velocity, and flow angle profiles at various locations on the test surface. A pure forced-flow, low-temperature set and the cold wall set were taken for baseline purposes. These data sets, which contained laminar and turbulent profiles, were compared with forced flow laminar and turbulent profiles reported in the literature.

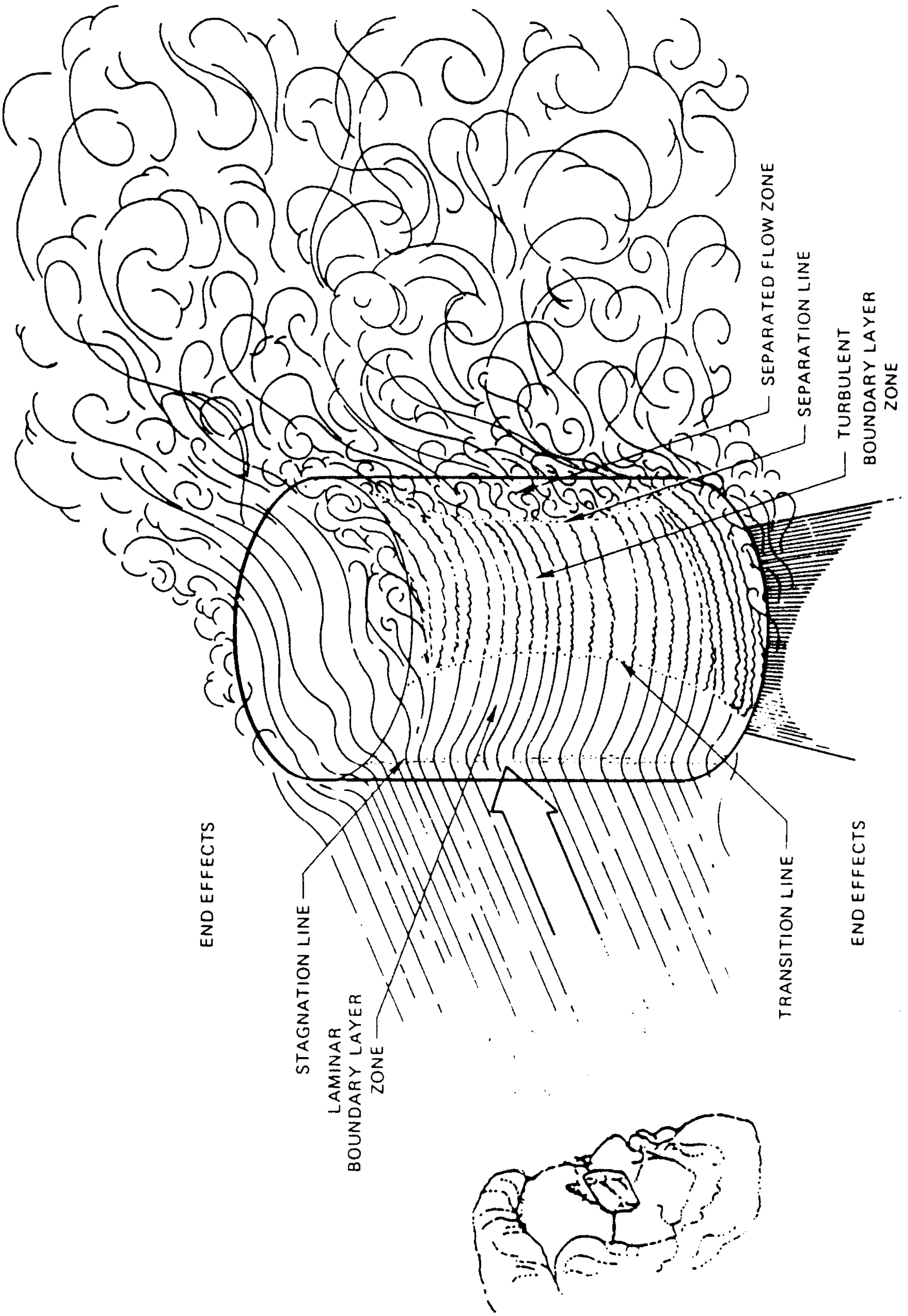

Fig. 1-1 Schematic of the Convection Heat Transfer Zones on an External Receiver.

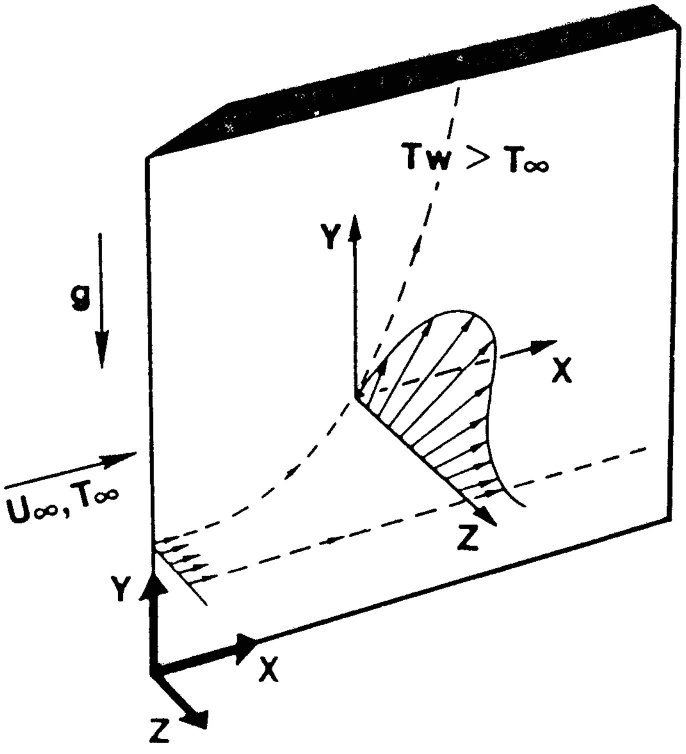

Fig. 1-2 Schematic of a Mixed Convection Boundary Layer on a Vertical Surface.

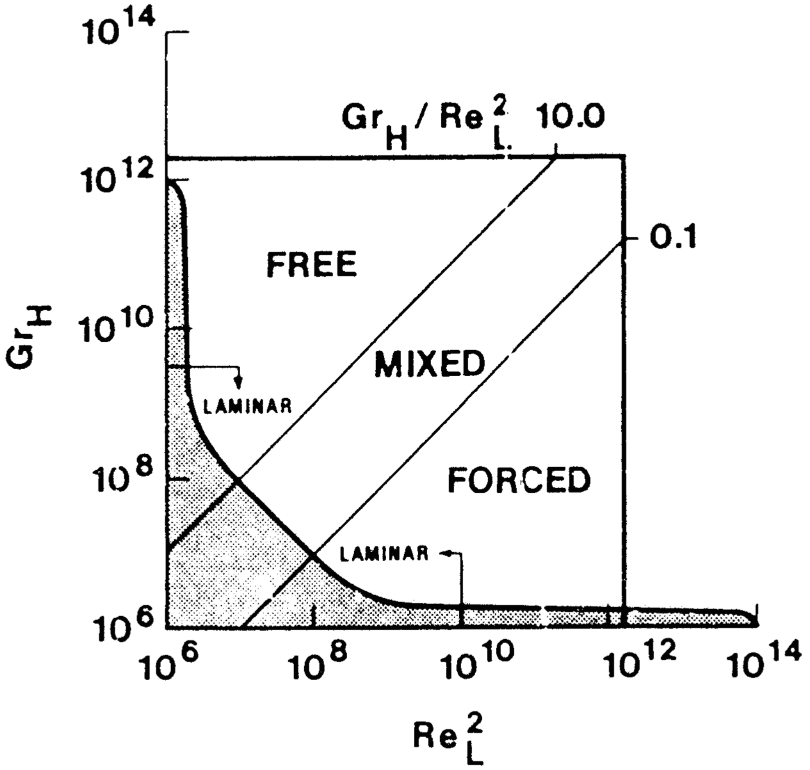

Fig. 1-3 Schematic of the Operating Domain of the Experiment in Terms of Gr_H and Re_L.

Chapter 2.

THE EXPERIMENTAL APPARATUS

The experimental apparatus consists of a wind tunnel, a flat electrically heated surface in one vertical wall of the wind tunnel, a probe traverser, and a system for acquiring and on-line reducing the data from various instrumentation. This apparatus is located at Nielsen Engineering and Research, Incorporated in Mountain View, California. The objective in building the apparatus was to provide a high quality repeatable environment in which to study heat transfer from a vertical, flat, high temperature surface parallel to a horizontal flow of air over a range of Grashof and Reynolds numbers which included pure free convection, pure forced convection, as well as mixed convection.

The following brief discussion of the apparatus is divided into several sections. First, there are discussions of the wind tunnel and the test surface designs. These are followed by discussions of the leading edge suction, the traverse mechanism, the test control and data acquisition systems, the sensors and instrumentation, and the data reduction. The final section presents experimental uncertainties of the individual measured quantities and the final reduced results.

More detailed discussions of the design philosophy, the design details, and the facility construction can be found in Ref. 27.

2.1 Wind Tunnel

The wind tunnel is an open-return draw-through wind tunnel located outside on the leeward side of a building. The principal design requirements on the wind tunnel were that it provide a test section with a 0.0 to 6.0 m/s, low turbulence, steady, uniform flow with no significant axial or vertical pressure gradients.

A photograph of the wind tunnel is shown in Fig. 2-1 and a schematic in Fig. 2-2. The schematic shows the backside of the wind tunnel, not visible in the photograph in Fig. 2-1. Starting foremost in the figures, the major features of the wind tunnel are: the inlet, a screen pack, a plenum, an inlet nozzle, a test section with the test surface in the back vertical wall, a transition nozzle, and a fan driven by a V-8 automobile engine.

The inlet is a screened-in antechamber four times the test section width (4.9 m wide, 4.3 m high, and 1.2 m deep) . It provides preliminary straightening of the air flow which may approach the tunnel from any direction depending upon the wind. The design is modeled after NASA's inlet design for the 80× 120 foot open return tunnel, which operates under the same ambient conditions as this tunnel [28]. This design minimizes the effects of external wind gusts on the quality of flow in the test section. In addition, the 0.61 *m* overhang at the top of the inlet minimizes flow distortion in the wind tunnel due to flow acceleration around the top lip of the tunnel. The ground serves this purpose on the bottom.

The screen pack consists of 5 screens with 58.8% open area (14× 18 mesh Aluminum wire 0.033 *cm* dia.) placed 30 *cm* apart. Both the screen pack and the plenum immediately following the screen pack are in a section approximately three times the test section width, but both have the same height as the test section (3.66 *m* wide by 4.3 *m* high). The inlet nozzle that follows the plenum is two-dimensional and has a 3:1 contraction into the test section. The test section is 1.12 *m* wide at the inlet, 4.3 *m* high, and 4.3 *m* long. There is a divergence of about 4 *cm* in the width of the test section in the downstream direction to minimize axial pressure gradients due to boundary layer growth on the tunnel test surface wall and the wall opposite the test surface.

The test surface is in a cutout approximately 3 *m* high and 3 *m* long in the backwall of the test section. Its location is shown in Fig. 2-2, the wind tunnel schematic. Vertically, the test surface starts 0.5 *m* from the floor and stops 0.8 *m* from the ceiling. Horizontally, it starts approximately 0.6 *m* from the upstream end of the test section and extends to about 0.6 *m* from the downstream end of the test section. The test surface protrudes 3 *cm* into the test section (2.8% of the test section width) to compensate for the boundary layer suction at the leading edge of the test surface, discussed in Section 2.3. This is about the thickness of the layer of fluid removed from the oncoming flow at the leading edge.

The test section is followed by another screen and a two-dimensional nozzle (the transition nozzle). The nozzle provides a 3.5:1 flow contraction into the tunnel fan. The autotransformers used for power control are located in the transition nozzle for cooling purposes. They had no detectable influence on the flow upstream in the test section.

The tunnel is driven by a Joy Mfg., Axivane Fan (Series 2000), 1.22 *m* diameter with vanes locked in the maximum flow position for the best match with the wind tunnel requirements. The fan is driven through a V-belt drive by a V-8 automobile engine with an automatic transmission. The drive range on the transmission was manually selected to achieve a stable engine RPM for the required tunnel air flow rate.

Thermal considerations affected the design of the wind tunnel in two ways. First, the hot inner portion of the boundary layer flow (approximately the inner 10% of the boundary layer thickness) passing off the top of the test surface, as a result of the vertical velocity component in the boundary layer, was removed by suction to minimize stratification in the test section. The suction was applied to three strips of perforated metal, 30% open area, located flush with and along the top of the test surface between the traverse support struts. This is visible in Fig. 2-3, a photograph of the test surface, at the top of the test surface. The ducting for the three suction strips was combined into one 20 *cm* diameter duct. This can be seen at the top of the test surface shown in Fig. 2-4, a photograph of the back of the test surface. The suction was provided by a 10 *cm* diameter ejector centered in the 20 *cm* exhaust duct. A one horsepower centrifugal blower supplied approximately 0.24 m^3/sec of air flow to the ejector nozzle.

The second impact of thermal considerations on the tunnel design was that tunnel wall cooling had to be provided as a result of the high radiant heat loads on the tunnel walls during high temperature tests. This was necessary not only for safety, but from an experimental uncertainty point of view. An uncertainty analysis on the calculation method for the surface heat transfer coefficient (in the design phase of the experiment) showed that the tunnel walls should be held below 70 *C*, even for the 600 *C* surface temperature tests. If this were done, the temperature of the tunnel walls would not have to be measured very accurately and the walls could be lumped together as one background temperature in the determination of the radiation heat transfer correction to the heat transfer coefficient calculation. These considerations led to the steel test section construction with water cooled walls, a water cooled aluminum floor in the test section, and a screen across the downstream end of the test section. The steel walls and ceiling construction provided an adequate conduction path so that cooling water could be applied on the outside of the tunnel walls. The floor was two sheets of aluminum with water flowing in the gap between the sheets. The screen downstream of the test section partially shielded the plywood downstream section from radiant energy from the test surface. The radiant energy absorbed in the screen was convected into the tunnel air leaving the test section. The upstream walls were not clearly visible to the test surface in a radiation heat transfer sense, so no cooling was necessary. The cooling systems kept the maximum tunnel wall temperature at or below 40 *C*.

2.2 Test Surface

The test surface is a 2.95 *m* long by 3.02 *m* high heated surface mounted vertically in the back wall of the wind tunnel. The principal design requirements were that the test surface be smooth, have a uniform heat flux, induce no pressure gradients in the tunnel, have known leading edge or starting conditions for the boundary layer, and be capable of operating from ambient to 600 *C*. It was also important to minimize conduction heat loss through the back, the time to reach steady-state, and the radiation heat loss from the front side.

The front and backside of the test surface are shown in the photographs in Figs. 2-3 and 2-4, respectively. Figures 2-5 and 2-6 are schematics of the front of the test surface and a cross-section of the test surface, respectively. The surface is composed of several layers as schematically shown in Fig. 2-6. First, there is a support frame made of steel weldment and expanded metal grid, which is seen from the back in Fig. 2-4. This support frame has a radius of curvature of 80 meters in a horizontal plane creating a 1.4 *cm* crown on the vertical centerline of the test surface. Next there is a 5.38 *cm* thick buildup of "Fiberfrax" insulation over the weldment as shown in Fig. 2-6. Stretched over the insulation is a layer composed of 21 parallel and horizontal strips of 304 stainless steel, 0.0127 *cm* thick by 14.43 *cm* wide. The strips are electrically heated to provide the uniform heat flux surface. These are the horizontal strips visible in Figs. 2-3 and 2-5.

The purpose of the surface curvature is to create a contact pressure between the stainless strips, which are held in tension by springs on the backside of the surface (see Fig. 2-4), and the insulation. This keeps the strips in tight contact with the surface and helps hold the insulation in place between the frame and heated stainless steel strips. The axial pressure variation in the tunnel caused by this curvature is insignificant (see Section 3.1).

The build-up of insulation material, shown in Fig. 2-6, consists of three layers of "Fiberfrax", a high temperature ceramic fiber insulation manufactured by the Carborundum Corporation. The first layer, wired to the metal frame, is a 1.27 *cm* thick layer of "Duraboard". The second layer is 3.81 *cm* thick layer of the same material. The surface of the second layer was sanded smooth and covered with a 0.15 *cm* layer of Fiberfrax "Paper", a soft felt-like material. The first two layers were cemented together and cracks filled with Fiberfrax "LD Moldable". The "Moldable" added another 0.15 *cm* of thickness to give a total measured thickness of 5.38 *cm* for the insulation layer. Appendix A gives the thermophysical properties of these materials.

The 21 stainless steel strips are wrapped around rollers, 10.2 *cm* in diameter, at each end of the test surface and attached to electrically insulated end clamps on the backside, as seen Fig. 2-4. Each strip is held in tension by two springs at one end which also take up the approximately 2 *cm* of expansion that occurs when the stainless steel is heated to 600 *C*. Details of the attachment can be found in Ref. 27. The nominal gap between strips is 0.64 *cm*. This gap assures electrical isolation between strips even with some lateral creep and expansion of the strips. The edges of each stainless steel strip are folded under as shown in Fig. 2-6. The amount of material folded under on each edge, 0.32 *cm*, is one-half the nominal gap width between strips. The fold serves two purposes. First, it prevents a form of wrinkling of the strips noted in prototype strip designs. Second, it provides an additional amount of heating locally to make up for the unheated gap between strips. Some of the stainless steel folded under is pulled into the soft Fiberfrax "Paper" because of the tension in the springs as indicated in Fig. 2-6. This minimizes the roughness caused by the gap between strips.

The emittance of the 304 stainless steel was 0.13 at room temperature and about 0.22 at the highest temperatures. This was repeatable and reproducible throughout most of the test as shown by the experimental measurements of the total, hemispherical emittance versus temperature presented in Appendix B.

Three-phase 208 *volt* AC power was used to resistance heat the test surface. Figure 2-7 shows a schematic of the power distribution system and power measurement instrumentation which will be discussed later. The strips are divided into three groups of seven, with the seven strips in a group being connected in series. The three groups of strips are connected either in "Y" configuration or a "Δ" configuration (as shown in Fig. 2-7) to the legs of the three phase power supply. The configuration chosen depended on the power requirements for the test. The "Y" gave better control at low power while the "Δ" allowed higher power settings. Each leg is controlled by a bank of six, parallel connected, 70 *amp* autotransformers.

The forced convection (vertical) leading edge starting condition on the test surface was a stagnation line formed downstream of the vertical leading edge suction slot. The leading edge suction removed the boundary layer developing on the tunnel wall upstream of the test section. This is schematically shown in Fig. 2-5 in the detail in the upper left corner and is discussed further in Section 2.3. The free convection (lower horizontal) leading edge of the test surface can be seen in Figs. 2-3 and 2-5. It consists of about 6 *cm* of unheated insulation which forms a smooth extension of the test surface (the crosshatched region at the bottom in Fig. 2-5). The unheated insulation is preceded by a step of about 3 *cm*. The step is caused by the test surface protruding 3 *cm* through the tunnel wall into the test section. Support struts for the traverse extend through the unheated insulation at the lower leading edge as shown in Figs. 2-3 and 2-5. The effect of the support struts on the flow is discussed in the tunnel qualification section, Section 3.1, and Appendix D.

The test surface design described in this section provided a heat transfer surface with the following characteristics:

1. Smooth, except for the roughness of the exposed insulation between the heating strips, which is felt-like, and the small step along the edges of each strip, which is nominally the strip thickness (0.127 *mm*),
2. Uniform heat flux, except for local resistance variations due to temperature variations (discussed in Section 2.7) and the gap between strips,
3. A response time of 80 to 120 minutes (time to reach steady-state),
4. A loss of energy by conduction through the insulation on the back of the test surface equal to 6-14% of the electric power dissipated,
5. A loss of energy by radiation from the front of the test surface equal to 4-50% (depends on the surface temperature) of the electric power dissipated,
6. Negligible effect on static pressure in the free-stream (discussed in Section 3.1),
7. Accurate power control,
8. A known vertical leading edge starting condition.

The roughness size described in item one above is small compared to the boundary layer thicknesses studied except very near the stagnation line at the vertical leading edge. The flow is aligned with the gaps between strips in that region which minimizes any effect of the roughness. The unheated gaps between strips is partly compensated for by the folded under edges of the strips which release additional energy locally.

2.3 Leading Edge Suction

The boundary layer developing on the upstream wind tunnel test section wall is sucked off through a slot at the leading edge of the test surface. This process establishes a two-dimensional stagnation line as the forced convection or vertical leading edge starting condition. A new boundary layer grows on the test surface downstream of the stagnation line location. This method of starting a boundary layer was used because of the difficulty in designing a sharp leading edge on this test surface. Figure 2-8 is a cross-section of the leading edge suction apparatus. Flow sucked off at the test surface leading edge, passes through a passageway around the rear of the test surface, and returns to the test section at the downstream end of the test surface. The return flow enters the test section as a wall jet approximately 1 *cm* thick through a slot facing downstream, as shown in Fig. 2-8. This was done to provide thermal protection of the downstream tunnel wall from the hot boundary layer leaving the downstream end of the test surface. This arrangement has no influence on the flow upstream on the test surface.

The upstream suction arrangement consists of two suction slots created by placing a strip of fiberglass, 13 *cm* wide and 3 *mm* thick, away from the leading edge of the test surface, as shown in Fig 2-8 (the fiberglass plate). The fiberglass plate extends the full vertical height of the test surface. The gap which faces upstream, between the fiberglass and the tunnel wall, forms a suction slot nominally 1.9 *cm* thick. The trailing edge of this plate is spaced 0.6 *cm* off the test surface and acts as a second suction slot facing downstream. The large slot facing upstream is used to remove the tunnel wall boundary layer. The smaller downstream facing slot is used to establish the stagnation line starting condition on the test surface and to remove the boundary layer that grows on the fiberglass plate, as shown in Fig. 2-8. This arrangement is visible in the photograph in Fig. 2-3 and is shown schematically in a detail in Fig. 2-5.

The 0.64 *cm* wide gaps between the stainless steel strips were covered with thin mica sheets from the rollers at the upstream end of the test surface to the upstream edge of the Fiberfrax insulation. This prevented three-dimensional leading edge flow patterns from developing as a result of suction through the gaps.

The passageway around the rear of the test surface was created by placing a 0.41 *m* deep plywood box over the back side of the test surface, as shown schematically in Fig. 2-8. This box was attached to the edges of the test section cutout for the test surface. A vertical header in this box divides the passageway into upstream and downstream sections. Mounted in the header is a 22.9 *cm* diameter, variable speed, axial flow, DC blower, which pumps air from the upstream compartment and discharges into the downstream compartment. This provides the suction for the leading edge. The blower is rated at 6550 RPM and produces a flow rate of 0.58 m^3/sec at 620 *Pa*. To maximize its performance, a rounded leading edge piece ducts airflow into the blower inlet, and a 2.1:1 diffuser is attached to the blower outlet.

2.4 Traverse Mechanism

The traverse mechanism has 4-degrees-of-freedom. It can position a probe at any x and y location on the test surface, traverse the probe normal to the test surface, and rotate the probe about an axis normal to the test surface. The traversing mechanism is seen schematically in Fig. 2-5 and in the photograph in Fig. 2-3. It consists of two horizontal shaft assemblies, one at the top and bottom of the test surface, a vertical shaft assembly (shown centrally located on the horizontal shafts in Fig. 2-5) that rides upstream and downstream on the horizontal shafts, and a commercial 2-degree-of-freedom probe traverser (shown centrally located on the vertical shafts in Fig. 2-5) that rides up and down on the vertical shafts.

The commercial 2-degree-of-freedom probe traverser unit consists of a Slosen stepper motor and a small DC motor. The Slosen is used to traverse the boundary layer probe normal to the test surface at 0.0127 *mm* per step. The DC motor is used to rotate the boundary layer probe about an axis perpendicular to the test surface. The horizontal shaft assemblies, top and bottom, consist of a precision ground shafts each attached to the tunnel wall with four support struts. The support struts hold the entire traverser unit about 0.3 *m* from the test surface, as shown in Fig. 2-5. The bottom assembly includes an ACME threaded shaft. The ACME threaded shaft is turned by a 1 *HP* DC motor. It drives linear bearings on the horizontal precision ground shafts axially to provide x-direction mobility. Attached to the linear bearings on the horizontal shafts is the vertical shaft assembly (the vertical shafts, drive motor, and commercial probe traverser unit). The vertical shaft assembly consists of two precision ground shafts. A linear bearing is driven up and down on these precision ground shafts by a vertical ACME threaded shaft that is turned by a 1 *HP* DC motor also. This provides y-direction mobility. The commercial unit is attached to the linear bearings on the vertical shafts.

The boundary layer probe is mounted in plastic bushings for electrical isolation from the probe mount on the commercial probe traverser unit. The probe stem is attached to the z-yaw drive system through a small, thin-walled bellows to provide stiffness in yaw but flexibility in the z-direction. The bellows was intended to prevent damage to the probe if the test surface was touched. The probe is discussed in Section 2.6.3.

Thermal protection is required for all parts of the probe traversing mechanism. The standoffs are water cooled. The horizontal shafts, ACME thread, and linear bearing assemblies have sheet metal radiation shields aligned parallel to the flow (see Fig. 2-3). These shields are fabricated from stainless sheet with a standard Number 4 Bright Finish to provide good reflection of the radiant energy away from the heated test surface. The vertical shaft and ACME thread are shielded by a water cooled copper shield which is in the shape of one side of an airfoil with 30 *cm* chord. Attached to the copper shield's trailing edge is an adjustable flap with a 13 *cm* chord. The flap is perforated sheet metal with a 30% open area. The shield and flap are approximately 30 *cm* out from the test surface. Adjustment of the shield and flap and their effects on the flow are discussed in Section 3.1.

The design of the traversing mechanism involved trade-offs between test section blockage and traversing mechanism stiffness. To greatly enhance the stiffness of the traverser without significantly increasing test section blockage, a remotely operated bar, called the snubber, was included on the traverse. The snubber was located on the commercial probe traverse unit on the side opposite the boundary layer probe, but on an axis parallel to the stem of the boundary layer probe. When extended a few centimeters, the snubber pressed firmly against the test section wall opposite the test surface and prevented the traverse and boundary layer probe from vibrating normal to the test surface. Maximum boundary layer probe head vibration with the snubber in place is ± 0.25 *mm* in the vertical direction. The snubber allowed essentially no probe vibration normal to the test surface.

2.5 Test Control and Data Acquisition

The activities of test control and data acquisition were centered in a test control room in the building alongside the wind tunnel. Test conditions were monitored on a continuous basis to ensure a steady state operation of the facility for each test case, which could last several hours, and to ensure a safe operation of the facility. For this purpose almost all test parameters, along with many parameters monitored solely for safety, were available as continuous readout on gauges or digital displays. These instruments are discussed in Ref. 27. This section deals only with control of the main test parameters and acquisition of the heat transfer and boundary layer data.

Control of the test involved control of four main parameters: test section air speed, leading edge suction rate, test surface power, and boundary layer probe position. Tunnel air speed was controlled manually by adjusting the engine throttle and transmission to settings which resulted in the desired tunnel speed. The throttle could be set from the control room. Leading edge suction rate was controlled by manually setting a DC power supply for the suction fan. Calibration of the suction rate versus suction fan speed and tunnel air speed are discussed in Section 3.1. Test surface power was controlled manually. A circuit breaker in the control room was used to switch power on and off. Power level was controlled by adjusting the three banks of autotransformers previously described. This was done by adjusting the control shafts, one from each bank of transformers, that extended through the tunnel wall in the transition nozzle, as shown in Fig. 2-2.

The boundary layer probe was positioned by use of the traverse controller located in the control room. The traverse controller consisted of x and y motor controls for the ACME threaded shafts, the traverse snubber control, the probe z-drive stepper motor translator logic and control, the probe yaw comparator logic and control, and the limit controls to prevent probe and traverse from being moved outside certain position limits for all directions. Also included was the sensor for probe-test surface contact detection.

The x and y motions were controlled by manual operation of the traverse controller. Movement in the z-direction was either by manual or mini-computer (the computer is discussed later) operation of the controller. Mini-computer operation of the controller for movement in the z-direction involved first locating the wall with the boundary layer probe. The probe was driven into the wall under control of the mini-computer until an electronic touch sensor indicated contact with the wall and stopped the probe motion. The probe was then backed away 1.5 *mm* and recontacted with the wall by the computer. This produced a repeatable wall touch which flexed the probe into the wall by 0.2 *mm*. This meant the probe stepper motor had to be stepped an equivalent of 0.2 *mm* outward from the wall before the probe tip left the wall again. With the wall located the boundary layer probe could now be stepped through the boundary layer at predetermined intervals by the mini-computer with the velocity, flow angle, and temperature data measured automatically after each step.

Probe yaw angle control was also done automatically. A feedback control system, called the probe yaw comparator, used the pressure difference between the probe yaw ports (see Section 2.6.3) to drive the traverse yaw motor until the pressure difference between those ports was zero. This pointed the probe in the flow direction. Since the response time of the probe yaw control system was very slow ($\approx$1 minute), the probe direction changed only as the mean flow direction changed.

Data acquisition from all sensors, with exception of the barometric pressure and surface emissivity, was done through the analog-to-digital converter of a mini-computer system. The computer reduced and displayed the data on-line and stored the "raw" data on hard disk for later detailed data analysis. In addition, the computer was used to control the movement of the boundary probe, as discussed earlier, and run some of the data acquisition equipment.

The mini-computer was an LSI-11/23 configured with a clock, analog-to-digital converters (A/D), digital-to-analog converters (D/A) and other special functions. The A/D was an Adac analog-to-digital converter with a 10 *volt* range and a 5 *mv* resolution. The system is based upon a PDP-11/23 CPU with 80K words of memory. Two hard discs provide permanent storage. Information was displayed on a CRT or by a printer.

Two simple diagnostic programs and three comprehensive data acquisition and reduction programs were written for the experiment. One diagnostic program was used to check the A/D function of the computer and cables from the computer to the signal conditioners. The other diagnostic program allowed an individual sensor in the experiment to be isolated. That sensor's performance could then be studied or known signals could be sent through its leads to check out the entire data acquisition system.

The data acquisition program for heat transfer data was "TEST". This program controlled the scanners (discussed later) which cycled all the transducer information through the computer A/D channels, processed the data from the A/D channels, converted it to engineering units, stored the raw voltage and converted signals on hard disk, and displayed some preliminary results. Data for heat transfer tests were taken at a 240 *hz* rate in a 900 sample burst, once for each of the scanner channels. The reduction of the sensor information in engineering units to heat transfer coefficients, etc. was done by a program called "REDUCE".

Boundary layer probe control, scanner control, data acquisition from A/D channels on the computer, data reduction, and data presentation of the boundary layer data were performed using one program, "BLTEST". After manually adjusting the probe to a desired x and y position on the test surface, the program would present the x and y position as read from the potentiometers, control the probe as it moved inward in the z-direction to find the wall, and step the probe away from the wall according to a selected schedule of positions, obtaining data at each position. Boundary layer data, including probe location, were taken at a 900 *hz* rate in 200 sample bursts 24-52 times per scanner channel. This data was then reduced and stored.

Appendix E contains the heat transfer data and the listings of "TEST" and "REDUCE". Appendix F contains the boundary layer data and a listing of the program "BLTEST". These versions of "TEST", "REDUCE", and "BLTEST" are different than the versions presented in Ref. 27, which were used for a preliminary data reduction. The major differences are: a temperature dependent emissivity for the stainless steel 304 has been included in the heat transfer data reduction (see Appendix B) rather than the constant value of 0.1 assumed originally; no transient energy storage correction was made in the heat transfer data reduction, none was found necessary; all probe and instrumentation manipulation and control portions were removed; the free-stream flow angle is no longer subtracted from remainder of the boundary layer flow angles for a given profile; the output format was changed; and finally, the program was changed to make it compatible with a larger computing system. As a result, the reduced data presented in Appendices E and F is different than Ref. 27. The present report is the final data reduction.

2.6 Sensors and Instrumentation

The sensors and instrumentation used to obtain heat transfer and boundary layer data are discussed in this section. The discussion is divided into four subsections. The first three sections contain discussions of instrumentation and sensors used to obtain the tunnel conditions, the test surface conditions, and the boundary layer profiles of velocity, flow angle, and temperature, respectively. The final section discusses instruments and hardware in common to the first three sections. Many additional sensors and instruments were used for routine monitoring of facility conditions such as engine temperature, engine oil pressure, fan speed, etc., as well as for monitoring safety aspects of the facility such as, smoke and fire detection. These are discussed in Ref. 27.

2.6.1 Tunnel Conditions

There were seven parameters measured to obtain the tunnel test conditions: the tunnel wall temperature, the tunnel inlet air temperature, the tunnel inlet stratification, the test section stratification, the test section air velocity, the environmental wind speed and direction, and the leading edge suction rate.

The wind tunnel inlet air temperature, tunnel wall temperatures, and test section stratification were measured with type-K (chromel-alumel) 30 gauge thermocouples with an arc welded junction (a bead). The inlet air temperature was measured at mid-height in the plenum of the wind tunnel. Thirty-five thermocouples were used to obtain the tunnel wall temperature. They were glued to the wood walls or peened into the metal test section walls. An array of four thermocouples was used to sense any air temperature stratification in the test section. These thermocouples were mounted in a four-port aspirated probe, one per port. The aspiration eliminated the need for any radiation correction. The probe is located at the downstream end of the test section with the ports on the probe distributed from the top of the test surface to the roof of the wind tunnel.

The wind tunnel inlet air temperature stratification was measured with two matched Iso-Curve (15K) thermistors made by Fenwall Electronics. They were located just downstream of the screen pack, one near the ceiling, the other near the floor. Neither the thermistors nor the inlet air temperature thermocouple discussed above were visible to the hot test surface, which eliminated the need for any radiation correction to their outputs.

A standard pitot-static tube with a tube diameter of 3.2 *mm*, the tunnel-Q probe, was used to obtain the test section air velocity. The probe is visible in Fig. 2-3: it is the small tube sticking out of the test section wall just ahead of the leading edge suction, about halfway up the test surface. The tunnel-Q probe is also shown schematically in Fig. 2-5.

Environmental wind speed and direction were measured with a four-bladed, fast response, 23 *cm* diameter propeller anemometer with tail vane made by R. M. Young Company. It was mounted on the roof of the office building adjacent to the wind tunnel. The location gave a higher wind speed indication than was actually experienced by the wind tunnel, which was located on the leeside of that building. The output was used to determine when tests could be conducted and when tests in progress had to be aborted.

The suction rate was set by measuring the velocity with a pressure probe at a fixed location in the diffuser outlet of the leading edge suction fan. The measured velocity distributions for several test cases were integrated to find the correlation between average velocity and the measured velocity at the fixed probe location. During the test program it was found suction rate could be set just as reliably by setting it based on the suction-fan RPM. When suction rate was set based on the suction-fan RPM, a suction rate was not measured or recorded in the output in Appendix E. The suction rate was always around 4% of the tunnel mass flow rate.

2.6.2 Test Surface Conditions

Parameters measured to obtain the test surface conditions were: the electric power dissipated in resistance heating the surface, the surface temperature, the temperature difference across the Fiberfrax insulation layer, and the surface total-hemispherical emittance. All except the surface emittance were measured during each test by the mini-computer. The emittance was obtained by measuring the emittance of samples of the surface material as a function of temperature from ambient to 600 *C* before and after testing (see Appendix B).

To obtain the electric power dissipated in the stainless steel covering the surface, the RMS voltage drop across each of the 21 stainless steel strips and the RMS current through each strip was measured. These RMS signals were obtained by integrating the digital output from the mini-computer A/D. The voltage drop on each strip was sensed across two small lead wires spot welded to each strip, one at the leading edge and one at the trailing edge of the test surface. The current through each strip was obtained by measuring the current in each of the three legs of the "Y" or "Δ" connection of the stainless steel strips discussed earlier. Since the seven strips in each leg are connected in series in a given leg, this current measurement gave the current through each strip in that leg. Current flow from the system to ground was monitored but none was detected, so all current measured in each leg was assumed to pass through the strips with no leakage through the insulation or test structure to ground. A power factor of one was assumed for each strip. This was confirmed by observing a Lissajous pattern for current and voltage on an oscilloscope. The measurement of the current, which ranged from 20 to 180 *amps*, was obtained by placing the lead cables from each leg of the "Δ" or "Y" through precision Weston Model 321 (.07% accurate) or 461 (.25% accurate) current transformers, as indicated in Fig. 2-7, and reading the voltage drop across a shunt in the secondary of each transformer. The shunts were properly sized for each transformer, and the voltage drop across the shunts was linearly related to the current in each respective leg.

Both the strip voltage and current measurements were calibrated for each test. In the case of the voltage drop measurement this was done by reading the voltage drop across a strip directly with an HP 3466A multimeter (true RMS) and comparing it to the minicomputer RMS output. In the case of the current measurement it could be done in three ways. The first method used three 100 *amp*, leaf shunts (Weston, 20 *amps/mv*) positioned as shown in Fig. 2-7. The voltage drop current relationships for the shunts are accurate to 1/2% up to 200 *amps* (1/4% at less than 100 *amps*). The voltage drops across these shunts were measured with the HP 3466A multimeter and compared to the minicomputer RMS output. The second method of current measurement calibration made use of Model 321 or 461 Weston current transformers. The current in the secondary was measured directly with the HP multi-meter or a Weston Model 904 ammeter. The third method of current measurement calibration made use of an Ohio Semitronics RMS current transducer with model CTIRV current transformer. This could be placed around any leg. The voltage output from the transducer was proportional to the current in the leg. The three current calibration techniques agreed within 0.7%.

The surface temperature was measured with the thermocouple arrangement shown in Fig. 2-9. Figure 2-9 is a schematic of a cross section and a top view of the surface thermocouple assembly. The cross section has been expanded in the figure and is not to scale. This thermocouple design is based on tests on a prototype heat transfer surface. Three type-K 30 gauge junctions are wired in parallel and spread evenly around a 3.81 *cm* radius to obtain a local average temperature over the circle, as shown in Fig. 2-9. A mica layer over the thermocouple provides electrical insulation between the thermocouples and the electrically heated surface. A stainless steel pad under the thermocouple beads prevents the beads from being pressed into the insulation by the force exerted by the stainless steel strips held in tension on the curved surface of the insulation, as discussed in Section 2.2. The pad of Fiberfrax "Paper" insulation under the stainless steel pad provides some spring and insures the assembly is pressed against the stainless strips. Figure 2-10 is a photograph of a surface thermocouple assembly before the heating strip was put in place over the thermocouple assembly. This entire assembly with mica in place was partially depressed into the soft top layer of Fiberfrax "Paper" insulation before placing the heating strips over it. As a result, no bulging or distortion of the stainless steel heating strips was evident because of the thickness of this thermocouple assembly. Any distortion of the stainless steel was clearly visible due to its mirror like finish.

This surface temperature measurement technique has been experimentally shown accurate to the larger of $\pm$ 2 *C* or $\pm$ 1% in the prototype tests. An array of 105 of these surface thermocouples were mounted on the surface at positions indicated by "+'s"in Fig. 2-11. They are located in 10 columns of equal spacing and in 21 rows defined by the 21 strips. The columns are staggered as shown in Fig. 2-11. The first column is 0.229 *m* downstream of the stagnation line. The stagnation line is the assumed start of the heat transfer surface.

In addition to the surface temperature thermocouples an array of 26 type-K 30 gauge "conduction" thermocouples were installed in the surface. The locations are shown as "O's" in Fig. 2-11. They are single bead, arc welded, conventional thermocouples placed between the 1.27 *cm* Fiberfrax Duraboard layer and the 3.81 *cm* layer, as shown in Fig. 2-9. These thermocouples are used in conjunction with the surface thermocouples, the Fiberfrax thermal conductivity, and thickness of the Fiberfrax layer to determine the loss of energy from the surface by conduction through the insulation on the back of the surface.

2.6.3 Boundary Layer

Boundary layer mean velocity, flow angle, and temperature profiles were taken simultaneously with a single probe shown in a photograph in Fig. 2-12. The basic probe design follows that described in Ref. 29 with the addition of a thermocouple for temperature measurement. The thermocouple is not visible in the photograph in Fig. 2-12 due to its small size, but is shown in the schematic of the probe tip in Fig. 2-13. The probe tip consists of a 0.052 *mm* diameter type-K thermocouple with each lead spot welded to another type-K thermocouple bead made from 36 gauge fiberglass coated thermocouple wire. On either side of the 0.052 *mm* diameter thermocouple are two total pressure ports made from 0.813 *mm* O.D. stainless steel tube. Attached on the outsides of these tubes are the probe yaw sensing tubes made from 1.47 *mm* O.D. stainless steel tubes flattened to the thickness of the total pressure tubes. Outboard of these are two static pressure tubes made from 1.47 *mm* O.D. stainless steel tubes.

The pressure sensing ports (total, static, and yaw angle) and the 0.052 *mm* thermocouple bead are located in the same plane, with the static and the total ports in-line, as shown in Fig. 2-13a. The plane containing the pressure ports and the 0.052 *mm* diameter thermocouple bead has a 2° to 3° forward tilt with respect to the probe stem. The 0.052 *mm* thermocouple bead is centered between the total ports and 2.4 *mm* in front of them, as shown in Fig. 2-13a. Since the entire probe tip tilts forward 2° to 3° with respect to the probe stem and since the thermocouple bead is located 2.4 *mm* in front of the total pressure ports, the temperature measurement point in the boundary layer is approximately 0.12 *mm* closer to the wall than the pressure sensing ports.

Figure 2-12 shows that all tubes lead aft into a tube bundle at the "gooseneck". All points on the "gooseneck" are slightly greater than 10 tube bundle diameters downstream of the pressure ports. The probe tip back to the "gooseneck" is gold plated and the "gooseneck" stem is wrapped in aluminum foil to minimize radiant heating of the pressure lines. This minimizes density variations in the pressure lines which would induce errors in the pressure measurements.

The two total pressure tubes are connected in parallel to one side of a pressure transducer described later. The two static tubes are connected in parallel to the other side of the transducer.

The thermocouple wiring arrangement for the fluid temperature thermocouple is shown schematically in Fig. 2-13b. This thermocouple arrangement was used for two reasons. The first was so that stronger lead wires could be used in the probe than the 0.052 *mm* diameter wires used on the tip. The second was so that approximate base temperatures were available for estimation of the conduction error in the fluid temperature measurement. Figure 2-13b shows that the signal across the outer two lead wires gives the fluid temperature, T_f, while the two other pairs of leads give the base temperatures, T_{b_1} and T_{b_2}. Only one signal (across two leads) was read at one time, with the other two pairs left as open circuits. The disadvantage to this arrangement is the noise pick up in the high voltage, high current environment by the extra wire attached to each thermocouple bead. The RMS measured noise level (in terms of degrees C) was around 1 to 2 C compared with about 0.3 C for a conventional single bead thermocouple in same environment.

The position of the boundary layer probe was sensed by reading the output of three calibrated 10-turn wire-wound potentiometers for the x and y positions and the yaw angle. The z-location was obtained by counting the number of pulses the probe was moved from the wall by the stepper motor, at 0.127 *mm* per pulse.

The probe design has the following characteristics summarized from the discussion above and the validation tests that were conducted on the probe to verify its performance:

1. The capability to measure velocity, temperature, and flow angle simultaneously, saving time and insuring a similar test condition for the three measurements.
2. Negligible viscous effects on the pressure measurements at low velocities as a result of the oblong front on the probe tip [30].
3. Negligible errors due to buoyancy induced pressure differences in the pressure lines which result from non-similar temperature variations in the various pressure lines coupled with elevation changes of the pressure lines. This was accomplished by passing all the pressure lines through the same temperature gradients, symmetrically placing them about the probe centerline, and gold plating and foil wrapping the stem.
4. Negligible effect of the probe yaw angle on the velocity measurement over a yaw angle range of ± 10°.
5. Negligible effect of the velocity gradient normal to the wall on the flow direction indicated by the yaw ports.

6. Negligible effect of the probe pitch angle on the velocity measurement over a ±20° pitch angle range and on the indicated flow direction over a smaller range of pitch angle.
7. A fluid temperature thermocouple with minimal temperature measurement error and with negligible influence on the velocity and flow angle measurements. In addition, since each wire of the boundary layer thermocouple was welded to a thermocouple junction, a conduction correction to the fluid temperature measurement, which was small, could be accurately made.

2.6.4 Additional Instrumentation

The pressure differences from the probes discussed in previous sections were sensed by Validyne DP103 differential pressure transducers rated at 55 *Pa* full scale (the dynamic head at about 7 m/s for air at the ambient temperature). The electronics for these transducers, a variable reluctance type, were provided by Validyne CD90 high gain, carrier demodulators. Each transducer, with its own CD90 unit, was calibrated using a Combist Instruments Ltd. micromanometer, which has a resolution of about 0.06 *Pa*. The response of the pressure transducer was very linear. The calibrations of the pressure transducer sensitivities were checked several times during the course of the experiment, using the micromanometer. No significant changes were noted. A calibration resistor was frequently used to check for changes in the pressure transducer read-out circuitry via a built-in system check.

The thermocouple circuitry used a thick-walled foam insulated box as a zone box. In the zone box, the leads from all the thermocouples described in previous sections plus the icebath thermocouple were connected to copper extension leads, which went from the zone box to a Hewlett Packard crossbar scanner in the control room. The connections, insulated from one another by a plastic coating on the connectors, were wrapped together to form a cylinder about 8 *cm* in diameter, covered with a piece of split heavy-walled aluminum tubing, and placed in the zone box. Aluminum tube helped reduce to a minimum any temperature difference between the various thermocouple-copper lead connections. The temperature difference across the aluminum tube was measured by one differencing thermocouple. This temperature difference rarely exceeded 0.5 *C*.

Over 200 signals from the different sensors involved in the experiment were conditioned by the instrumentation both for display on meters and for acquisition by the mini-computer. The number of channels of conditioning equipment and the number of computer A/D channels needed was greatly reduced by the use of two crossbar scanners. Both scanners had gold plated contacts and manual and remote operation modes. Both scanners were programmed to switch three channels at a time, each channel being connected to one A/D channel on the computer. On the first scanner the thermistors, the 21 strip voltages, and the current for each of the three phases were switched in 21 steps. Each of the current readings was repeated seven times while the seven voltages corresponding to that current were being read. The second scanner covered all thermocouples, three at a time in 63 steps. For each data set the first scanner was stepped three times through while the second was stepped once through the thermocouples.

The signals from the six scanner channels, the pressure transducers, the wind speed and direction indicator, and the thermistors were conditioned by a 32 channel differential amplifier (Analog Devices hybrid circuits). Gains ranged from 1.2 to 500, depending upon the input voltage. All amplifiers had 2 *hz* low pass filters except for the channel with the 60 *hz* A/C *amps* and *volts* signals, which were filtered at 500 *hz*. Additional signal conditioning in the form of overvoltage protection for the computer was provided on some channels where there was a possibility of a short to the test surface.

2.7 Data Reduction

This section discusses the data reduction process for several important parameters, flow angle, temperature, velocity, and heat transfer coefficient.

The flow angles were deduced from a direct measurement of the probe angle through use of a calibrated potentiometer. A small correction was made based on the residual pressure difference between the yaw tubes (if any) and the probe yaw angle calibration. This correction was generally very small since the probe was continuously driven so as to point upstream into the flow. This pointing, if perfect, would have resulted in a zero pressure difference between the two yaw tubes.

Temperatures were deduced from the thermocouple signals using the thermocouple temperature-voltage relationships in Ref. 31 for type-K chromel-alumel thermocouples. Corrections were made to the temperatures measured with the surface thermocouples and the fluid temperature thermocouple. The correction made to the surface temperature thermocouple accounted for the fact that it was not in direct contact with the surface. It was found experimentally that this correction could be modeled as an 0.2 *mm* air gap with conduction and radiation heat transfer across the gap. The correction was positive and equal to 1/2 to 1% of the measured temperature.

For the boundary fluid temperatures, an effective temperature at a given velocity measurement location was determined from the actual boundary layer temperature data. This was done for convenience in reducing and displaying the boundary layer data. Recall from Section 2.6.3, that the temperature and velocity measurement locations were not at the same location due to the 2° to 3° forward tilt of the probe tip combined with the fact that the thermocouple bead location was 2.4 *mm* in front of the velocity measurement point. This placed the actual temperature measurement location 0.12 *mm* closer to the wall than the velocity measurement point. A linear interpolation between two successive temperature measurements surrounding any given velocity measurement point in a profile was used to determine the effective temperature at the given velocity measurement point. This effective temperature only differed significantly from the actual temperature measured 0.12 *mm* away from a given velocity measurement point for locations very near the wall (within about 1 *cm* of the wall). The major impact of the use of the effective temperature was that it simplified the data display and data reduction. Errors introduced by the linear interpolation were insignificant compared to the overall data uncertainty to be presented later.

A correction accounting for both radiation and conduction errors was made to the boundary layer fluid temperature measurement (determined as described in the previous paragraph). A four-zone, diffuse, gray body, radiation model was used to account for radiation heat transfer to or from the fluid temperature thermocouple. The zones were the tunnel wall, the test surface immediately below thermocouple, the remainder of test surface, and the thermocouple itself. The net radiant heat flux to or from the thermocouple, determined from the four-zone model using the measured temperatures of each zone as boundary conditions, was used to determine an effective radiation heat transfer coefficient for the thermocouple. This was added to the convection heat transfer coefficient for the thermocouple calculated from the fluid velocity at the measuring point. The overall convection-radiation heat transfer coefficient was used as a boundary condition in a fin-type conduction correction to the thermocouple reading, as described in Ref. 32. The base temperatures for the fin correction were the temperatures measured by the 36 gauge type-K thermocouples onto which the 0.052 mm diameter boundary layer thermocouple leads were spot welded (see Section 2.6.3). The base temperatures were 50 C below the fluid temperature at the peak surface temperature of 580 C, when the probe was near the test surface. The overall conduction-radiation correction was a maximum of about $+20$ C near the wall and less than -5 C in the free-stream at the 580 C test condition, the condition for which the corrections were a maximum. No corrections were made to any other thermocouple readings.

Velocities were deduced from pressure signals using Bernoulli's equation. No corrections for effects due to wall proximity or velocity gradients across the face of the probe tip were made to the velocity measurement [30]. Those two error sources were relatively small in the thick boundary layers considered. The local fluid temperature and the barometric pressure were used with the ideal gas assumption to calculate the density of air in Bernoulli's equation. Since the convection heat transfer coefficient needed in the corrections to the fluid temperature measurement depended on both velocity and density, and since the density (in Bernoulli's equation) depended on fluid temperature, an iteration scheme between fluid temperature and velocity was used to obtain both quantities. The first guess at fluid temperature was the uncorrected fluid thermocouple measurement. With this guess, the iteration scheme converged in two or three steps to the correct velocity and temperature.

The heat transfer coefficient was deduced from the data by an indirect means. At each of the 105 surface temperature measurement locations in Fig. 2-11 the following relationship was used:

$$h(x,y) = \frac{q_{ele}(x,y) - q_{rad}(x,y) - q_{cond}(x,y)}{T_w(x,y) - T_\infty(y)} \tag{2-1}$$

The electric power released from the surface was determined as follows:

$$q_{ele}(x,y) = \frac{EI}{A} A_c R_c \tag{2-2}$$

The voltage E and current I are RMS values measured for each heating strip, and the area A is the area measured for each strip between voltage leads, when the strips were cold. The term A_c is a correction to the strip area which accounts for the thermal expansion of a strip when heated. The term R_c is a local correction term which accounts for resistance variations due to temperature variations along a strip. Appendix C discusses the surface heat flux measurement in more detail.

The radiation energy transfer from the surface to the tunnel walls, q_{rad}, was determined from a three zone, diffuse, gray body radiation heat transfer model. The zones in the model were the tunnel walls, the local spot on the surface where h was being calculated, and the remainder of the test surface. Shape factors between the zones were trivial: 0, 1, or a simple area ratio in the case of the tunnel wall to test surface shape factor, for example. The temperature boundary conditions for the zones were respectively, the average tunnel wall temperature calculated from the 35 tunnel wall thermocouples, the local surface temperature measurement on the test surface, and the average test surface temperature measurement calculated from the 105 surface temperature measurements. The tunnel wall temperature rarely exceeded 40 C at any spot so average tunnel wall temperature was always near ambient and not a significant factor in Eqn. (2-1). The surface emissivities used are given in Appendix B. The term q_{rad} ranged from 4% at low temperatures to about 50% of the energy transferred from the surface at 580 C.

The conduction term, q_{cond}, accounted for energy transferred through the Fiberfrax insulation on the back of the test surface into the air passage for the leading edge suction system (behind the test surface as seen in Fig. 2-8). It was first calculated at the 20 locations on the test surface which had thermocouples that were (1) sandwiched between the two layers of Fiberfrax Duraboard below a surface thermocouple location and (2) more than 8 cm away from an edge of the test surface (see Fig. 2-11). The calculation was based on a one-dimensional conduction model between the surface temperature measurement point and the conduction thermocouple location. Variation of the thermal conductivity of the insulation, with temperature, was accounted for in the one-dimensional model, as were the thermal conductivities of the different layers of insulation. A numerical, three-dimensional conduction analysis of the insulation showed that the one-dimensional conduction model was accurate to within 1% for areas of the test surface 8 cm away from its edges.

The conduction energy transfer rates determined at the 20 "conduction" thermocouple locations were divided by the driving potential for heat transfer through the insulation: the local difference between the surface and the air temperature in the leading edge suction passageway behind the test surface. This gave the heat transfer resistance to conduction through the insulation at each of the 20 locations, which was then least squares fit versus the temperature difference (local surface to backside air). It was this curve fit that was used to calculate the conduction heat loss through the insulation at all the 105 surface temperature measurement locations, based on the local surface to backside air temperature difference at each location. The 105 locations included the 20 locations which were used to generate the least squares fit. For the thermocouple locations on the top and the bottom heating strips, which were within 8 *cm* of an edge of the test surface, the one-dimensional conduction loss through the insulation was increased by 5% based on the results of the numerical three-dimensional conduction analysis.

The wall temperature in the denominator of Eqn. (2-1), T_w, is the local wall temperature reduced as discussed earlier. The free-stream air temperature, T_∞, was generally uniform in the test section except for the high temperature free convection cases. There was up to a 10 *C* difference between the air at the middle and the top of the test surface, for the highest temperature free convection case, 520 *C*. This was measured with the stratification probe. For these cases a local free-stream temperature was used in determining h, obtained by assuming a linear variation of the free-stream temperature in the vertical direction over the top half of the test surface.

Transient energy storage was not considered directly in calculating the surface heat transfer coefficient, since data were taken only under steady-state conditions. The steady-state condition was determined, however, by estimating a transient energy storage term. Each data set recorded for a given test condition consisted of two sets taken several minutes apart. The transient energy storage term for the insulation was estimated by determining the mass average temperature change of the insulation, which contained most of the system thermal capacity, over the time period between the two data sets. Data were kept only when this term was less than about 1% of the electric power dissipated. The term is printed out with each heat transfer data set in Appendix F.

The thermal boundary layer thickness, the displacement thickness in the x-direction, and x-momentum thickness in the x-direction, used in presenting the boundary layer data in Chapters 3 and 4, were calculated based on the following definitions, respectively:

$$\delta_t = \int_o^\delta (\frac{i - i_\infty}{i_w - i_\infty}) dz \tag{2-3}$$

$$\delta_x = \int_o^\delta \frac{(\rho_\infty U_\infty - \rho u)}{\rho_\infty U_\infty} dz \tag{2-4}$$

$$\delta_{xx} = \int_o^\delta \frac{\rho u (U_\infty - u)}{\rho_\infty U_\infty^2} dz \tag{2-5}$$

The integrals were evaluated with an adaptive Simpsons-rule integration routine [33]. The velocity and temperature profiles were interpolated as needed by the integration routine with quasi-Hermite spline fit (piece-wise cubic polynomials with continuous first derivatives) [34]. This same method was used to evaluate the rest of the integral boundary layer parameters defined in Appendix F. The enthalpy of air was obtained from a table search of enthalpy versus temperature.

The material properties used in the data reduction are given in Appendix A.

2.8 Experimental Uncertainty

An *n'th* order uncertainty analysis of the four main quantities deduced from the data was performed. These include the local surface heat transfer coefficient and the boundary layer velocities, temperatures, and flow angles. An uncertainty analysis was also used initially as part of the experimental planning process. In the planning stage it served as the principal criterion for choosing among alternative measurement techniques and for setting the standards for acceptable accuracy on the individual measurements. The uncertainty analysis followed the single sample uncertainty analysis method recommended by Kline and McClintock [35]. This method can be summarized as follows:

If the data reduction equation is given by

$$F = f(x_1, x_2, ..., x_n) \tag{2-6}$$

where F is the reduced quantity and the x_i's are n-measured quantities needed to calculate F, the single sample uncertainty in F is

$$\delta F = \left[\sum_{i=1}^{n} (\frac{\partial F}{\partial x_i} \delta x_i)^2 \right]^{1/2} \tag{2-7}$$

The δx_i are the uncertainty intervals in each of the measured quantities and $\partial F/\partial x_i$ are the sensitivities of F to each of the measured quantities.

The method is based on two important assumptions. The first is that the measured quantities are independent and uncorrelated. The second is that the uncertainty in each measured quantity is a stochastic uncertainty with the same confidence or odds on happening. The second assumption implies that a zeroed centered experiment has been designed having no biased (non-random) errors.

Based on this method of analysis, the *n'th* order uncertainty in the four main reduced quantities (expressed in some cases as a percent of the absolute value) are given in Table 2-1. The upper range of uncertainty on the surface heat transfer coefficient applies for high temperature, low velocity runs. The upper limit on uncertainty for boundary layer velocity, flow angle, and temperature are average uncertainties that apply near the wall. The uncertainty in parenthesis for velocity and temperature is the worst case uncertainty for those parameters. The worst case uncertainties occurred when the probe was near the wall during a high temperature low velocity test (T_w=420 C and U_∞=1.5 m/s). The uncertainty values were higher than the rest because of the very low velocities near the wall for that test. Two or three data points away from the wall for those profiles, the uncertainty was again in the ranges given in Table 2-1.

The single sample uncertainties in the measured quantities used in the uncertainty analysis above, as well as uncertainties in other important reduced parameters, are given in Table 2-2.

Table 2-1
Results of the Uncertainty Analysis for the Four Main Reduced Parameters

Parameters	Uncertainty
Local convective heat transfer coefficient	6% to 10%
Boundary Layer Velocity	3% to 6% (20%)
Boundary Layer Flow Angle	2° to 4°
Boundary Layer Air Temperature	2C to 4% (7%)

Table 2-2
Input Uncertainties to the Uncertainty Analysis for the Four Parameters
in Table 2-1, Plus the Uncertainties for Other Parameters

Parameter	Uncertainty
x- or y-distances on the test surface	±0.3 *cm*
z-distance from wall	±0.12 *mm*
Stainless steel thickness	±1%
Uniformity of stainless steel energy release	±1%
Insulation thickness	±0.1 *cm*
Insulation thermal conductivity	±5%
Voltage drop across a strip	±1%
Current in each phase	±0.7%
Resistivity of stainless steel - 304	±5%
Thermal expansion coefficient for stainless steel - 304	±10%
Surface temperature	±2 *C* or 1%
Free-stream temperature	±1 *C*
Average tunnel wall temperature	±2 *C*
Thermocouples before correction	±1 *C* or 3/8%
Barometric pressure	±130 *Pa*
Dynamic pressure differences	±0.06 *Pa*
Emissivity of stainless steel - 304	±0.01
Emissivity of tunnel wall	±0.1
Minicomputer A/D (resolution)	±5.0 *mv*

Fig. 2-1 Photograph of the Wind Tunnel.

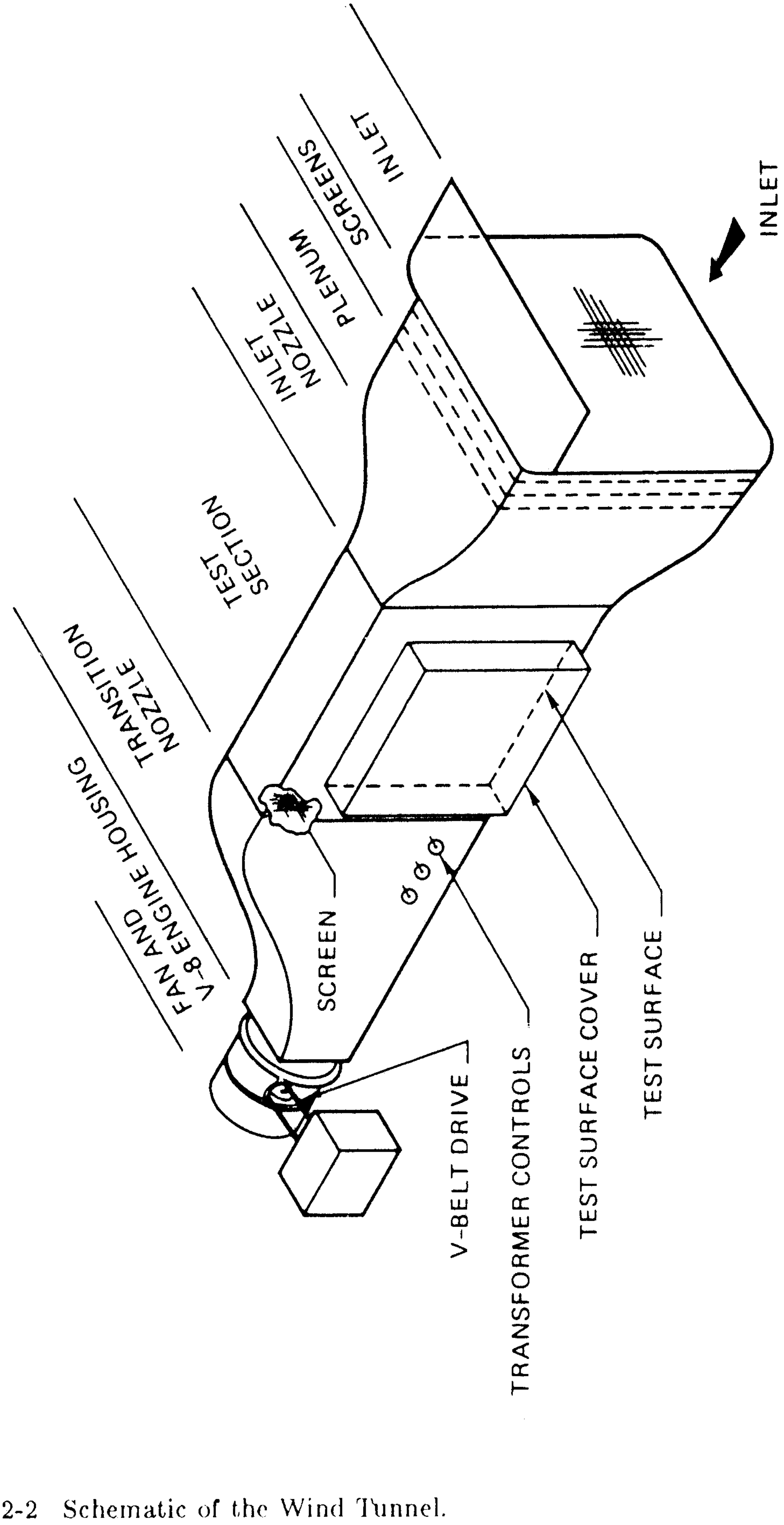

Fig. 2-2 Schematic of the Wind Tunnel.

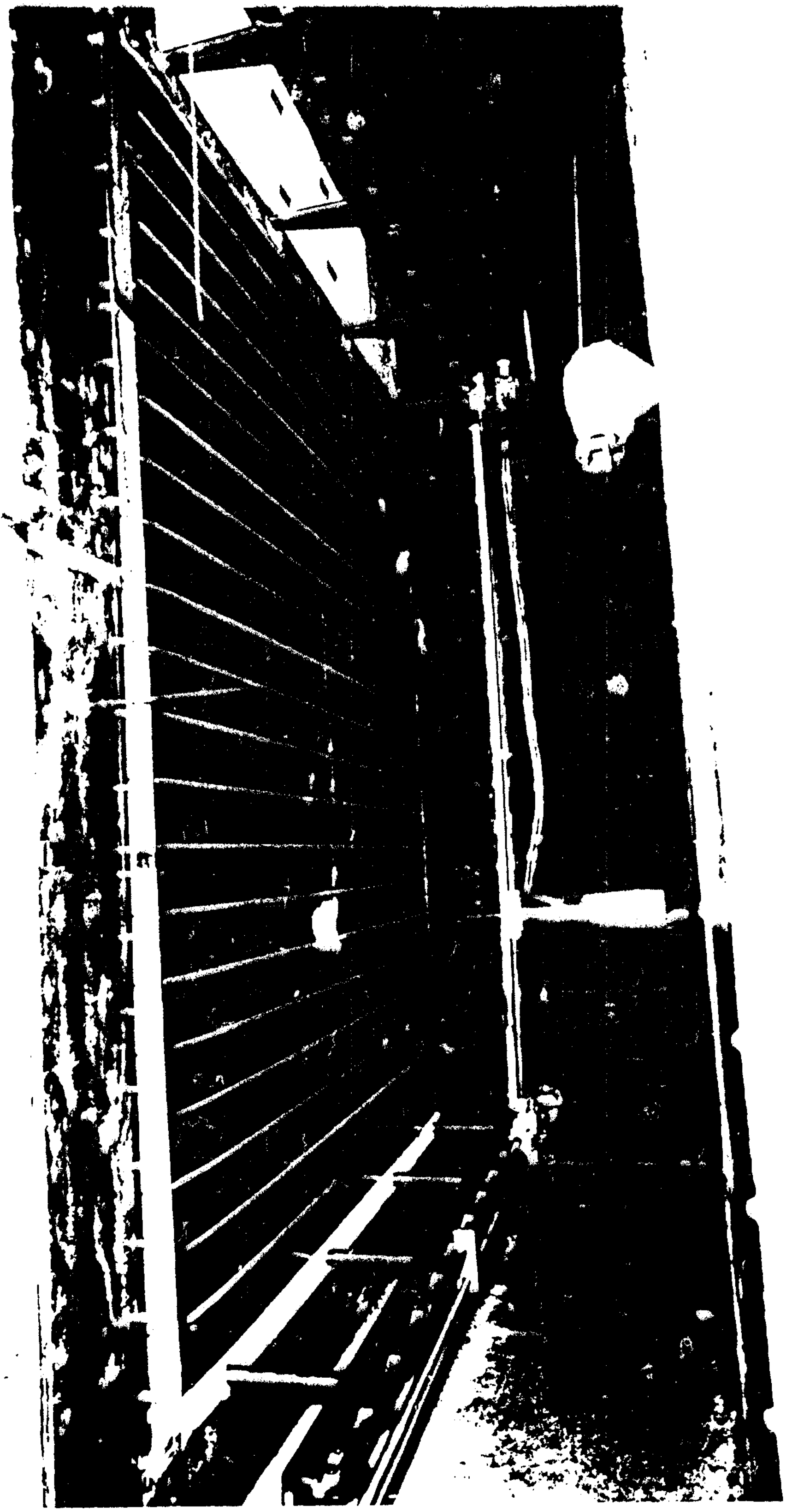

Fig. 2-3 Photograph of the Front of the Test Surface as Viewed from the Inlet Nozzle.

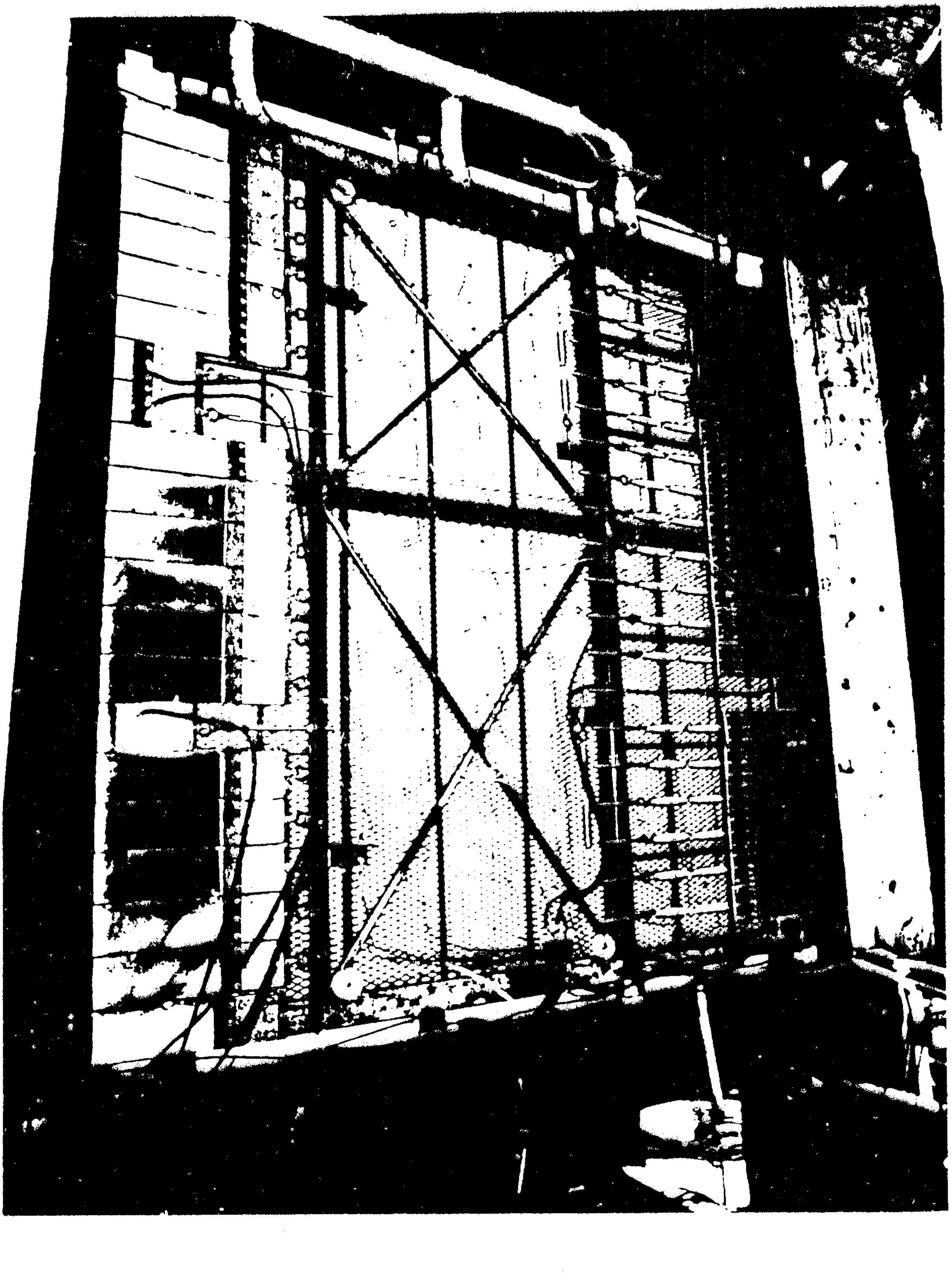

Fig. 2-4 Photograph of the Back of the Test Surface (Rear cover open).

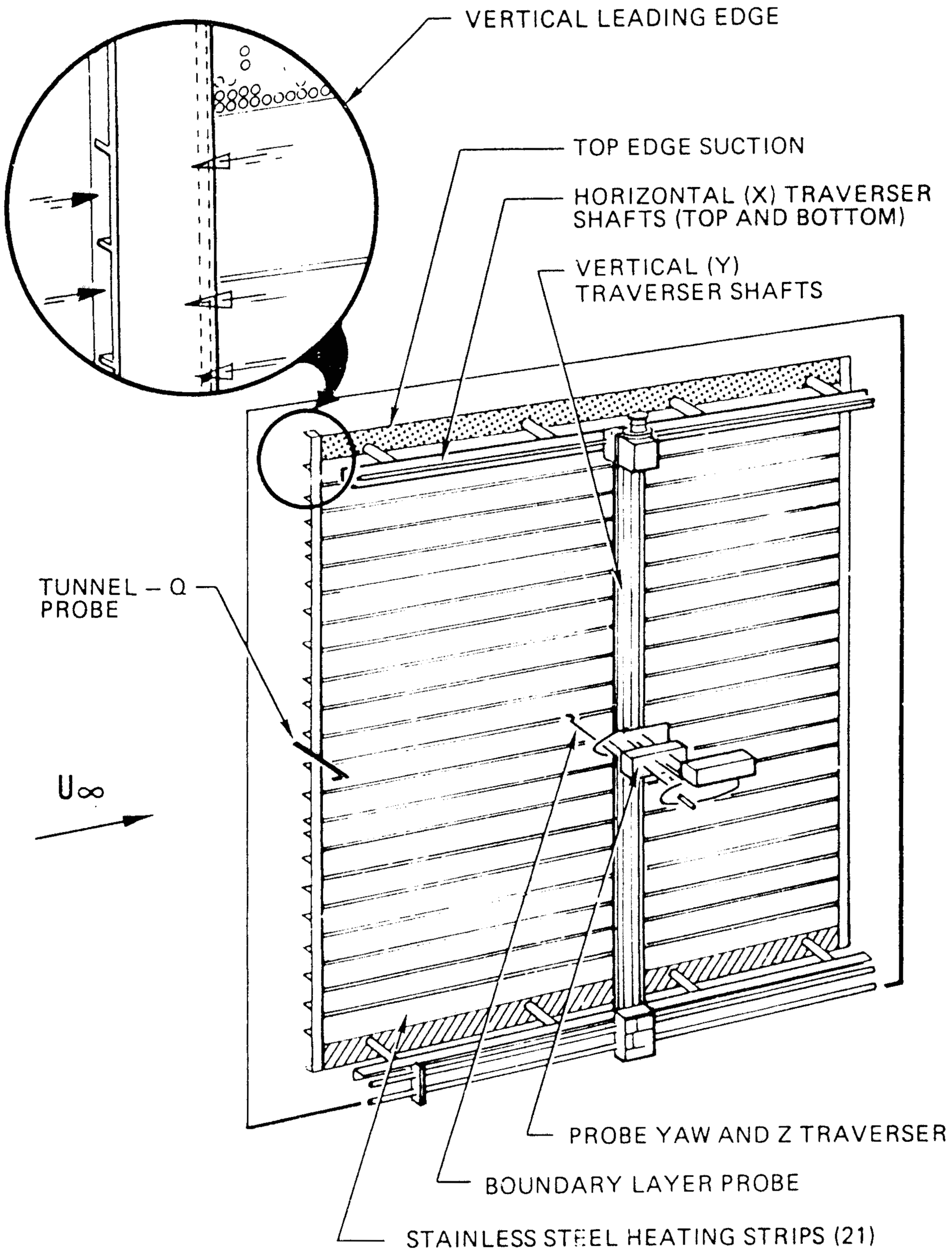

Fig. 2-5 Schematic of the Front of the Test Surface, Including the Traverse and the Leading Edge Suction.

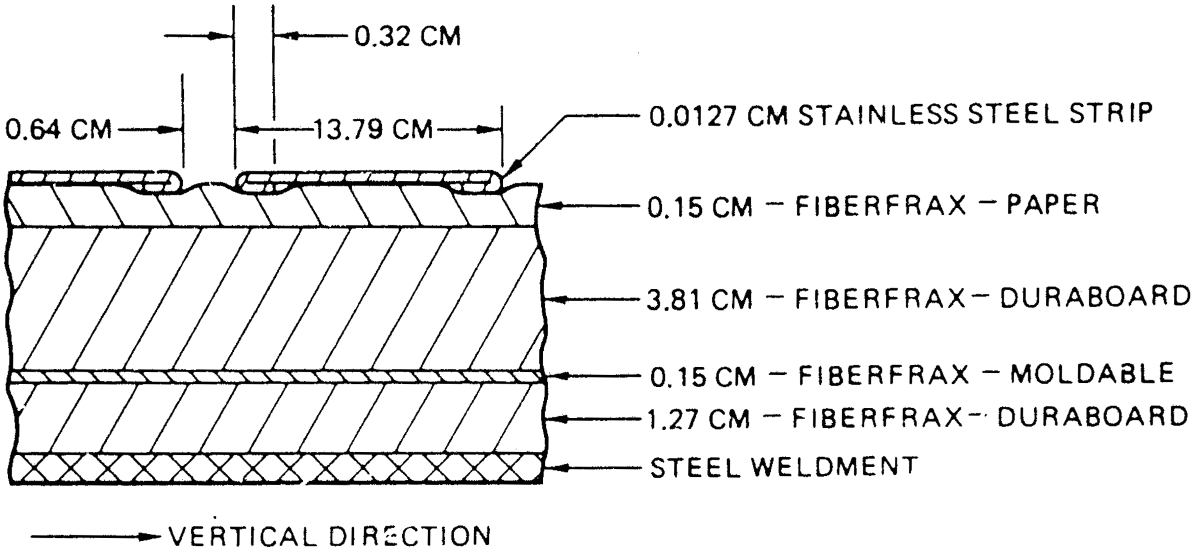

Fig. 2-6 Schematic of a Cross Section of the Test Surface.

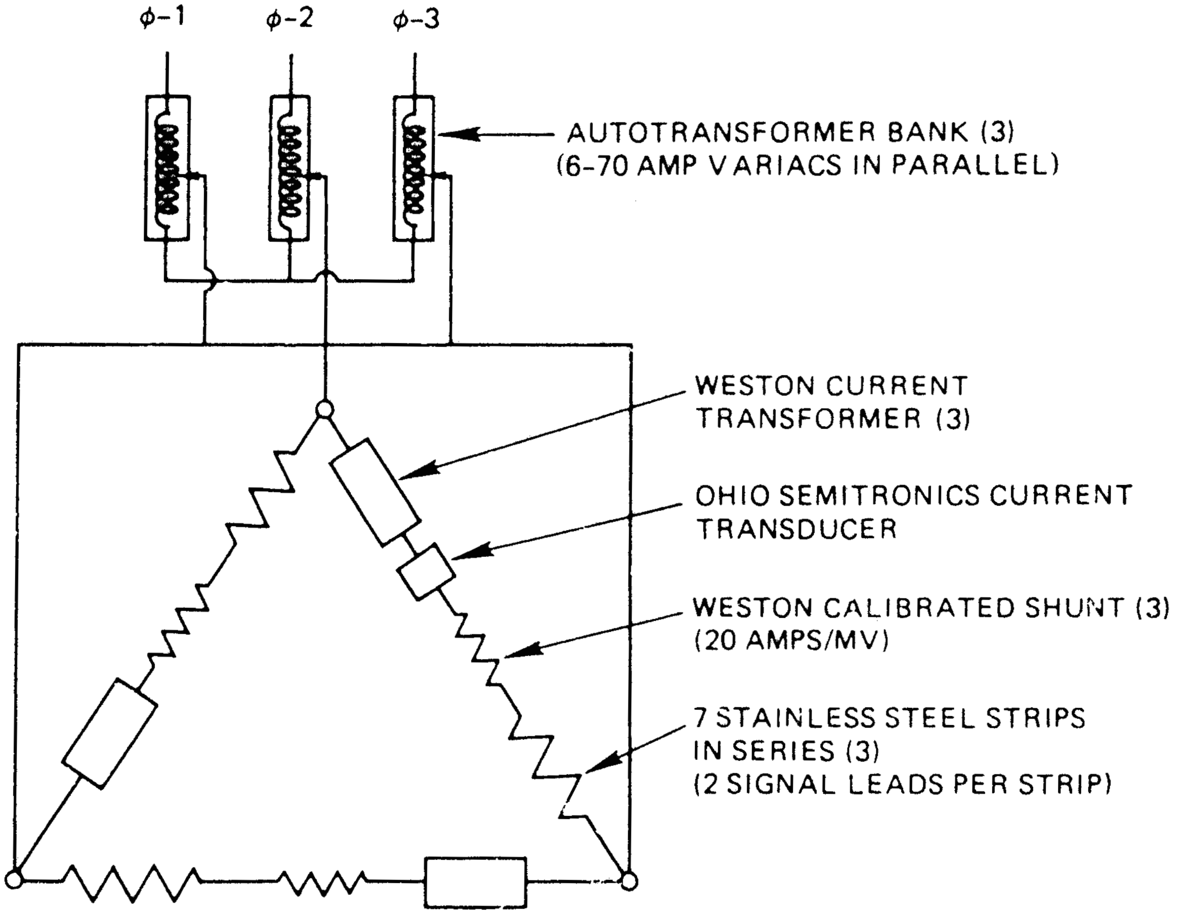

Fig. 2-7 Schematic of the Power Supply, the Voltage Sensors, and the Current Sensors ("Δ"-Configuration).

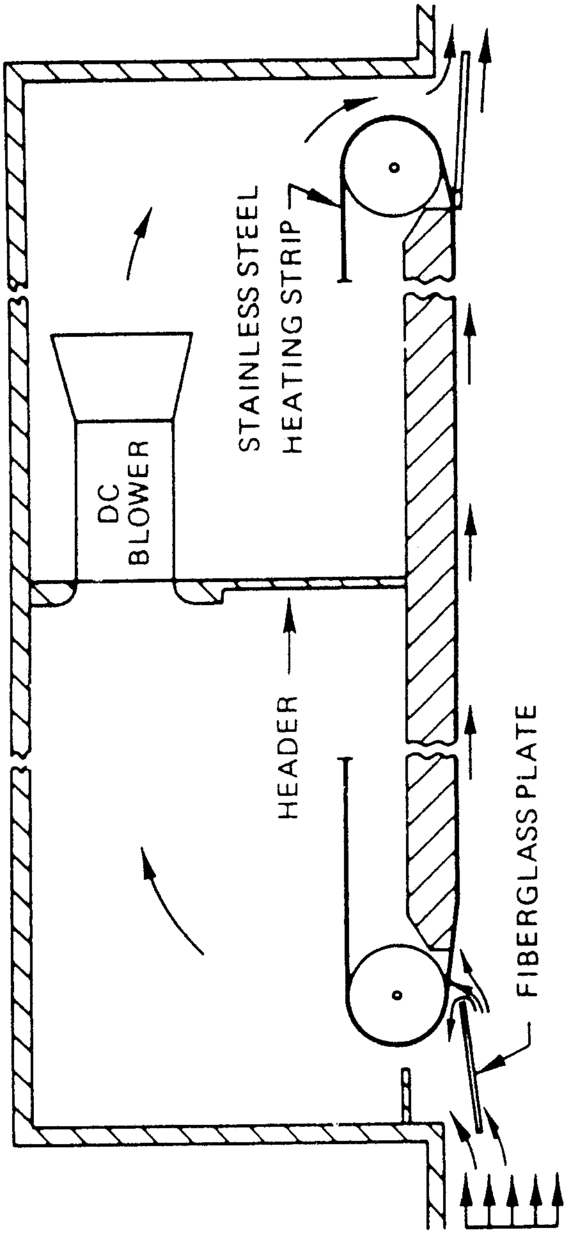

Fig. 2-8 Schematic of a Cross Section of the Leading Edge Suction.

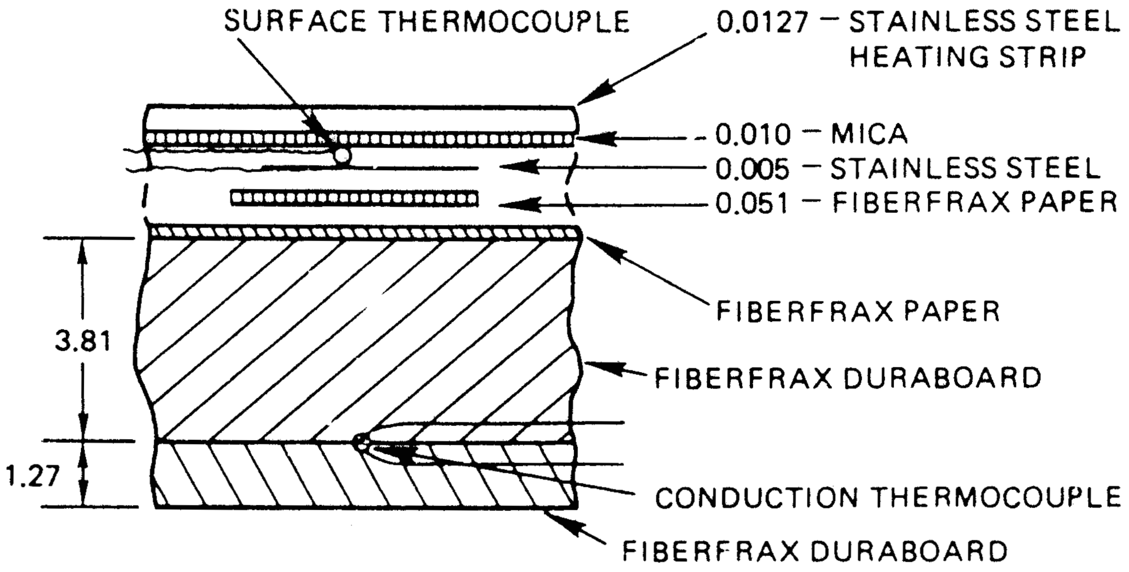

Fig. 2-9a Schematic of a Cross Section of the Test Surface with a Surface Thermocouple Assembly and a Conduction Thermocouple Shown (Dimensions in *cm*).

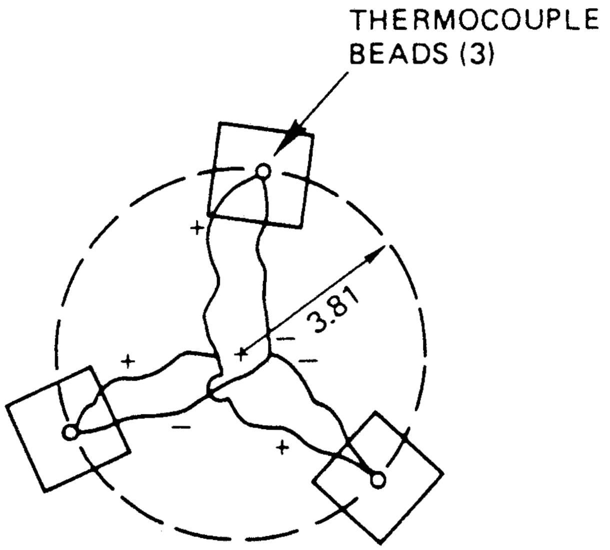

Fig. 2-9b Schematic of a Top View of a Surface Thermocouple Assembly (Dimensions in *cm*).

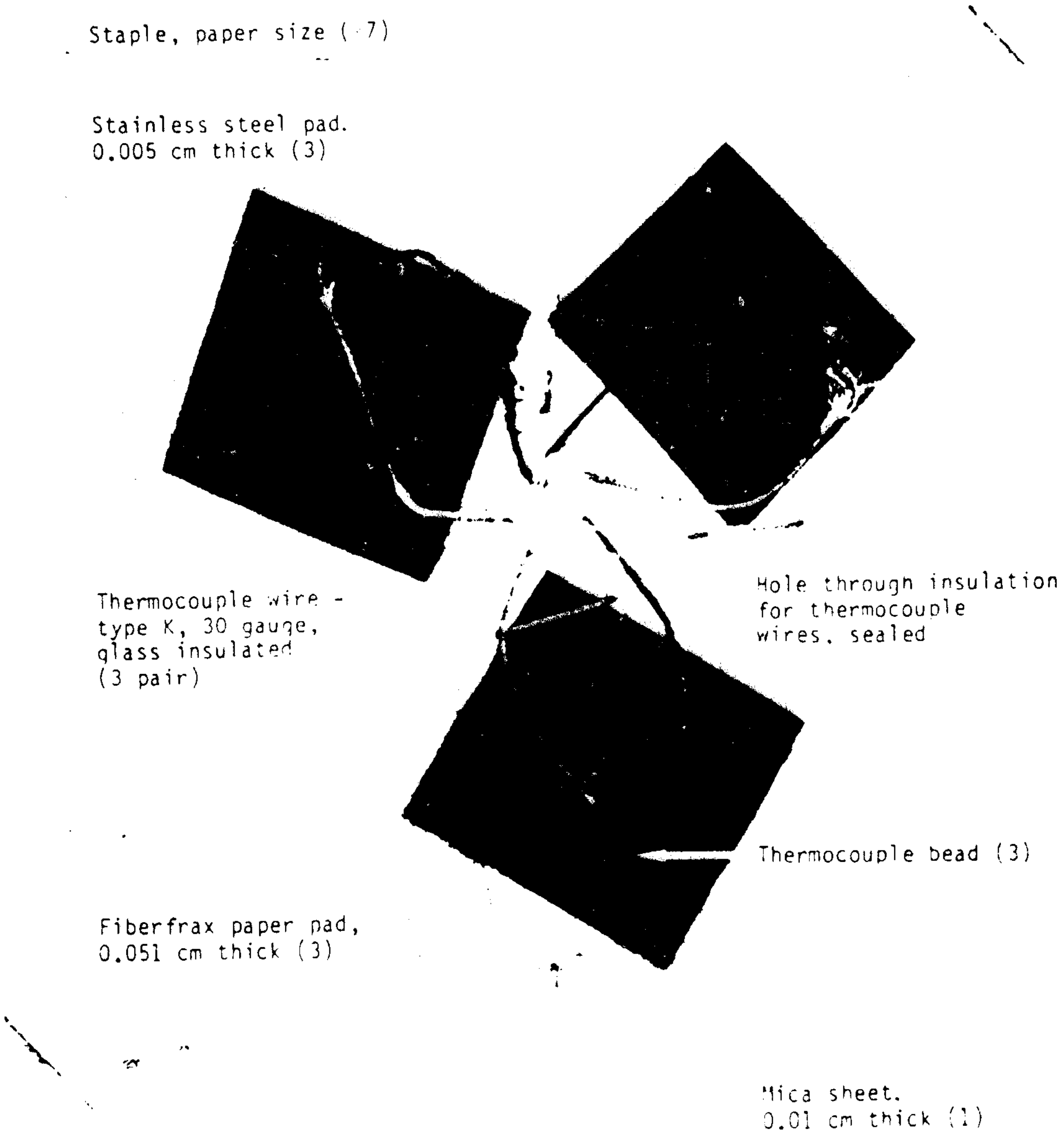

Scale: approximately 1.3 x full scale

Fig. 2-10 Photograph of a Surface Thermocouple Assembly.

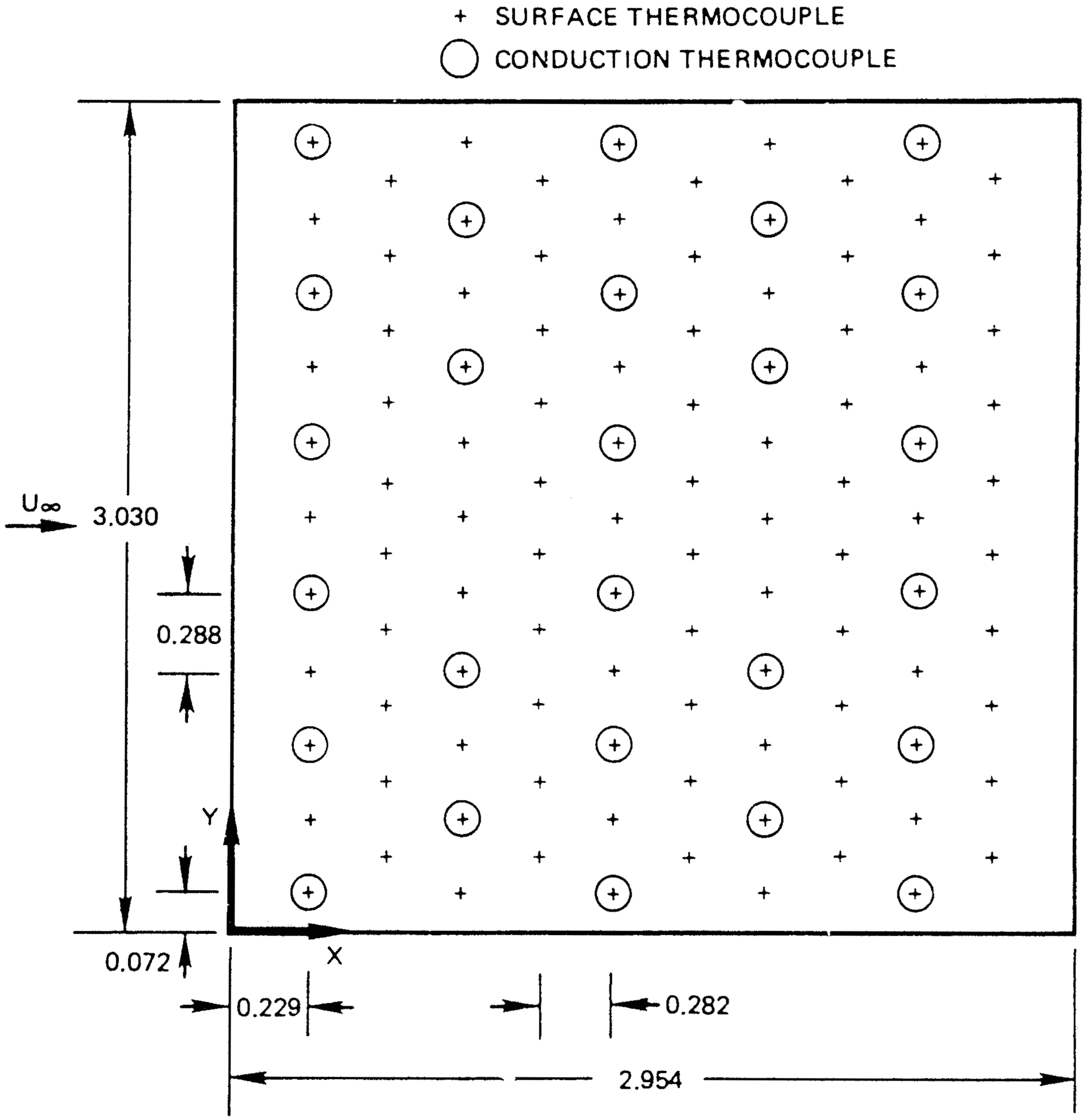

Fig. 2-11 Schematic of the Surface and the Conduction Thermocouple Locations on the Test Surface (Dimensions in *m*).

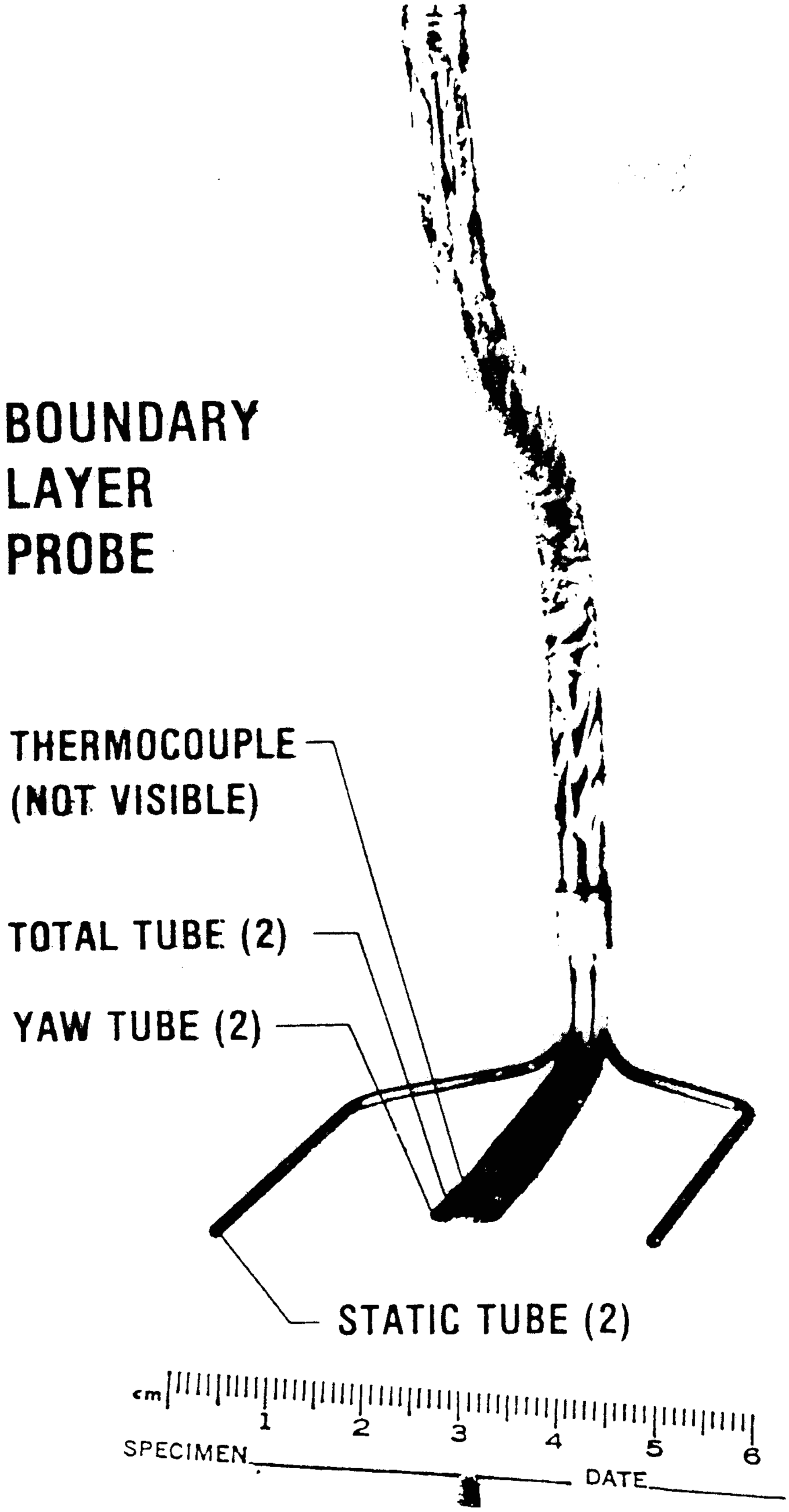

Fig. 2-12 Photograph of the Boundary Layer Probe.

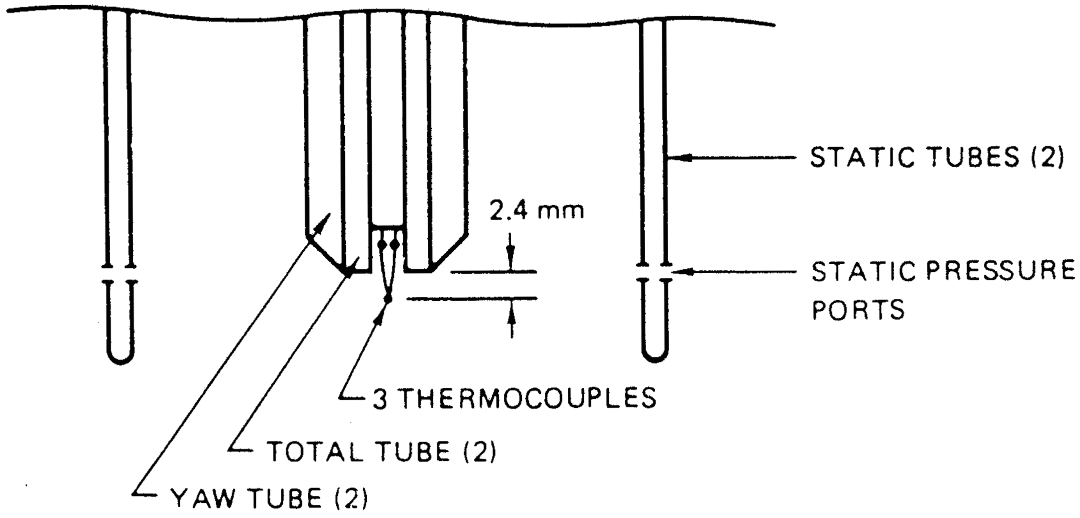

Fig. 2-13a Schematic of the Boundary Layer Probe Tip.

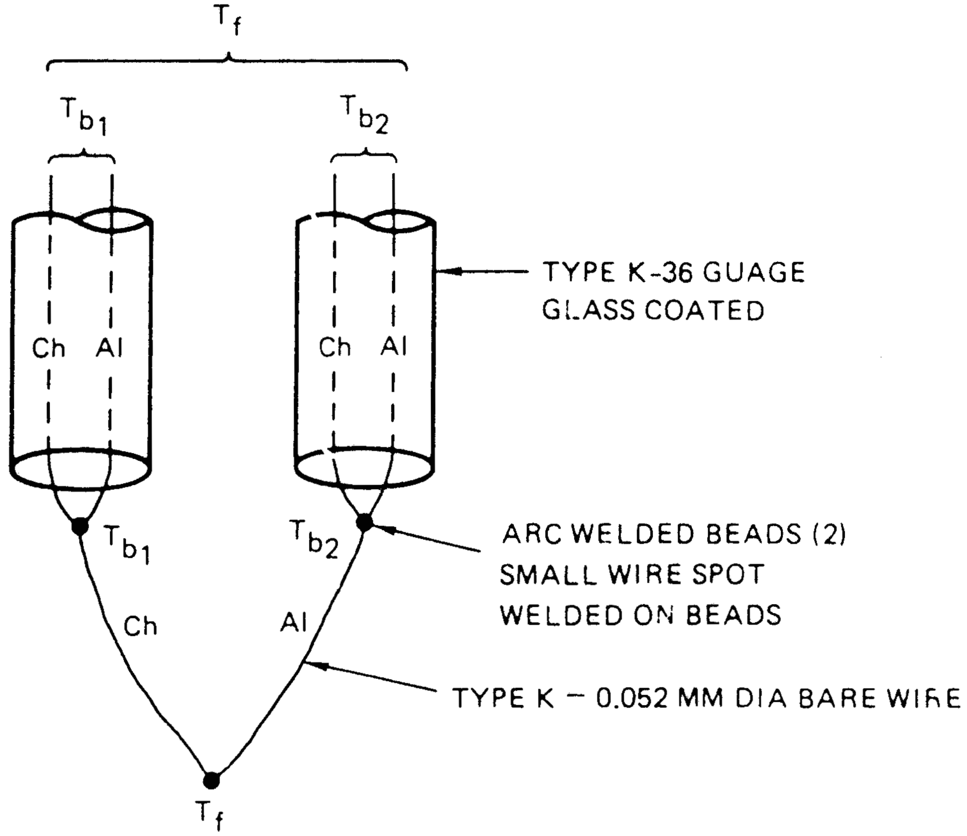

Fig. 2-13b Schematic of the Fluid Temperature Thermocouple.

Chapter 3.

QUALIFICATION TESTS AND RESULTS

Qualification tests were performed to verify the design of the apparatus and the performance of the instrumentation and the data reduction process. The first section deals with the wind tunnel flow qualification tests. This includes a discussion of the leading edge suction, the test section flow quality, and the effects of the traverse on the flow, which were small. The next section discusses baseline surface heat transfer tests conducted to verify the heat transfer aspects of the apparatus. The final section discusses the baseline boundary layer profiles taken to verify the boundary layer aspects of the apparatus.

3.1 Wind Tunnel

Qualification of the wind tunnel started before the test surface was completed. A plywood wall was used to fill the cutout for the test surface in the test section back wall. During this phase of testing the flow quality at the inlet of the test section was documented. The quantities measured at the inlet of the test section were the mean velocity distribution, the mean vertical flow angle with reference to a horizontal plane, the small scale turbulence level, the flow steadiness, and the vertical temperature gradient.

The mean velocity and the mean flow angle distribution at the test section inlet were measured with a three-hole "cobra" probe for a test section air velocity of 4 m/s and an atmospheric wind speed of 1.8 m/s.* The measurements were made by traversing the "cobra" probe horizontally across the width of the test section through 5 access ports, each at a different vertical elevation in the side of the wind tunnel. A total of 35 measurements were made, 7 across the width of the test section at each of the 5 access port vertical locations. The velocity was obtained from the pressure difference between the "cobra" probe total pressure port and the static pressure port of the tunnel-Q probe fixed at the location described in Section 2.6.1. The flow angle was obtained from the pressure difference-flow angle calibration for the two yaw ports of the "cobra" probe. The angle measured was the vertical angle

---

*The cobra probe was calibrated for yaw sensitivity and checked for viscous effects at low speed. Viscous effects were found to be negligible above 2 m/s (a probe tip Reynolds number of about 150, based on the outer diameter).

of the flow with respect to a horizontal plane. Each pressure difference at a given location was sampled several hundred times by the mini-computer over a 1 to 2 minute period.

The results of the inlet velocity uniformity and flow angle tests are shown in Fig. 3-1. Figure 3-1 is a plot of the velocity defect and flow angle (with respect to a horizontal plane) versus distance across the test section for the five vertical positions where measurements were made at the test section inlet. The velocity is plotted as the deviation from the mean inlet velocity divided by the mean inlet velocity. Figure 3-1 shows:

> There is no significant trend in the velocity data. The spatial non-uniformity of the velocity at the inlet of the test section was less than 1%.
>
> The average flow angle (from horizontal) was approximately 1° upward near the test surface wall, 1° down near the wall opposite the test surface wall, and zero on the test section centerline.

The dashed line on the flow angle plot is the average variation of the flow angle across the width of the test section. The scatter in the data is the result of a 1° uncertainty in the flow angle measurement with the "cobra" probe. The flow angle measurements indicate that there is a secondary flow, a large vortex, in the tunnel. The presence of the vortex was also indicated by a slight deformation of the smoke sheet, a flow visualization technique discussed later, as the smoke sheet moved through the tunnel. The source of this vortex was external to the tunnel. Wind coming over the building alongside the tunnel from the prevailing direction generated a vortex in the separated flow region on the leeside of the building. The tunnel, although protected from the direct effects of the wind, is located in that separated region longitudinal to the axis of the vortex. Flow visualization accomplished by releasing smoke from the roof of the building next to the tunnel showed the vortex is sucked into the tunnel.

The effect of this vortex on the test section flow quality, as well as other detrimental effects of the atmospheric wind, such as effects of gusting, were minimized by conducting tests between midnight and 10:00 a.m. Local wind conditions during this time were very calm with wind speeds much less than the 1.8 m/s reported for the qualification tests above. Free-stream flow angles should therefore be smaller than 1.0 degree. Tests were never attempted on gusting or stormy nights.

The small scale turbulence level was measured with a standard TSI model 1050 anemometer with a model 1210 probe tip. It was also observed qualitatively with smoke flow visualization. The large scale flow fluctuations or flow unsteadiness, caused by tunnel fan speed variation or wind gusts, were obtained from velocity measurements with pressure probes and fan RPM measurements. The vertical temperature gradient at the tunnel inlet was measured by the two inlet thermistors for measuring inlet air temperature, discussed in Section 2.6.1.

The smoke flow visualization mentioned above was accomplished by dropping very hot droplets of mineral oil from a droplet generator through an access port in the ceiling of the tunnel just behind the inlet screens. Each drop of hot oil left a smoke streak from ceiling to floor as it fell. Larger drops produced an array of small spiral rings along their trace. By adjusting the drop rate from the generator for a given tunnel air speed, a vertical sheet of smoke could be generated which extended from the inlet of the tunnel all the way through the test section. The sheet of smoke was composed of individual vertical streaks spaced about 0.1 *m* apart. This is visualized schematically in Fig. 3-2. Attempts to photograph the smoke sheet were unsuccessful due to the long, narrow test section passage.

Results of the tests concerning turbulence level, large scale fluctuation, and temperature gradient were:

> The hot wire measurement showed that the turbulence level was less than 0.3%. Smoke visualization also indicated very low small scale turbulence. The features of the smoke sheet, in particular the spiral rings caused by larger oil drops, could be visually tracked from the tunnel inlet to the end of the test section with no loss of their structure, indicating that very little turbulent diffusion was occurring.
>
> The larger scale flow disturbances or unsteadiness caused by fan or atmospheric effects were negligible. The fan speed varied less than 1% during a 2-3 hour test. Typical standard deviations of the flow angle and air speed measurements made with pressure probes at the test section inlet were 0.3° and 0.3%, respectively.
>
> The temperature stratification at the inlet of the tunnel was less than 1 *C* for the night and early morning test period.

Once the test surface and traverser were installed, the leading edge suction, the axial and vertical free-stream velocity variations over the test surface, and the effects of blockage due to the traverse gear were investigated. First, the leading edge suction rate and vertical uniformity of the leading edge suction were examined.

The vertical uniformity of the suction was achieved and verified by several measurements:

> A column of flow visualization tufts was strung vertically just beyond the outer edge of the inlet to the upstream suction slot. The suction slot size was adjusted locally until all the tufts had the same angle with respect to each other and the test section vertical walls.
>
> Smoke visualization verified that a vertical stagnation line was created by the leading edge suction (see Fig. 2-8) on the test surface, and that it was located a vertically uniform distance of 0.6 *cm* downstream of the leading edge suction plate (the fiberglass plate in Fig. 2-8).
>
> The measured convective heat transfer coefficients and boundary layer profiles were very uniform in the vertical direction near the leading edge. (see Sections 3.2 and 3.3, respectively).

The suction rate applied at the leading edge was about 4% of the tunnel mass flow rate. As long as the suction rate was within about ±20% of this value, the surface heat transfer and boundary flow were not significantly affected by the suction rate. The suction rate requirements were based on the following:

> Boundary layer measurements upstream of the leading edge suction slot [27] showed that a suction rate equivalent to at least 3% of the tunnel mass flow rate was required to remove the boundary layer developing on the tunnel wall upstream of the test surface.
>
> The test surface was set into the tunnel by 3 *cm* which required at least 3% of the tunnel mass flow be removed to prevent pressure gradients on the test surface as result of the blockage of the test section by the test surface.
>
> Smoke visualization showed a stable stagnation line was created as the starting condition on the test surface when the suction rate was approximately 4% of the tunnel mass flow rate at the leading edge.

Some effects of incorrect suction were noted, which provided evidence of poor adjustment of the suction:

> When suction rates significantly less than 4% were applied, an intermittent separated flow region or unstable stagnation line would develop downstream of the suction plate on the test surface. This would act as a boundary layer trip for the rest of the test surface, and early transition would result.
>
> When more suction than 4% of the tunnel flow rate was applied the test section free-stream velocity was lowered proportionally. This did not affect the surface heat transfer if the proper free-stream velocity was used

> to correlate the data. The tunnel-Q probe did not measure the correct test section velocity in this case, however, since it was located ahead of the suction slot.
>
> With significantly more suction than 4% of the test section flow rate, not only was the test section velocity lowered, but significant pressure gradients and streamline curvature occurred near the leading edge of the test surface.

With the leading edge suction adjusted, the axial and vertical variations of the free-stream velocity over the test surface were measured with two probes: (1) the boundary layer probe discussed in Section 2.6.3, and (2) a 0.95 *cm* diameter pitot-static probe. The boundary layer probe was in its probe mount on the traverse with the tip 15 *cm* away from the test surface. The pitot-static probe was the same distance from the surface, but 1 *m* in front of and 15 *cm* above the boundary layer probe position on a temporary sting attached to the traverse. This placed the pitot-static probe outside the zone of influence of the traverse shield (discussed later). The probes were traversed axially down the tunnel at four different vertical locations with the traverse. The measurements started at the stagnation line just behind the leading edge suction, the origin for the test surface.

The axial and vertical velocity variations over the test surface are shown in Fig. 3-3, at four vertical locations. The measured velocities are normalized by the tunnel-Q probe measurement. The figure shows that:

> There is a slight favorable pressure gradient in the test section. The total increase in free-stream velocity over the length of the test surface is about 7%, with most of that occurring close to the vertical leading edge. The free-stream axial velocity variation is equivalent to $U_\infty(x) = 0.99 U_Q x^{0.024}$. The average value for K ranges from 0.01×10^{-6} to 0.06×10^{-6} for the velocity range considered. The maximum K near the vertical leading edge ranges from 0.08×10^{-6} to 0.3×10^{-6} for the velocity range considered.
>
> The vertical free-stream velocity variations are less than 1%. This was verified by more detailed measurements in the vertical direction at two axial locations.
>
> The magnitude of the test section velocity has a negligible effect on the normalized velocity variation, as shown by the points for U_Q equal to 2.6 and 5.2 m/s.

The axial velocity variation near $x = 0$ was due to local effects of the leading edge suction. The flow is laminar there for all cases, as will be shown in

Chapter 4. Based on the Falkner-Skan wedge flow solutions for laminar flow, the pressure gradients at the leading edge will cause less than a 2% increase in the convective heat transfer at the leading edge and only a slight increase in velocity near the wall compared to the zero pressure gradient case. Downstream, the axial velocity variation was due to boundary layer growth on the test section walls. The variations downstream were minimal because the test section walls diverged. In the downstream region the boundary layer was generally turbulent. For the values of K that occur, Refs. 36-38 show that the effects of the free-stream velocity variations on the convection heat transfer and boundary layer flow were negligible in the turbulent flow regions downstream.

The measurements in Fig. 3-3 demonstrate two other points:

> The tunnel-Q probe measures the mean free-stream velocity over the test surface, since the curves are centered on a value of one.
>
> The leading edge suction was uniform, since all the velocity measurements near x of zero agree within 1%.

The effects of blockage due to the traverse gear on the flowfield in the tunnel were caused mainly by the airfoil shaped, water-cooled shield covering the vertical shafts (see Section 2.4) and the traverse support struts extending from the wall to the horizontal shafts on the bottom leading edge and the top edge of the test surface (see Fig. 2-3). The effects of the struts along the top of the test surface were insignificant. This is shown in Appendix D. The effects of the struts along the bottom edge were not clear from the results of this experiment. Convective heat transfer is significantly higher on the bottom heating strip than the strips above, for forced convection dominated flows, and significantly higher on the bottom two strips for mixed convection flows. This may be the nature of the lower leading edge starting condition, or it may be an effect of the struts, or it may be a combination of both. This is discussed more in Appendix D.

Boundary layer profiles were taken along the lower leading edge to supply starting conditions for the numerical modeling being conducted at Stanford University on this problem.

Several points should be noted about the flow and heat transfer along the bottom leading edge. First, the effects of the struts on interpretation of the data, if any, are limited to the data downstream of the first strut on the lower 2 or 3 heating strips of the test surface. Second, the effects of the struts become less significant on the lower heating strips as free convection begins to dominate the flow. Third, the boundary layer flow was always turbulent along the lower leading edge, except in pure free convection flows. Finally, the boundary layer became significantly thinner along bottom edge as the vertical buoyant force became larger, which may help explain the higher heat transfer at the bottom edge.

The effects of the airfoil shaped shield covering the traverse gear on the test section flow were determined from measurements with pressure probes and measurements of the surface heat transfer. The surface heat transfer tests are presented with the heat transfer baseline tests in Section 3.2. The pressure probe measurements show two effects of the traverse shield, one on the free-stream velocity upstream of the shield and one on the free-stream flow angle. Both effects are small. The effect of the shield on the free-stream velocity upstream of the shield was determined from two static pressure differences. One pressure difference was between a fixed static tap on the test surface and one of the static tubes on the boundary layer probe (see Section 2.6.3), which was positioned 15 *cm* away from the test surface. The second pressure difference was between a reference static tube at a fixed location upstream (away from the shields influence) and the second static tube on the boundary layer probe. The first pressure difference gave the effect of the shield on the static pressure at the location of the wall static tap as the shield and traverse moved forward in the tunnel. The second pressure difference gave the axial static pressure variation in the tunnel with the effect of the shield on the measurement the same at every axial location. This pressure difference was equivalent to the undisturbed axial static pressure variation in the tunnel.

Assuming the total pressure was constant in the free-stream, the difference in the two static pressure variations can be used to describe the "footprint" of the traverse: it's effect on the apparent velocity field upstream of the shield. This is shown in Fig. 3-4. The ordinate in the figure is the difference between the actual free-stream velocity ahead of the shield and the velocity that would have been present at that location with no shield. The abscissa is the distance ahead of the boundary layer probe velocity measuring point. The figure shows:

> The velocity at the measuring point is the same as would have been present without the shield.

The effect of the shield on the upstream velocity variation is approximately independent of tunnel velocity for the range of velocities considered, 2.6 to 5.3 m/s.

The effect on free-stream velocity starts 1 m upstream as a slight deceleration ($K > -0.2 \times 10^{-6}$) followed at 0.25 m upstream by an acceleration ($K < 0.5 \times 10^{-6}$). The maximum effect upstream is about a 3% decrease in free-stream velocity 0.25 m upstream of the measuring point.

The acceleration extends downstream of the velocity measuring point.

Zero error in velocity at the measuring point was achieved by adjusting the angle of attack of the shield and the flap attached to the downstream edge of the shield. Adjusting the shield and flap in this manner allowed the zero crossing point in Fig. 3-4 to be moved upstream or downstream.

The first point above was also shown in Fig. 3-3, which contains the velocity distributions measured with the boundary layer probe on the traverse and the probe attached to a sting outside the zone affected by the shield (more than 1 m in front of the traverse). The axial velocities measured by the two probes compare well and the comparison is independent of velocity to within about 1%. Figure 3-3 also shows that the effect of the shield is uniform in the vertical direction, since the comparison is equally good for all vertical heights considered. This was verified by more detailed measurements in the vertical direction.

Based on the results in Refs. 36-38, the effects of the pressure gradients induced by the shield upstream will be negligible. In addition, the slight deceleration followed by the acceleration upstream should tend to cancel at the measuring point.

Flow angle measurements in the free-stream indicate that the shield caused a small negative free-stream flow angle between the shield and the test surface. The average measured free-stream flow angle was $-4.4°$ for a Gr_H/Re_L^2 of 21.7, $-1.5°$ for a Gr_H/Re_L^2 of 7.4, and approximately zero for a $Gr_H/Re_L^2 < 3.0$. This effect is not very significant, since the free-stream flow angle is less than or equal to the flow angle uncertainty ($\approx 2°$) throughout the mixed convection heat transfer regime, $0.7 < Gr_H/Re_L^2 < 10.0$. In the free convection regime, $Gr_H/Re_L^2 > 10.0$, where this effect becomes larger ($\approx 4°$ to $5°$), the free-stream flow is of little importance, since the boundary flow is driven largely by forces internal to the boundary layer, not the free-stream.

No correction has been made to the reported flow angle measurements for this effect. For this reason some boundary layer profiles show a negative free-stream flow angle. The effect of the free-stream flow angle is discussed more in Section 4.2.3, where it is shown that small variations in free-stream flow angle effect mainly the very outer region of the boundary layer.

The negative flow angles were caused by the occurrence of a thicker boundary layer near the top of the test surface than near the lower free convection leading edge when buoyancy dominated the flow. The increased displacement thickness at the top made the flow path between the traverse shield and test surface appear smaller at the top and forced a downward flow angle between the shield and test surface.

Two other effects of the shield were checked and found to be negligible. First, the traverse shield effect on the tunnel-Q probe was negligible for the closest axial distance between the two. Second, the measured static pressure gradient normal to the test surface caused by the shield was 0.001 Pa/cm at the peak velocity of 6.0 m/s. This was measured by measuring the pressure difference between a wall static tap and the static pressure tubes on the boundary layer probe as the boundary layer probe was traversed normal to the wall near the wall static tap. This gradient was extremely small and should have had little effect on velocity measurements, since the static pressure was measured locally by the boundary layer probe.

3.2 Heat Transfer Baselines

Two sets of heat transfer baselines were taken, a forced convection set and a free convection set. These were compared with data in the literature for each case. The first subsection presents the forced convection baseline results and the second subsection presents the free convection baseline results. Both sets of baseline data were taken with low wall-to-free-stream temperature difference to minimize variable properties effects. The forced convection cases used for baselines had a small buoyant force present, but it will be shown later that the effects of buoyancy were insignificant for the Gr_H/Re_L^2 of each of these tests. All properties were evaluated at the T_∞ in this section.

The baseline results in the first two subsections will show that the test surface closely resembled the desired zero pressure gradient, smooth, flat, uniform heat flux surface. The comparisons to existing correlations for this situation are good, especially in the turbulent flow region. The small variations from the desired test surface features that are noted near the vertical leading edge, where the flow is laminar, will be shown to be the result of small axial variations in the free-stream velocity and wall heat flux noted near the vertical leading edge, not heat transfer data reduction or measurement errors.

The last subsection presents some checks that were made on the heat transfer coefficients determined with Eqn. (2-1). The heat transfer coefficients determined with Eqn. (2-1) are compared with heat transfer coefficients determined by two other methods from the data.

3.2.1 Forced Convection Baselines

Figure 3-5 shows the forced-convection baseline data in St versus $Re_{\Delta_{\boldsymbol{tx}}}$ coordinates. Figure 3-6 shows the same data in Nu_x versus Re_x coordinates. The solid lines in each figure represent the accepted correlations for constant heat flux, zero pressure gradient laminar and turbulent flows. In enthalpy thickness coordinates these correlations are [24]:

$$Turbulent: \quad St = 0.0125 Re_{\Delta_{\boldsymbol{tx}}}^{-0.25} Pr^{-0.5} \tag{3-1}$$

$$Laminar: \quad St = 0.205 Re_{\Delta_{\boldsymbol{tx}}}^{-1} Pr^{-4/3} \tag{3-2}$$

In Re_x coordinates they are [24]:

$$Turbulent: \quad Nu_x = 0.0307 Re_x^{0.8} Pr^{0.6} \tag{3-3}$$

$$Laminar: \quad Nu_x = 0.453 Re_x^{1/2} Pr^{1/3} \tag{3-4}$$

The ten data points shown for each test in Figs. 3-5 and 3-6 are column-wise averages of the heat transfer data measured in each of the ten columns of thermocouples in Fig. 2-11. The data were taken with test surface temperatures between 45 and 57 C and free-stream temperatures between 17 and 20 C. Variable properties effects were accounted for by shifting the lines representing the constant properties correlations (above) according to the temperature ratio of the test using:

$$h = h_{cp}\left(\frac{T_w}{T_\infty}\right)^n \tag{3-5}$$

The term h_{cp} is the value of the heat transfer coefficient which would be expected for the same Reynolds number, with the wall at nearly the same temperature as the free-stream. The values of n used were 0.0 for laminar flow and -0.40 for turbulent flow, since the wall is hotter than the free-stream [24].

The term $Re_{\Delta_{\boldsymbol{tx}}}$ was calculated from the convective heat flux information, not measured. The two-dimensional energy integral equation was used:

$$Re_{\Delta_{tx}} = \frac{\int_0^x q_{conv}(x')dx'}{c_p\mu[T_w(x) - T_\infty]} \tag{3-6}$$

The integration started at the observed location of the stagnation line on the test surface, 0.6 cm downstream of the suction slot.

These baseline data were taken before any other test data and were rechecked twice: once midway through the program and again after all of the data of record were taken. The range of all of the data for all the replicates of the baseline conditions is indicated by the scatter in the data in Figs. 3-5 and 3-6. The coherence of the baseline data provides important evidence concerning the stability of the experiment, since several months of running elapsed between the first and the last baseline data sets. The RMS variation within a column of data was generally less than $\pm 2\%$ in the laminar and turbulent regions. This also gives an indication of the uniformity of the leading edge suction.

The agreement between data and correlations is good in both the laminar and turbulent flow regions. The agreement indicates the closeness of the design to the desired zero pressure gradient, smooth, uniform heat flux flat surface. The only deviation of data from the desired case is seen in Fig. 3-5 in the laminar region where the data are consistently high by about 5%, which, however, is within the uncertainty of the data. In both figures the 2.0 m/s data show that the entire test surface was either laminar or transitional; not until the velocity reached 4.1 m/s did a significant turbulent region emerge at this low temperature. In test *ID*-553 at 6.1 m/s, a boundary layer transition trip was installed at the first column of thermocouples (a 1.0 mm diameter insulated thermocouple wire stretched tightly across the surface). The data with the trip in place smoothly extend the untripped turbulent data to lower Reynolds numbers.

There is an apparent contradiction in the laminar results in Figs. 3-5 and 3-6 if the results are examined closely. The laminar data is consistently higher than the desired solution, as described in the previous paragraph, when given in St versus $Re_{\Delta_{tx}}$ coordinates, as in Fig. 3-5. The same data in Nu_x versus Re_x coordinates in Fig. 3-6 agrees very closely with the desired solution. The apparent contradiction is explained by examining the Falkner-Skan type solution to the wedge flow heat transfer problem for $U_\infty = ax^{0.024}$ and $T_w(x) - T_\infty = bx^{0.45}$. These are the measured T_w and U_∞ variations for low-T_w forced convection cases near the vertical leading edge, the laminar flow region. The U_∞ variation was discussed previously in Section 3.1. For the T_w variation, the exponent on x would be 0.5 instead 0.45 for a uniform convective heat flux surface.

The solution to the wedge flow heat transfer problem with the above T_w and U_∞ x-dependencies is given by the dashed line in Fig. 3-5. The solution and actual data agree very well as shown in Fig. 3-5. The solution in Nu_x versus Re_x coordinates is almost indistinguishable from Eqn. (3-4) and therefore not shown in Fig. 3-6. It would be located only about 0.5% higher than Eqn. (3-4) in Fig. 3-6, thus explaining the trends shown by Figs 3-5 and 3-6 in the laminar flow region. This also shows that the convective heat transfer measurement technique works very well.

Figure 3-7 shows that the pressure gradients induced by the traverse shield, discussed in Section 3.1, did not affect the convection heat transfer upstream of the traverse. The figure shows St versus $Re_{\Delta_{tx}}$ for a low-temperature pure forced convection case, the same as in Fig. 3-5, with the traverse in three axial locations. The first location (ID=762) is the most downstream location, at the very downstream edge of the test surface. Here, the traverse shield has no effect on the surface heat transfer. The data are the same as the baseline data presented in Fig. 3-5 with the same good agreement to accepted correlations. In the second location (ID=763), the traverse is moved so that the probe tip aligns with the seventh column of surface thermocouples (see Fig. 2-11). Again, no effect is seen on the heat transfer data upstream of the traverse location. Downstream there are significant effects. At location three (ID=764), the traverse is moved so that the boundary layer probe tip is at the second column of thermocouples which is at the end of the laminar flow region for this test. No effects are seen upstream. Again, downstream the heat transfer is significantly altered.

The effect of the shield on heat transfer was all downstream of the shield. All boundary layer traverses were started at the downstream end of the test surface and progressed in a vertical direction first at each axial location before moving upstream to take profiles. This meant it was not necessary to wait for steady state heat transfer after every profile, since the heat transfer upstream on test surface was not affected by the shield.

3.2.2 Free Convection Baselines

The free convection baseline heat transfer results are shown in Fig. 3-8. Two free convection baseline heat transfer tests were taken with T_w equal to 60 and 128 C and T_∞ equal to 15 and 18 C, respectively. They are plotted in Nu_y versus Gr_y coordinates in Fig. 3-8 with fluid properties evaluated at T_∞. The 21 points shown for each test are each the average of the five data points along one horizontal heating strip (see Fig. 2-11). The RMS variation of the 5 data points along a heating was 3% or less.

The solid line in the laminar flow region in Fig. 3-8 ($Gr_y < 10^9$) represents an accepted free convection correlation for laminar flow on a vertical, uniform heat flux surface in air [24]:

$$Nu_y = 0.404 Gr_y^{1/4} \tag{3-7}$$

In the turbulent flow region ($Gr_y > 10^{10}$), three lines are shown. The two solid lines represent the range of correlations in the literature for turbulent free convection from a vertical surface. The dashed line is a "best fit" line through the data in the literature, represented by:

$$Nu_y = 0.096 Gr_y^{1/3} \tag{3-8}$$

Equation (3-8) is the correlation recommended by Churchill and Chu [39] for turbulent free convection from a vertical surface with the coefficient, 0.096, evaluated for a Pr of 0.71. The equation is based on their survey of the then current data (1975).

The free convection data were taken with a hatch in the roof of the tunnel open and with the top-edge suction on, to minimize stratification. Flow visualization with smoke showed that the air in the test section was essentially at rest, with no discernible cross-flow or recirculation in the tunnel. The only motion was in the boundary layer on the heated test surface.

Figure 3-8 shows three main points. First, the agreement between laminar baseline data and accepted correlation is good. Second, the turbulent data lie within the range of correlations appearing in the literature and agree very well with the "best fit" correlation of Churchill and Chu [39]. Third, the transition location agrees with other data in the literature that show transition between Gr_y of 10^9

and 10^{10}. This close agreement between baseline data and the data in the literature qualifies the apparatus and instrumentation. In addition the close agreement shows that the small horizontal gaps between the 21 heating strips have little, if any, effect on the results. This was expected, since the total area of the gaps is small compared to the heated area of the test surface and the depth of the step created by the gap ($\approx 0.15\ mm$) is small compared to the boundary layer thicknesses, which were as large as 15 cm.

3.2.3 Special Heat Transfer Checks

In addition to the baseline heat transfer tests, two consistency checks were made on the heat transfer coefficients determined by Eqn. (2-1) as part of the apparatus and instrumentation qualification. The first check was a comparison of the local h determined by Eqn. (2-1) at a given location with an h that could be determined from a boundary layer temperature profile measured at that same location by the following expression:

$$h = k\frac{d\theta}{dz} \tag{3-9}$$

The term θ is the dimensionless temperature in the boundary layer. The derivative $d\theta/dz$ is evaluated between the wall and the first temperature measurement point away from the wall by a linear approximation. The conductivity k is evaluated at the average of the wall temperature and the temperature at the first measurement point away from the wall.

This check was made for 43 cases which had boundary layer temperature profiles with temperature measurements well into the viscous sublayer of the turbulent boundary layer or the inner region of the laminar boundary layer ($\theta < 0.2$), where the definition for h given by Eqn. (3-9) is valid. Two of the profiles were for free convection, and 41 were for forced or mixed convection. These profiles were for T_w's in the 200 to 600 C range, for different locations on the test surface, and for various U_∞'s. The average ratio of h determined from Eqn. (2-1) to h determined from Eqn. (3-9) was 1.008 with a standard deviation of 14% for the 43 cases. The closeness of this ratio to 1.0 is a check on the validity of the measurement scheme for h given by Eqn. (2-1) over the entire temperature range of the experiment. The large standard deviation and time required for a single measurement of h by Eqn. (3-9) are the reasons that this method was not used.

The second consistency check on h was made by comparing an average h, determined from the average of the 105 measurements of h with Eqn. (2-1), to an average h for the same test condition, determined from a control volume analysis of the boundary layer flow. The control volume analysis assumed that the net energy convected into the boundary layer at the wall was equal to the difference between the energy contained in the air entrained into the boundary layer and the energy contained in the air leaving the top and downstream end of the test surface in the boundary layer flow. Based on this definition, the convected energy could be determined directly from boundary layer total velocity, flow angle, and temperature profiles along the top and downstream end of the test surface.

The comparison between the average h determined by Eqn. (2-1) and the control volume analysis was good over the entire temperature range of the experiment. The average ratio of the test surface average h determined from the control volume analysis to the average h determined by Eqn. (2-1) for 7 separate test conditions was 0.993 with a standard deviation of $\pm 6\%$. The 7 test conditions were cases where enough profiles were taken along the top and downstream end of the test surface to make the comparison possible. The T_w's for the test cases ranged from 200 to 600 C and the U_∞'s ranged from 1.5 to 5.0 m/s.

3.3 Boundary Layer Baselines

Baseline boundary layer profiles were taken during qualification testing. These consisted of velocity and temperature profiles in the laminar and turbulent flow regions for low-temperature pure forced convection cases. Also, velocity profiles were taken for some cold wall cases. These profiles are compared to the accepted zero pressure gradient, uniform heat flux profiles in the literature. No serious effort was made to get velocity or temperature profiles for a low-temperature free convection baseline. The velocities for free convection with a small temperature difference $(T_w - T_\infty)$ were too low to measure with the pressure probe and pressure transducers used. In any event, there is no agreement in the literature on a baseline profile for turbulent free convection.

This section will confirm the design of the boundary layer instrumentation and test surface and validate the data reduction of the boundary layer data. Boundary layer baseline profiles will be shown to compare very closely to the desired uniform heat flux, zero pressure gradient, smooth, flat surface profiles that exist in the literature for both turbulent and laminar flow. The small deviations that are noted near the leading edge, where the flow is laminar, will be shown to be the result of the small axial variations in the free-stream velocity and wall heat flux noted near the vertical leading edge, not the boundary layer probe or data reduction errors.

3.3.1 Laminar Forced Convection Baselines

Figure 3-9 shows forced convection laminar velocity profiles for a cold wall case ($T_w = T_\infty = 15\ C$) and a low T_w case taken near the leading edge of the test surface. The profiles are compared to the Blasius solution for laminar, zero pressure gradient flow represented by the solid line. Also, shown as a dashed line is the wedge solution for the small free-stream axial velocity gradient measured near the vertical leading edge (see Sections 3.1 and 3.2.1). The data and analytic solutions are shown as u/U_∞ versus z/δ_{xx}. Figure 3-9 shows the comparison to the Blasius solution is good. The only significant difference is near the wall where the profiles, in general, are displaced a few percent above the Blasius velocity profile. The upward displacement of the data near the wall is accounted for by the small free-stream velocity gradient measured near the vertical leading of the test surface, as shown by the dashed line in Fig. 3-9. The scatter in the data near the wall is explained by the $\pm$ 0.012 *cm* uncertainty in the z coordinate. An uncertainty band based on this uncertainty alone, which is the major contributor to the uncertainty of the quantities plotted in Fig. 3-9, is shown for the data point closest to the wall. The uncertainty band appears very large due to the logarithmic coordinates. All data lie within this uncertainty band near the wall.

Figure 3-10 shows forced convection temperature profiles for a low T_w case compared to a temperature profile from the solution to a laminar, uniform heat flux, zero pressure gradient flow, the solid line. Also shown is the temperature profile for the wedge flow solution for the measured free-stream velocity and wall temperature variations near the vertical leading edge, the dashed line, which is discussed in Section 3.2.1. Figure 3-10 shows that the agreement between the measured profiles and the laminar uniform heat flux, zero pressure gradient flow is good. The measured profiles are only a few percent below the desired profiles. This difference is accounted for by the small variations in free-stream axial velocity and surface heat flux (i.e., temperature) noted near the vertical leading edge, as shown by the dashed line in Fig. 3-10.

The baseline boundary profiles in this section have shown the closeness of the design to the desired zero pressure gradient, smooth, flat, uniform heat flux surface. Only minor deviations from the desired test conditions were noted in the laminar flow region near the vertical leading edge. These deviations were small relative to the uncertainty of the data, discussed in Section 2.8. The baseline profiles have also confirmed the boundary layer data acquisition and reduction methods. In addition, the cold wall profiles (T_w=15 C) in Fig. 3-9, which were taken within moments of each other at three different vertical locations just downstream of the vertical leading edge, emphasize the vertical uniformity of the leading edge suction, since all the profiles are essentially the same, with the same δ_x and δ_{xx}. The δ_x is nominally 0.123 $\pm$0.003 cm and the δ_{xx} is nominally 0.049$\pm$ 0.001 cm for the three cold wall profiles.

3.3.2 Turbulent Forced Convection Baselines

Velocity and temperature profiles in the turbulent flow region further downstream on the test surface were taken for similar test conditions as the laminar flow cases in Fig. 3-10. The velocity profiles for a cold wall are shown in Fig. 3-11 and the velocity and temperature profiles for a heated wall in Fig. 3-12. The profiles in both figures are in wall coordinates and compared to accepted correlations for the logarithmic region of a turbulent, zero pressure gradient boundary layer flow on a smooth, flat surface [24]. The skin friction was obtained by least squares fit of the velocity data to the accepted zero pressure gradient profile. The convective heat transfer coefficient used in plotting the temperature profiles in wall coordinates is the experimentally measured value obtained from Eqn. (2-1) for the surface location where the data was taken.

The agreement with accepted correlations is good. The expected wake, logarithmic, and laminar sublayer regions are seen. For each profile, the skin friction obtained from the least squares fit of the measured velocity profile to the accepted profile compares within $\pm$4% to the skin friction calculated with the momentum thickness Reynolds number skin friction relationship presented in Kays and Crawford [24] for a zero pressure gradient flow on a flat plate. The momentum thickness used in the momentum thickness Reynolds number in that relationship was obtained by an integration of the measured velocity profile.

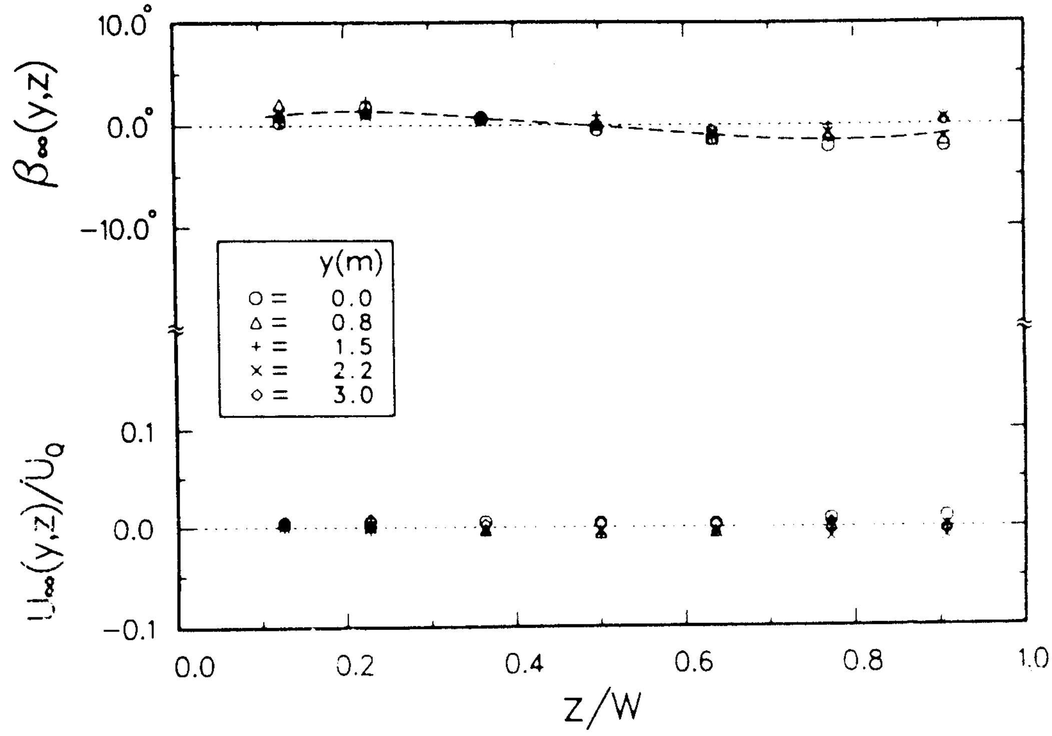

Fig. 3-1 Velocity Uniformity and Flow Angle Variation at the Inlet of the Test Section for a U_∞ of 4 m/s and an Environmental Wind Speed of 1.8 m/s.

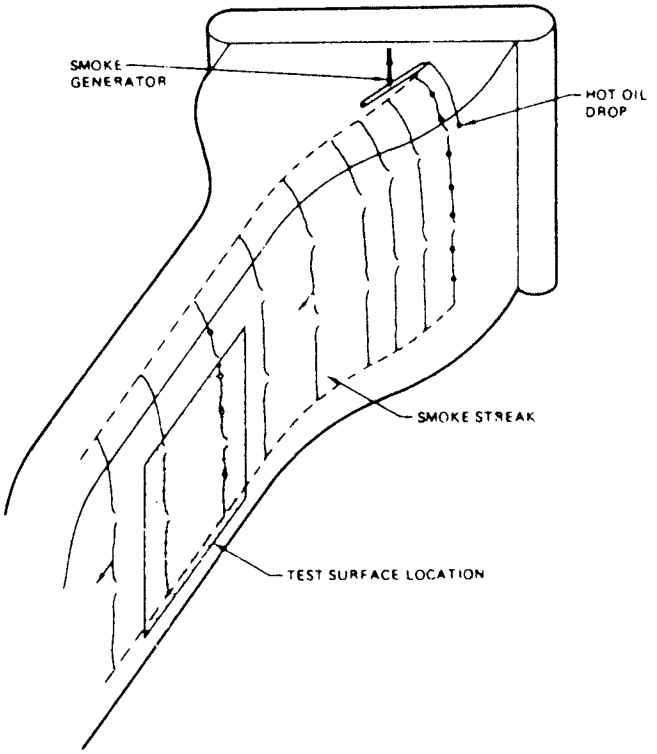

Fig. 3-2 Schematic of the Test Section Smoke Flow Visualization.

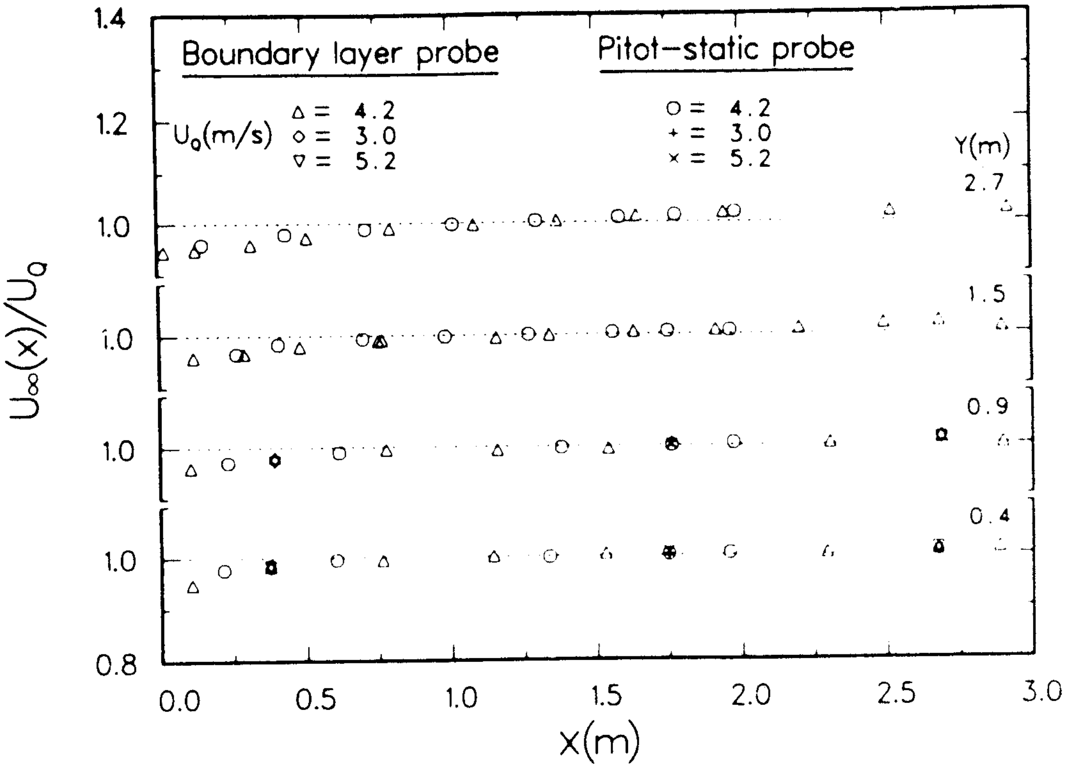

Fig. 3-3 The Axial and the Vertical Free-stream Velocity Variation Over the Test Surface.

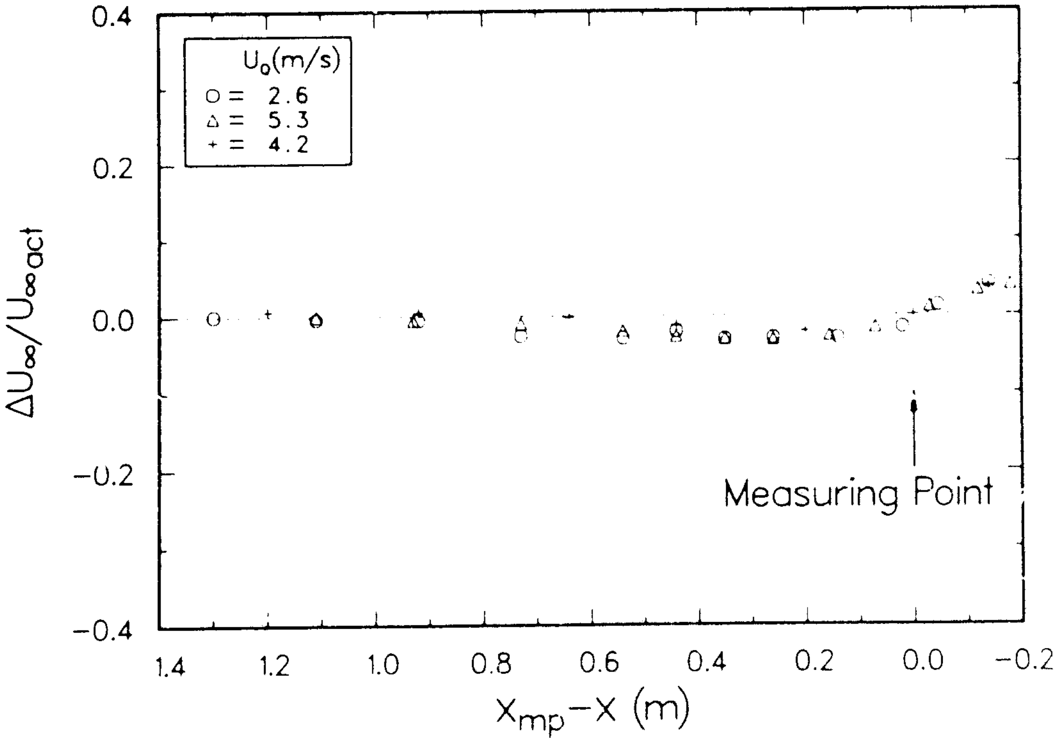

Fig. 3-4 The Effect of the Traverse Shield on the Free-stream Velocity Upstream of the Shield.

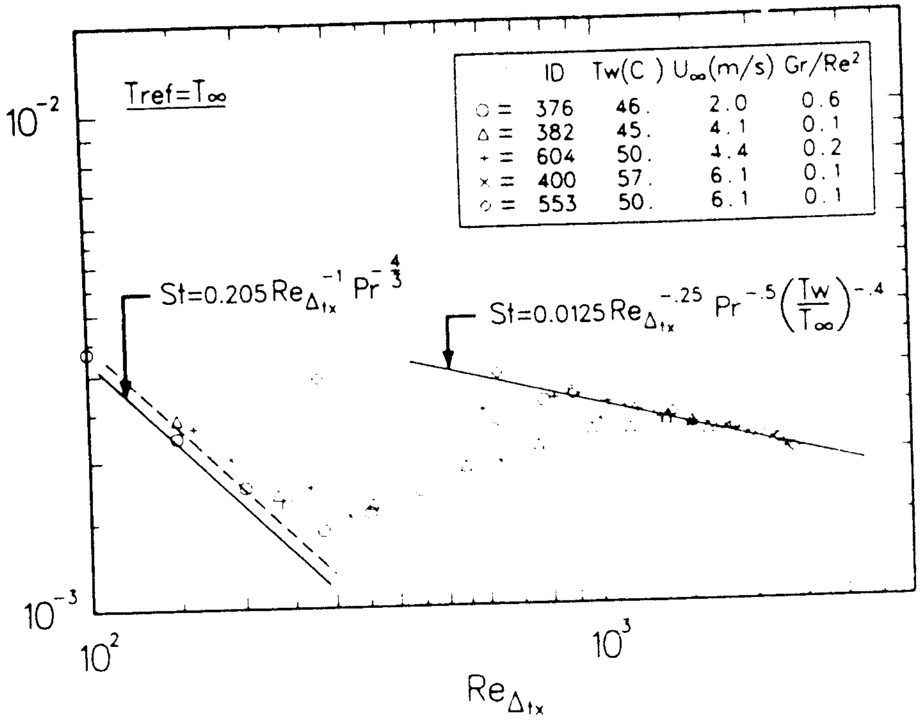

Fig. 3-5 Baseline Forced Convection Heat Transfer Results, St versus $Re_{\Delta_{tx}}$.

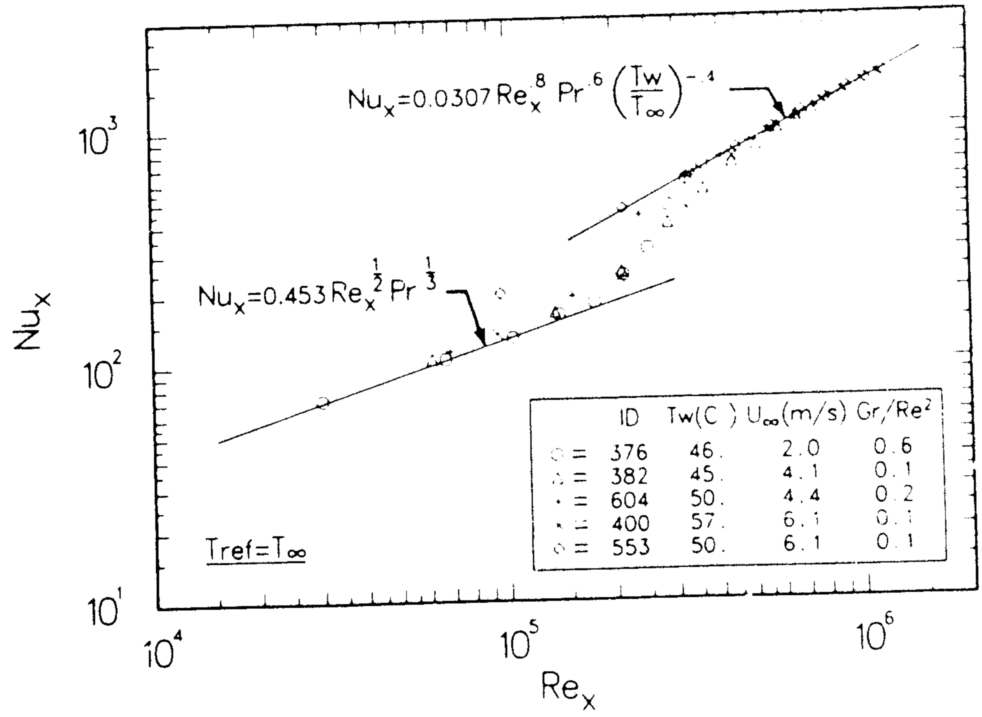

Fig. 3-6 Baseline Forced Convection Heat Transfer Results, Nu_x versus Re_x.

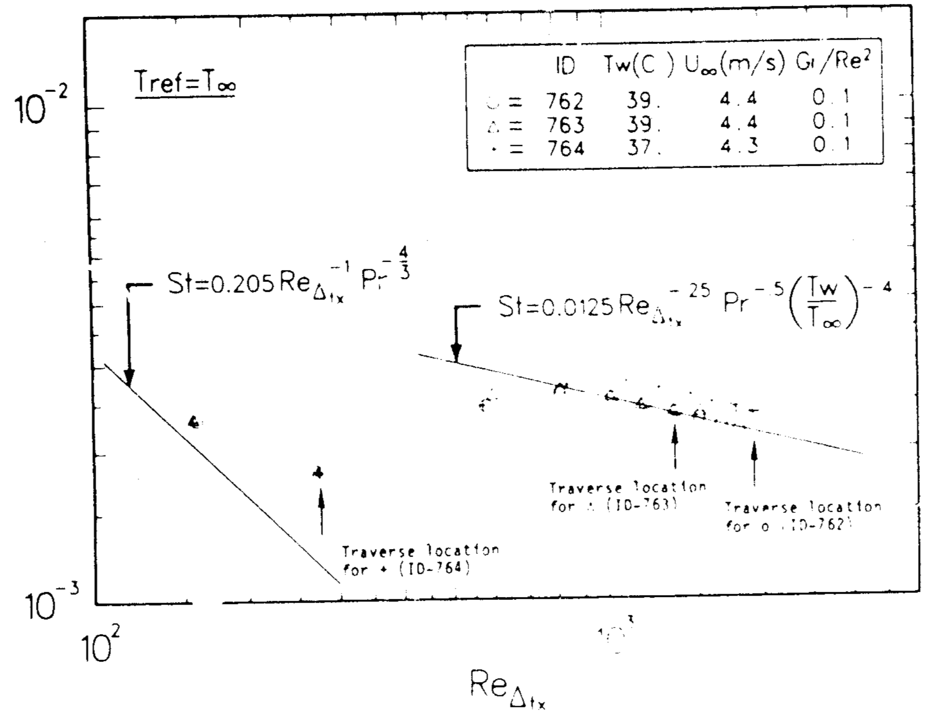

Fig. 3-7 The Effect of the Traverse Shield on Convection Heat Transfer.

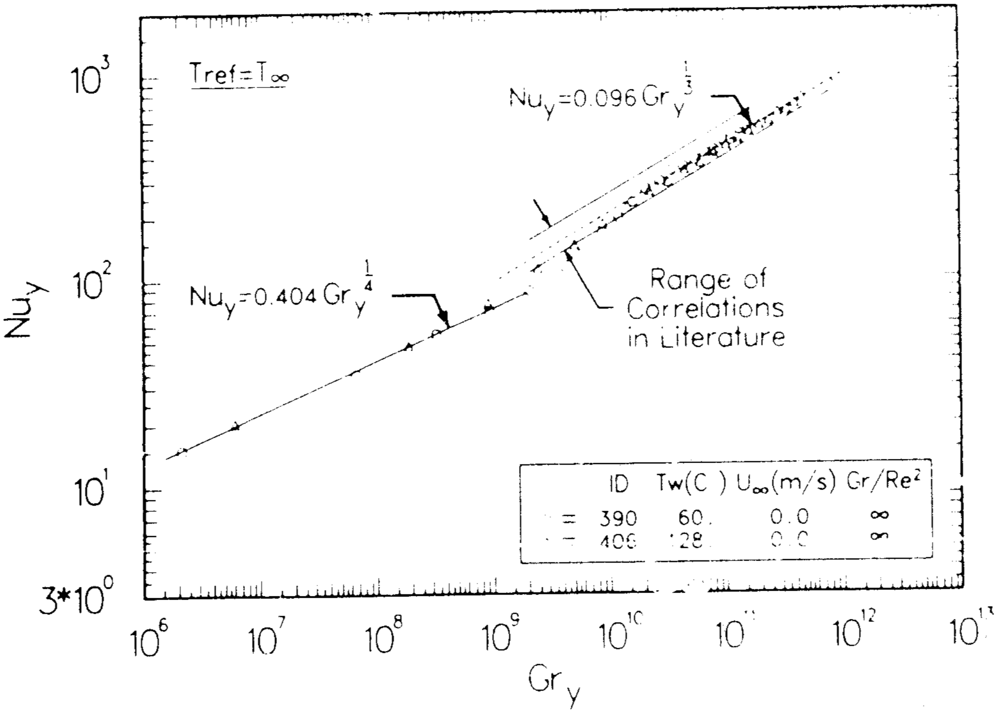

Fig. 3-8 Baseline Free Convection Heat Transfer Results, Nu_y versus Gr_y.

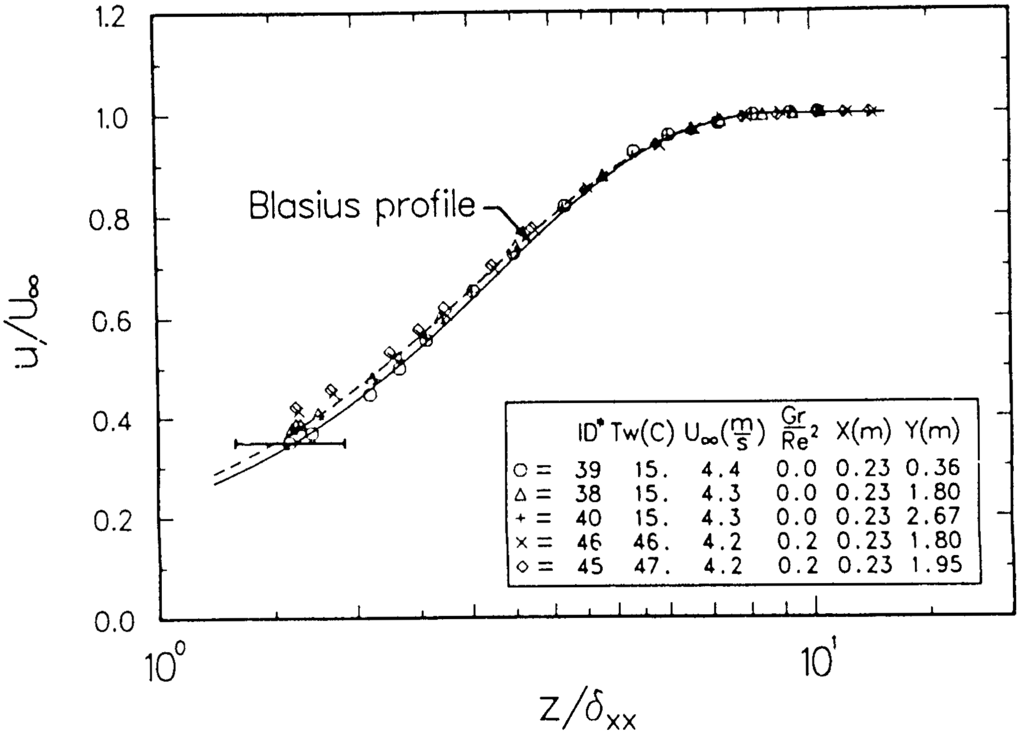

Fig. 3-9 Baseline Forced Convection Laminar Boundary Layer Velocity Profiles.

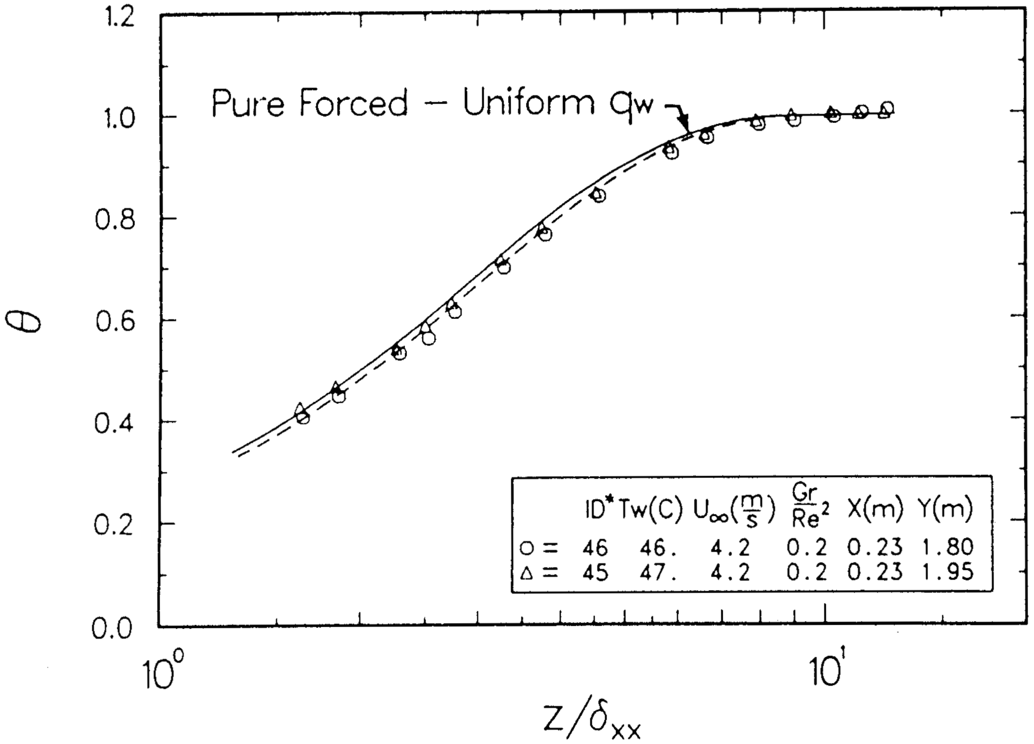

Fig. 3-10 Baseline Forced Convection Laminar Boundary Layer Temperature Profiles.

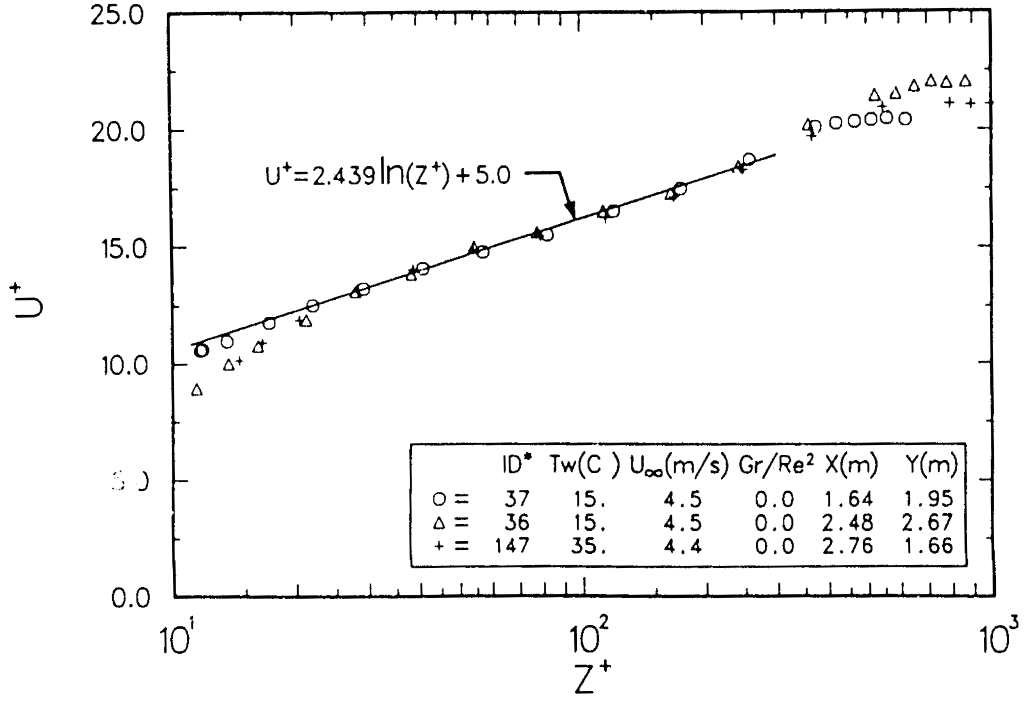

Fig. 3-11 Baseline Turbulent Forced Convection Boundary Layer Velocity Profiles ($C_f=4.7\times 10^{-3}$, 4.2×10^{-3}, 4.4×10^{-3} and $Re_{\delta_{**}}=940$, 1470, 1220 for ID^*'s 37, 36, 147, respectively).

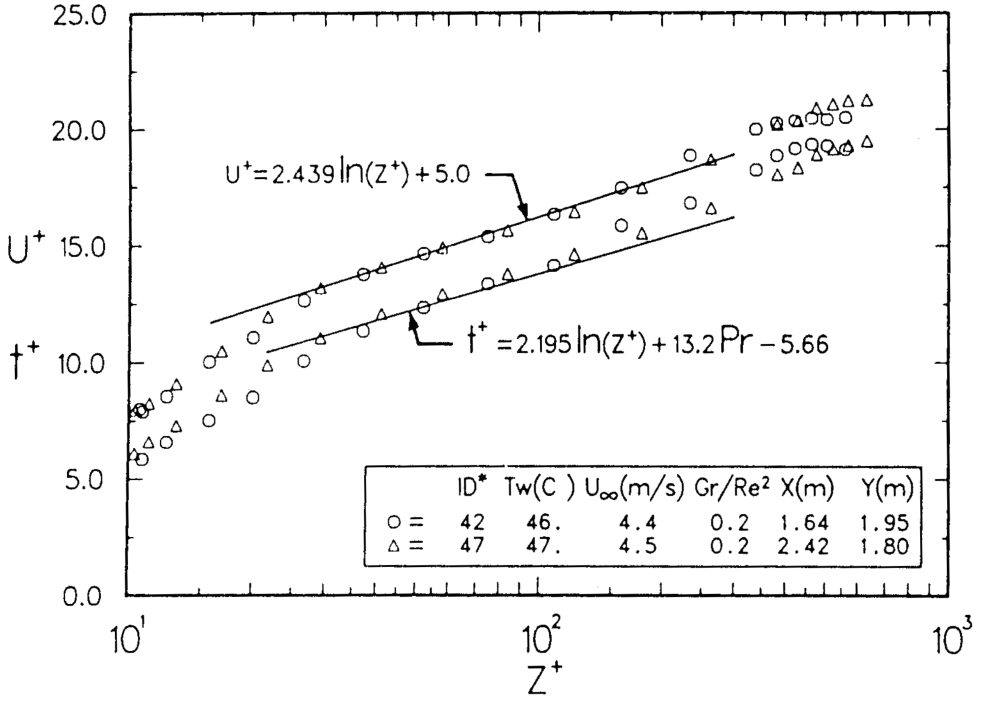

Fig. 3-12 Baseline Turbulent Forced Convection Boundary Layer Velocity and Temperature Profiles ($C_f=4.6\times 10^{-3}$, 4.3×10^{-3} and $Re_{\delta_{**}}=870$, 1240 for ID^*'s 42, 47, respectively).

Chapter 4.
RESULTS AND DISCUSSION

This chapter is divided into two main sections: the heat transfer results and discussion, and the boundary layer flow results and discussion. A third section presents a brief discussion of some observations made on transition from laminar to turbulent flow based on both the heat transfer and boundary layer flow results.

4.1 Heat Transfer

The heat transfer section is subdivided into five sections. The first section discusses variable properties effects on pure free and pure forced convection with the emphasis on turbulent free convection. The second section presents the average convective heat transfer from the test surface for forced, mixed, and free convection modes of heat transfer. This section shows what test conditions generate forced, mixed, or free convection on the average. Section three describes the variation of the local heat transfer coefficient over the test surface, as a function of test conditions. The fourth section presents methods for estimating the average and the local mixed convection heat transfer coefficients, based on the results of this experiment. These are then compared with recommendations in the literature. The final section presents some concluding remarks and overall observations about mixed convection heat transfer with orthogonal driving forces. All properties, unless otherwise specified, are evaluated at the T_∞, approximately 20 C in all cases (the exact T_∞ can be found in Appendix E for each test). The legend contained in most figures has the following information for each test condition plotted in a figure: the ID number, the average T_w, the U_∞, and the value of Gr_H/Re_L^2. The ratio Gr_H/Re_L^2 is used as a convenient descriptor of the ratio of the buoyant to the inertia force for a given test. It is not proposed as a general correlating parameter for mixed convection heat transfer except in special cases, as will be shown.

4.1.1 Variable Properties Effects

This section presents and discusses the effects of significant property (ρ, k, c_p, and μ) variations on free convection heat transfer from a vertical, flat surface and forced convection heat transfer from a flat, zero pressure gradient surface based results of these experiments. The primary emphasis is on variable properties effects on turbulent free convection heat transfer from a vertical surface. The comments apply to air or gases with similar property variations.

Figure 4-1 shows the free convection heat transfer results in terms of Nu_y and Gr_y from the vertical test surface. The range of wall temperatures studied was 60 C to 520 C. The ambient temperature was approximately 20 C for each data set. These conditions resulted in ratios of T_w/T_∞ from 1.1 to 2.7. All properties, including β, for the results in Fig. 4-1 are evaluated at the T_∞ of each test. The 21 data points shown in Fig. 4-1 for each surface temperature, are each the average of the five data points along one of the 21 horizontal heating strips, the same as in the baseline cases in Fig. 3-8. The RMS variation along a strip was generally less than $\pm 4\%$. For all tests except test ID 585, the test surface was within $\pm 1\%$ of steady state. Test 585, which had to be stopped before steady state was reached, has a transient energy storage correction equal to -5% of electric power dissipated. This correction accounted for energy being stored in the insulation. The correction was based on measurements of the insulation temperature taken over a 10-minute interval and was made along with the radiation and conduction corrections in Eqn. (2-1).

The tests were conducted with a hatch in the roof of the tunnel open and the top edge suction on the test surface on, to minimize stratification in the tunnel test section. Smoke visualization for each test showed no significant air motion in the test section except within the boundary layer itself. The largest stratification occurred for the 520 C test case: 10 C difference between the air at the center and the top of the test surface. In the stratified regions the local T_∞ was used in reducing the data, as described in Section 2.7.

In the turbulent region ($Gr_y > 10^{10}$), the data in Fig. 4-1 show two important points. First, there is a small decrease in Nu_y for a given Gr_y as T_w increases, when properties are evaluated at T_∞. Second, each data set for each temperature remains parallel to the low-temperature difference Nusselt-Grashof number correlation given by Eqn. (3-8) (the solid line) from Churchill and Chu [39]; this is most visible for test 585. This latter point means that Nu_y remains dependent on $Gr_y^{1/3}$ in the turbulent flow region with increasing temperature difference across the boundary layer, or in other words, the heat transfer coefficient remains uniform in the turbulent region. Only the coefficient in Eqn. (3-8) is changing with increasing temperature.

It decreases from the 0.096 value for a small temperature difference across the boundary layer to a value of 0.08 for the 520 C test, a decrease of 15%. This decrease does not imply that the turbulent free convective heat transfer coefficient at a fixed location is lower for higher T_w. It only indicates that the heat transfer coefficient is less than would be predicted by the low temperature-difference constant-properties correlation with properties evaluated at T_∞ as a result of property variations across the boundary layer.

In the laminar region ($Gr_y < 5 \times 10^8$) in Fig. 4-1, there is a small decrease in Nu_y for a given Gr_y as T_w increases. The decrease in Nu_y with increasing T_w is most clearly shown by the lowest Gr_y data point for each T_w. The lowest Gr_y data point lies progressively further below the uniform heat flux Nusselt-Grashof number correlation given by Eqn. (3-7), the upper line in the laminar region.

The decrease in Nu_y with increasing T_w in the laminar region is not totally due to variable properties effects though, as was the case in turbulent flow. The decrease in Nu_y is partly due to a change in the convection heat transfer boundary condition on the test surface as T_w increases. At low temperatures, the convection boundary condition is a uniform heat flux condition, as described earlier. At high temperatures, the convection boundary condition approaches a uniform temperature condition as a result of the radiation heat transfer from the surface. For the highest temperature case, 520 C, the test surface is within 2% of a uniform temperature surface in the laminar and transition regions. The Nusselt-Grashof number correlation for uniform surface temperature is the lower line in the laminar region in Fig. 4-1 [24]. A combination of variable properties effects and a change in boundary condition are indicated by the fact that the highest temperature laminar data point lies about 8% below the uniform surface temperature relationship.

Unlike the situation in the laminar region, a change in boundary condition does not occur in the turbulent region. A surface with a turbulent free convection flow is simultaneously a uniform temperature and a uniform heat flux surface (i.e., h is spatially uniform for a given T_w). Churchill and Chu's [39] uniform temperature and uniform heat flux correlations based on "best fits" of data in the literature are only different by 2% for a Pr of 0.71. The difference is well within the uncertainty of the data available.

When all the properties are evaluated at T_∞, the variable properties effects noted in Fig. 4-1 for turbulent free convection in air are accounted for by the following correlation:

$$Nu_y = 0.098 Gr_y^{1/3} \left(\frac{T_w}{T_\infty} \right)^{-0.14} \tag{4-1}$$

This is based on a "best fit" of the free convection data in Fig. 4-1, where the 1/3 power on Gr_y was assumed as a result of the lack of dependence of h on y that is shown by each set of heat transfer coefficient data for each T_w. The coefficient in Eqn. (4-1) is 2% higher than that in the baseline equation, Eqn. (3-8), and a temperature ratio correction has been added to account for the effects of variable properties.

Figure 4-2, where the Nusselt number, Nu'_y, is defined so that it includes the temperature ratio correction term in the definition of Nusselt number, shows that Eqn. (4-1) accounts for the small systematic decrease in Nu_y with increasing temperature that appeared in Fig. 4-1. The turbulent data (the same data as in Fig. 4-1) collapse to within ±6% of the correlation given by Eqn. (4-1). This is within the uncertainty band on the heat transfer data.

The variable properties effects on turbulent free convection could also have been accounted for, without a separate temperature ratio correction, by evaluating all the properties, except β in Gr_y, at a T_r defined as:

$$T_r = 0.3 T_w + 0.7 T_\infty \tag{4-2}$$

The term β should still be evaluated at T_∞.

The correlation for laminar heat transfer data in air, with all properties evaluated at T_∞, is:

$$Nu_y = a Gr_y^{1/4} \left(\frac{T_w}{T_\infty} \right)^{-0.04} \tag{4-3}$$

The term a equals 0.404 for a uniform heat flux surface and 0.356 for a uniform temperature surface, the values reported in the literature. Equation (4-3) agrees with the numerical predictions made by Siebers [1] for $T_w/T_\infty < 3.0$, with the more detailed laminar data for $T_w/T_\infty < 1.5$ from the experiments of Pirovano et al. [23], and with the various analyses for air [21,22]. Equation (4-3) demonstrates that variable properties effects on laminar free convection heat transfer are small. The difference in h calculated from Eqn. (4-3) with and without the T_w/T_∞ correction at a T_w/T_∞ of 3.0 would only be 4%. The small variable properties effect on laminar free convection agrees with the small effects noted in laminar forced convection also [24,25].

Instead of using the temperature correction in Eqn. (4-3), the effects of variable properties on laminar free convection heat transfer can also be accounted for by evaluating all properties, except β in Gr_y, at T_f, as noted by Sparrow and Gregg [22] and Pirovano et al. [23]. The term β should still be evaluated at T_∞, as in turbulent flow.

The trends noted in the turbulent free convection region are new. No experiments were found in the literature for high-temperature turbulent free convective flows on a vertical surface with large temperature differences across the boundary layer. The highest temperature experiment with turbulent flow in gases was by Pirovano et al. [23], with temperatures up to 150 C and $T_w/T_\infty < 1.5$. The one experiment that had large temperature variations across a turbulent boundary layer was at cryogenic temperatures. Clausing and Kempka [26], who conducted this experiment, noted different trends.

Table 4-1 shows a comparison of the effects of variable properties on turbulent natural convection heat transfer from a vertical surface in air predicted by various recommended methods to account for those effects. In the table, the effects predicted by five recommendations appearing in the literature (Refs. 13, 23, 24, 26, and 40) are compared to the effects predicted by the method proposed in this paper. The present work recommends evaluating all properties in the constant properties heat transfer relationship at T_∞ and making the wall-to-ambient temperature ratio correction, $(T_w/T_\infty)^{-0.14}$, shown in Eqn. (4-1).

For each of the five methods, the table gives the T_r at which properties are evaluated, the temperature used to determine β, and the ratio of h predicted by that method to h predicted by Eqn. (4-1) for three different values of T_w (300, 600, and 900 C) and a T_∞ of 20 C. The first two methods listed (Refs. 23 and 26) are recent recommendations reported in the literature based on experimental data. The next three (Refs. 24, 13, and 40) are recommendations reported in most basic heat transfer textbooks. All of the methods except Clausing and Kempka's [26], the second method, are reference temperature methods. Clausing and Kempka [26] evaluate all properties, including β, at T_f and make a large correction based on T_w/T_∞ (given in Fig. 5 in Ref. 26) to account for variable properties effects.

The constant properties Nusselt-Grashof number correlation to which all the recommended methods given in Table 4-1 are applied is given by Eqn. (4-1) without the $(T_w/T_\infty)^{-0.14}$ term. The correlation represented by Eqn. (4-1) without the temperature ratio term is not significantly different than the constant properties correlations used in each of the references in Table 4-1. The only difference is in the coefficient (0.098 in Eqn. (4-1)) in each correlation. Applying all methods to one constant properties correlation allows the different methods of handling variable properties to be compared, without introducing the small differences in the coefficient of the constant properties relationship that is recommended in each work. Effectively, this means that Table 4-1 compares the relative trend in the variable properties effects predicted by each method for increasing T_w with that predicted by Eqn. (4-1).

Table 4-1
A Comparison of Recommendations for Evaluating Variable Properties Effects on Turbulent Free Convection (T_∞=20 C).

Ref.→	[23]	[26]	[24]	[13]	[40]
T_r →	$0.2T_w$ $+0.8T_\infty$	T_f, Fig. 5 [26]	T_f	T_f	$0.62T_w$ $+0.38T_\infty$
β →	$1/T_\infty$	$1/T_f$	$1/T_\infty$	$1/T_f$	$1/T_\infty$
↓$T_w(C)$	h/h predicted by Eqn. (4-1)				
300	1.03	1.30	0.95	0.82	0.90
600	1.04	1.17	0.90	0.71	0.87
900	1.06	1.10	0.88	0.65	0.82

Table 4-1 shows that the first method, from Pirovano et al. [23] (the most closely related experiment to this one), predicts substantially the same variable properties effect as Eqn. (4-1) for all temperatures. This reference temperature method uses a T_r heavily weighted toward T_∞, given by Eqn. (1-10), with β evaluated at T_∞. It is based on an experiment with values of T_w up to 150 C. The second method in the table, the method recommended by Clausing and Kempka [26] based on their data at cryogenic temperatures, predicts 30% higher heat transfer at 300 C and 10% higher heat transfer at 900 C. These differences indicate that their method predicts a different trend than Eqn. (4-1) with regard to the effect of variable properties on turbulent free convection with increasing T_w. The last three methods in Table 4-1 - - the text book methods - - predict increasingly lower heat transfer coefficients with increasing T_w. This is particularly true for the fourth method, where β is evaluated at T_f along with the rest of the properties.

The disagreement between the methods recommended in this work and the last three methods is most likely explained by the fact that these recommendations are based on forced convection experience or on a laminar flow free convection analysis by Sparrow and Gregg (found in Ref. 22). No turbulent free convection data with variable properties effects was available. Recommendations based on forced convection experience should not be expected to work, a priori, for turbulent free convection. Similarly, recommendations based on Sparrow and Gregg's [22] laminar flow analysis should not be expected to work, a priori, for turbulent free convection, since, first, the analysis was for laminar free convection heat transfer and, second, the variable properties effects on which they based their conclusions in that analysis were only a few percent for the realistic gas models and temperature ranges studied ($330\ K < T < 1000\ K$, $T_w/T_\infty < 3.0$). For example, if an h for air predicted using T_f as the reference temperature in the laminar heat transfer relationship, Eqn. (3-7), is compared to an h predicted with the same relationship using Sparrow and Gregg's [22] recommended reference temperature, given by Eqn. (1-9), there would be less than a 1% difference in the h's for T_w at 600 C and T_∞ at 20 C ($T_w/T_\infty \approx 3.0$). The disagreement with the results of Clausing and Kempka [26] may be the result of the fact that their experiment was conducted at cryogenic temperatures in nitrogen, where the property variations and their effects on turbulent free convection may be different.

Forced convection variable properties effects were also observed in this experiment. Qualitatively, the laminar forced convection results indicate the effects of variable properties on laminar forced convection were small. This agrees with the more detailed information presented by others [24]. Quantitative variable properties effects on laminar forced convection were not possible to obtain. The problem in the laminar forced convection regions was the same as for laminar free convection: the boundary condition changed with increasing T_w making it difficult to separate the effects of variable properties from the effects of a change in the boundary condition. Not even for the highest temperature forced convection case did the surface approach a uniform temperature surface as it did in pure free convection.

Variable properties effects on turbulent forced convection in this experiment were significant. These effects are correlated by the following expression:

$$Nu_x/Re_x^{0.8} = 0.025\left(\frac{T_w}{T_\infty}\right)^{-0.4} \tag{4-4}$$

This correlation agrees with the one recommended in Kays and Crawford [24] to account for the effects of variable properties on turbulent forced convection in gases. In addition, the variable properties effect predicted by Eqn. (4-4) for air is not substantially different from that predicted when properties are evaluated at the film temperature to account for the effects of variable properties, instead of making the $(T_w/T_\infty)^{-0.4}$ correction as in Eqn. (4-4). Use of a film temperature in air is equivalent to using an exponent of -0.35 on T_w/T_∞ in Eqn. (4-4). Film temperature is the recommendation most often made in the literature to account for variable properties effects on forced convection, but that recommendation is generally based on results from compressible, high-speed, high-temperature flow experiments [24], unlike the results from this low speed experiment. At a temperature ratio of 3.0, there is only a 6% difference in the answer predicted using the two different values, -0.35 and -0.40, for the exponent on T_w/T_∞ in Eqn. (4-4).

The variable properties effect on turbulent forced convection that is given by Eqn. (4-4) was obtained from a "best" fit of a method for estimating mixed convection heat transfer to all the data from this experiment, forced, mixed, and free convection. The "best" fit will be discussed in detail in Section 4.1.4. This method was used to determine the effects of variable properties on turbulent forced convection because it allowed the effects of variable properties and the effects of buoyancy on turbulent forced, both of which became important with increasing T_w, to be separated.*

The combined effects of variable properties and buoyancy on turbulent forced convection in air as a function of T_w, that were discussed above, are shown in Fig. 4-3. The figure is a plot of the average value of $Nu_x/Re_x^{0.8}$ determined from data in the turbulent flow region versus T_w/T_∞ (where T_∞ is a constant) for various Gr_H/Re_L^2 tests. The number given near each data point in Fig. 4-3 is the Gr_H/Re_L^2

---

* Effects due to a change in the heat transfer boundary condition on turbulent forced convection with increasing T_w, from uniform heat flux to uniform temperature, were not a problem. The maximum possible effect on heat transfer of a complete change in the boundary condition would have only been 4% [24].

of the test. For tests with a $Gr_H/Re_L^2<4.0$, the value of $Nu_x/Re_x^{0.8}$ was a constant to within the uncertainty of the data for the entire turbulent flow region of each test, so the average value plotted for those tests is representative of that constant value. For tests with a $Gr_H/Re_L^2>4.0$, there was some variation in the value of $Nu_x/Re_x^{0.8}$ in the x-direction in the turbulent flow region and the value plotted for those tests is only an average value. Also shown in Fig. 4-3 is Eqn. (4-4), which is the curve the data would fall on if only variable properties effects were present.

Figure 4-3 shows that for cases with increasing T_w/T_∞, but with approximately the same value of Gr_H/Re_L^2 (i.e., a fixed ratio of buoyant to inertia forces), the value of $Nu_x/Re_x^{0.8}$ decreases due to the effects of variable properties. For cases with a fixed T_w/T_∞, the value of $Nu_x/Re_x^{0.8}$ increases with increasing Gr_H/Re_L^2 due to the effects of buoyancy. The figure also shows that none of the data, except for cases with very low T_w/T_∞ and Gr_H/Re_L^2, lie exactly on Eqn. (4-4). This difference is the result of the importance of buoyancy, even for cases with values of Gr_H/Re_L^2 as low as 0.7 (most of the data shown in the figure). The effects of buoyancy on convection heat transfer from the surface will be discussed in detail in the next section.

The uncertainty of the exponent in Eqn. (4-4), -0.4, is about ± 0.07, based on the average uncertainty of the heat transfer coefficient data. Considering only the uncertainty of the exponent, the uncertainty in a heat transfer coefficient estimated with Eqn. (4-4) would be about $\pm 8\%$ at a temperature ratio of 3.0.

4.1.2 Average Heat Transfer

A three-dimensional plot of the average convection heat transfer coefficient for the test surface versus the U_∞ and the average value of $T_w - T_\infty$ is shown in Fig. 4-4. Figure 4-5 is the same information expressed in terms of Nusselt number versus Grashof number and Reynolds number. The surfaces were generated from bicubic spline fits of the average heat transfer coefficient and average Nusselt number as functions of the respective independent parameters in each figure. A total of 46 data points were used in the surface fits, 37 of which were distinct test conditions, 9 of which were replications of test conditions (see Appendix E). The data are evenly spread over the surface in Fig. 4-4. The surfaces fit the data to within $\pm 3\%$ on the average. The largest deviation, between actual data and the surfaces shown, was less than 10%.

The average heat transfer coefficient is an average of the 105 measurements of local surface heat transfer coefficient made at the locations shown in Fig. 2-11. The average includes the laminar, transitional, and turbulent zones. The reference temperature for all property evaluations in Fig. 4-5 is T_∞. The average Nusselt number is calculated from the average heat transfer coefficient. The characteristic lengths in the Reynolds and Grashof numbers are the test surface length and height, respectively. The characteristic length in the Nusselt number is given by

$$LH = [H^2 sin^2(B_{max}) + L^2 cos^2(B_{max})]^{1/2} \tag{4-5}$$

This characteristic length in the Nusselt number provides a smooth transition of characteristic length from L for pure forced convection to H for pure free convection based on the maximum flow angle in the boundary layer flow leaving the upper or downstream end of the test surface, B_{max}. As B_{max} approaches zero, pure forced convection, LH approaches L. As B_{max} approaches 90°, pure free convection, LH approaches H. The angle B_{max} can be determined from a relationship for β_{max}, the maximum flow angle in the boundary layer at any location on the test surface, given in Section 4.2.3. This choice of characteristic length allows the high Grashof, low Reynolds number data to be compared to the existing free convection data in the literature, since in most works the Nusselt and Grashof numbers are based on the characteristic length in the free convective flow direction, H in this case. This choice also allows the high Reynolds number, low Grashof number data to be compared to the forced convection data in the literature, since in most works the Nusselt and Reynolds numbers are based on the characteristic length in the forced flow direction, L in this case.

Figure 4-4 shows a smooth variation in average convective heat transfer coefficient over the range of surface temperatures and free-stream velocities studied. The average heat transfer coefficient in the zero velocity plane is the turbulent free convection heat transfer coefficient. The heat transfer coefficient at low temperature difference and at high velocity is the turbulent forced convection heat transfer coefficient. At high velocities, there is a decrease in heat transfer coefficient with increasing temperature difference due to the strong effect of variable properties on turbulent forced convection.

When the data are plotted in dimensionless form, as shown in Fig. 4-5, the surface still has a smooth appearance, but three distinct regions of convection heat transfer appear. These regions are highlighted on Fig. 4-5. The approximate dividing lines between regions are lines of constant Gr_H/Re_L^2 equal to 0.7 and 10.0. Extending from the free convection baseline to the line along which $Gr_H/Re_L^2 \approx$ 10.0 is a region where the average heat transfer can be estimated to within 5% by considering only free convection as a mechanism for heat transfer. For this region, the average heat transfer coefficient can be calculated using correlations for pure free convection. Extending from the forced convection baseline out to the line along which $Gr_H/Re_L^2 \approx 0.7$ is region where the average heat transfer can be estimated to within 5% by considering only forced convection as a mechanism for heat transfer. For this region, the average heat transfer coefficient can be calculated using correlations for pure forced convection.

In between Gr_H/Re_L^2 of 0.7 and 10.0 is the region of mixed convection heat transfer. It is a smooth fairing between the free and forced convection regions. Both free and forced convection mechanisms must be considered in calculating the average heat transfer coefficient. The line $Gr_H/Re_L^2 \approx 3$ is the bisector of the mixed convection region.

The boundary values quoted in terms of Gr_H/Re_L^2 for the mixed convection region and the value for the bisector in terms of Gr_H/Re_L^2 are for an L/H of 0.98. They are indicative but not precisely known, since the mixed convection effects come on slowly and smoothly.

The regions of "pure" forced and "pure" free convection heat transfer do not imply that the hydrodynamic behavior in those regions is unaffected by mixed convection. Measurements of boundary layer flow direction (shown later) made far inside the free convection region, show significant flow components in the direction of the free-stream flow, while free convection effects (upwards flow within the boundary layer) are clearly visible well inside the forced convection region. Only when there is no free-stream flow, or no wall-to-free-stream temperature difference, are the hydrodynamics driven only by a single mechanism. Also, existence of these regions, the "pure" forced and "pure" free convection regions, does not imply that the local heat transfer is affected only by a single mechanism everywhere on the test surface for test conditions inside those regions. It will be shown later for example, that in the "pure" free convection region there are still regions on the test surface where local heat transfer is dominated by forced convection, but not enough to significantly effect the overall average convective heat transfer.

Also shown in Fig. 4-5 is an extension of the pure free convection heat transfer plane through the box below the heat transfer surface. This plane represents the minimum convection heat transfer from the surface, the situation with no air flow. The difference between the "Free Only plane and the average heat transfer surface is the incremental effect of adding forced convection to the pure free convection case. For example, the mixed convection heat transfer occurring along the line $Gr_H/Re_L^2 \approx 0.7$ is higher than pure free convection by about 95%.

4.1.3 Local Heat Transfer

Figure 4-6 shows the distribution of the local convection heat transfer coefficient over the test surface for four different test conditions with U_∞ ranging from 0.0 to 6.1 m/s and with the average T_w at a nominally constant value of 225 C. Each of the four surfaces in the figure was generated from a bicubic spline fit of the 105 local measurements of h, normalized by the average heat transfer coefficient, $\overline{h}$. The value of $\overline{h}$ for each test condition is the average of the 105 local measurements h for that test condition. The surfaces do not show data for the top and bottom heating strips because of possible edge effects. Each surface fits the 105 local h measurements for that test within $\pm 2\%$, on average. The largest deviation between the surfaces shown and the actual data is about 15%. The fit is poorest in the transition zone, where large variations in h occur over small spanwise distances.

The top surface in Fig. 4-6 shows a case of pure free convection with the T_w at 222 C. The heat transfer coefficient is uniform over most of the test surface, as expected for pure turbulent free convection. There is a small transition region along the lower edge of the test surface. A laminar region occurs on the first heating strip, but the data are not shown. The average h was 7.8 W/m^2C for this condition.

The second surface down shows the results for a U_∞ of 1.5 m/s, representing a Gr_H/Re_L^2 of 9.6, a condition which is just inside the mixed convection region defined in Fig. 4-5. The horizontal free convection transition zone, seen in the surface above this one, has disappeared from the lower edge, and a vertical transition zone has appeared on the upstream vertical leading edge. The heat transfer coefficient is uniform on the downstream end of the test surface like pure turbulent free convection. A vertical "hump" or high point in heat transfer appears just downstream of the vertical transition zone. There is no significant vertical dependence anywhere on the surface. The average heat transfer coefficient was 7.7 W/m^2C, approximately the same as for the pure free convection case shown above this one.

The third surface down, for a U_∞ of 2.5 m/s, represents a Gr_H/Re_L^2 of 3.3. This is near the center of the average mixed convection region. The data show a dominant laminar forced convection pattern near the vertical leading edge with no variation in the vertical direction and a vertical transition zone. The transition occurs at an Re_x of about 130,000 which is less than the value of 300,000 to 400,000 noted for pure forced flows in this experiment. This is true even if a film temperature is used to determine properties in Re_x. The region downstream of the transition shows a noticeable x-dependence similar to turbulent forced convection flows. There appears to be no vertical dependence in the turbulent region as with turbulent free convection, except for near the bottom of the test surface. The increase in heat transfer on the lower edge is probably the result of a combination of effects, some caused by the traverse support struts on the bottom edge and some caused by the buoyant forces in the boundary layer in that region. The buoyant forces cause the streamlines in the boundary layer to diverge along the lower leading edge, resulting a thinner boundary layer in that region, and thus higher heat transfer (see Appendix D). The average heat transfer coefficient for this case was 8.5 W/m^2C.

The bottom surface in Fig. 4-6, at a Gr_H/Re_L^2 of 0.6, shows a condition just at the forced convection boundary of the mixed convection domain defined in Fig. 4-5. The distribution of h is typical of pure forced convection, except for some small disturbances along the lower edge, at the downstream end. The average h on the surface was 15.6 W/m^2C, the same as for a pure forced convection case for the same maximum Reynolds number at a T_w of 50 C. The fact that the average is the same as for pure forced convection at a lower wall temperature is the result of an increase in heat transfer caused by the buoyant force at a Gr_H/Re_L^2 of 0.6 and a compensating decrease in heat transfer caused by variable properties effects.

These four surfaces traced a path across the T_w, U_∞ operating domain at a nominally constant T_w. Hence, any effects due to variable properties should be approximately the same for all the cases in Fig. 4-4 and should not affect the relative changes demonstrated.

Figure 4-6 has shown that even though the average h is constant for the upper two surfaces inside the average free convection region, changes are noted in the distribution of local h as the value of Gr_H/Re_L^2 approaches the bounding value of 10.0 from within the average free convection region in Fig. 4-5. In the mixed convection region both the distribution of h and the average h are changing. The average h increases with increasing velocity for the bottom three surfaces. The figure also shows that the vertical leading edge is always dominated by forced convection, as long as any forced flow is present, and lower leading edge effects are only significant up to the second strip for $Gr_H/Re_L^2 \approx 3.0$.

Figure 4-7 shows four cases at a nominally constant U_∞ of 2.4 m/s, with T_w ranging from 54 to 588 C. These trace a path across the T_w, U_∞ operating domain, which intersects the constant T_w path shown in the previous figure, Fig. 4-6, about in the middle of the mixed convection region in Fig. 4-5.

The bottom surface in Fig. 4-7 shows a forced convection transitional flow situation at an average T_w of 54 C. The boundary layer is laminar near the vertical leading edge, turbulent at the downstream edge, and transitional everywhere else on the test surface. It is a case on the edge of the average forced convection region in Fig. 4-5. The average h is 6.5 W/m^2C.

The second surface up in Fig. 4-7, at an average T_w of 231 C, shows behavior typical of the middle of the mixed convection region, at a Gr_H/Re_L^2 of 3.3. This is the same surface as the third one up in Fig. 4-6. The transition is moved upstream compared with the surface below it. The heat transfer coefficient has a similar dependence on x as it does for pure turbulent forced convection ($h \sim x^{-0.2}$). The average h is 8.5 W/m^2C.

On the third surface up, at a Gr_H/Re_L^2 of 6.4, the transition zone is moved even further forward. The heat transfer coefficient still has a strong laminar forced convective pattern near the vertical leading edge. In the turbulent region, the dependence of h on x changes from a forced convection like x dependence to a free convection pattern of nearly uniform h in a short x-distance. There is little vertical dependence anywhere on the surface. The higher h on the lower strip noted on the surface below for Gr_H/Re_L=3.0 is becoming less prominent. The average h is 9.0 W/m^2C.

In the top surface, at a Gr_H/Re_L^2 of 10.2, only a small portion of the transition zone remains near the vertical leading edge of the test surface where the flow is still dominated by forced convection. The "hump" in h downstream of transition, seen in the second surface down in Fig. 4-6 at a Gr_H/Re_L^2 of 9.6, appears for this case also. Over the rest of the surface h is uniform, within the uncertainty in the data, a characteristic of turbulent pure free convection. The average h is 9.3 W/m^2C.

Figure 4-7 has shown that increasing the average T_w from 54 to 231 C at a nominally constant U_∞ of 2.4 m/s induced a significantly earlier transition on the test surface. Further increases in the average T_w, to 354 C and then to 588 C, moved transition even further forward, but not as much as the first increase in T_w. The distribution of h over most of the surface changed from one typical of pure forced convection with laminar, transitional, and turbulent zones to one typical of high Grashof number turbulent free convection with a uniform h. The vertical leading edge was always dominated by forced convection. The lower, horizontal, leading edge had higher convection heat transfer relative to the rest of the surface for a Gr_H/Re_L^2 less than 10 but greater than about 1.

Figure 4-8 shows four cases for a nominally constant Gr_H/Re_L^2 of 3.2. The cases lie along a path in the middle of the mixed convection region in Fig. 4-5. The mean values of h are 8.5, 9.4, 10.4, and 11.0 W/m^2C, going from the bottom to the top in Fig. 4-8. These four surfaces show a striking similarity in their appearances. The distributions of h on the test surface are almost identical in all four cases. Forced convection dominates on the vertical leading edge with a laminar zone having no vertical dependence and a vertical transition zone. The dependence of h on x is the same for all cases in the turbulent zone, and similar to the $x^{-0.2}$ dependence for a pure forced convection turbulent boundary layer. For each case, the lower leading edge has the same rise in h relative to the rest of the surface. The only apparent difference is that the transition zone seems to be moving slightly forward with increasing T_w and U_∞. But when the properties in the transition Re_x are evaluated at the film temperature, instead of T_∞, the transition Re_x is nominally 85,000 $\pm 10\%$. The transition Re_x is defined as the Reynolds number that occurs halfway between the lowest and the highest values of h in the transition zone. Transition is discussed more in Section 4.3.

Figure 4-9 shows four more surfaces for a nominally constant Gr_H/Re_L^2 of 10.0. These surfaces are on the edge of the free convection region in Fig. 4-5. The average heat transfer can be predicted to within approximately 5% by pure free convection correlations for these tests. The local h distribution resembles turbulent free convection on the downstream two-thirds of the test surface. The heat transfer coefficient is approximately uniform in that region with a small ($<10\%$) rise very near the bottom edge. This is most likely due to lower edge effects discussed in Appendix D. At the vertical leading edge there is an increase in h just downstream of the leading edge equal to 10 to 15% of the average h. This "hump", which was noted previously in cases with Gr_H/Re_L^2 around 10.0, is approximately uniform in the vertical direction. The "hump" is also at approximately the same location on each surface emphasizing the similarity in heat transfer for constant Gr_H/Re_L^2 noted in Fig. 4-8.

The variation of h between the vertical leading edge and the downstream base of the "hump" in Fig. 4-9 resembles dominant forced convection heat transfer. Actually, the laminar convection heat transfer upstream of the "hump" is identical to pure laminar forced convection heat transfer and the turbulent convection heat transfer on the downstream side of the "hump" has similar x-dependence as pure turbulent forced convection. Figure 4-10 shows this more clearly. It is a plot of Nu_x versus Re_x for several Gr_H/Re_L^2 cases at a nominally constant average T_w of 230 C. The data is column averaged in the same way as was the baseline data in Fig. 3-7. Column averages are a valid way of looking at the mixed convection heat transfer data, since it was shown in Figs. 4-6 through 4-9 that the mixed convective heat transfer had little if any dependence on vertical distance, even though it was generated by a three-dimensional flowfield. The correlations in Fig. 4-10, the solid lines, are the same as those in Fig. 3-6. The location of the turbulent baseline correlation in Fig. 4-10 takes into account variable properties effects on pure forced convection for a T_w of 230 C. Variable properties considerations should not affect the relative locations of the data in this comparison, since all the data in Fig. 4-10 are at approximately the same average T_w.

Figure 4-10 shows that all the data in the laminar region near the vertical leading edge, for all the Gr_H/Re_L^2 cases shown, fall on the laminar, forced convection, constant heat flux, Nusselt-Reynolds number relationship. This includes data for Gr_H/Re_L^2 up to and including 9.6. Buoyancy has no effect on the heat transfer until further downstream in the turbulent region where the data lie progressively further above the turbulent forced convection correlation as the Gr_H/Re_L^2 increases. For Gr_H/Re_L^2 up to 3.4, the turbulent data lie above but on lines parallel to the turbulent forced convection correlation. For Gr_H/Re_L^2 equal to 9.6, only the first two turbulent data points lie on a line parallel to the turbulent forced convection correlation. These two data points are on the downstream side of the "hump" in the heat transfer coefficient noted for $Gr_H/Re_L^2=10.0$ in Fig. 4-9. The data in the turbulent region, that are parallel to the forced convection correlation, have an x-dependence similar to forced convection.

The trend shown in Fig. 4-10 in the laminar region near the vertical leading edge, the dominance of forced convection, is not a new phenomena. It is the "principle of independence" for laminar flow discussed by Kraabel [42] with regard to heat transfer from a yawed infinite cylinder in a cross flow and in White [43] with regard to fluid flow on infinite yawed surfaces. Kraabel [42] has shown that forced convective heat transfer in the laminar boundary layer on an infinite yawed cylinder depends only on the free-stream velocity component normal to the cylinder and not on the free-stream velocity component parallel to the axis of the cylinder. This results from the fact that no velocity or temperature gradients can develop in the boundary layer in the axial direction on an infinite yawed cylinder, so no net heat transfer can occur in the axial direction.

The same "principle of independence" is governing the heat transfer on the vertical leading edge in this experiment. Except for very high Gr_H/Re_L^2 flows or for locations very close to the bottom corner, the test surface seems like an infinitely high vertical surface to the horizontal free-stream flow. The boundary layer flow at all vertical elevations near the vertical leading edge has the same history. Even though the flow develops a vertical velocity component, there can be no vertical temperature or velocity gradients in the boundary layer near the vertical leading edge. This means the heat transfer will be independent of any effects of buoyancy or vertical distance. This statement is true as long as the flow is laminar and does not "see" any of the effects of the lower corner of the leading edge. How far up the test surface effects of the lower upstream corner reach depends on the distance downstream and the ratio of buoyant to inertia forces, as will be shown later.

The "principle of independence" has a different meaning for skin friction in laminar flow. Even though there are no gradients of velocity and temperature in the vertical direction, there is still a vertical velocity component and a gradient of the vertical velocity component normal to the wall. This will result in a component of skin friction in the vertical direction. However, the component of skin friction in the vertical direction will be uniform over the vertical height of the surface near the vertical leading edge, since there are no gradients of the vertical velocity component in the vertical direction. This means the vertical component of the skin friction and the total skin friction for laminar flow near the vertical leading edge will be affected by buoyancy, but uniformly so in the vertical direction.

In the turbulent flow zones, even though derivatives of the mean velocity and temperature with respect to the vertical direction disappear on an infinitely high surface, buoyancy will still have an effect on turbulent velocity and temperature fluctuations, and as a result, heat transfer and skin friction in turbulent flow. The "principle of independence" does not apply for turbulent flow. This has been demonstrated on infinite, yawed surfaces in a turbulent forced flow situation by Ashkenas and Riddell [44]. This can also be seen in Fig. 4-10 for mixed convection heat transfer, since the Nusselt numbers in the turbulent region lie above the pure forced convection correlation. This is true even for the low Gr_H/Re_L^2 cases where the effects of the bottom corner of the vertical leading edge are not felt very far up on the test surface.

Figure 4-11, the distribution of h for four values of T_w with a nominally constant U_∞ of 1.4 m/s, indicates that forced convection dominates along the vertical leading edge well into the free convection region in Fig. 4-5. The Gr_H/Re_L^2 varies from 9.6 on the bottom surface to 30.2 on the top surface. The region before the "hump" is dominated by laminar forced convection.

Figure 4-11 also shows that the "hump" in h is about the same size for each case, that the "hump" moves forward slightly with increasing Gr_H/Re_L^2, and that a "depression" in h appears just downstream of the "hump" for higher values of Gr_H/Re_L^2. The value of h in the "depression" is less than that in the region dominated by free convection, the downstream two-thirds. In addition, Fig. 4-11 shows that there is no increase in heat transfer in the downstream turbulent free convection region along the bottom edge as a result of lower leading edge effects for any of the cases shown. This is because the free-stream flow is of little importance at these high Gr_H/Re_L^2's, for locations away from the vertical leading edge.

4.1.4 Estimation of Mixed Convection Heat Transfer

The average heat transfer coefficient, shown in Fig. 4-4 can be estimated accurately over the entire operating domain of this experiment by the method discussed earlier in Section 1.4:

$$\overline{h}_{mx} = (\overline{h}_{fc}^{\,a} + \overline{h}_{fr}^{\,a})^{1/a} \tag{4-6}$$

The average forced convection, $\overline{h}_{fc}$, and free convection, $\overline{h}_{fr}$, heat transfer coefficient estimates in Eqn. (4-6) are obtained by accounting for both the laminar and turbulent regions on the test surface. The term $\overline{h}_{fc}$ is obtained by integrating in the x-direction, the forced convection laminar and turbulent correlations over the respective laminar and turbulent regions on the surface with the integration starting at the vertical leading edge. The term $\overline{h}_{fr}$ is obtained by integrating in the y-direction, the free convection laminar and turbulent equations over the respective laminar and turbulent regions on the surface with the integration starting at the lower edge. The correlations used to determine $\overline{h}_{fc}$ and $\overline{h}_{fr}$ are those reported earlier, Eqns. (3-3), (3-4), (3-5), (3-7), and (4-1):

Forced Convection:

$$\begin{aligned} &Laminar: & Nu_x &= 0.453 Re_x^{1/2} Pr^{1/3} && (3\text{-}4)\\ &Turbulent: & Nu_x &= 0.0307 Re_x^{0.8} Pr^{0.6}\left(\frac{T_w}{T_\infty}\right)^n && (3\text{-}3)\&(3\text{-}5)\end{aligned}$$

Free Convection:

$$\begin{aligned} &Laminar: & Nu_y &= 0.404 Gr_y^{1/4} && (3\text{-}7)\\ &Turbulent: & Nu_y &= 0.098 Gr_y^{1/3}\left(\frac{T_w}{T_\infty}\right)^{-0.14} && (4\text{-}1)\end{aligned}$$

The transition locations from laminar to turbulent flow are those noted experimentally. Transition is discussed in Section 4.3.

The exponents, a in Eqn. (4-6) and n in Eqn. (3-5), are:

$$a = 3.2 \tag{4-7}$$

$$n = -0.4 \tag{4-8}$$

These were determined from a "best" fit of Eqn. (4-6) to the average heat transfer data. The fit was judged good when the average deviation between the actual data and Eqn. (4-6) was a minimum and the magnitude and sign of the deviation appeared random for all the test cases. The average of the absolute values of the deviations was $\pm 3\%$ and the largest deviation between the actual data and Eqn. (4-6) was less than 10%.

The primary effect of varying n was to alter the fit of Eqn. (4-6) to the data in the forced convection region and the forced convection dominated side of the mixed convection region in Fig. 4-5. If a smaller n was used ($n > -0.4$), the data in those regions were underpredicted. If a larger n was used ($n < -0.4$), the data in those regions were overpredicted.

The effects of varying a were to alter the apparent size of the mixed convection domain and to alter the fit of Eqn. (4-6) over the entire mixed convection domain. For too large an a, heat transfer coefficients in the mixed convection region were underpredicted and the mixed convection region appeared smaller. The opposite trends were true for too small an a. The fit was not very sensitive to a, however. For example, in the middle of the mixed convection zone, where $\overline{h}_{fr} = \overline{h}_{fc}$, the difference in $\overline{h}_{mx}$ for values of a equal to 3.4 and 3.0 is only 3%.

Local heat transfer coefficients can be estimated in a similar manner to the average heat transfer coefficients, if local forced and free convective estimates of heat transfer coefficients are used in Eqn. (4-6). Thus, the local heat transfer coefficient would be given by:

$$h_{mx}(x,y) = (h^a_{fc}(x) + h^a_{fr}(y))^{1/a} \tag{4-9}$$

The values of a above and n in Eqn. (3-5) are 3.2 and -0.4, respectively, the same as for Eqn. (4-6).

Specifically, the local mixed convection heat transfer coefficient would look as follows (one possible form) for laminar and turbulent flows on a uniform heat flux, flat surface in air:

Laminar :

$$h_{mx}(x,y) = 0.404\frac{k}{x}Re_x^{1/2}\left\{1+\left[\frac{x}{y}\frac{Gr_y^{1/4}}{Re_x^{1/2}}\right]^{3.2}\right\}^{\frac{1}{3.2}} \tag{4-10}$$

Turbulent :

$$h_{mx}(x,y) = 0.025\frac{k}{x}Re_x^{0.8}\left(\frac{T_w}{T_\infty}\right)^{-0.4}\left\{1+\left[3.92\frac{x}{y}\frac{Gr_y^{1/3}}{Re_x^{0.8}}\left(\frac{T_w}{T_\infty}\right)^{0.26}\right]^{3.2}\right\}^{\frac{1}{3.2}} \tag{4-11}$$

No variable properties correction is included in the laminar equation, since the correction is small for laminar forced and free convection and would tend to cancel. Such a correction could easily be incorporated. The temperature ratio in the turbulent equation results from the different turbulent forced and free convection variable properties corrections.

Equation (4-11) fits the present local turbulent heat transfer coefficient data within $\pm 3\%$ on the average. The largest deviations from the actual data were approximately 10-15%. The large errors were systematic, not random. Equation (4-11) cannot predict some of the trends noted in the turbulent flow regions such as the "humps" and "depressions" of heat transfer coefficients in Figs. 4-9 and 4-11, nor can Eqn. (4-11) predict the proper x-dependence in turbulent flow areas shown in Fig. 4-10. Equation (4-11) predicts a smooth variation of h in turbulent flow regions.

Figure 4-12 demonstrates the accuracy of Eqn. (4-11) for predicting the local h for turbulent flow and shows its limitations. The figure is a plot of the column averaged value of $Nu_x/0.025Re_x^{0.8}(T_w/T_\infty)^{-0.4}$ versus the column averaged value of $3.92(T_w/T_\infty)^{0.26}xGr_y^{1/3}/yRe_x^{0.8}$, the mixed convection parameter in brackets in Eqn. (4-11). The data points for each test condition are obtained by column averaging the data measured in each column in Fig. 2-11 in turbulent flow regions, excluding the data from the bottom and top strips. Column averages are used since the data show little vertical dependence and Eqn. (4-11) predicts none for turbulent flow. The vertical dimension, y, appears in the mixed convection parameter in Eqn. (4-11), but actually cancels out since Gr_y contains a y^3.

Figure 4-12 shows that Eqn. (4-11), given by the solid line, goes through approximately the center of each data set for each test case. Equation (4-11) is a good approximation in the turbulent region, predicting local heat transfer within $\pm 10\%$. The dashed lines in Fig. 4-12 form a $\pm 10\%$ band around Eqn. (4-11). However, Eqn. (4-11) does not predict the exact local variation in heat transfer for each test case. For tests with values of Gr_H/Re_L^2 up to approximately 3, Fig. 4-12 shows that the data in the turbulent region still has a forced convection x-dependence, which is represented by a horizontal line in Fig. 4-12 (a horizontal line of value one represents pure forced convection). For values of Gr_H/Re_L^2 greater than approximately 3, the data on the downstream end of the test surface begin to show a free convection like pattern (i.e., a uniform convection heat transfer coefficient), which is represented by a line of unity slope. The "transition" between the regions on the test surface with turbulent forced and turbulent free convection like heat transfer coefficient variations occurs over a very short distance. Equation (4-11) does not predict this. Instead, Eqn. (4-11) predicts a much more gradual change from a forced convection like heat transfer dependence x to a free convection like pattern of uniform convection heat transfer, as shown in Fig. 4-12. For tests with high values of Gr_H/Re_L^2, the "hump" and "depression" in heat transfer in Figs. 4-9 and 4-11, which appear as "depressions" for $Gr_H/Re_L^2 > 9.6$ in Fig. 4-12, are not predicted either.

The limited laminar flow data is largely dominated by forced convection as shown in previous figures. This makes it impossible to check Eqn. (4-10) for laminar flow in detail. Equation (4-10) does, however, predict the dominance of forced convection noted in the laminar vertical leading edge area. For increasing vertical distance on the test surface, the mixed convective parameter in Eqn. (4-10) ($xGr_y^{1/4}/yRe_x^{1/2}$) becomes very small not far from the lower edge, and the heat transfer coefficient predicted by Eqn. (4-10) equals that for pure forced convection. For example, the mixed convection effect on heat transfer at the first column of thermocouples for laminar flow (see Fig. 2-11) is less than 10% by the fourth heating strip for a Gr_H/Re_L^2 of 10. This means only the data point for the one thermocouple at the lower upstream corner on the first heating strip (see Fig. 2-11) would show any significant laminar mixed convective effect for a Gr_H/Re_L^2 up to 10.0. For Gr_H/Re_L^2 higher than this the laminar zone begins to disappear and detection of any laminar mixed convection effect is impossible. It should be noted that h for this one data point, for the lowest most upstream thermocouple in Fig. 2-11, always lies above the pure forced convective laminar heat transfer coefficient by approximately the amount predicted by Eqn. (4-10) for each test condition. This location, unlike the rest of the first heating strip, is upwind of any strut effects or significant lower leading edge effects.

Some of the other methods discussed earlier in Section 1.4 do not work as well as Eqns. (4-6) and (4-9) for estimating mixed convection heat transfer (local or average). In the middle of the mixed convection domain, taking the smaller of the forced and free estimates [13] underpredicts by about 25% the actual h (equivalent to $a = \infty$ in Eqn. (4-6)) and adding the two estimates together overpredicts by 75% the actual h (equivalent to a=0 in Eqn. (4-6)). Root-sum-squaring Nusselt numbers [14] and the method of finding an effective Reynolds number to use in the forced convective correlation [15] are more difficult to apply than Eqns. (4-6) and (4-9) in this orthogonal driving force problem. In addition to an effective Nusselt number in the first method and Reynolds number in the second method, an effective characteristic length must be determined for both methods to work properly in the orthogonal driving force problem. Neither reference recommending these methods properly treats this point. The proposing authors discuss the problem of orthogonal driving forces, but only with regard to a situation with one characteristic length, specifically the average heat transfer from an infinite, heated, horizontal cylinder in a crossflow. Without proper consideration of the characteristic length, these methods will predict incorrect x and y dependencies in the mixed convection region and will not work over the entire T_w, U_∞ operating domain. With proper consideration of the characteristic length, they can probably be made to work, but not in as straightforward a fashion as Eqns. (4-6) and (4-9).

4.1.5 Concluding Remarks on Heat Transfer

Equations (4-10) and (4-11) can be used to summarize some general aspects of heat transfer from a vertical surface parallel to a horizontal flow of air. Equation (4-10) gives the mixed convection parameter which governs laminar mixed convection heat transfer, $xGr_y^{1/4}/yRe_x^{1/2}$. This parameter is also the similarity parameter, or is directly related to the similarity parameter, in the laminar mixed convection problems in Refs. 3, 5, and 6, discussed in Section 1.4. It gives the ratio of conditions which determine when forced, mixed, or free convection heat transfer are important for laminar flow. Based on Eqn. (4-10), heat transfer is equally influenced by forced and free convection when $xGr_y^{1/4}/yRe_x^{1/2}$ equals 1.0. When this parameter is 0.57, the heat transfer coefficient is only 5% greater than that predicted by considering pure forced convection acting alone. When it is 1.75, the heat transfer coefficient is only 5% greater than that predicted by considering pure free convection acting alone. These values depend on the value for a in Eqn. (4-9).

The values of the mixed convection parameter, $xGr_y^{1/4}/yRe_x^{1/2}$, equal to 0.57 and 1.75 can be used to define boundaries between zones of forced, mixed, and free convection: the lower value defining the forced-mixed convection boundary and the higher value defining the free-mixed convection boundary. The heat transfer in the free convection and the forced convection zones defined by these constant values of $xGr_y^{1/4}/yRe_x^{1/2}$ would be within 5% of the heat transfer predicted by considering a single mechanism for heat transfer in each respective zone.

Figure 4-13 is a schematic of a surface showing the relative locations of the boundaries and zones of forced, mixed, and free convection defined by the lines of constant $xGr_y^{1/4}/yRe_x^{1/2}$ equal to 0.57 and 1.75. The vertical distance on the surface is normalized on test surface height and horizontal distance on test surface length. The boundaries are parabolas given by:

$$\frac{y}{H} = 9.4\left(\frac{L}{H}\right)^4 \frac{Gr_H}{Re_L^2}\left(\frac{x}{L}\right)^2 \tag{4-12}$$

$$\frac{y}{H} = 0.11\left(\frac{L}{H}\right)^4 \frac{Gr_H}{Re_L^2}\left(\frac{x}{L}\right)^2 \tag{4-13}$$

Equation (4-12) is the forced-mixed boundary and Eqn. (4-13) is the free-mixed boundary. The locations of the boundaries shown in Fig. 4-13 are for an arbitrary value of $(L/H)^4(Gr_H/Re_L^2)$. Their locations will vary with the value of $(L/H)^4(Gr_H/Re_L^2)$ as indicated in Eqns (4-12) and (4-13).

The figure shows that forced convection dominates a region near the vertical leading edge with the width of the region increasing in size away from the origin. Free convection dominates a region near the lower edge with the height of the region increasing in size away from the origin. Mixed convection occurs in between the forced and free convection regions. Also, by examining the boundary equations, Eqns. (4-12) and (4-13), it is apparent that for small $(L/H)^4(Gr_H/Re_L^2)$, the forced convection zone will dominate the surface and for large $(L/H)^4(Gr_H/Re_L^2)$, the free convection zone will dominate heat transfer on the surface.

The zone dominated by forced convection was noted in the experiment as discussed earlier. There were only indications of the laminar mixed convection region in the lower upstream corner due to transition of the flow to turbulent flow. The laminar free convection region did not occur along the lower leading edge possibly due to effects discussed in Appendix D.

Figure 4-14 shows the relative locations of the forced, mixed, and free convection heat transfer zones for turbulent flow. The boundaries for turbulent flow are defined in the same way as laminar flow, only using Eqn. (4-11) instead. The vertical dependence disappears in turbulent flow since turbulent free convection heat transfer has no vertical dependence as discussed earlier. The boundaries are given by:

$$\frac{x}{L} = 6.5 \times 10^{-5}\left[\frac{Re_L^{0.8}}{Gr_L^{1/3}}\left(\frac{T_\infty}{T_w}\right)^{0.26}\right]^5 \tag{4-14}$$

$$\frac{x}{L} = 1.8 \times 10^{-2}\left[\frac{Re_L^{0.8}}{Gr_L^{1/3}}\left(\frac{T_\infty}{T_w}\right)^{0.26}\right]^5 \tag{4-15}$$

The Grashof number is based on length to emphasize the lack of dependence on the vertical direction. The boundaries are shown as dashed lines to emphasize that all three zones of heat transfer, as defined by Eqns. (4-14) and (4-15), cannot occur over significant portions of the test surface simultaneously (as shown in the Fig. 4-14). This is because the values of x/L predicted by Eqns. (4-14) and (4-15) differ by a factor of 270 units of x/L, and x/L has a maximum value of one. The figure only shows the general locations of the zones of forced, mixed, and free convection. The boundary locations in Fig. 4-14 do not represent boundaries for any particular value of $(Re_L^{0.8}/Gr_H^{1/3})(T_\infty/T_w)^{0.26}$.

Equations (4-14) and (4-15) show that the location and size of the zones depend on the overall test conditions. For high Reynolds number, low temperature ratio flows, the forced convection zone dominates the surface and for high Grashof number, high temperature ratio flows, the free convection zone dominates.

All of these zones of turbulent convective heat transfer were noted in the experiment. Eqn. (4-11) accurately predicts the zones of mixed, forced, and free convection heat transfer for turbulent flow as defined in this section, but not the proper x-dependence, as shown before.

One last point, Eqn. (4-11) indicates a possible contradiction based on results presented earlier in the chapter. It was shown in Figs. 4-8 and 4-9 for this fixed aspect ratio test, $L/H = 0.98$, that heat transfer in turbulent regions was similar for similar Gr_H/Re_L^2, not $(Gr_H^{1/3}/Re_L^{0.8})(T_w/T_\infty)^{0.26}$, as Eqn. (4-11) would indicate. It was also stated in Fig. 4-5 that lines of constant Gr_H/Re_L^2 equal to 0.7, 3.0, 10.0 were the approximate boundaries and bisector of the average mixed convection heat transfer zone, not lines of constant $(Gr_H^{1/3}/Re_L^{0.8})(T_w/T_\infty)^{0.26}$. This apparent contradiction is explained as follows. First, Gr_H/Re_L^2 has been used in figures to identify the approximate ratio of buoyant to inertia forces for a given test, which in general had both laminar and turbulent flow. The parameter Gr_H/Re_L^2 was not intended as a general correlating parameter for mixed convective heat transfer. It is only a correlating parameter for laminar flows for a given aspect ratio. Second, lines of constant $(Gr_H^{1/3}/Re_L^{0.8})(T_w/T_\infty)^{0.26}$ are approximately parallel to lines of constant Gr_H/Re_L^2 in a Grashof-Reynolds number domain for this experiment.

This is due to the fact that larger Grashof numbers were achieved by increasing the wall temperature in this experiment. This introduced the temperature ratio term into the turbulent mixed convection parameter as a result of variable properties effects. Without the temperature ratio term, lines of constant mixed convection parameter (i.e., $Gr_H^{1/3}/Re_L^{0.8}$) are not parallel to lines of constant Gr_H/Re_L^2 in a Grashof-Reynolds number operating domain.

The equivalent boundaries for forced, mixed, and free convection in terms of constant Gr_H/Re_L^2 predicted for the average turbulent convection heat transfer data by an equation similar to Eqn. (4-11), using average turbulent heat transfer correlations instead of local correlations, are 0.9 and 15.0, respectively, with 4.0 as the bisector of the turbulent mixed convection zone. In other words, these are lines of constant Gr_H/Re_L^2, which in a Grashof-Reynolds number operating domain fall approximately on lines of constant $(Gr_H^{1/3}/Re_L^{0.8})(T_w/T_\infty)^{0.26}$. Considering some of the flow for each test was laminar, and the boundary values for the average laminar convective heat transfer zones for an aspect ratio of 0.98 are 0.61 and 1.90 with a mixed convection zone bisector of 1.08, the Gr_H/Re_L^2 values of 0.7, 3.0 and 10.0 observed in Fig. 4-5 for the boundaries and bisector, respectively, are reasonable, since both laminar and turbulent flow are included in the average data in Fig. 4-5.

4.2 Boundary Layer Flow

The boundary flow results are divided into three sections. The first presents results from the boundary layer velocity, temperature, and flow angle measurements made within turbulent mixed convection boundary layers. The second presents velocity and temperature profiles measured within laminar mixed convection boundary layers. The third section discusses the direction of flow in the constant-angle region of turbulent mixed convection boundary layers.

The turbulent mixed convection boundary layer results in the first section will show that near the wall there is a region of flow angle within turbulent "mixed-convective" boundary layers which is constant with respect to the distance normal to the wall. Only the magnitude of the velocity vector is changing in that constant-angle region. The constant-angle region will be shown to extend from the wall out to the location where u/U_∞=0.71, which encompasses the inner 5-7 percent of the boundary layer thickness. This constant-angle region, which was unexpected, will be shown to exist for turbulent flow independent of the test conditions and the location on the test surface. The peak vertical velocity will be shown to occur at the outer edge of the constant-angle region. In the outer region of the turbulent mixed convection boundary layer, the flow angle will be shown to vary linearly with the local temperature. The first section will also show that the velocity and temperature profiles vary smoothly from pure forced convection profiles to pure free convection profiles as the ratio of the buoyant force to the inertia force increases, and that there is evidence that momentum added to the flow in vertical direction by buoyancy is transferred to the horizontal direction, possibly by turbulence.

The laminar mixed convection boundary layer results in the second section will verify that the "principle of independence" applies near the vertical leading edge, as noted from the heat transfer results earlier. The laminar results also show that there is no constant flow angle region within the laminar mixed convection boundary similar to that in the turbulent mixed convection boundary layer.

In the third section, the variation of the flow angle of the constant flow angle region of the turbulent mixed convection boundary layer with respect to position on the test surface will be discussed. A relationship will be developed which predicts the direction of flow within the constant-angle region. This relationship has the form $y = bx^{\text{[illegible]}}$, where b depends on the test conditions.

The legend in most figures contains the profile ID^{*} number, the local T_w, the local U_∞, the location of the profile (x, y) on the test surface, and for turbulent profiles, the maximum flow angle measured in a given profile. Each profile was taken above a surface temperature measurement location. Since a companion heat transfer data set was taken for each set of profiles, surface heat transfer data is available in Appendix E at the location of each profile. Only profiles for laminar or fully turbulent regions are shown. No profiles in transition zones and no profiles along the bottom leading edge are presented. Detailed data for profiles in regions not shown, along with the rest of the profiles, are available in Appendix F. Approximately 12 to 14 profiles were taken for each of 7 combinations of U_∞ and T_w and 3 to 5 profiles were taken for another 5 combinations of U_∞ and T_w.

4.2.1 Turbulent Boundary Layer Flow

This section presents the turbulent "mixed-convection" boundary layer results obtained for various test conditions. It is divided into seven parts: the first four present the total velocity profiles, the flow angle profiles, the vertical and horizontal velocity profiles, and the temperature profiles, respectively; the fifth presents polar plots of the total velocity vector (i.e., plots of the vertical velocity component versus the horizontal velocity component); the sixth shows how the flow angle varies with temperature through the boundary layer; and the final part shows further evidence of the constant angle region.

The distance normal to the wall, z, in the figures in this section has been scaled by the thermal boundary layer thickness, δ_t, defined in Eqn. (2-3), but this is not proposed as a general scaling parameter for mixed convection boundary layers. It is used only, for convenience. The boundary layer thickness, δ_t, is one of the few boundary layer thicknesses which does not contain a vector quantity that makes it specific to one direction and which is well defined for all profiles for all values of Gr_H/Re_L^2. Also, the use of δ_t for velocity, flow angle, and temperature profiles allows an easy cross comparison of various regions in each figure.

In some figures, predictions of boundary layer profiles for pure forced and pure free convection made with STAN5, a numerical boundary layer heat transfer code [1,41], are shown. The reason for presenting the profiles predicted with STAN5 is to provide a representative shape for pure free convection and pure forced convection profiles to compare with the shape of the measured mixed convection profiles. The predicted profiles are used for cases for which widely accepted profiles are not available in the literature, such as for turbulent free convection or low speed high temperature variable properties flows.

a. Total Velocity Profiles

The first figure in this section, Fig. 4-15, shows the total velocity, Q, versus z/δ_t, for turbulent flow. The data shown are for four different values of U_∞ at a nominally constant T_w of 420 C. Since all the profiles are for approximately the same T_w, variable properties considerations are negligible. The value of Gr_H/Re_L^2 ranges from 1.7 to 21.7. The location on the test surface is approximately the same for each profile, $x \approx 2.7\ m$, $y \approx 2.7\ m$. The total velocity is normalized by the root-sum-square of U_∞ and V_g. The velocity V_g is the buoyant reference velocity defined as:

$$V_g = U_\infty tan(\beta_{max}) \tag{4-16}$$

The term β_{max} is the maximum measured flow angle in a given boundary layer profile, which is the flow angle in the constant flow angle region for the turbulent profiles. This choice of reference velocity will be discussed later, in Section 4.2.3. The pure turbulent forced convective velocity profile and the pure turbulent free convection velocity profile (the solid lines) were obtained from predictions by this author with STAN5 for a T_w of 420 C.

Figure 4-15 shows that as the U_∞ decreases from 4.9 m/s to 1.5 m/s, the total velocity profile shape changes from the pure forced convection shape toward the pure free convection shape. For the two highest Gr_H/Re_L^2 cases, the peak velocity occurs in the interior of the boundary as opposed to the free-stream. This is the result of the vertical acceleration of the fluid by the buoyant force. The peak occurs at a z/δ_t of about 0.7 and a $Q/\sqrt{U_\infty^2 + V_g^2}$ of about 0.7 to 0.75. A "dimple" in the profile appears in the region of peak velocity for Gr_H/Re_L^2 of 21.7. This is characteristic of the turbulent profiles for the Gr_H/Re_L^2 of 21.7 test conditions.

In the inner region of the total velocity profiles in Fig. 4-15 (for $z/\delta_t < 0.3$), the data are approximately parallel for all values of Gr_H/Re_L^2. This region is, however, shifting from the forced convection reference profile toward the free convection reference profile with increasing Gr_H/Re_L^2. By comparison to the pure forced convection profile, the inner region of the mixed convection boundary layer is inside the logarithmic region of a pure forced convective profile and in the same location as the laminar sublayer and the buffer sublayer.

For a given Gr_H/Re_L^2, the distribution of velocity within the boundary layer will be different at different locations on the surface. This is shown in Fig. 4-16, a plot of three turbulent total velocity profiles at a y of 2.67 m and three different x locations for a Gr_H/Re_L^2 of 7.4. Upstream at x=1.07 m, the profile looks more forced convection dominated. Further downstream at x=2.76 m, the profile looks more free convection dominated with a peak in the velocity in the interior of boundary layer.

The change in shape with distance downstream is the result of the fact that the free convection flow in the vertical direction is driven by an acceleration of the fluid by a buoyant force and thus, time is required (i.e., distance) before the effect of the buoyant force becomes significant relative to the horizontal forced flow. This also means that the flow will eventually become dominated by free convection in the upper-downstream region of an infinitely large surface no matter what the test conditions are, since the flow will continue to accelerate vertically while the free-stream remains at a constant velocity.

Figure 4-17 shows three total velocity profiles for three different values of wall temperature with a nominally constant U_∞ of 4.5 m/s at a nominal location of x=2.7 m and y=1.8 m. The lowest T_w case, T_w=47 C, is a baseline case in Fig. 3-12. The trends in Fig. 4-17 are the same as in Fig. 4-15 but not as prominent, since the Gr_H/Re_L^2 does not vary over as large a range as in Fig. 4-15. With increasing buoyant force (i.e., Gr_H/Re_L^2), the velocity in the interior of the boundary layer is increasing relative to the free-stream.

b. Flow Angle Profiles

Boundary layer flow angle profiles are shown in Fig. 4-18 for turbulent flow. This is a plot of the tangent of the flow angle divided by the tangent of the maximum flow angle measured in a given profile versus z/δ_t. Several profiles are shown for various test conditions and locations on the test surface. The most striking feature in the figure is the region of nearly constant flow angle near the wall ($z/\delta_t<0.4$). The angle is constant to within $\pm 1.5°$ for each profile and the variations noted were random. The constant-angle region covers the inner 5% to 7% of the boundary layer thickness from the wall out to u/U_∞=0.71, as shown in this figure. By comparison to Fig. 4-15, it can be seen that the constant-angle region covers the region of the boundary layer containing the laminar sublayer and the buffer sublayer for a pure forced convective flow. The constant-angle region extended as close to the walls as measurements were made, which was 1% of the boundary layer thickness in some cases.

The possible existence of a constant-angle or collateral region near the wall has been noted before in three-dimensional flows where the cross-stream flow was driven by a pressure gradient [45-48], but never before when the cross-stream flow was driven by buoyant forces. In general, these previous works lack measurements sufficiently close to the wall to define the extent of any collateral flow region near the wall. One exception is the work of Hebber and Melnik [49] in a relaxing three-dimensional turbulent boundary. This work shows a collateral region in the laminar sublayer region of the boundary layer, similar to that found in this mixed convection flow.

Figure 4-18 shows several other features of the flow angle variation in the boundary layer. First, all the flow angle change occurs for z/δ_t greater than 0.4. Next, there is a similarity in flow angle profiles for different test conditions and locations on the test surface for turbulent flow and for Gr_H/Re_L^2 less than 7.4. Only the Gr_H/Re_L^2 of 21.7 case has a significantly different flow angle profile shape in this plot. In the outer region of the boundary, the ratio, $tan(\beta)/tan(\beta_{max})$, is higher for a given z/δ_t for the Gr_H/Re_L^2 of 21.7 case. This might be expected, since as Gr_H/Re_L^2 approaches infinity, the flow angle should approach 90° everywhere in the boundary layer except very near the free-stream. This would result in a straight line of value 1.0 in Fig. 4-18.

Finally, with the exception of the Gr_H/Re_L^2 of 21.7 case, there appears to be a region where $tan(\beta)$ varies linearly with the log_{10} of z/δ_t between z/δ_t of 0.4 and 1.5. For Gr_H/Re_L^2 of 21.7, the logarithmic region is smaller. Each individual set of data has this logarithmic region, within the uncertainty of the flow angle measurement. Later, this region will be shown to correspond to the region around the peak vertical velocity location.

The similarity in flow angle profiles breaks down in the outer region of the boundary layer in the coordinates used in Fig. 4-18, as is shown in Fig. 4-19. Figure 4-19 is a plot similar to Fig. 4-18, except with linear axes. The figure shows flow angle profiles for three of the four cases in Fig. 4-15, with a nominally constant T_w of 420 C and a nominally fixed location. The data from the outer region of the flow, which was compressed by the log_{10} scale in Fig. 4-18, is now more clearly visible. In the outer region there is an increase in flow angle for a given z/δ_t with increasing Gr_H/Re_L^2. Only closer to the wall do the profiles collapse, the lower Gr_H/Re_L^2 's first. The region of flow angle similarity in the coordinates used in Fig. 4-18 encompasses the constant-angle region near the wall and the logarithmic region pointed out in Fig. 4-18.

c. Horizontal and Vertical Velocity Profiles

Figure 4-20 is a plot of the vertical and the horizontal velocity components versus z/δ_t. The horizontal velocity component has been normalized by U_∞ and the vertical velocity component by the buoyant reference velocity V_g. The three cases shown in Fig. 4-20, three of the four cases previously shown in Fig. 4-15, are for a nominally constant T_w of 420 C at a nominally constant location on the test surface. The pure forced and free convection velocity profiles in Fig. 4-15 are again shown for reference (the solid lines).

In the inner region of the boundary layer, $z/\delta_t < 0.4$, both profiles have the same approximate shape. This is expected, both the "pure" free and "pure" forced profiles shown in the figure have approximately the same shape in the inner region. This is also the region of constant flow angle shown in Fig. 4-18. The point at which the vertical and horizontal velocity profiles begin to differ marks the end of the constant-angle region, $z/\delta_t \approx 0.4$. In the outer region of the flow, both profiles change shape with varying test conditions. The horizontal velocity profile begins to bulge upward with increasing Gr_H/Re_L^2 in what would be the logarithmic (highly turbulent) region of the pure forced convection profile ($0.4 < z/\delta_t < 3.0$). For the vertical velocity profile in the region outside the peak v/V_g, the velocity increases for a given z/δ_t, approaching the pure free convection profile shape. The peak v/V_g does not change significantly. The "dimple", seen in the $Gr_H/Re_L^2 = 21.7$ case at the peak total velocity in Fig. 4-15, is present near the peak in the vertical velocity profile in this figure. The "dimple" is characteristic of the vertical velocity profiles for the case with Gr_H/Re_L^2 equal to 21.7.

Figure 4-21 shows three more plots of the vertical and horizontal velocity components versus z/δ_t. These are for a nominally constant U_∞ of 4.5 m/s and a nominally fixed location. The value of Gr_H/Re_L^2 varies from 1.1 to 3.1, and T_w varies from 235 C to 575 C. The trends noted are similar to those in Fig. 4-20, but not as prominent, since the Gr_H/Re_L^2 does not vary over as large a range as in Fig. 4-20.

One possible reason for the upward "bulge" in velocity in the logarithmic region of the horizontal velocity component profile with increasing buoyant force, seen in Figs. 4-20 and 4-21, may be the coupling of the momentum transfers in the horizontal and vertical directions through turbulence. The bulge occurs in the region noted for high turbulence in pure forced convection flows, as well as in pure free convection flows. Some of the momentum being added to the flow by the vertical buoyant force is possibly being transferred by turbulence to the horizontal direction. The transfer of momentum from the vertical direction to the horizontal direction might also account for the vertical velocity profile for mixed convection falling below the pure free convection profile in the outer region of the boundary layer.

d. Temperature Profiles

Temperature distribution is shown in Fig. 4-22 in the form of enthalpy profiles. The enthalpy is determined directly from the measured temperature (see Appendix A). Figure 4-22 shows plots of dimensionless enthalpy, θ_i, versus z/δ_t, where θ_i is defined so that it is zero at the wall and one in the free-stream. Three of the cases in Fig. 4-15 are shown in Fig. 4-22. They have a nominally constant T_w of 420 C and are from approximately the same location on the test surface. Pure forced and pure free convection enthalpy profiles are shown for comparison. The pure forced convection profile (the solid line) is a STAN5 prediction for a T_w of 420 C. The pure free convection profile (the dashed line) is an average of two pure free convection profiles from this experiment taken at a T_w of 420 C. The two free convection profiles were almost identical in the coordinates shown in Fig. 4-22.

As with the total velocity profiles, the enthalpy profile shape changes from a pure forced to a pure free convection shape as Gr_H/Re_L^2 increases from 1.9 to 21.7. For the forced convection dominated cases, laminar sublayer, "logarithmic", and wake regions are visible. For the free convection dominated cases, a "forced convection" like "laminar sublayer" region is visible with a "logarithmic" region in the outer portion of the profile, $z/\delta_t > 1.0$. The Gr_H/Re_L^2 case of 21.7 has a region where the temperature profile lies above the measured pure free convection profile. It is most pronounced around z/δ_t of 0.5. This is the location of the "dimple" noted in the vertical velocity profile for the same case in Fig. 4-20, and is characteristic of the Gr_H/Re_L^2 of 21.7 profiles.

Figure 4-23 is another plot of enthalpy profiles similar to Fig. 4-22. These are four cases at a nominally constant U_∞ of 4.5 m/s. The Gr_H/Re_L^2 varies from 0.1 to 3.1 while T_w varies from 47 C to 575 C. The four cases shown have a "forced convection" like appearance even for a Gr_H/Re_L^2 of 3.1. This trend agrees with the heat transfer data in Fig. 4-12, where it was shown that for Gr_H/Re_L^2 less than about 3.0 to 4.0 the heat transfer coefficient had a forced convection x-dependence ($h \sim x^{-0.2}$) in the turbulent flow region.

e. Polar Plots of the Velocity Vector

The constant-angle region is again seen in Fig. 4-24, a polar plot of the total velocity versus the flow angle or, equivalently, a plot of the vertical velocity component versus the horizontal velocity component. The horizontal component is normalized by the U_∞. The vertical is normalized by the free convection reference velocity, V_g, defined in Eqn. (4-16). These choices of reference velocities collapse any region of flow angle equal to β_{max} for a given profile to a line of unity slope. This can be shown from the definition of flow angle:

$$\frac{v}{u} = tan\beta \qquad (4\text{-}17)$$

For any region where $\beta = \beta_{max}$, Eqns. (4-16) and (4-17) result in:

$$\frac{v}{V_g} = \frac{u}{U_\infty}$$

Therefore,

$$\frac{d(v/V_g)}{d(u/U_\infty)} = 1.0$$

Figure 4-24 shows that the turbulent flow data for various Gr_H/Re_L^2 and various locations on the test surface fall on a line of unity slope for u/U_∞ less than about 0.71 and v/V_g less than about 0.71 ($\sim 1/\sqrt{2}$). This is the constant flow angle region. Only the magnitude of the velocity vector is changing in this region of the boundary layer, decreasing as the wall is approached.

The peak v/V_g of approximately 0.71 occurs at a u/U_∞ of 0.71, the outer edge of the constant-angle region. This value is approximately independent of Gr_H/Re_L^2 for turbulent boundary layer flow. The peak v/V_g of 0.71 indicates the maximum vertical velocity is approximately the $\sqrt{2}$ smaller than the reference velocity given by Eqn. (4-16) for a turbulent mixed convective boundary layer flow.

The outer region of the boundary layer flow, $u/U_\infty > 0.71$, does not collapse in these coordinates. This is shown more clearly in Fig. 4-25. This is a polar plot of four different profiles at the same location on the test surface and a nominally constant T_w of 420 C. The Gr_H/Re_L^2 ranges from 1.9 to 21.7. The constant-angle characteristic is again seen in the inner region, on the line of unity slope. In the outer region, the magnitude of the v/V_g is increasing with increasing Gr_H/Re_L^2 for a given u/U_∞ or vice versa. The flow angle is approaching 90° everywhere in the boundary layer except very near the free-stream as the buoyant force begins to dominate.

f. Flow Angle versus Temperature

Another feature of the boundary layer flow angle is shown in Fig. 4-26. This is plot of the $tan(\beta)/tan(\beta_{max})$ versus the dimensionless temperature, θ. Profiles for various test conditions and locations on the test surface are shown, but all for $Gr_H/Re_L^2 < 10$. The constant flow angle region is visible in this figure for θ less than 0.6. More importantly, the figure shows that in the outer region of the turbulent boundary layer, for θ greater than about 0.7, the tangent of the local flow angle is linearly related to the local dimensionless temperature. The following expression gives the approximate relationship between flow angle and temperature.

$$tan(\beta) = 3.0tan(\beta_{max})(1 - \theta) \qquad (4\text{-}18)$$

Equation (4-18) is represented by the solid line in Fig. 4-26. Equation (4-18) only holds for the tests with Gr_H/Re_L^2 up to 7.4. Figure 4-27, a similar plot of the $tan(\beta)/tan(\beta_{max})$ versus the local dimensionless temperature, shows that as Gr_H/Re_L^2 becomes larger than 7.4 the region of linear variation of the $tan(\beta)$ with local dimensionless temperature begins to significantly decrease in size. For the profile at Gr_H/Re_L^2 of 21.7, a linear variation appears only for θ greater than 0.9 as shown by the dashed line.

g. Further Evidence of the Constant-Angle Region

So far in this section several important features of the turbulent "mixed-convection" boundary layer flow have been shown: (1) from the wall out to about $u/U_\infty = 0.71$, the flow is all at the same angle with respect to the free-stream; (2) in the outer region of the boundary layer, the tangent of the local flow angle is linearly dependent on the local dimensionless temperature; (3) there appears to be a significant transfer of momentum from the vertical direction (the buoyant flow direction) to the horizontal direction (the forced flow direction); (4) the tangent of the flow angle appears to depend logarithmically on z/δ_t in the vicinity of the peak vertical velocity; and (5) the temperature profile looks forced convection like up to a Gr_H/Re_L^2 of approximately 3 or 4.

Of these features the most surprising is the constant flow angle region near the wall. It was originally believed that since the buoyant force, defined as

$$buoyant\ force = g(\rho - \rho_\infty), \qquad (4\text{-}19)$$

varied continuously from the free-stream to the wall because of the continuous density variation (i.e., temperature variation), the flow angle should vary continuously from the free-stream to the wall. This did not occur as demonstrated by the flow angle measurements presented in several figures. All the evidence supports the existence of a constant flow angle region near the wall. The constant-angle region extended to within 1% of the boundary layer thickness from the wall (the point of closest measurement) and was constant to within the uncertainty of the flow angle measurements.

As a check on the pressure probe measurement of flow angle in the constant-angle region, the probe was offset as much as 30° in either direction from the indicated flow direction on several occasions and allowed to return under servo-control. Each time the probe would return to the same angle: the measurement was repeatable.

In addition to the probe measurements, corroborating photographic proof of the constant flow angle region was obtained. These photographs are shown in Figs. 4-28a through 4-28d. The four photographs shown are several-second time exposure photographs of the probe and test surface. What is shown in the photograph is what was actually visible in the wind tunnel. No special film was used. The surface was glowing red (visible if color photos are used in this version of the report). The photographs were taken with a camera mounted on the wall opposite the test surface aimed normal to the test surface, approximately along the axis of the boundary layer probe stem. The flow is left to right and the probe is located in the right center of each photograph. The stem of the probe is the dark line extending from the oval shaped dark region on the right. The probe tip is the three pronged dark feature near the surface (see Section 2.6.3 for probe description). The dark oval shape and dark vertical region on the right of the oval are part of the probe mount and the traverse shield, respectively, and are located about 30 *cm* away from the test surface. They are dark because they are cold. The test conditions were U_∞=4.2 m/s and T_w=560 C resulting in a $Gr_H/Re_L^2 \approx 3.2$. Each photograph shows the probe tip at a different location in the boundary layer. The probe tip is at z/δ_t of 0.1, 0.28, 0.39, and 0.79 in Figs. 4-28a, 4-28b, 4-28c, and 4-28d, respectively.

There are three angles to notice in each photograph: (1) the angle of the dark streak behind the probe, (2) the angle of the other streaks on the test surface, and (3) the angle of the probe center body, all with respect to the horizontal lines on each photograph. The dark streak behind the probe is caused by the increased heat transfer from the test surface in the wake of the probe which results in a slightly lower surface temperature. This streak angle marks the local flow angle behind the probe. The other curved streaks on the test surface mark the streamlines of the constant flow angle region.* This is true because it will be shown that the flow angles measured with the pressure probe in the constant-angle region at a given location agree with the angles on the streaks at the same location in the photographs. The probe center body angle marks the direction in which the probe is facing. The horizontal dark lines are the gaps between heating strips.

The figures show that there is mutual agreement between the angle of the dark streak behind the probe, the other streaks around the probe, and the angle of the probe center body. The figures more importantly show that as the probe is moved away from the wall neither the probe center body angle, nor the angle of the streak behind the probe, change with respect to the angle of the streaks on the test surface around the probe until the probe reaches a z/δ_t of 0.79. At this point the probe angle deviates from the angle of the streaks around the probe and from the angle of the dark streak behind the probe caused by its wake. This can be more clearly seen by comparing the actual flow angle measured with the probe, β_{meas}, to the measured angle of the streak behind the probe and the streaks around the probe, β_{streak}, given in the figure titles. The streak angle is approximately 20° in each figure. The angle measured with the probe is approximately the same, except for the Fig. 4-28d, where the probe is at $z/\delta_t=0.79$, which is outside the constant flow angle region indicated in Fig. 4-18 earlier. The measured angle at z/δ_t of 0.79 is 18.2° compared with a streak angle of 20°. On the next step out from the wall to z/δ_t of 1.16, the angle measured with the probe was 15.7°, and there was no dark streak visible behind the probe.

Figures 4-28a through 4-28d support the evidence of the constant flow angle region and its extent, from the wall to $z/\delta_t<0.4$. These observations agree with the pressure probe measurements presented earlier. If this region did not exist, i.e., if the pressure probe measurements were in error, the streak angle and probe angle would have diverged as the probe moved away from the wall. Fluid moving under

---

*These streaks are regions of alternately high and low heat transfer most likely caused by either small disturbances introduced at the vertical leading edge or by large scale structures inherent in the mixed convection boundary layer.

the probe with a greater flow angle, for example, would have traced the probe wake (i.e., the dark streak behind the probe) at an angle given by the inner flow, while the probe alignment angle would have been determined by the flow at the elevation of the pressure ports.

4.2.2 Laminar Boundary Layer Velocity and Temperature Profiles

The next several figures show some laminar enthalpy and total velocity profiles for situations which would be described as laminar mixed convection. Figure 4-29 shows three laminar enthalpy profiles at x=0.23 m. Note especially that these profiles are from locations very near to the vertical leading edge. The profiles are for a nominally constant U_∞ of 4.2 m/s and for T_w varying from 47 C to 562 C, resulting in a Gr_H/Re_L^2 range of 0.2 to 3.1. The data are plotted as dimensionless enthalpy, θ_i, versus z/δ_t. The profile for ID^* 45 represents a baseline profile, from Fig. 3-10. Also shown on Fig. 4-29 as solid lines are variable properties numerical predictions of two pure forced convection enthalpy profiles for U_∞ equal to 4.0 m/s, made with STAN5. One profile is for a uniform heat flux surface with T_w approximately equal to 60 C and the other profile is for a uniform T_w surface with T_w equal to 580 C. These boundary conditions for the numerical predictions approximate the test conditions for ID^*'s 45 and 132, respectively.

Figure 4-29 shows the enthalpy profiles near the vertical leading edge are predictable by the pure forced convection laminar flow theory, even for a Gr_H/Re_L^2 up to 3.1. The boundary layer behavior in the region near the vertical leading edge is dominated by forced convection, as shown earlier by the convection heat transfer results in Section 4.1.3. Figure 4-29 lends added support to the "principle of independence" applying along the vertical leading edge, previously discussed in Section 4.1.3.

The next figure, Fig. 4-30, shows the total velocity profiles for the same three cases as in Fig. 4-29. Also shown is a numerical prediction of a pure forced convection velocity profile made with STAN5 (the solid line), for a uniform T_w of 580 C and a U_∞ of 4.0 m/s. The figure shows that buoyancy has an effect on the total velocity near the vertical leading edge. The data for Gr_H/Re_L^2=3.1 lies above the predicted pure forced convection velocity profile. The total velocity increases in the inner region of the laminar boundary layer relative to the free-stream with increasing Gr_H/Re_L^2. This is the result of the vertical velocity component induced by buoyancy.

The fact that buoyancy has an effect on the velocity profiles shown in Fig. 4-30, but not the temperature profiles shown in Fig. 4-29, does not contradict the "principle of independence". The "principle of independence" only states there should be no gradients of velocity or temperature along the vertical leading edge (i.e., the temperature and velocity profiles should be invariant in the vertical direction, near the leading edge). For heat transfer this means that buoyancy should have no effect on the heat transfer along the vertical leading edge. For the hydrodynamics this only means that the velocity distribution should be invariant near the vertical leading edge, the magnitude of the velocity, and therefore the skin friction, will be affected by buoyancy. In other words, the equations governing the horizontal and the vertical momentum transfers near the vertical leading edge will contain no terms involving derivatives of velocity with respect to the vertical direction.

The invariance of the enthalpy and velocity profiles along the vertical leading edge is demonstrated in Figs. 4-31 and 4-32. These are profiles for the Gr_H/Re_L^2 of 21.7 test case near the vertical leading edge at x=0.23 *m*. The vertical locations of the profiles range from the bottom to the top of the test surface, y=0.3 *m* to y=2.67 *m*. The enthalpy and velocity profiles shown in Figs. 4-31 and 4-32 are essentially the same for all vertical locations. The boundary layer thickness δ_t is approximately 0.35 ±.05 *cm* for the profiles in the figures with no detectable trend in the variation. This figure shows that the "principle of independence" can be further extended along the vertical leading edge to test conditions with Gr_H/Re_L^2 of 21.7, as was also shown in the heat transfer results in Section 4.1.3.

Flow angle profiles for the laminar region at the vertical leading edge, found in Appendix F, show no constant-angle region near the wall similar to that found in turbulent flow. A continuous variation of flow angle was noted between the free-stream and the wall.

As a final point, Fig. 4-32 also shows a limitation for the pressure probe used for these laminar profiles. There is much scatter in the velocity data for z/δ_t less than 1.0 . This is most likely the result of the large size of the probe when placed in the small laminar boundary layers near the vertical leading edge. The laminar boundary layers were of the order of 0.5 *cm* thick in Fig. 4-32, for example. The horizontal bars on two data points show the relative thickness of the probe tip at those locations in the boundary layer. The large probe size in a thin boundary layer results in large variations of velocity and flow angle across the face of the probe tip. The large variations limit the boundary layer size in which the probe can be used. The probe size was not a factor for the temperature measurement, as shown in Figs. 4-29 and 4-31, since the fluid temperature thermocouple was an order of magnitude smaller than the pressure probe. The probe size was also not a problem in the turbulent flow regions, since the boundary layers were on the average about 10 *cm* thick.

4.2.3 Variation of the Direction of the Constant-Angle Region

Figures 4-33 is a photograph of the test surface with an average T_w=560 *C* and U_∞=4.4 *m/s*. These conditions result in a Gr_H/Re_L^2 of 3.1. This photograph is similar to the photographs in Figs. 4-28a through 4-28d, except that it is a photograph of the whole surface as viewed from inside the tunnel in the inlet nozzle. The left-most side is the upstream end of the test surface with the free-stream flow from left to right, parallel to the horizontal dark lines on the test surface. The main feature to be noted is that there are streaks, which mark the direction of the flow in the constant-angle region, and that the angles on the streaks are independent of height on the surface for streaks which originate from the vertical leading edge.

The fact that the flow angle is independent of height can also be seen in Figs. 4-34 through 4-39. These are plots showing the flow direction over the entire surface for the constant flow angle region of the boundary layer for various test conditions. The angle of each arrow with respect to a horizontal represents the average flow angle determined from 3 to 5 flow angle measurements taken inside the constant-angle region at the location of the arrow. The curves represent predictions of the flow direction within the constant-angle region, based on an analysis to be discussed later in this section.

The figures demonstrate that the measured flow angles are independent of height on the test surface for streamlines which originate at the vertical leading edge. The figures also show that the streamlines originating from the free convection leading edge diverge. The later point can be more clearly seen in Fig. 4-39, a plot of predicted streamlines and measured flow angles for the constant-angle region for a Gr_H/Re_L^2 of 21.7. All the streamlines from the free convection leading edge diverge for this case.

The simplicity of the constant-angle region and the variation of its angle over the test surface led to an analysis that resulted in an expression for flow angle as a function Gr_L/Re_L^2, the x-position on the test surface, and the point at which the streamline originated (x_o, y_o). The term x_o is zero if the streamline originated at the forced convective leading edge, and the term y_o is zero if it originated at the free convective leading edge.

The analysis deals with the "average" velocity in the constant-angle region. The vertical component of the average velocity, $\overline{v}$, in the constant-angle region will depend on several factors: the surface temperature, free-stream temperature, the gravitational acceleration, how long the flow in the constant-angle layer has been on the test surface, t, and some constant times the vertical free-stream velocity, if present. The vertical component of velocity can be expressed as follows:

$$\overline{v} = a_y t = C_1 g\left(\frac{T_w - T_\infty}{T_\infty}\right)t + C_2 V_\infty \tag{4-20}$$

A vertical free-stream velocity has been included because for high Gr_H/Re_L^2 a small negative free-stream flow angle was noted. This analysis will show the small negative free-stream flow angles that occurred in the experiment had little effect on the constant-angle region.

The horizontal component of the average velocity, $\overline{u}$ is assumed to be some fraction of U_∞, the same fraction that $\overline{v}$ was of V_∞ in Eqn. (4-20). The velocity $\overline{u}$ is also assumed to be equal to the average distance traveled in the x-direction by the fluid in the constant angle layer, $x - x_o$, divided by the time to travel that distance, t:

$$\overline{u} = C_2 U_\infty = \frac{x - x_o}{t} \tag{4-21}$$

From Eqn. (4-20) and (4-21) and the definition of a streamline, the following results:

$$\frac{\overline{v}}{\overline{u}} = tan(\beta_{max}) = \frac{C_1}{C_2}\left(\frac{T_w - T_\infty}{T_\infty}\right)\frac{g(x - x_o)}{U_\infty^2} + \frac{V_\infty}{U_\infty} \tag{4-22}$$

Equation (4-22) can be simplified to,

$$tan(\beta_{max}) = C\frac{Gr_L}{Re_L^2}\left(\frac{x - x_o}{L}\right) + tan(\beta_\infty) \tag{4-23}$$

Equation (4-23) states the flow angle within the constant-angle region depends on the overall Gr_L/Re_L^2, how long the flow has been on the test surface and heated,

$x - x_o$, and the tangent of the free-stream flow angle. Notice that the vertical height does not appear in the problem. For this reason, the Grashof number has been based on length. The use of the term $tan(\beta_\infty)$ acknowledges the effect of free-stream flow angle on the constant-angle layer. The effect is small for the small negative free-stream flow angles noted (even for the high Gr_H/Re_L^2 tests), because of the nature of the tangent function.

If Eqn. (4-23) is valid, a plot of $tan(\beta_{max})$ versus $(Gr_L/Re_L^2)(x - x_o)/L$ should yield a straight line of slope C. This plot is shown in Fig. 4-40. The angle β_{max} is an the average of the flow angle measurements in the constant-angle region for a given profile. The free-stream flow angle term in Eqn. (4-23) has been omitted for simplicity. If included by subtracting $tan(\beta_\infty)$ from $tan(\beta_{max})$ in Fig. 4-40, it would move the data for Gr_H/Re_L^2 equal to 21.7, the data on the right in Fig. 4-40, up a distance equal to the size of a data symbol in the figure. The lower Gr_H/Re_L^2 data, the data on the left in Fig. 4-40, would not be significantly affected.

Figure 4-40 shows that Eqn. (4-23) is only approximately true over the operating domain of the experiment. The tangent of the flow angles do not fall on a perfectly straight line. The slope of a "best" fit line through the data that is constrained to go through the origin in Fig. 4-40 is 0.19, which yields:

$$tan(\beta_{max}) = 0.19\frac{Gr_L}{Re_L^2}\left(\frac{x - x_o}{L}\right) \tag{4-24}$$

Equation (4-24) is shown in Fig. 4-40 as a solid line. At low $(Gr_L/Re_L^2)(x - x_o)/L$, the measured $tan(\beta_{max})$ falls above Eqn. (4-24) and at high $(Gr_L/Re_L^2)(x - x_o)/L$, the measured $tan(\beta_{max})$ falls below Eqn. (4-24).

Figure 4-41 compares the actual flow angle of the constant-angle region, β_{max}, in degrees to those predicted by Eqn. (4-24). Equation (4-24) predicts flow angles to within about $\pm 8°$. The figure also shows the flow angles at high values of $(Gr_L/Re_L^2)(x - x_o)/L$ are approaching $90°$, which they should as free convection becomes more important.

The dashed lines in Fig. 4-40 are lines which fit data at high and low values of $(Gr_L/Re_L^2)(x - x_o)/L$. The slope of the line through the low values is 0.26 and the slope of the line through the high values is 0.13, a factor of two different. The slope of 0.13 at high $(Gr_L/Re_L^2)(x - x_o)/L$ is significant. Based on this slope, it can be shown that the maximum vertical velocity in the boundary layer for free convection dominated flows approaches:

$$v_{max} = 0.36\sqrt{g\left(\frac{T_w - T_\infty}{T_\infty}\right)(y - y_o)} \tag{4-25}$$

This can be obtained from Eqns. (4-16), (4-24), and (4-27) (to come) and the fact that v/V_g has a peak value of 0.71, which means $v_{max} = V_g/\sqrt{2}$. The coefficient in Eqn. (4-25) for v_{max}, 0.36, is in the middle of the range of values reported in the pure free convection literature, 0.3 to 0.39 [50]. Also, the coefficient is only slightly less than the value of 0.37 obtained from predictions of turbulent free convection heat transfer made by this author with STAN5, a numerical boundary layer heat transfer code [1,41]. The predicted value of 0.37 is an average value for a surface at uniform T_w of 420 C, the temperature for the rightmost data in Fig. 4-40. This value did vary about 5% from the bottom to the top of the turbulent region in the numerical predictions.

For forced convection dominated flows, low $(Gr_L/Re_L^2)(x - x_o)/L$, v_{max} is given by:

$$v_{max} = 0.51\sqrt{g\left(\frac{T_w - T_\infty}{T_\infty}\right)(y - y_o)} \tag{4-26}$$

Comparing Eqns. (4-25) and (4-26) shows the flow is accelerated faster in the vertical direction for forced convection dominated flows than for pure free convection.

Equation (4-24) can be integrated to obtain an equation for the streamlines in the constant-angle region, since by definition $tan(\beta_{max}) = d(y - y_o)/d(x - x_o)$. This results in:

$$\frac{y - y_o}{L} = 0.095\frac{Gr_L}{Re_L^2}\left(\frac{x - x_o}{L}\right)^2 \tag{4-27}$$

This is the equation used to draw the streamlines that are shown in Figs. 4-34 through 4-39.

Figures 4-34 through 4-39 have shown that there is good agreement between the streamline angles predicted by Eqn. (4-27) and the flow angles measured with the boundary layer probe. There is, however, significant disagreement near the leading edges, which is accented in Fig. 4-39. The disagreement stems from the fact that near the leading edges, the flow is laminar. Neither Eqn. (4-24) or (4-27) apply for laminar flow. Figure 4-42, a photograph of the forced convective leading edge for a Gr_H/Re_L^2 of 25.9, points this out more clearly. The first vertical light area on the left (a vertical red area if a color photo is used in Fig. 4-42) is the end of the upstream laminar flow region for this case, where h is very low and T_w is high. The darker region just to the right of it is the transition flow region, where h reaches a maximum and T_w is low. Continuing downstream (to the right) from that dark region is the turbulent flow zone. The second light area, which is in the turbulent flow region (the second red region for color photos), is the region where the depression in h downstream of the transition zone was noted for the high values of Gr_H/Re_L^2 in Fig. 4-11.

Figure 4-42 shows that the laminar region streaks have sharper angles with respect to the horizontal than the streaks in the transition region just downstream. After transition the flow angles increase again in the turbulent region. The decrease in flow angle in the transition zone is probably caused by cold, low-vertical-momentum fluid being injected into the hot inner region of the laminar boundary layer by large scale turbulence when transition begins to occur. This would decelerate the vertical motion of the fluid, thus decreasing the flow angle.

Something not pointed out before is that Figs. 4-35, 4-36, and 4-37, which are for a nominally constant Gr_H/Re_L^2 of 3.4, show a striking similarity in hydrodynamic results. This agrees with the heat transfer similarity noted in Fig. 4-8 for a nominally constant Gr_H/Re_L^2 of 3.2.

4.3 Observations on Transition from Laminar to Turbulent Flow

This section presents and discusses some observations on the transition from laminar to turbulent flow. First the effect of wall temperature on the Grashof number at which a free convective flow transitions is presented. Next, the effect of buoyancy and wall temperature on transition in a mixed convective flow are presented and discussed.

Note: Properties are based on film temperature in this section. Film temperature was used largely because transition starts in the laminar boundary where T_f correlates the heat transfer data best, as discussed in Section 1.4 and 4.1.1.

4.3.1 Free Convection Transition

Figure 4-43 shows the effect of T_w on the free convection transition from laminar to turbulent flow for fixed T_∞. The figure is a plot of the Grashof number based on y_c, the location of either the minimum h or the maximum h, versus T_w/T_∞. The free-stream temperature, T_∞, is approximately 20 C for all cases.

Minimum h occurs where h begins to deviate from the laminar values. Maximum h is the first point at which h equals its fully turbulent value, a constant. The spatial resolution in determining these locations is not very good: plus or minus the width of one heating strip. Uncertainty bands based on this resolution are shown in Fig. 4-43. The upper value for Gr_{y_c} at each T_w/T_∞ corresponds to the location of maximum h; the lower value corresponds to the minimum h location. The zone between the minimum and maximum h is defined here as the "transition zone" (the crosshatched area). All properties in this figure have been based on T_f with the exception of β, which is evaluated at T_∞. The solid lines connecting the data points are for visual reference only.

Figure 4-43 shows that T_w has a significant effect on the stability of the boundary layer for a fixed T_∞. As T_w/T_∞ increases, the Grashof number at which transition occurs, Gr_{y_c}, decreases significantly up to a T_w/T_∞ of 1.75. Furthermore, the size of the transition zone, in terms of the difference in Gr_{y_c} between the minimum and maximum h location, decreases. This is also true in terms of vertical distance. However, the ratio of Grashof numbers at the minimum and maximum h locations remains fixed at approximately 5.0. These results agree closely with the results of Pirovano et al. [23] for T_w/T_∞ up to 1.5. The very low temperature ratio case agrees with the results of Cheesewright [51].

Beyond a T_w/T_∞ of 1.75, the transition zone size and location in terms of Gr_{y_c} appear fixed. This apparent trend is believed due to a loss of resolution in locating the transition zone. By $T_w/T_\infty = 1.75$, the transition zone has moved down to the first three heating strips on the test surface (see Fig. 2-11) and is occurring over a very short distance ($\approx$1 strip). On the basis of the resolution of the transition zone location, accurate location of the transition zone is impossible when T_w/T_∞ exceeds 1.75. It is only clear that the transition zone does not move upward on the surface for $T_w/T_\infty > 1.75$.

4.3.2 Mixed Convection Transition

Before the experiment it was guessed that the zone for transition from laminar to turbulent flow in mixed convection would consist of a vertical zone along the forced convection leading edge, a horizontal zone along the lower horizontal leading edge, and a smooth fairing of the vertical and horizontal zones in the vicinity of the lower, upstream corner. The shape of the zone was expected to resemble an equation of the form $(x - a)(y - b) = C$, where a, b, and C are constants. This did not occur, however. A transition zone did occur near the vertical leading edge as described above, but a transition zone along the lower leading edge was only seen for pure free convection, as is visible in Fig. 4-6. As soon as there was any free-stream air flow, the transition zone along the lower leading edge disappeared. There was only a hint in the heat transfer data near the lower, upstream corner that the vertical transition zone turned and became a horizontal transition zone for a few very high Gr_H/Re_L^2 tests (>20). For these high Gr_H/Re_L^2 cases, the vertical laminar zone near the vertical leading edge extended slightly further downstream near the lower, upstream corner. This can be observed by looking at the detailed heat transfer results in Appendix E. In spite of the longer laminar zone, the fully turbulent state near the lower, upstream corner was reached at the same x-location as flow higher up on the test surface. No conclusions can be drawn about transition along the lower leading edge based on this experiment. This is discussed further in Appendix D.

The transition zone along the vertical leading edge was visible in Figs. 4-6 through 4-10 and Fig. 4-12. Figure 4-44 shows the location of the vertical transition zone in terms of Re_{x_c} versus Gr_L/Re_L^2. The crosshatched area is the transition zone determined from the locations of the minimum and maximum h's. The dashed lines through the data are for visual reference only. Properties have been evaluated at the film temperature. If the free-stream temperature were used, there would be a much greater scatter in the data. For example, the upper cluster of data at a Gr_L/Re_L^2 of about 3.0 would lie in a range of Re_{x_c} from 1.0×10^5 to about 3×10^5. The length L has been used in the Grashof number in Gr_L/Re_L^2 in Fig. 4-44, instead of H, since the transition zone is vertical and cannot depend on H. No cases with boundary layer trips are shown, only cases with a natural transition. The uncertainty interval for Re_{x_c} is $\pm 10\%$. This is largely the result of the spacing between vertical columns of thermocouples (see Fig. 2-11) The column spacing fixes the spatial resolution for determining the location of the minimum and maximum h. The uncertainty in Gr_L/Re_L^2 is about 2-3%.

Figure 4-44 shows that as Gr_L/Re_L^2 increases, transition occurs at lower Re_{x_c} and over a smaller range of Re_{x_c}. This was shown to be true in x-coordinates, as well, in Fig. 4-6 through 4-10. The effect of buoyancy is to destabilize the laminar boundary layer. At high Gr_L/Re_L^2 the vertical transition zone disappears as the flow becomes more and more vertical in the boundary layer (i.e., approaches free convection with flow in the vertical direction).

The small amount of scatter in the data indicates that film temperature adequately accounts for variable properties effects on transition in this mixed convective flow. The average T_w varies from 60 C to 580 C for various cases shown in Fig. 4-44 and not monotonically with increasing Gr_L/Re_L^2.

The parameter Gr_L/Re_L^2 was used in Fig. 4-44 to show how well ordered the transition data are for this test. It is not, however, a good correlating parameter. If the test surface were longer, for example, Gr_L/Re_L^2 would be larger, but the Re_{x_c} location of transition would not change. Figure 4-45 shows the same information that was shown in Fig. 4-44, except the mixed convection parameter is now based on x_c, instead of L. This plot has more scatter because $Gr_{x_c}/Re_{x_c}^2$ and Re_{x_c} both have $\pm 10\%$ uncertainties based largely on the resolution of x_c. The uncertainty bands are shown for several data points.

The plot in Fig. 4-45 should be more general for transition in orthogonal mixed convective flows near a vertical leading edge. It shows basically the same trends as Fig. 4-44. The solid line through the center of the zone gives the approximate location of the middle of the transition zone in terms of $Gr_{x_c}/Re_{x_c}^2$. The equation for the line is

$$Re_{x_c} = \frac{4.0 \times 10^5}{1 + 6.4\left(\dfrac{Gr_{x_c}}{Re_{x_c}^2}\right)^{1.5}} \qquad (4\text{-}28)$$

The two dashed lines are for reference only.

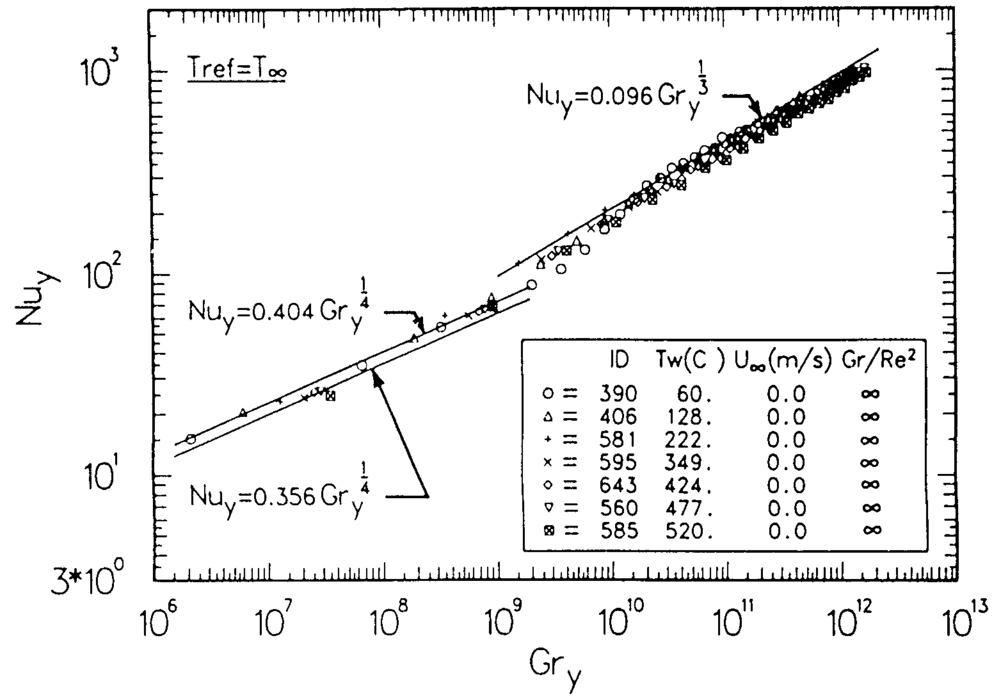

Fig. 4-1 The Effects of Variable Properties on Free Convection from a Vertical Surface in Air ($T_\infty \approx 20\ C$).

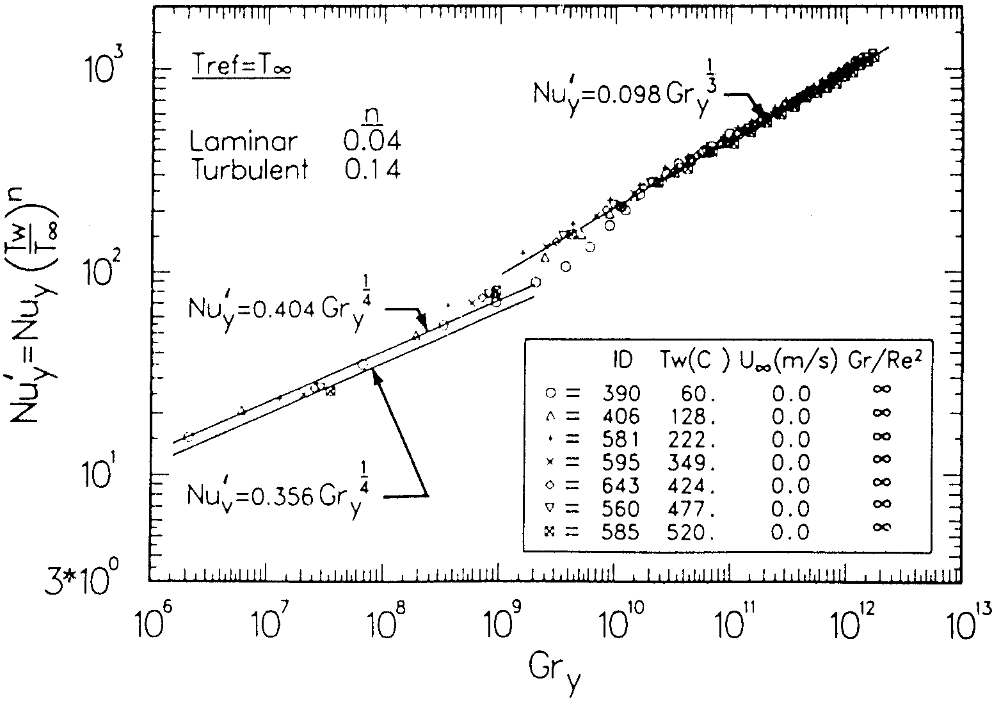

Fig. 4-2 Correlation of Variable Properties Effects on Free Convection from a Vertical Surface in Air ($T_\infty \approx 20\ C$).

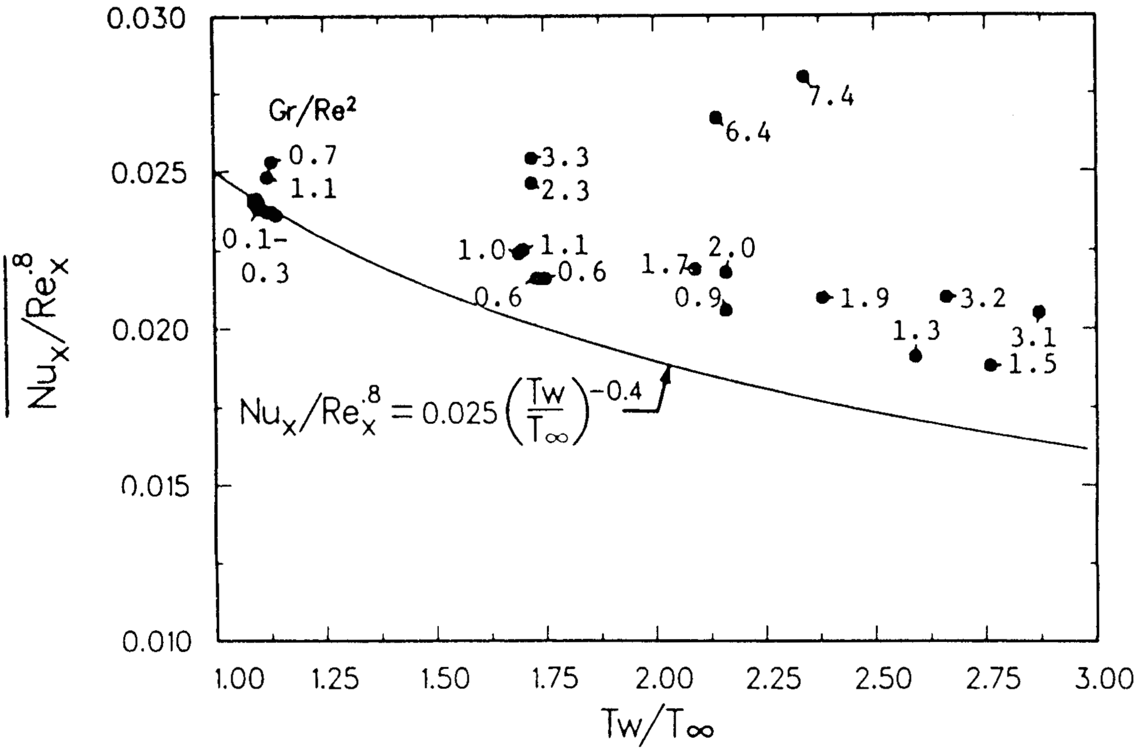

Fig. 4-3 The Effects of Variable Properties and Buoyancy on Turbulent Forced Convection from a Flat Surface in Air ($T_\infty \approx 20\ C$).

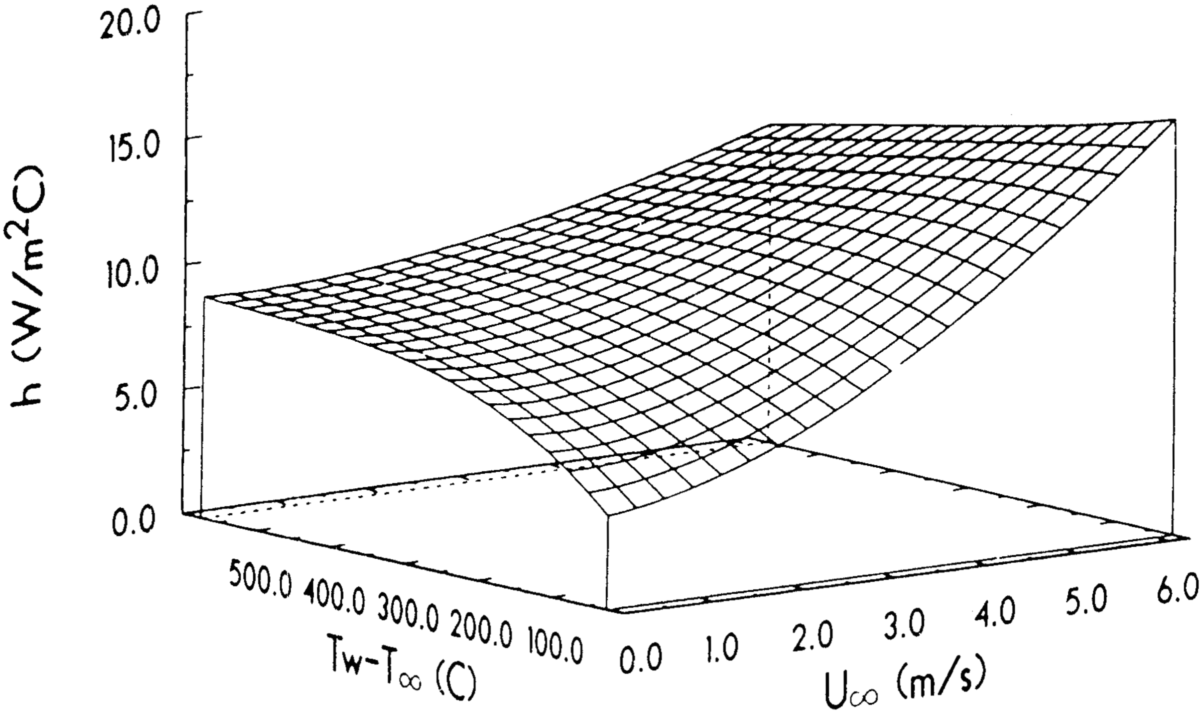

Fig. 4-4 The Average Convection Heat Transfer Coefficient versus U_∞ and $T_w - T_\infty$.

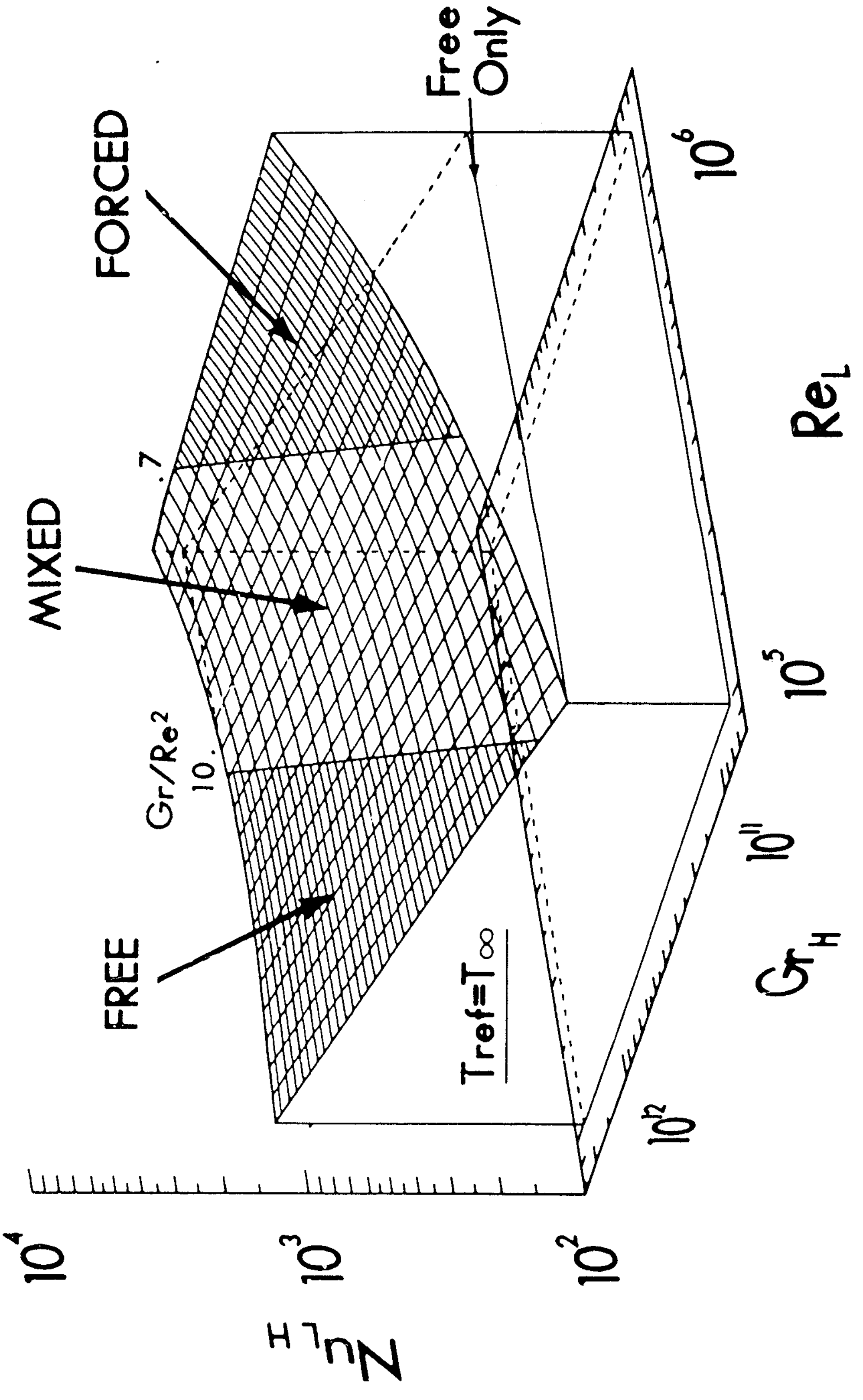

Fig. 4-5 The Average Nusselt Number Based on *LH* versus the Test Surface Grashof and Reynolds Numbers.

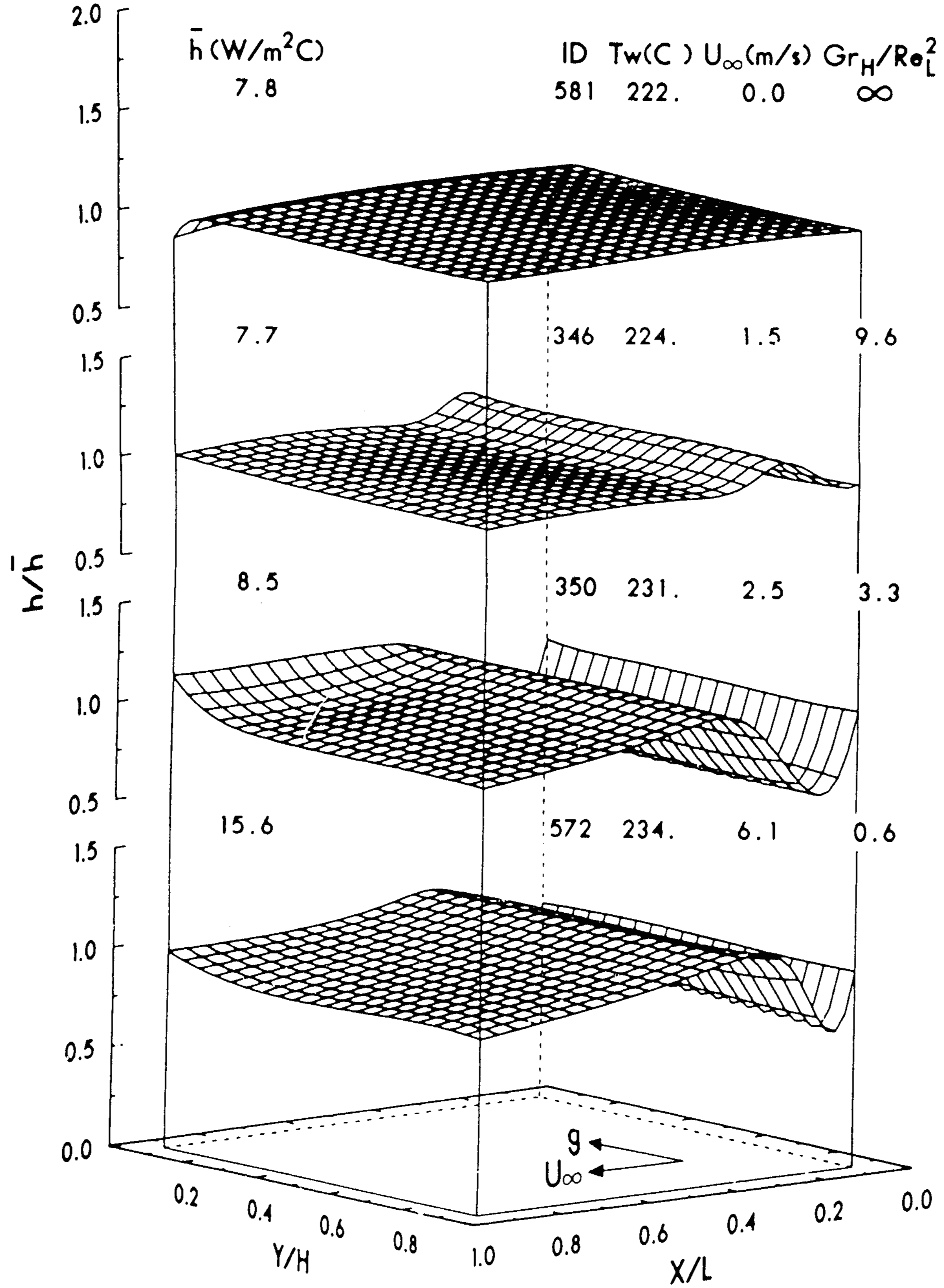

Fig. 4-6 The Effect of U_∞ on the Local Convection Heat Transfer Coefficient Variation at a Nominally Constant T_w of 225 C.

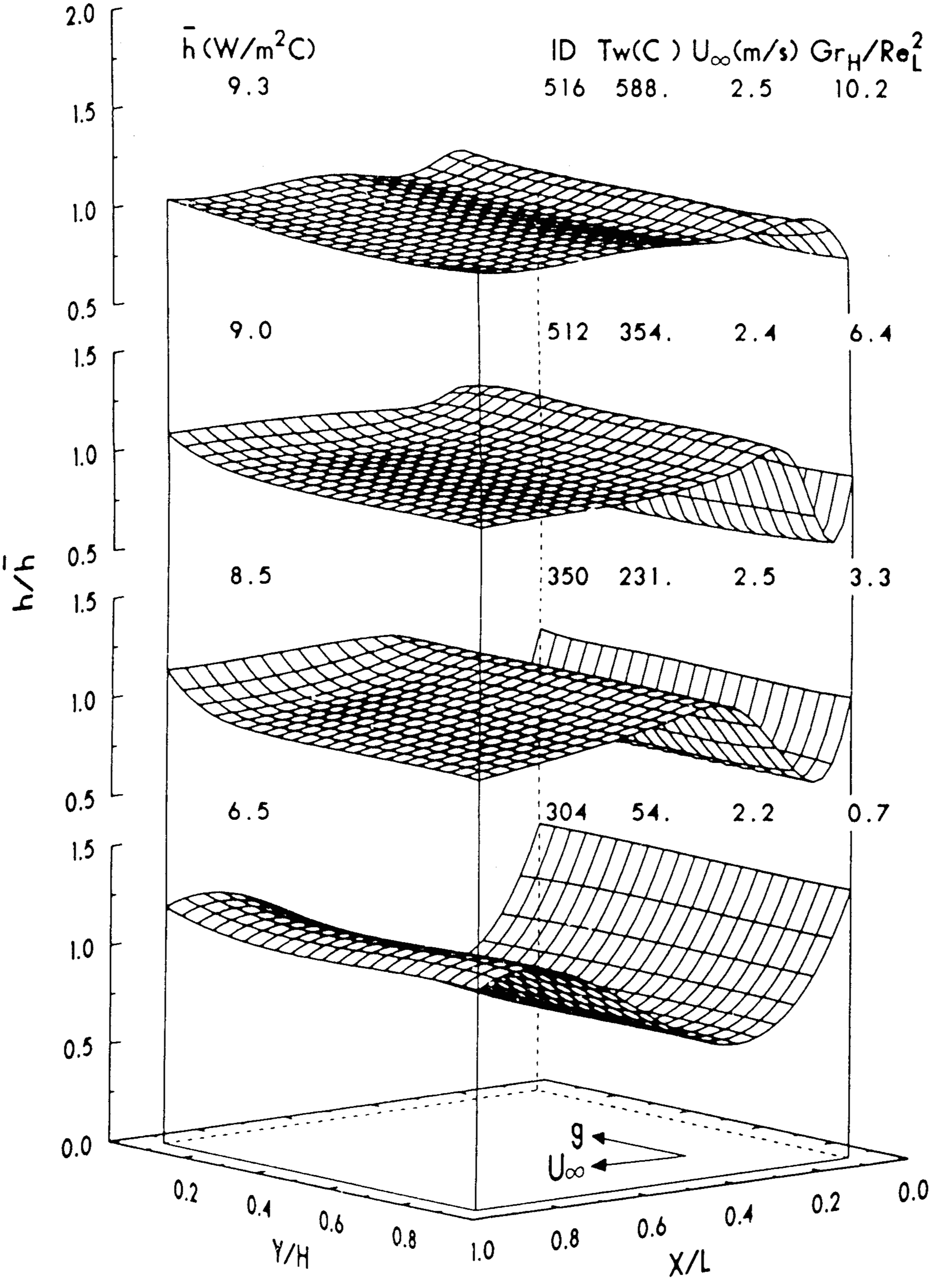

Fig. 4-7 The Effect of T_w on the Local Convection Heat Transfer Coefficient Variation at a Nominally Constant U_∞ of 2.4 m/s.

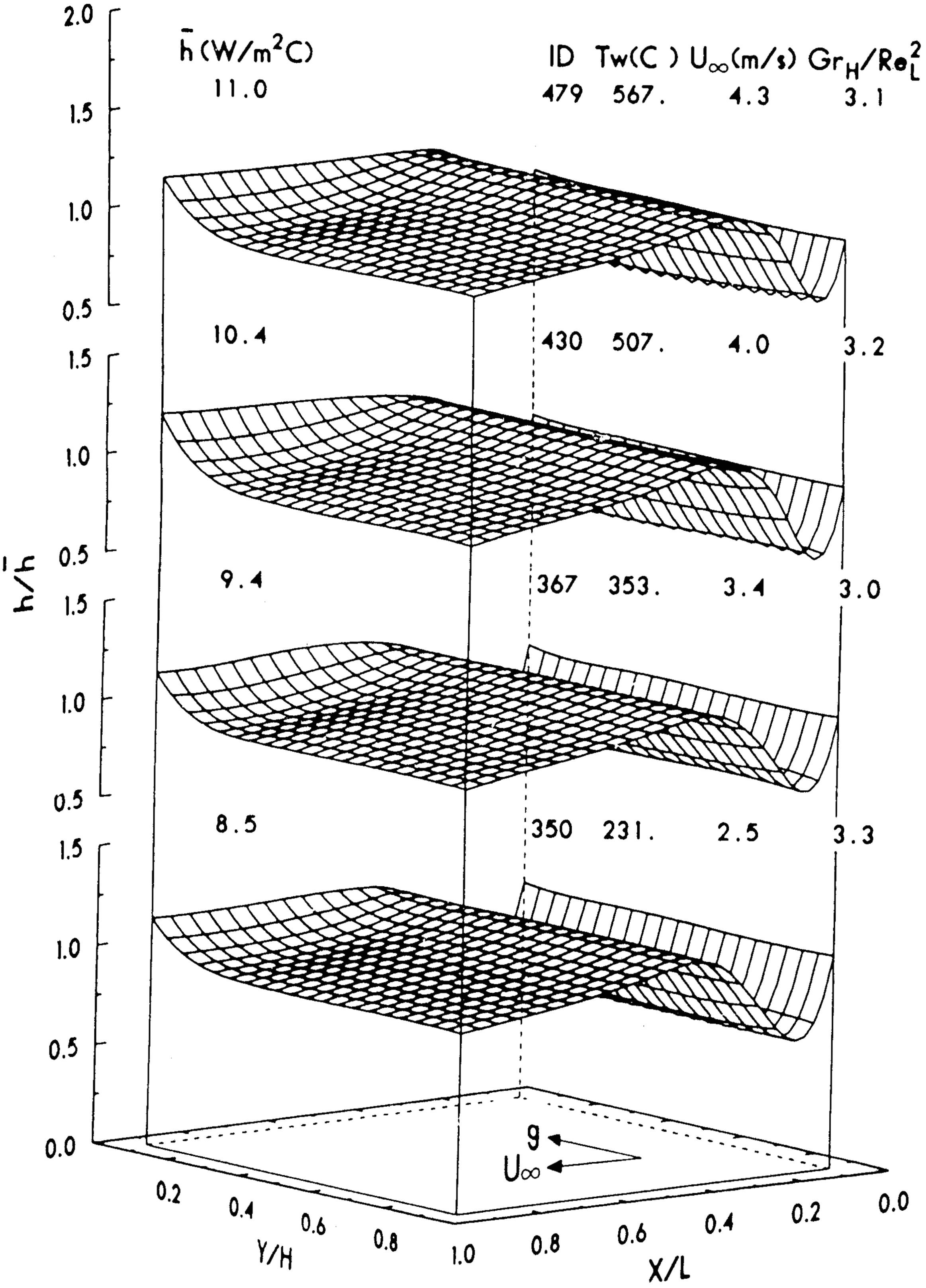

Fig. 4-8 Local Convection Heat Transfer Coefficient Variation for a Nominally Constant Gr_H/Re_L^2 of 3.2.

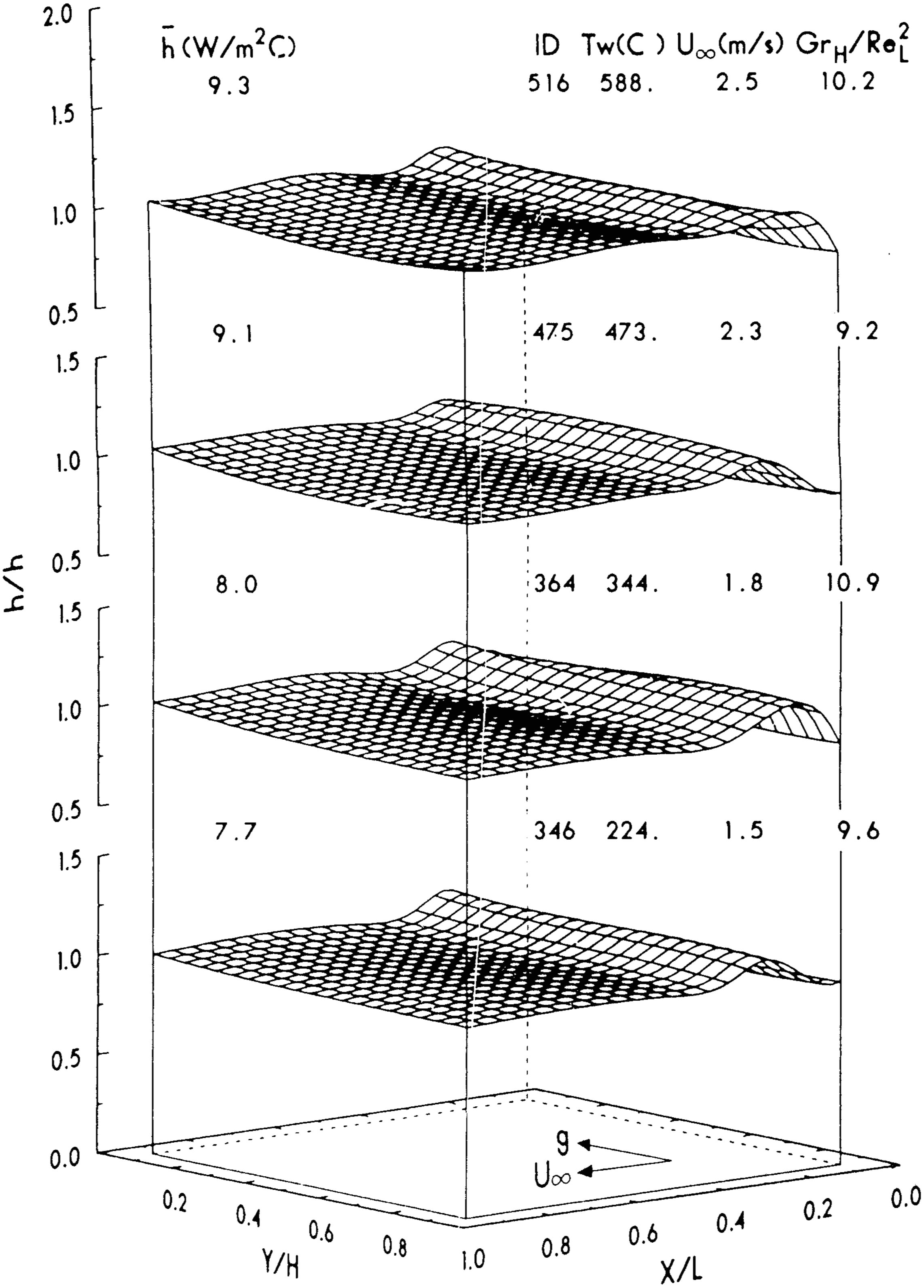

Fig. 4-9 Local Convection Heat Transfer Coefficient Variation for a Nominally Constant Gr_H/Re_L^2 of 10.0.

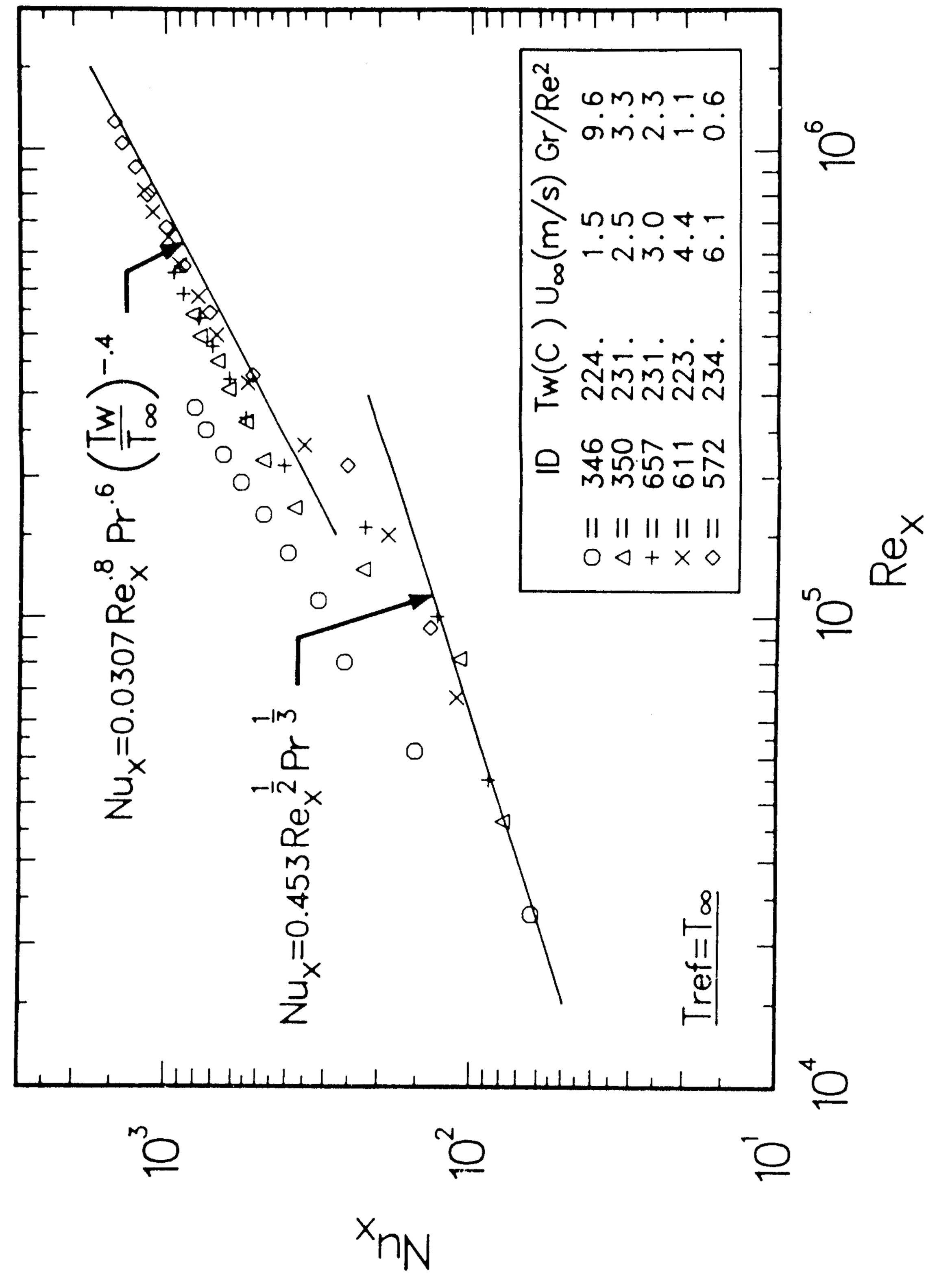

Fig. 4-10 The Effect of Buoyancy on the Column Averaged Nusselt Number versus Reynolds Number.

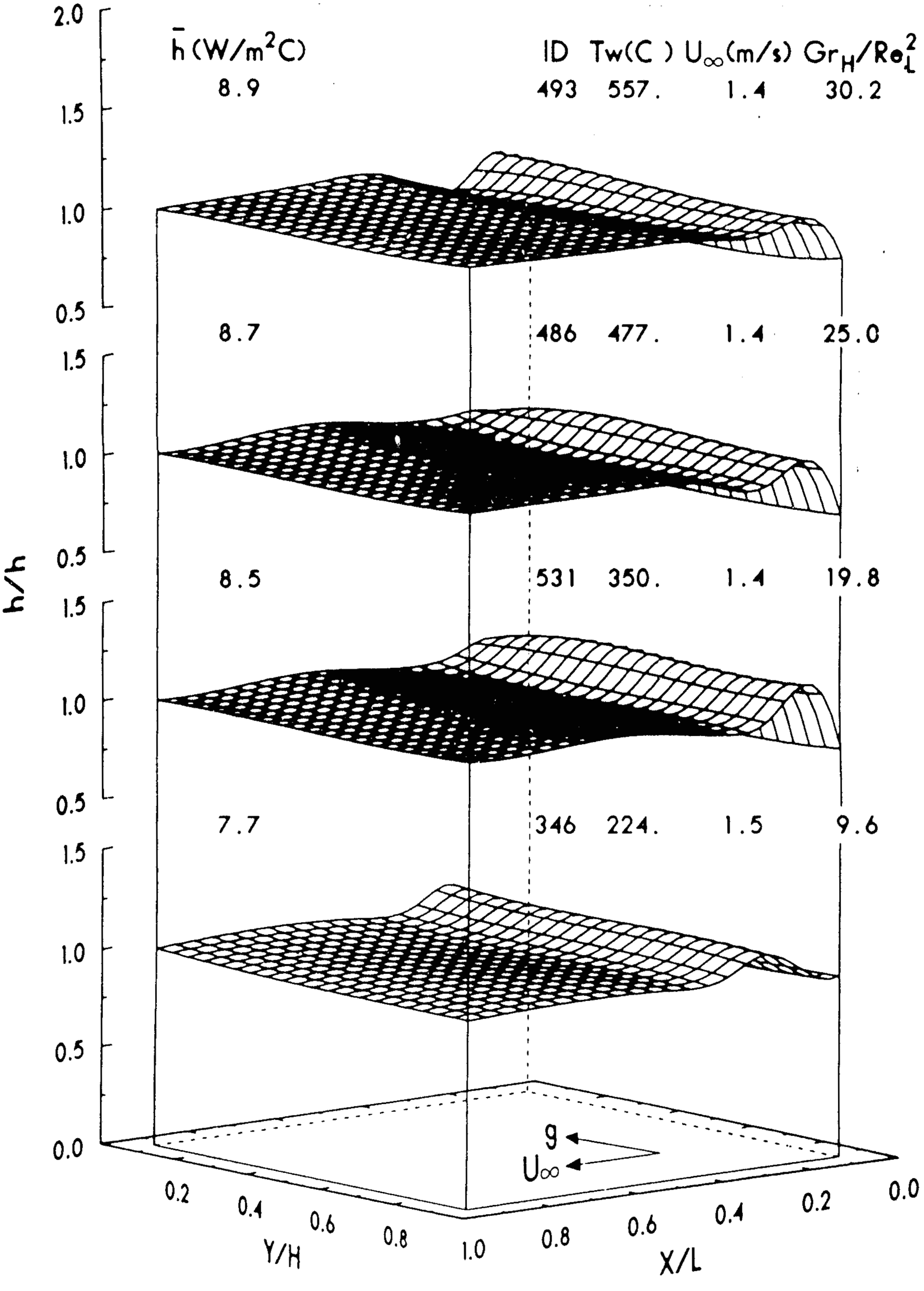

Fig. 4-11 The Effect of T_w on the Local Convection Heat Transfer Coefficient Variation at a Nominally Constant U_∞ of 1.4 m/s and $Gr_H/Re_L^2 > 9.6$.

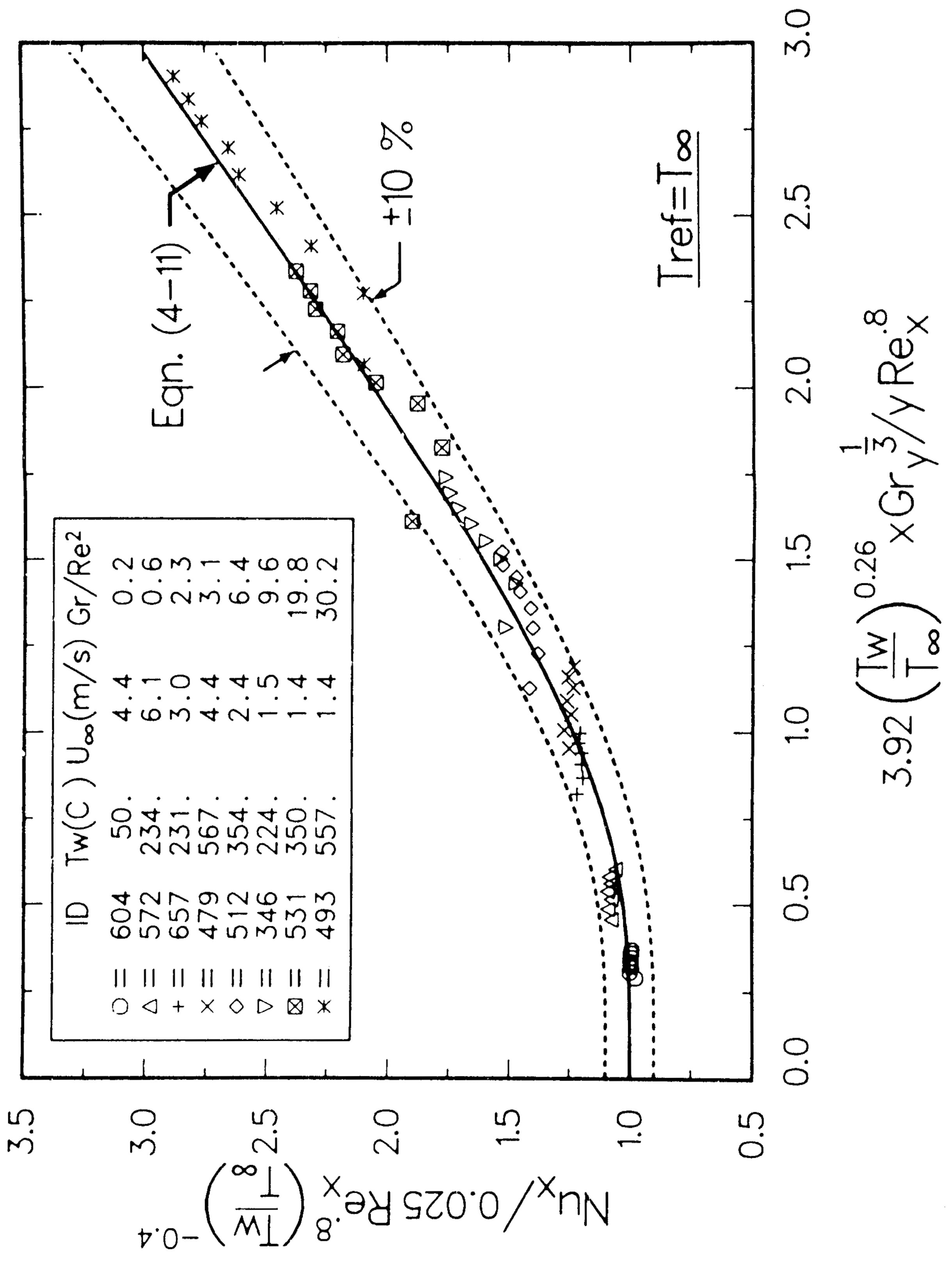

Fig. 4-12 A Comparison of the Measured Local Turbulent Mixed Convection Heat Transfer with that Predicted by Eqn. (4-11).

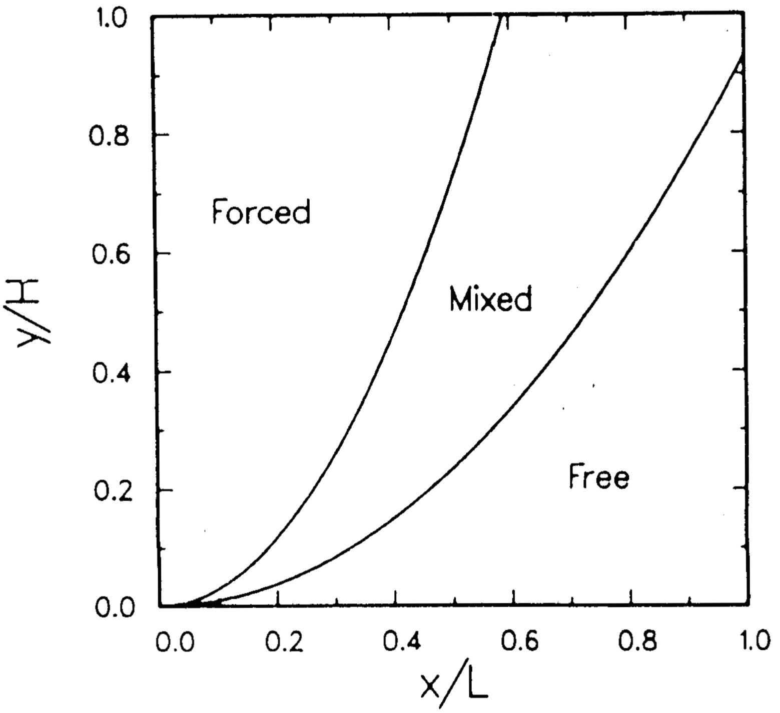

Fig. 4-13 The Laminar Zones of Forced, Mixed, and Free Convection Predicted by Eqn. (4-10) (The locations of the zones are only representative).

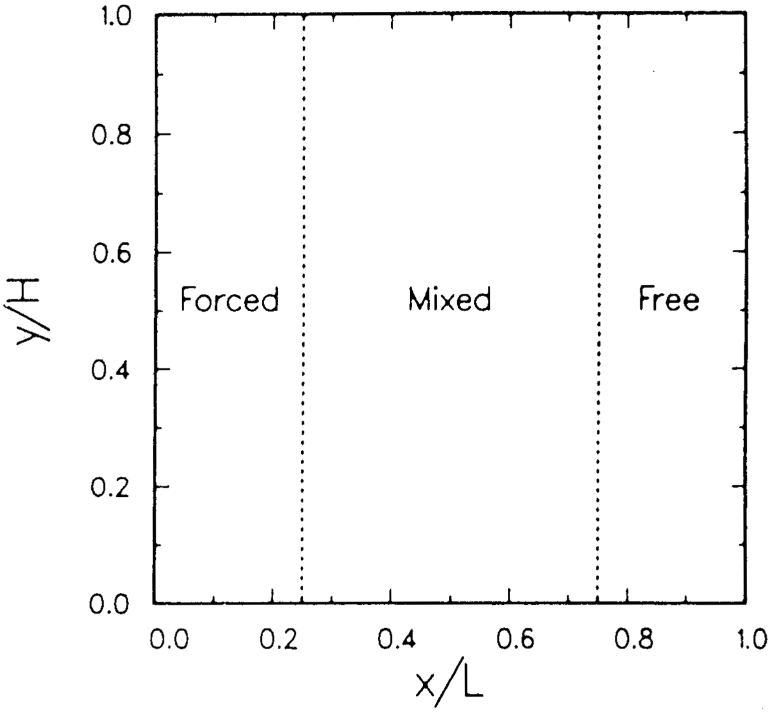

Fig. 4-14 The Turbulent Zones of Forced, Mixed, and Free Convection Predicted by Eqn. (4-11) (The locations of the zones are only representative).

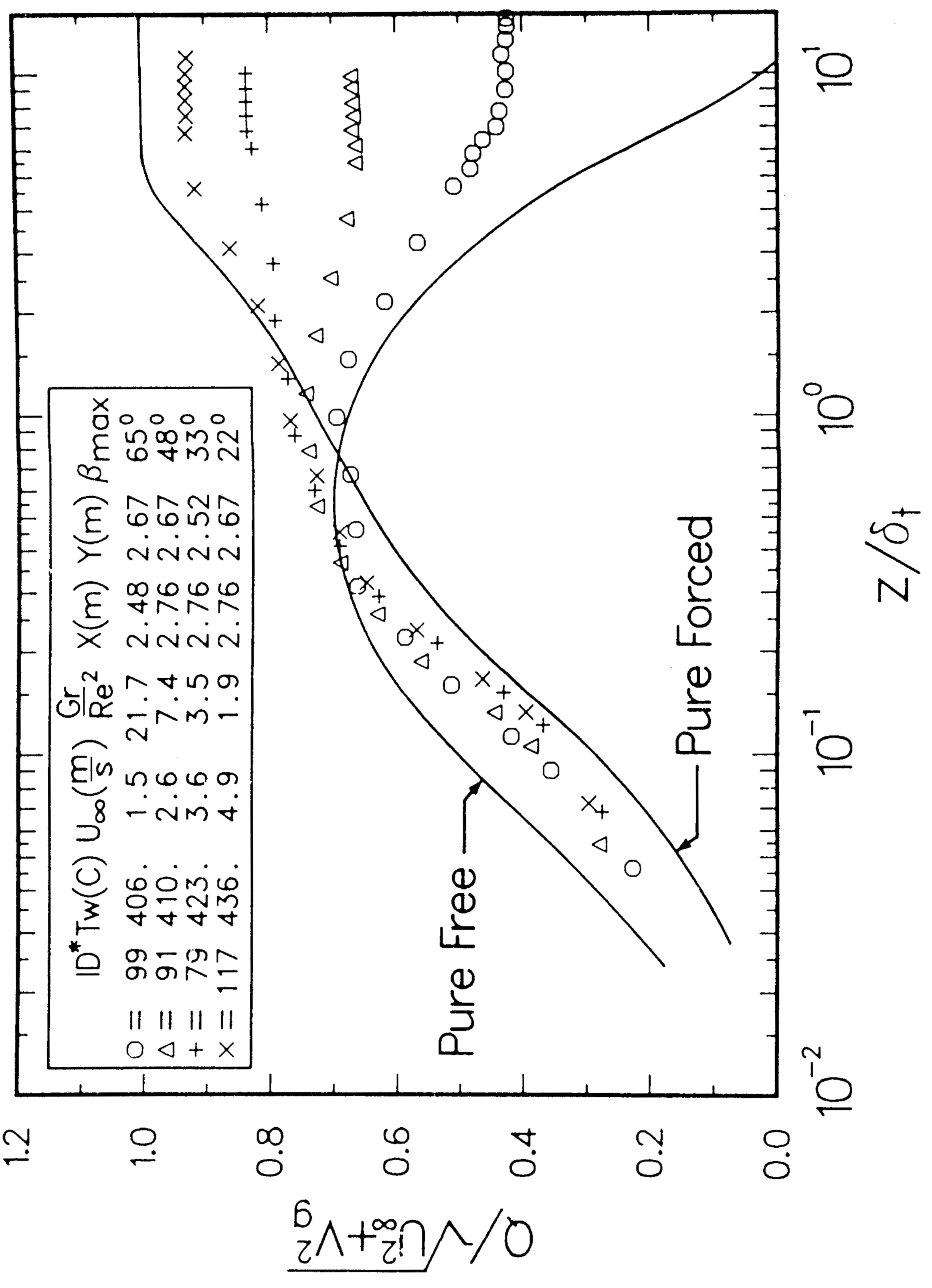

Fig. 4-15 Turbulent Flow Total Velocity Profiles for a Nominally Constant T_w of 420 C and a Nominally Constant x and y Location.

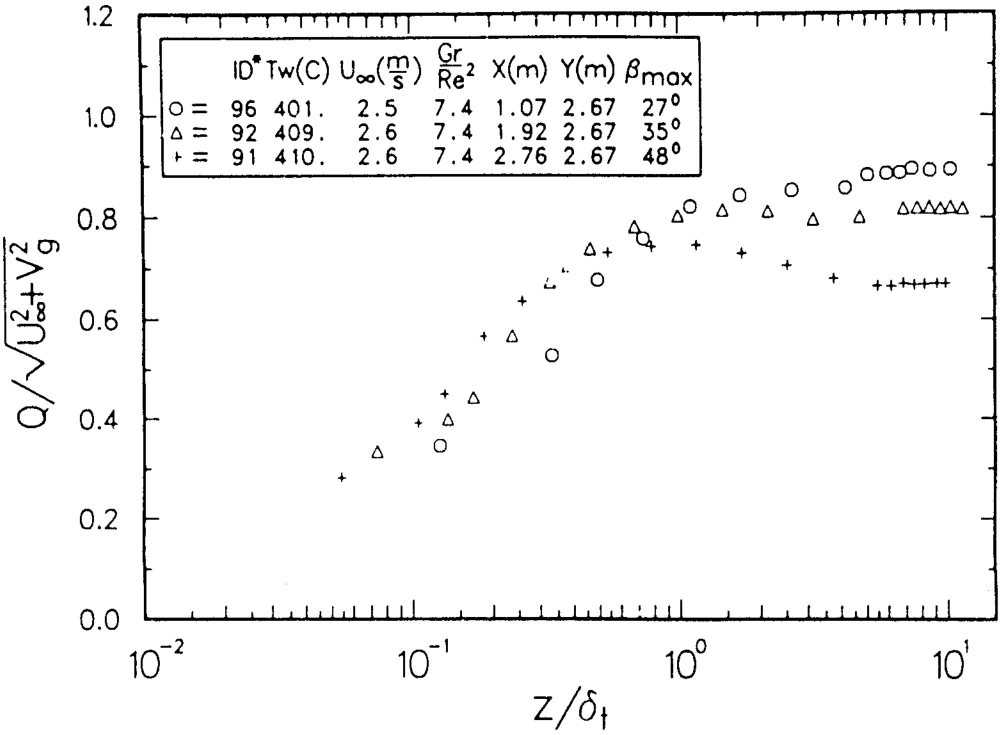

Fig. 4-16 Turbulent Flow Total Velocity Profiles for a Gr_H/Re_L^2 equal to 7.4 and a Constant y Location.

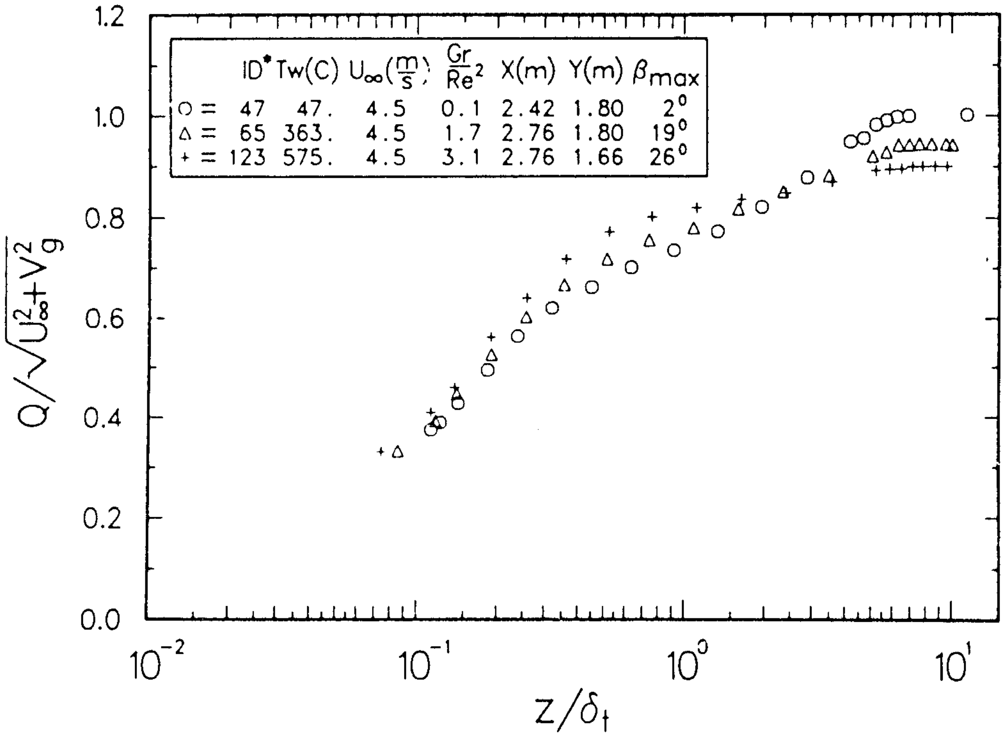

Fig. 4-17 Turbulent Flow Total Velocity Profiles for a Nominally Constant U_∞ of 4.5 m/s and a Nominally Constant x and y Location.

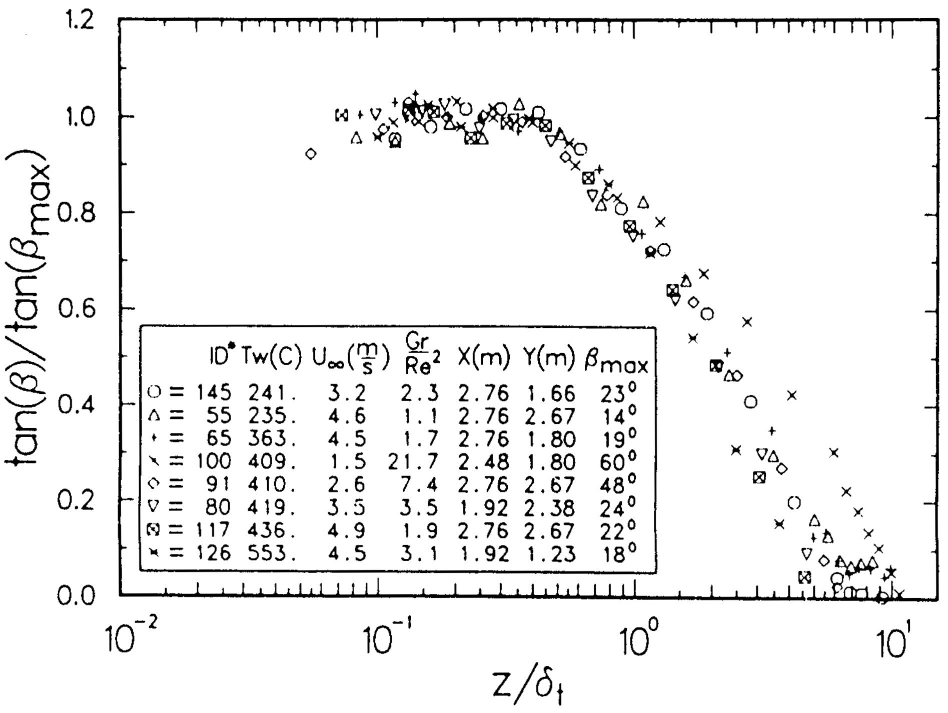

Fig. 4-18 Flow Angle Profiles for Turbulent Flow for Various Test Conditions and Various x and y Locations.

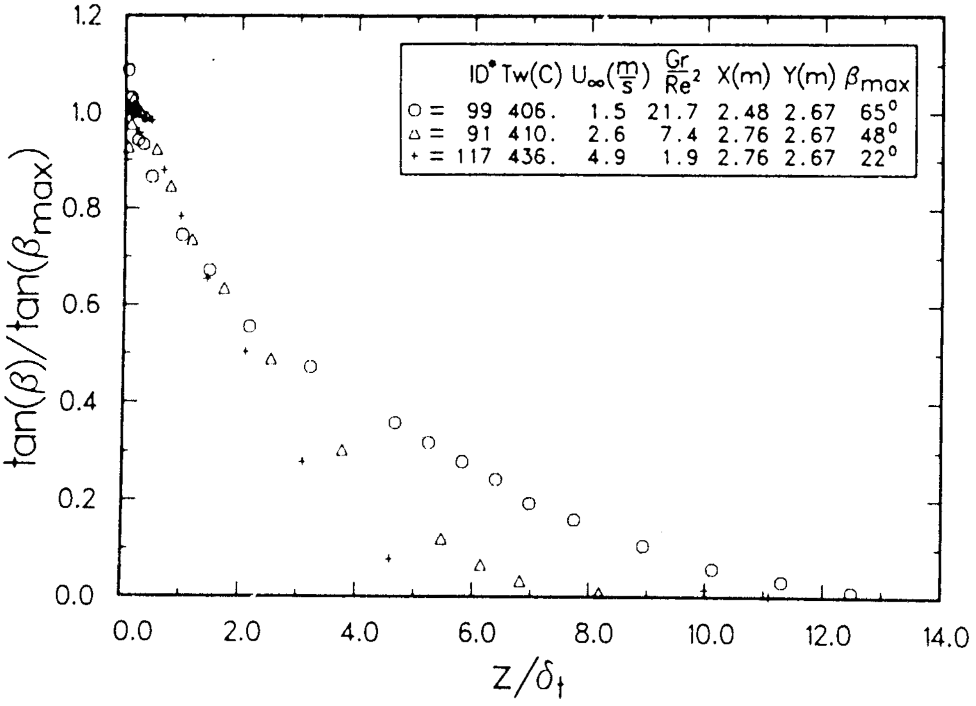

Fig. 4-19 Flow Angle Profiles for Turbulent Flow for a Nominally Constant T_w of 420 C and a Nominally Constant x and y Location.

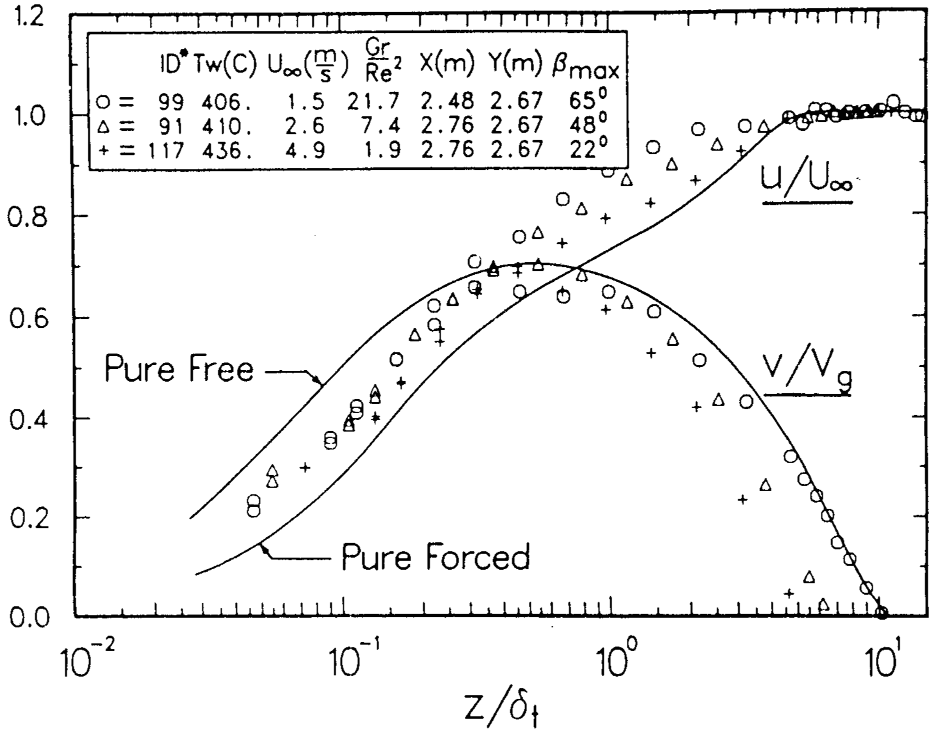

Fig. 4-20 Turbulent Flow Horizontal and Vertical Velocity Component Profiles for a Nominally Constant T_w of 420 C and a Nominally Constant x and y Location.

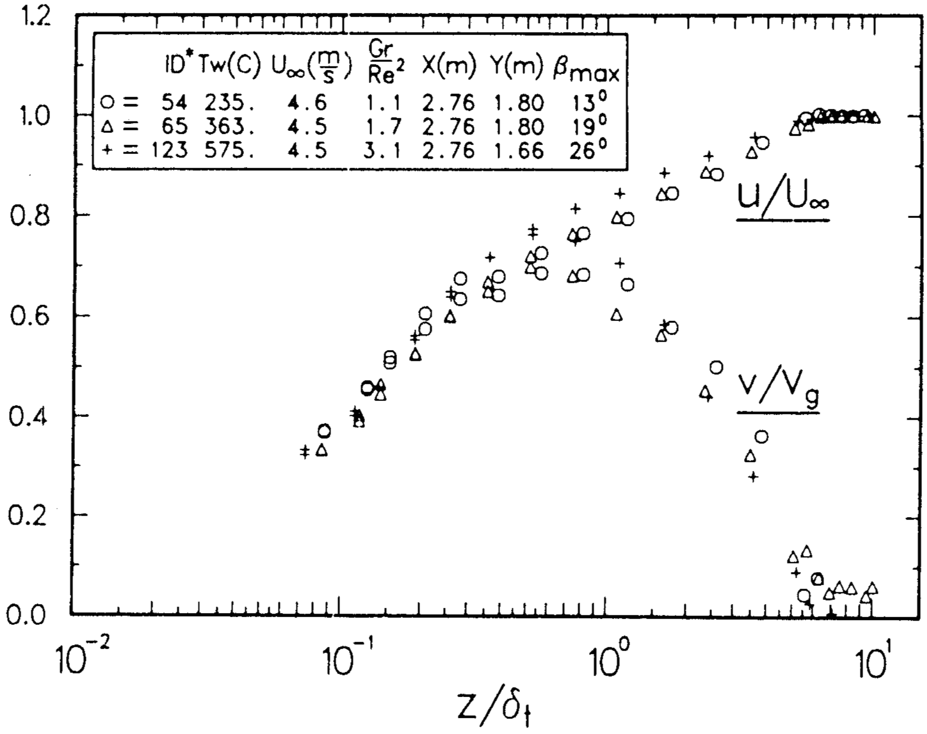

Fig. 4-21 Turbulent Flow Horizontal and Vertical Velocity Component Profiles for a Nominally Constant U_∞ of 4.5 m/s and a Nominally Constant x and y Location.

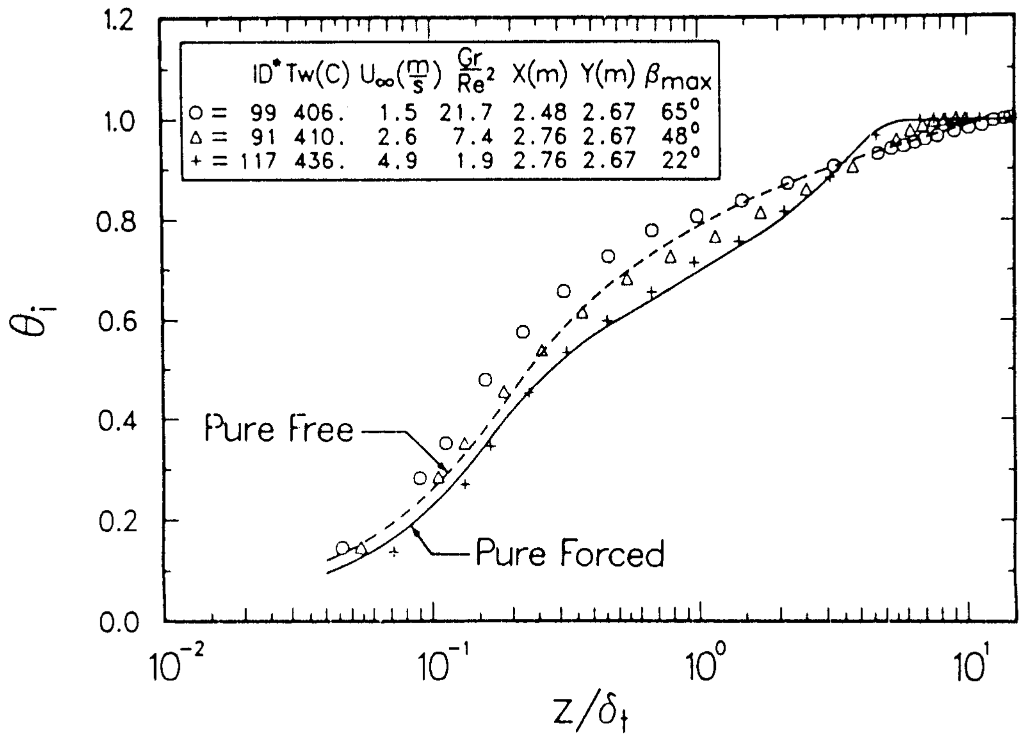

Fig. 4-22 Turbulent Flow Enthalpy Profiles for a Nominally Constant T_w of 420 C and a Nominally Constant x and y Location.

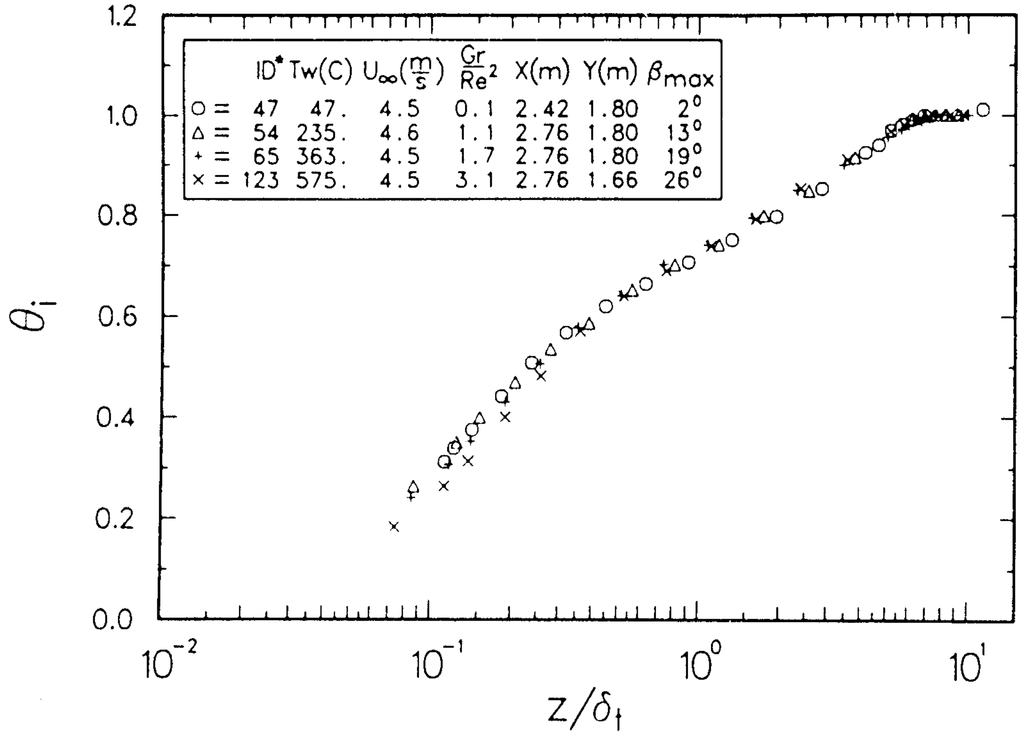

Fig. 4-23 Turbulent Flow Enthalpy Profiles for a Nominally Constant U_∞ of 4.5 m/s and a Nominally Constant x and y Location.

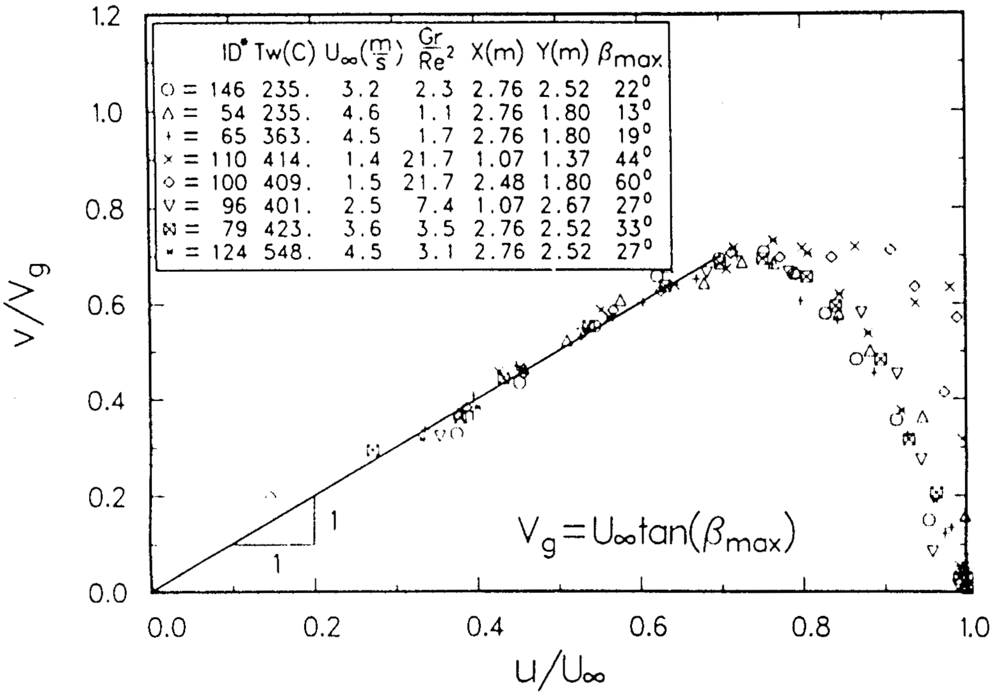

Fig. 4-24 The Horizontal Velocity Component versus the Vertical Velocity Component for Turbulent Flow for Several Test Conditions and Various x and y Locations.

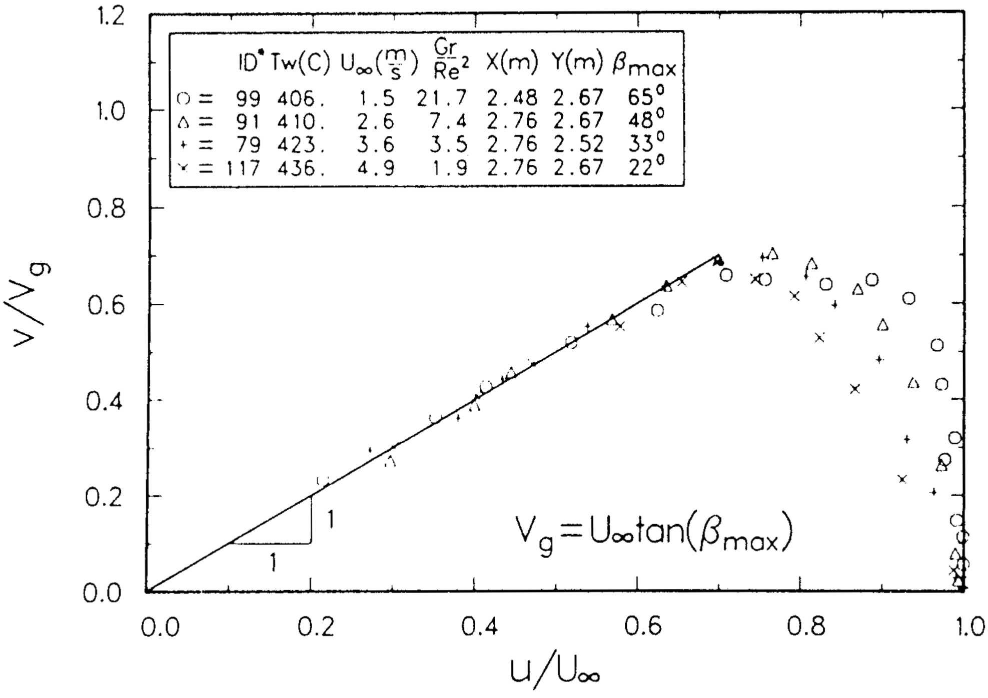

Fig. 4-25 The Horizontal Velocity Component versus the Vertical Velocity Component for Turbulent Flow for a Nominally Constant T_w of 420 C and a Nominally Constant x and y Location.

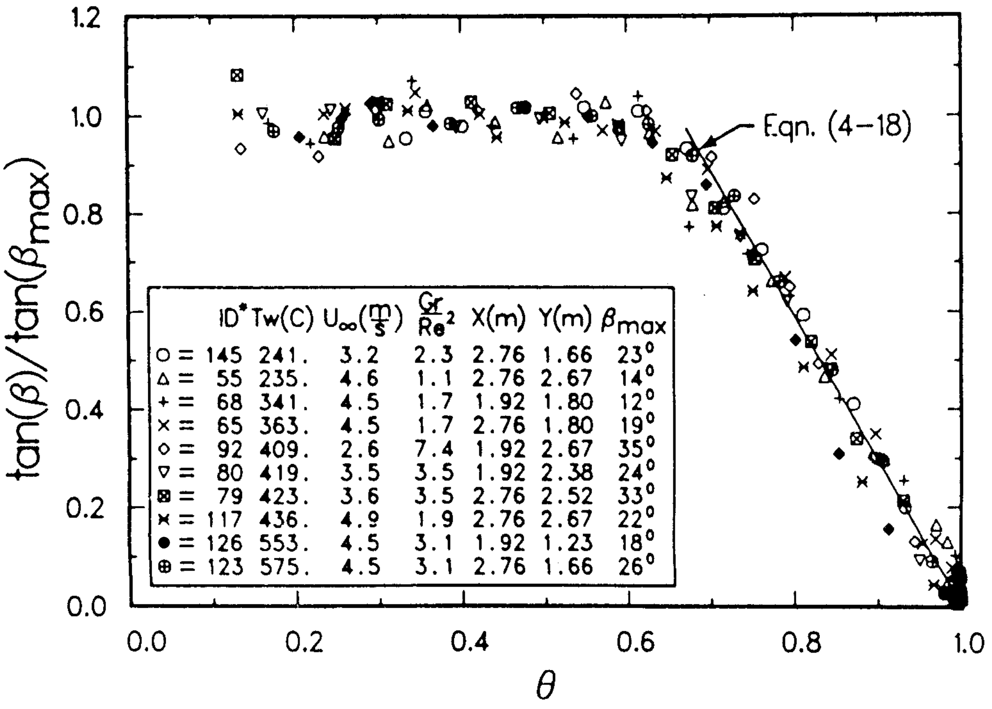

Fig. 4-26 Flow Angle versus Dimensionless Temperature for Turbulent Flow for Several Test Conditions and Various x and y Locations.

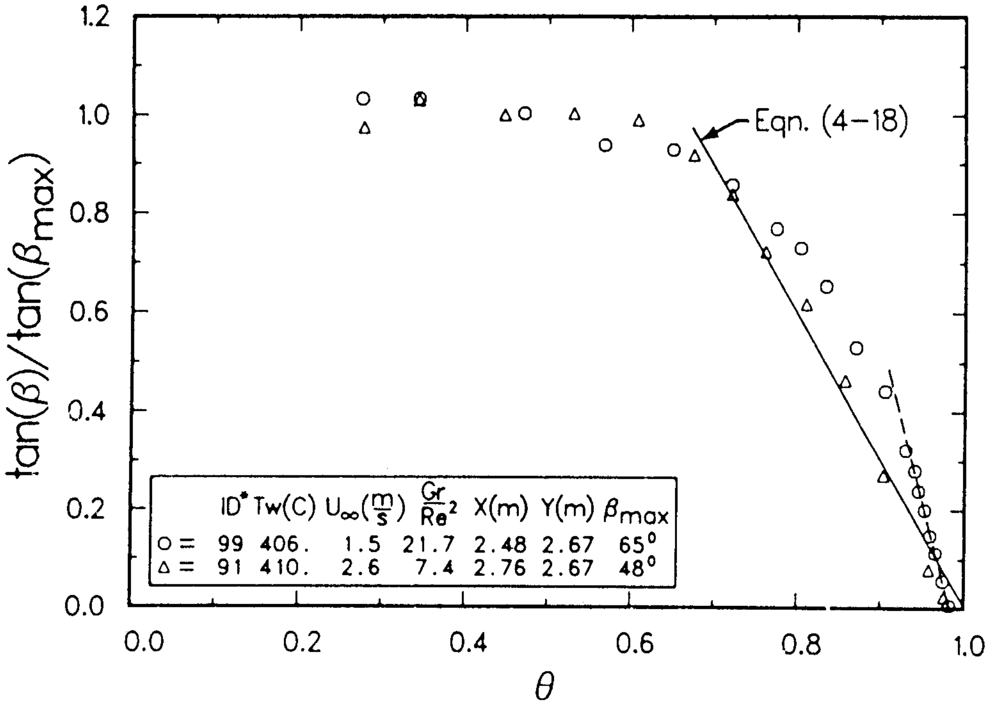

Fig. 4-27 Flow Angle versus Dimensionless Temperature for Turbulent Flow and High Gr_H/Re_L^2.

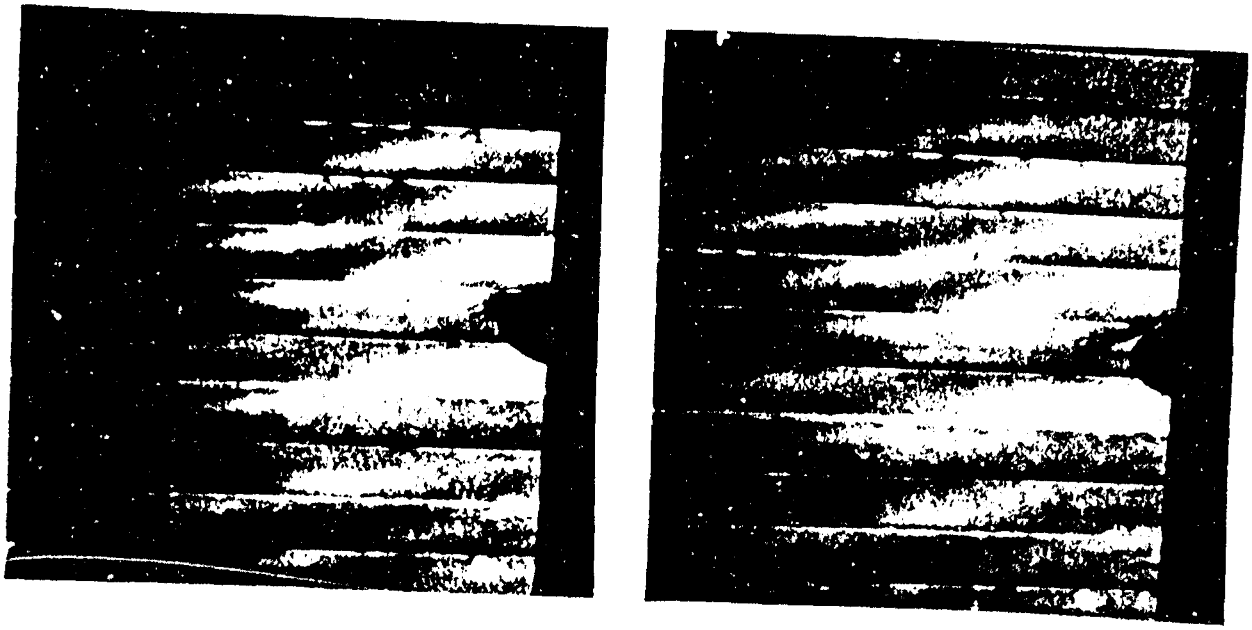

a. $z/\delta_t=0.10$, $\beta_{meas}=20.8°$, and $\beta_{streak}=21.0°$

b. $z/\delta_t=0.28$, $\beta_{meas}=21.0°$, and $\beta_{streak}=21.0°$

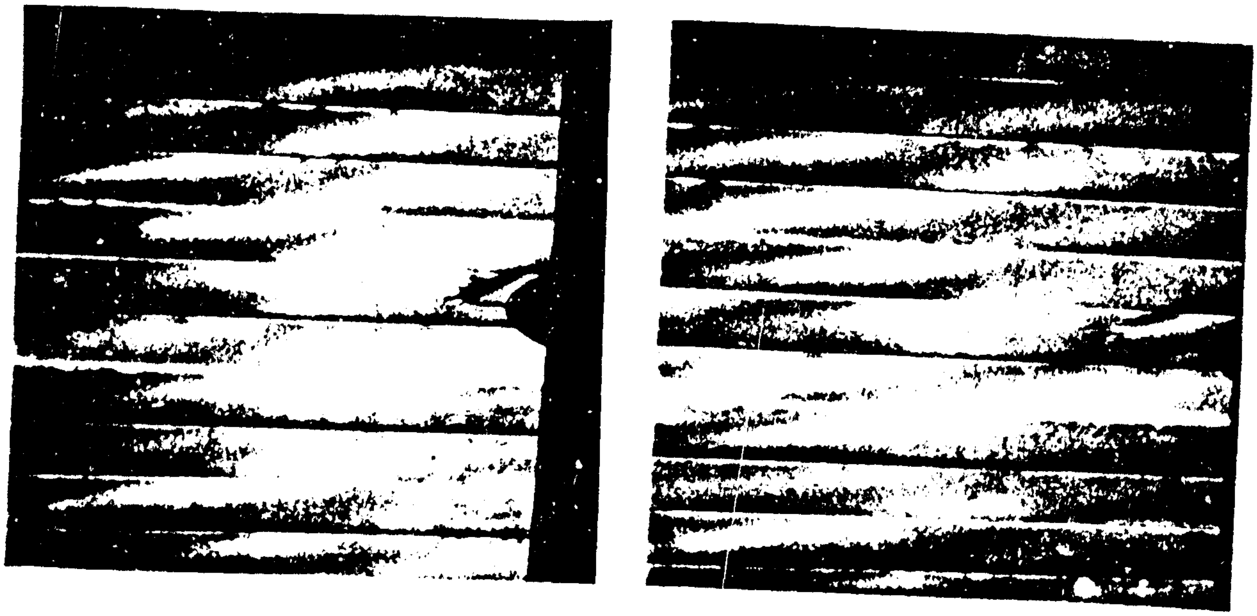

c. $z/\delta_t=0.39$, $\beta_{meas}=20.6°$, and $\beta_{streak}=20.0°$

d. $z/\delta_t=0.79$, $\beta_{meas}=18.2°$, and $\beta_{streak}=20.0°$

Fig. 4-28 Photograph of the Angle of the Boundary Probe and the Flow Angle in the Constant-Angle Region, $T_w=560$ C, $U_\infty=4.2$ m/s, and $Gr_H/Re_L^2=3.2$.

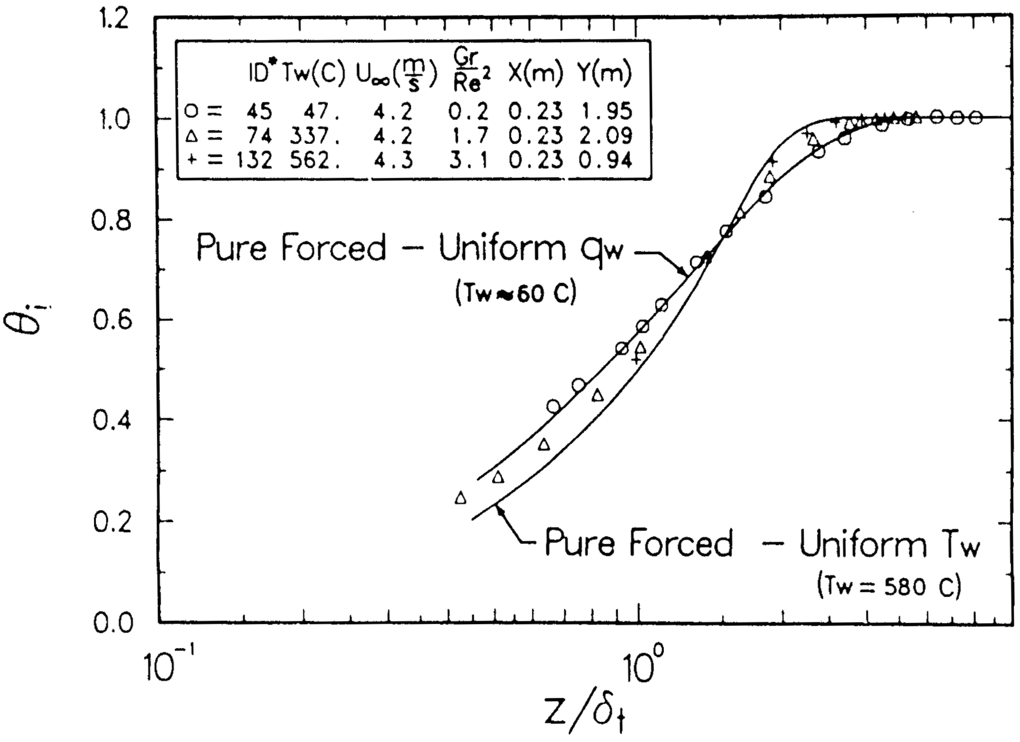

Fig. 4-29 Laminar Flow Enthalpy Profiles for a Nominally Constant U_∞ of 4.2 m/s and an x of 0.23 m.

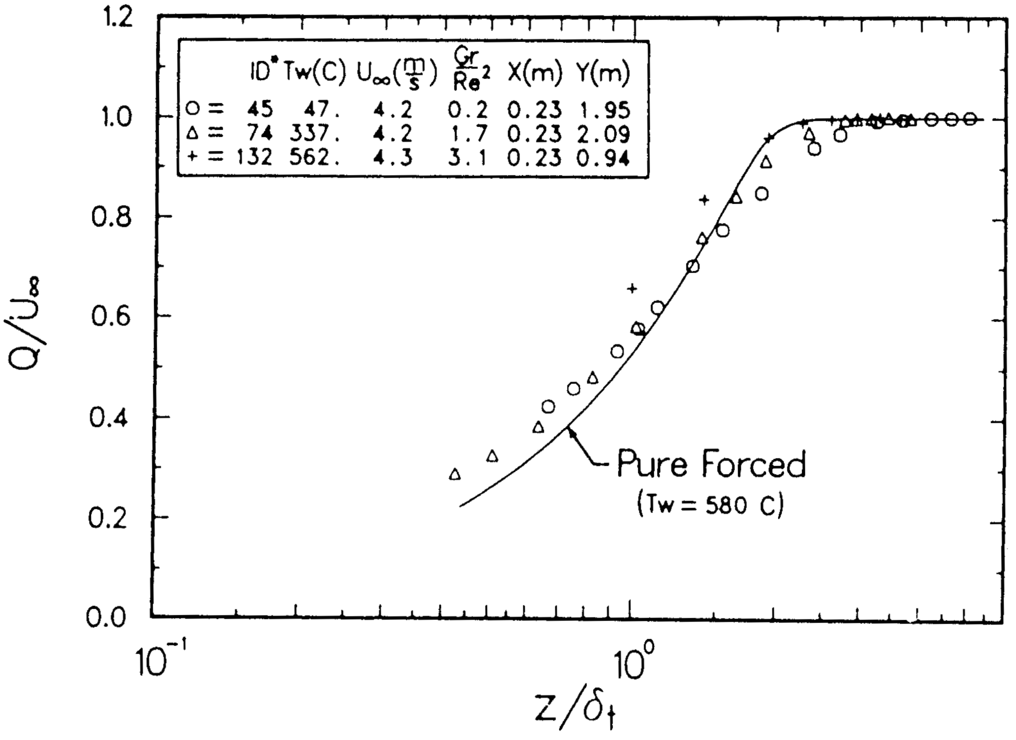

Fig. 4-30 Laminar Flow Total Velocity Profiles for a Nominally Constant U_∞ of 4.2 m/s and an x of 0.23 m.

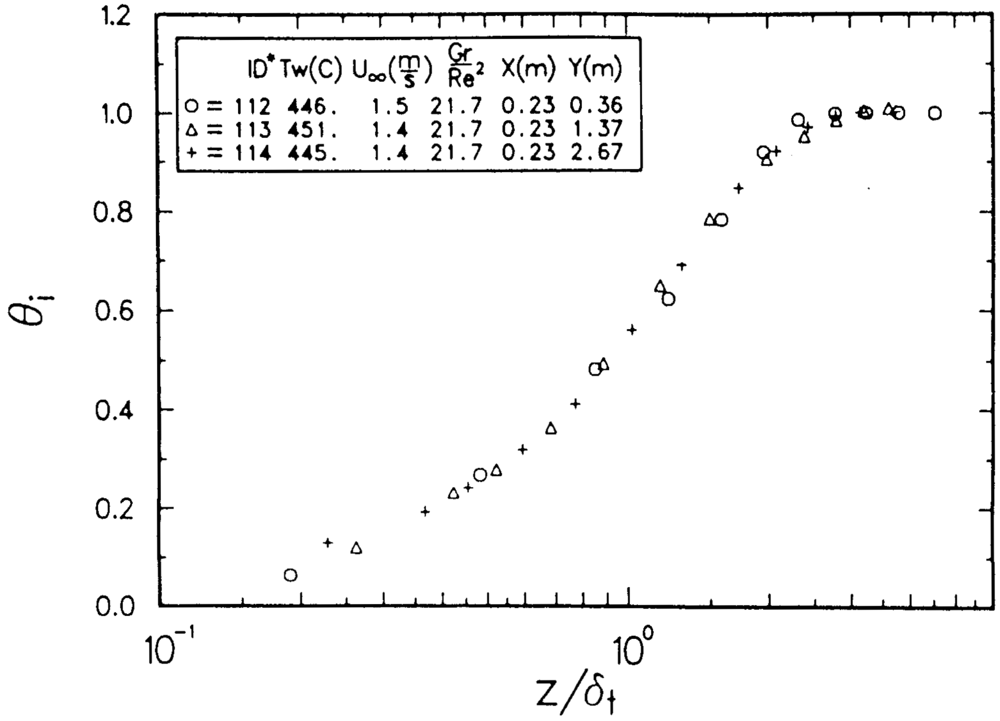

Fig. 4-31 Laminar Flow Enthalpy Profiles for a Nominally Constant T_w of 450 C, Gr_H/Re_L^2=21.7, and an x of 0.23 m.

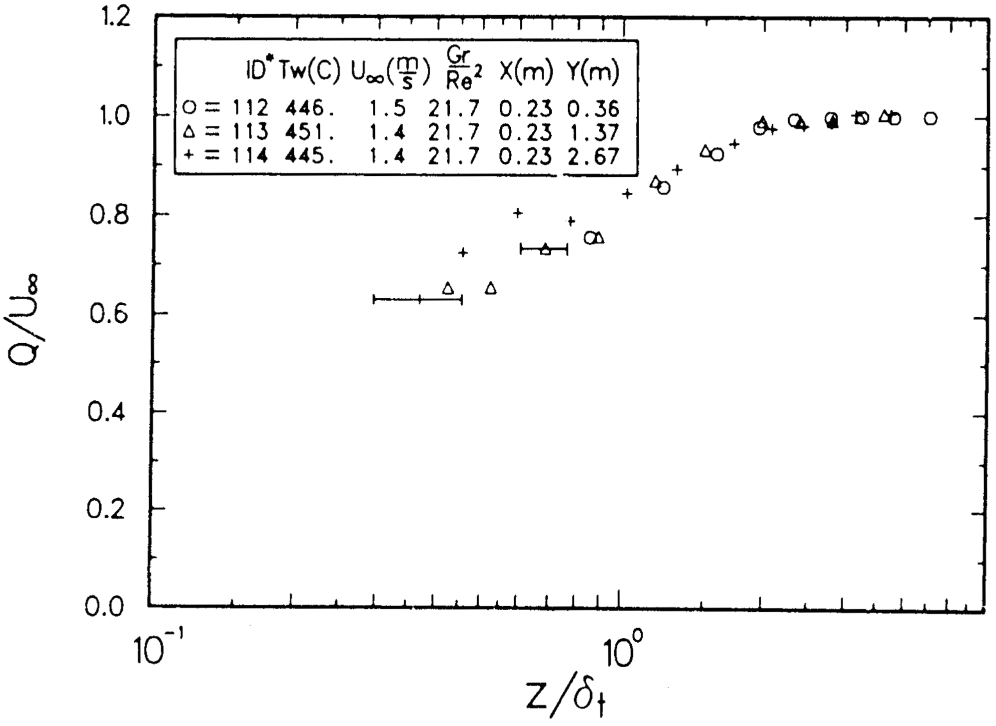

Fig. 4-32 Laminar Total Velocity Profiles for a Nominally Constant T_w of 450 C, Gr_H/Re_L^2=21.7, and an x of 0.23 m.

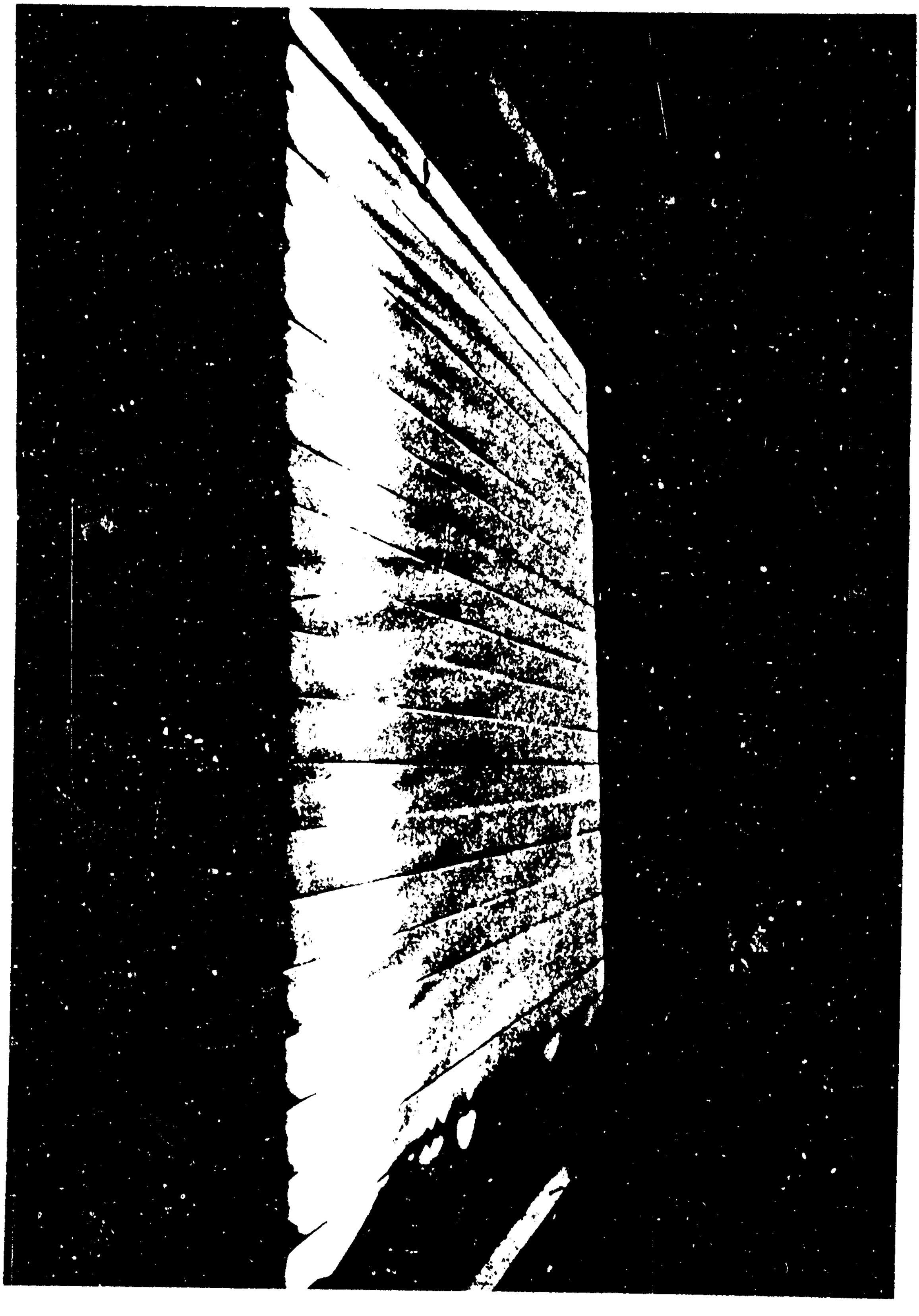

Fig. 4-33 Photograph of Test Surface for T_w=560 C, U_∞=4.3 m/s, and Gr_H/Re_L^2=3.1 (ID=648).

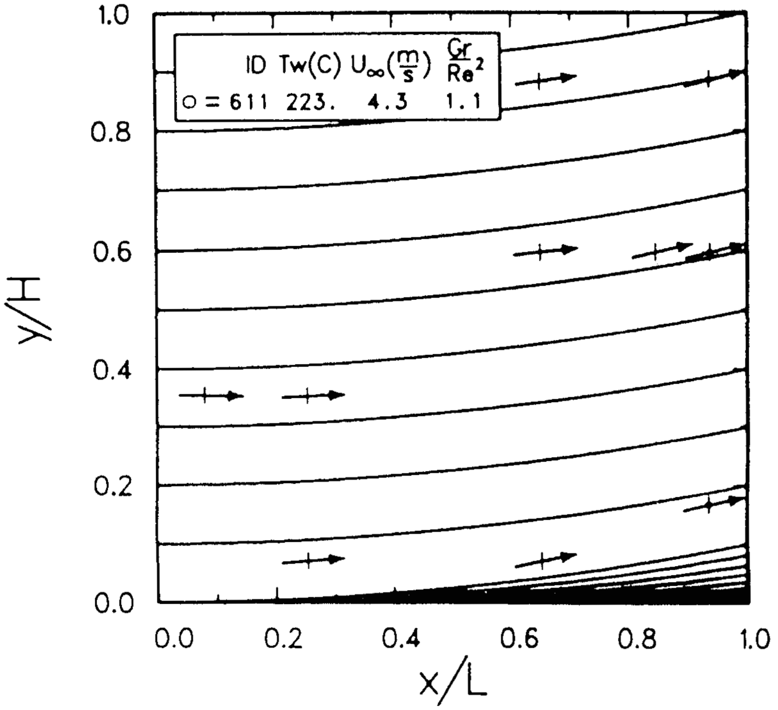

Fig. 4-34 Measured Flow Angles and Predicted Streamlines of the Constant-Angle Region for T_w=223 C, U_∞=4.3 m/s, and Gr_H/Re_L^2=1.1.

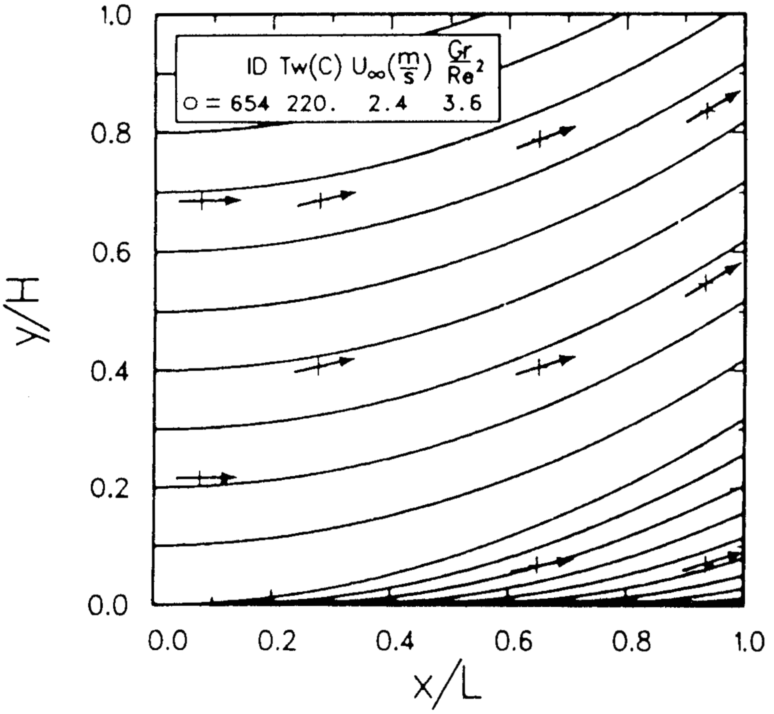

Fig. 4-35 Measured Flow Angles and Predicted Streamlines of the Constant-Angle Region for T_w=220 C, U_∞=2.4 m/s, and Gr_H/Re_L^2=3.6.

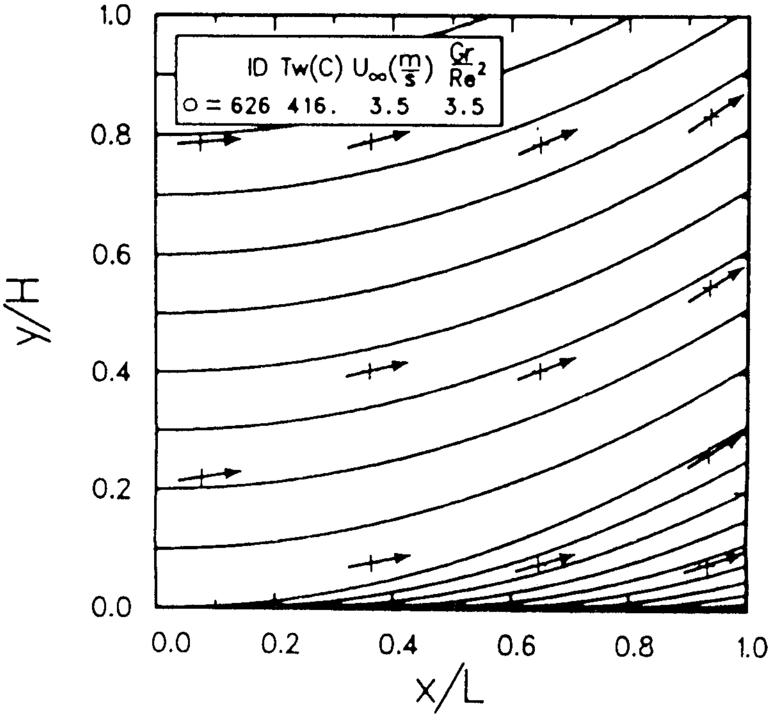

Fig. 4-36 Measured Flow Angles and Predicted Streamlines of the Constant-Angle Region for T_w=416 C, U_∞=3.5 m/s, and Gr_H/Re_L^2=3.5.

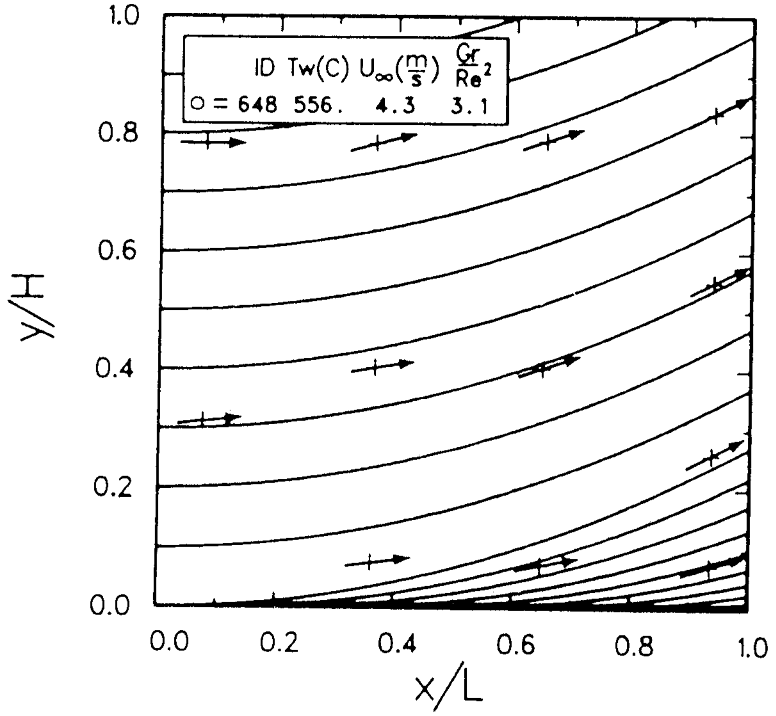

Fig. 4-37 Measured Flow Angles and Predicted Streamlines of the Constant-Angle Region for T_w=556 C, U_∞=4.3 m/s, and Gr_H/Re_L^2=3.1.

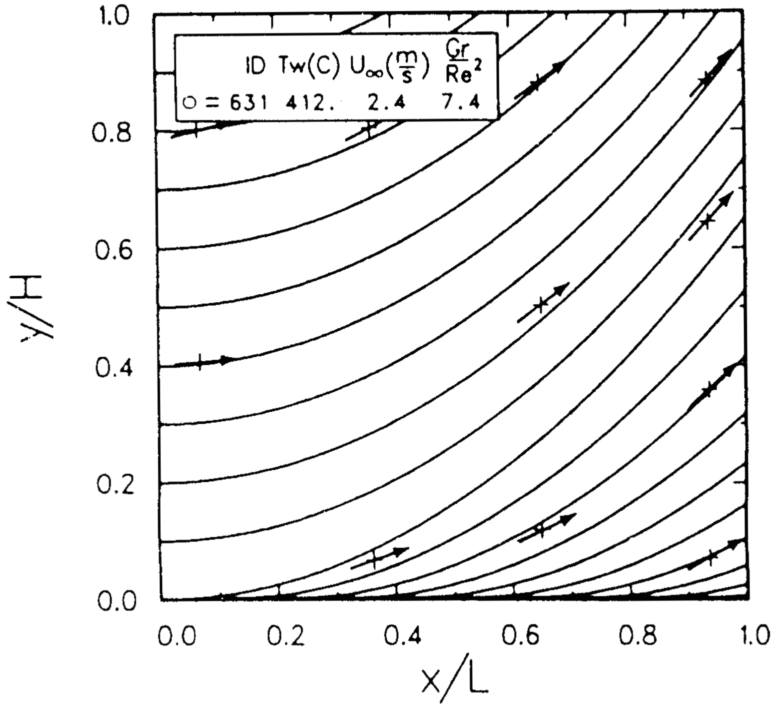

Fig. 4-38 Measured Flow Angles and Predicted Streamlines of the Constant-Angle Region for T_w=412 C, U_∞=2.4 m/s, and Gr_H/Re_L^2=7.4.

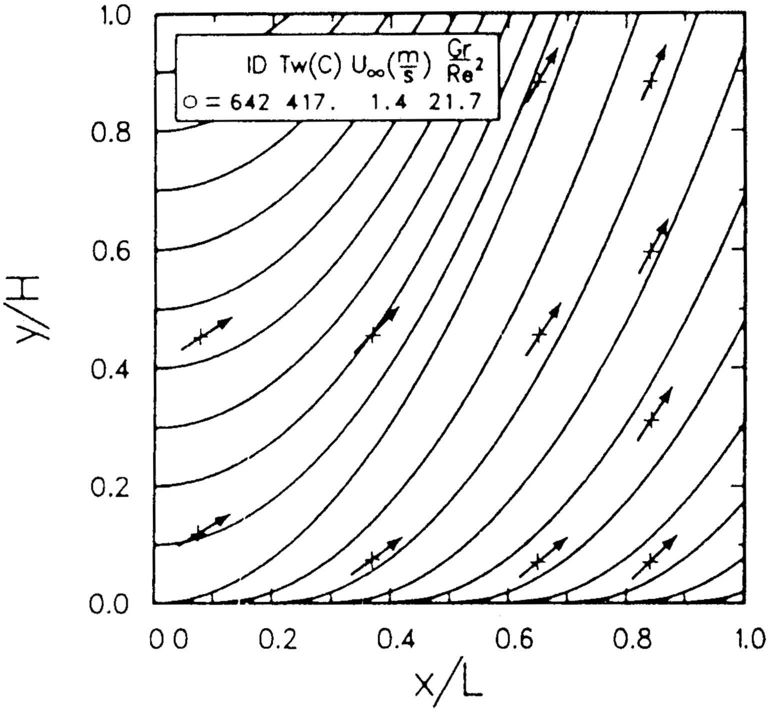

Fig. 4-39 Measured Flow Angles and Predicted Streamlines of the Constant-Angle Region for T_w=417 C, U_∞=1.4 m/s, and Gr_H/Re_L^2=21.7.

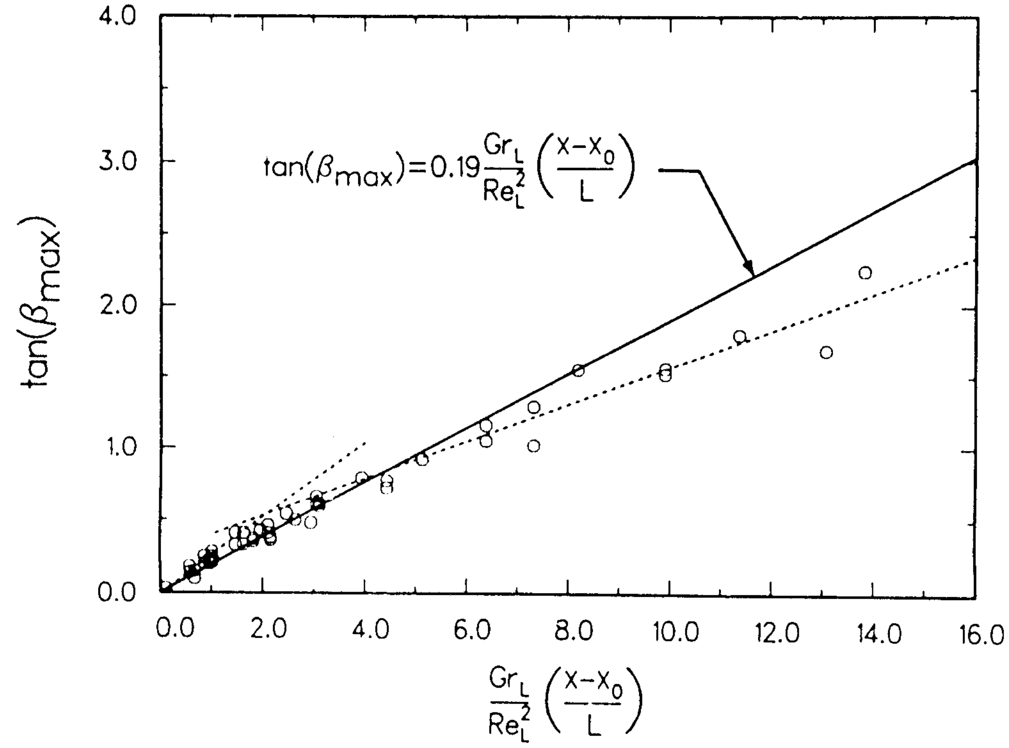

Fig. 4-40 Tangent of the Flow Angle in the Constant-Angle Region, $tan(\beta_{max})$, versus $(Gr_L/Re_L^2)(x - x_o)/L$ for Turbulent Flow.

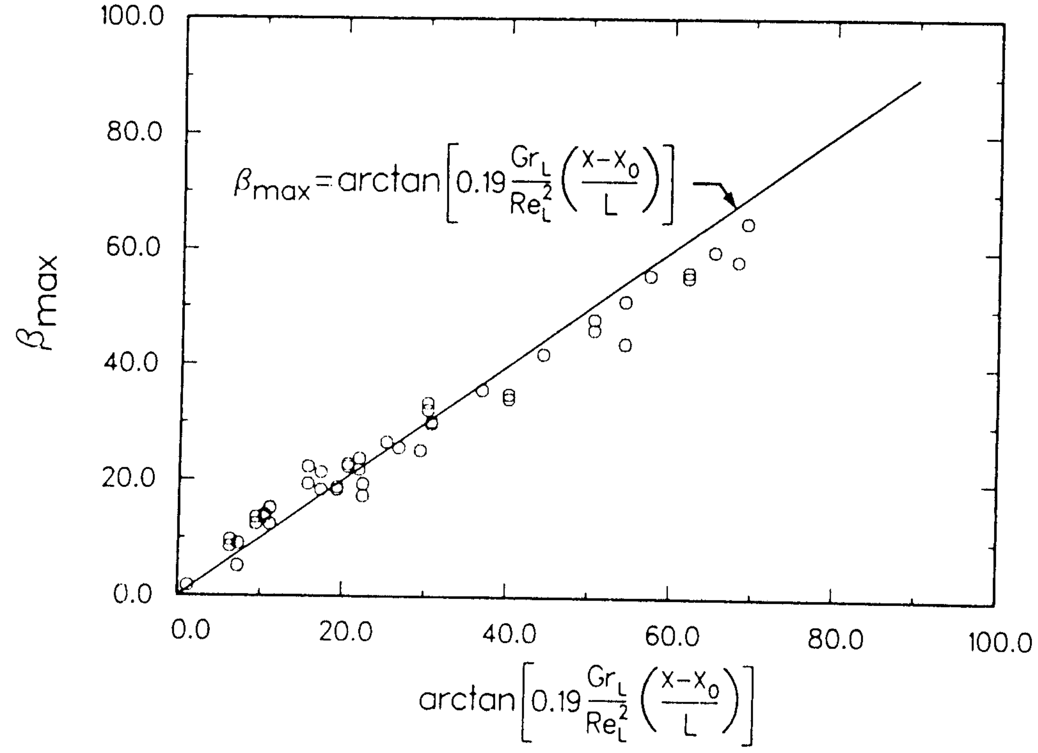

Fig. 4-41 Comparison of Measured Flow Angle of Constant-Angle Region to Flow Angles Predicted by Eqn. (4-24).

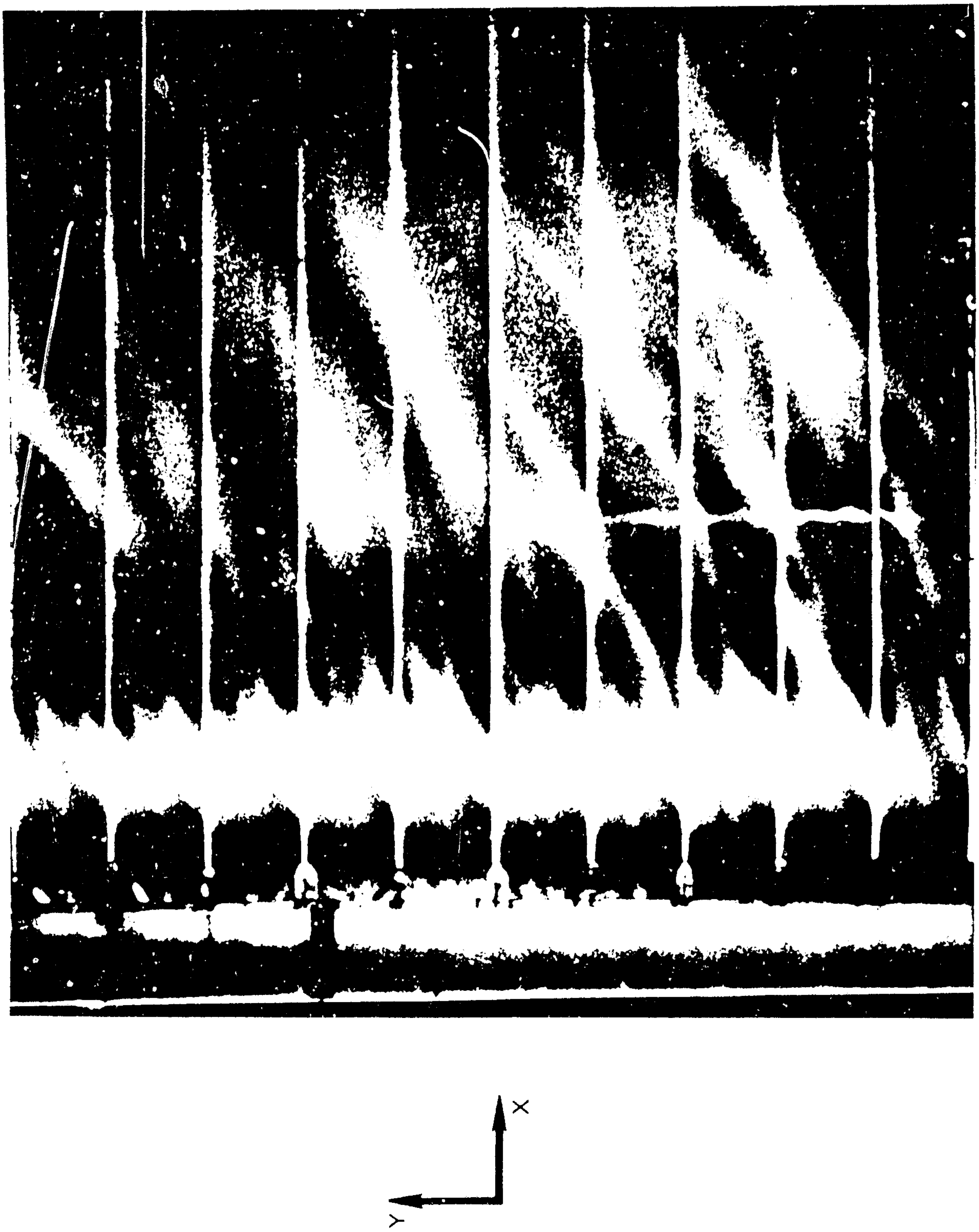

Fig. 4-42 Photograph of Lower Upstream Portion of the Test Surface, $T_w=534$ C, $U_\infty=1.5$ m/s, and $Gr_H/Re_L^2=25.9$ ($ID=589$).

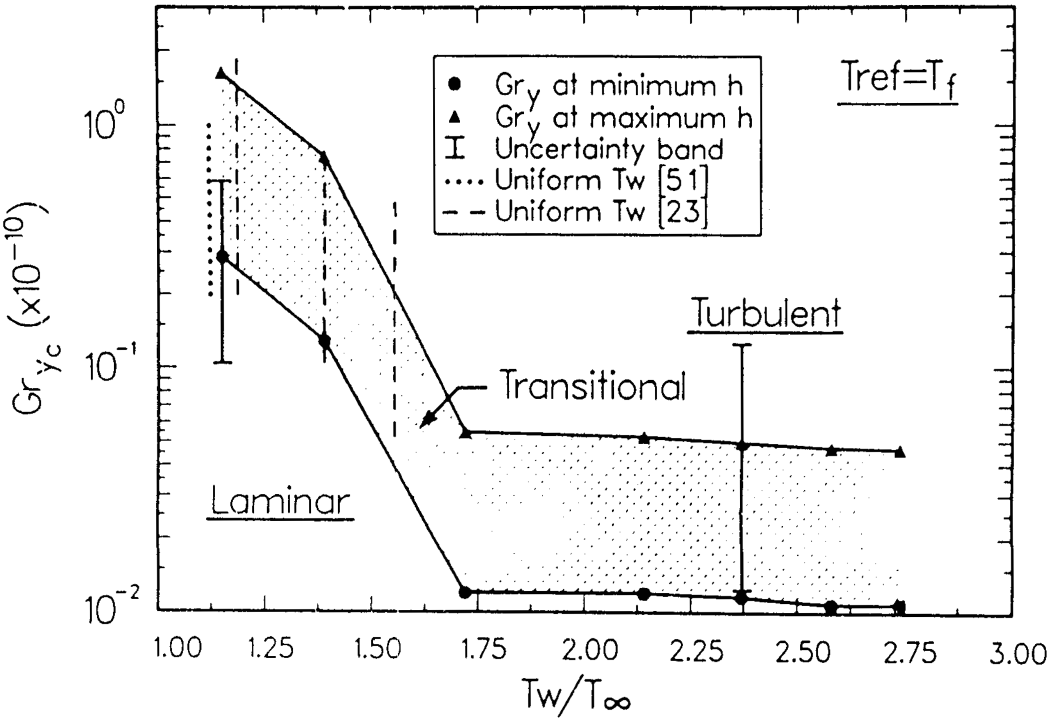

Fig. 4-43 The Effect of Wall Temperature on the Grashof Number at Transition in Free Convection from a Vertical Surface.

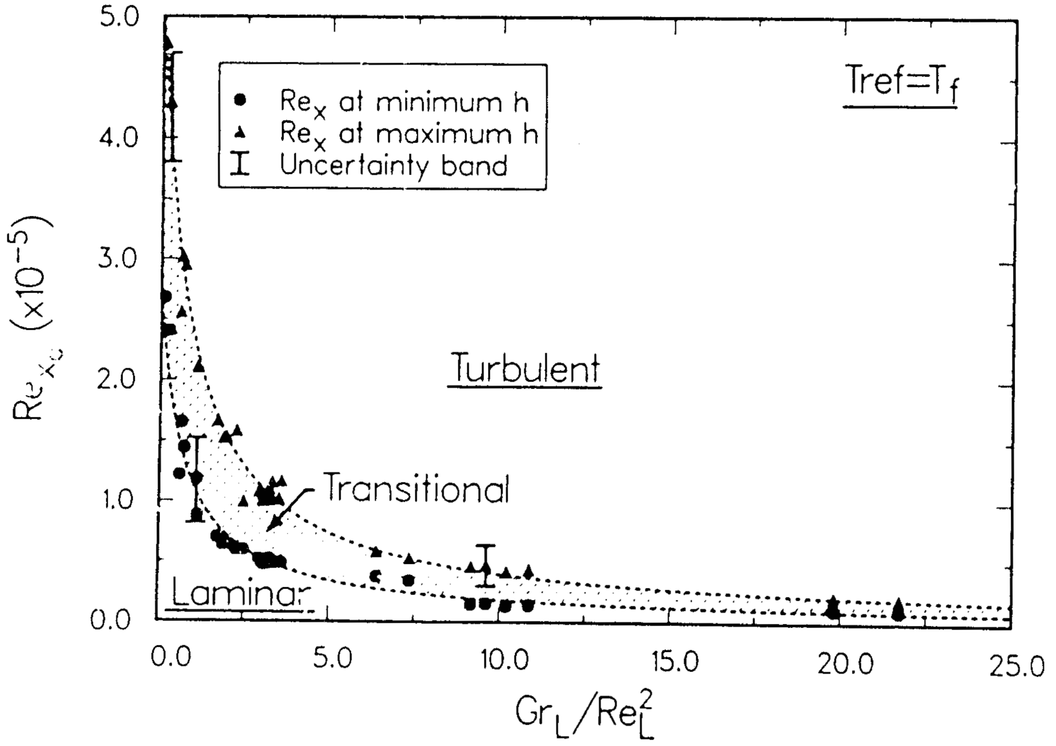

Fig. 4-44 The Effect of Buoyancy on the Reynolds Number at Transition in Mixed Convection from a Vertical Surface.

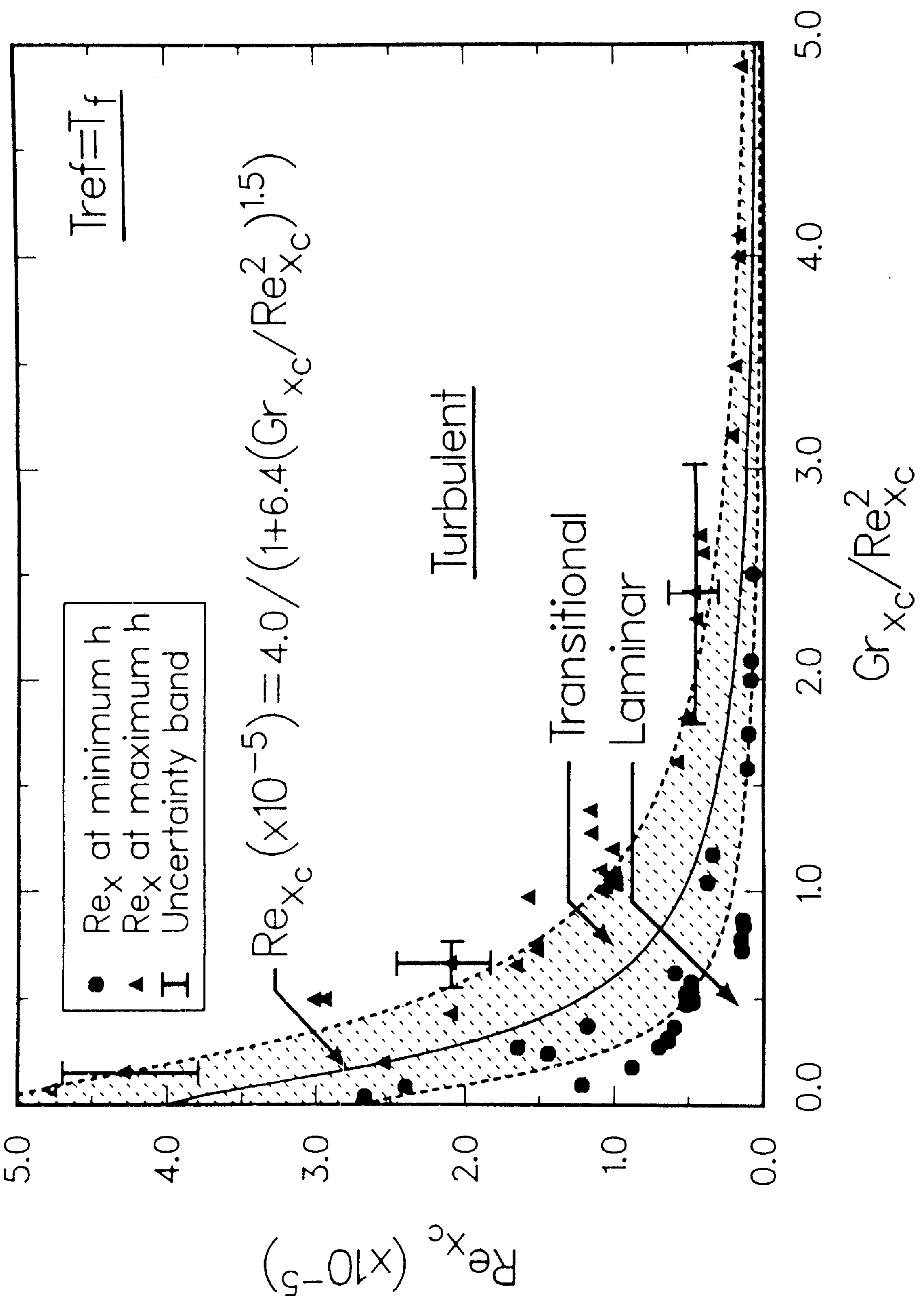

Fig. 4-45 The Transition Reynolds Number versus the Mixed Convection Parameter, $Gr_{x_c}/Re^2_{x_c}$.

Chapter 5.

CONCLUSIONS AND RECOMMENDATIONS

5.1 Conclusions

This work presents and interprets the results of an experimental study of the convection heat transfer from a large (2.95 m long by 3.02 m high), vertical, electrically heated, smooth surface in air. The convection heat transfer varied from forced, to mixed (combined forced and free convection), to free convection. Both the boundary layer structure (i.e., mean velocity, flow angle, and temperature) and the surface heat transfer were studied. The boundary layer flow on the vertical surface was driven by orthogonal forces, a vertical buoyant force resulting from density variations across the boundary layer and a horizontal inertia force resulting from a horizontal free-stream air flow. The boundary layer that developed was three-dimensional with flow angles (with respect to horizontal) varying from zero at the free-stream to as much as 90° inside the boundary layer. The maximum flow angle in the boundary layer depended on the ratio of the buoyant force to the inertia force and on the location on the test surface. The boundary layer flow was initially laminar at the leading edge but transitioned to turbulent flow downstream. Both the vertical buoyant force and the horizontal inertia force caused by the free-stream flow, affected the transition to turbulent flow and the convection heat transfer from the test surface.

The free-stream air velocity ranged from 0 to 6 m/s. The electric power dissipated ranged from 200 to 13,000 W/m^2, resulting in average wall temperatures in the 40 to 600 C range. Convection heat transfer coefficients were measured at 105 locations on the test surface. The boundary layer profiles of the mean velocity, temperature, and flow angle were measured at as many as 14 locations on the test surface for a given test condition.

The heat transfer results support the following conclusions for mixed convection heat transfer:

1. The region where the average heat transfer coefficient should be described as "mixed convection" lies approximately between Gr_H/Re_L^2 values of 0.7 and 10.0. For conditions outside this region, the average convective heat transfer can be determined within 5% by considering a single mechanism

for heat transfer, forced convection for $Gr_H/Re_L^2 < 0.7$ and free convection for $Gr_H/Re_L^2 > 10.0$.

2. The average convection heat transfer coefficient changed smoothly from forced convection, to mixed convection, to free convection as the ratio of the buoyant force to the inertia force increased.

3. The distribution of the convection heat transfer coefficient on the test surface was similar in form for test conditions which had the same overall ratio of buoyant force to inertia force, in spite of very different wall temperatures and free-stream velocities.

4. The distribution of the convection heat transfer coefficient in the turbulent flow regions resembled either pure forced convection (i.e., $h \sim x^{-0.2}$) or pure free convection (i.e., a spatially uniform h). The change from a forced-convection-like dependence on x to a free-convection-like uniform h occurred over a very short distance. (This does not imply, however, that the magnitude of the local heat transfer coefficient was the same as for either pure forced or pure free convection acting alone.)

5. When there was a free-stream flow, results show that forced convection dominated the heat transfer in the laminar boundary region at the vertical leading edge. The dominance of forced convection was the result of the "principle of independence" applying near the vertical leading edge: the flow at each elevation on the vertical leading edge had the same history (except for very near the lower, upstream corner), and therefore no gradients of velocity or temperature existed in the vertical direction. Since no gradients of temperature or velocity were present in the vertical direction, the energy equation shows that the heat transfer will be independent of the effects of buoyancy near the vertical leading edge.

6a. The average mixed convection heat transfer coefficient can be predicted by the following relationship:

$$\overline{h}_{mx} = (\overline{h}_{fc}^{\;3.2} + \overline{h}_{fr}^{\;3.2})^{1/3.2}$$

The average forced convection term $\overline{h}_{fc}$ and the average free convection term $\overline{h}_{fr}$ are estimates obtained by considering a single mechanism of heat transfer, either forced or free convection, acting alone. Any representative (and accurate) pure forced and pure free convection correlations can be used for this purpose. The above relationship generally predicts the measured average convection heat transfer coefficient to within $\pm 3\%$. This relationship applies for pure forced and pure free convection heat transfer also, since it approaches the results for pure free and pure forced convection in the limit.

6b. When estimates of local forced and free convection heat transfer coefficients are used, a similar expression predicts the local turbulent mixed convection heat transfer coefficients to within $\pm 10\%$. However, the distribution of the predicted local heat transfer coefficient will not be exactly the same as that measured in the turbulent region.

7a. The transition zone on the test surface was vertical for all test conditions; no horizontal transition zone was found except for pure free convection.

7b. Buoyancy significantly changed the Re_x at which transition took place, moving the transition zone to lower Re_x (i.e., earlier on the test surface).

The heat transfer results showed the following effects of variable properties on heat transfer:

1. When all properties were evaluated at the free-stream temperature, the effects of variable properties on pure free convection heat transfer from a vertical surface were correlated by

$$\begin{aligned} \textit{Laminar flow}: \quad Nu_y &= aGr_y^{1/4}\left(\frac{T_w}{T_\infty}\right)^{-0.04} \\ \textit{Turbulent flow}: \quad Nu_y &= 0.098Gr_y^{1/3}\left(\frac{T_w}{T_\infty}\right)^{-0.14} \end{aligned}$$

   The constant a in the laminar flow equation is 0.404 for a uniform heat flux surface and 0.356 for a uniform temperature surface. The correlations apply for air with T_w in the 40 to 600 C temperature range.

2. The effects of variable properties on pure forced convection agreed with the effects reported in Kays and Crawford [24] for a boundary layer flow in a gas.

3. The transition results (forced, mixed, and free) correlated best when properties were evaluated at the film temperature.

4. The value for Gr_y at which transition from laminar to turbulent flow occurred in pure free convection decreased as T_w/T_∞ increased.

The results from the three-dimensional mixed convective boundary layer flow measurements showed the following important points about the mixed convection boundary layer:

1. From the wall out to the location where u/U_∞=0.71, the three-dimensional mixed convection boundary layer had a constant flow angle (i.e., collateral flow). This encompassed the inner 5-7% of the boundary layer thickness and was observed for all test conditions in the turbulent flow regions.

2. The tangent of the flow angle of the constant-angle region near the wall was related to the overall test conditions and to the location on the surface by a simple relationship:

$$tan(\beta_{max}) = C\frac{Gr_L}{Re_L^2}\left(\frac{x - x_o}{L}\right)$$

3. The maximum vertical velocity component occurs at v/V_g and u/U_∞ approximately equal to 0.71, the outer boundary of the collateral flow region.

4. There was evidence that some of the vertical momentum which was added to the turbulent flow by the vertical buoyant force was transferred to the horizontal direction, possibly by turbulence.

5. The tangent of the local flow angle in the outer region of the turbulent mixed convection boundary layer varied linearly with the local dimensionless temperature.

6. The velocity profiles and the temperature profiles changed smoothly from forced-convection-like profiles to free-convection-like profiles as the local ratio of the buoyant force to the inertia force increased.

7. The laminar three-dimensional mixed convection boundary layer showed no constant-angle region similar to the turbulent boundary layer.

5.2 Recommendations

The following are recommendations for future work in the area of mixed convection.

1. Apply flow visualization techniques to the mixed convective boundary layer flow to learn more about the structure of the mixed convective boundary layer, in particular the structure of the constant-angle region.
2. Add a pressure gradient in the free-stream flow direction to assess the effects of a pressure gradient on the mixed convection heat transfer from a vertical, flat surface. Pressure gradients occur on a cylindrical-type external receiver.
3. Add free-stream turbulence to assess its effects on mixed convection heat transfer. In a real solar central receiver environment, the free-stream air flow will be turbulent.
4. Study quantitatively the turbulence structure of the boundary layer to assist the modeling of turbulence for mixed convection flows. This research could be done at lower temperatures, since the experiment showed similarity in heat transfer and boundary layer flow over the entire operating domain.

REFERENCES

1. Siebers, D., "Natural Convection Heat Transfer From an External Receiver", SAND78-8276, Sandia National Laboratories, Livermore, CA (1978).
2. Jaluria, Y., Natural Convection Heat and Mass Transfer, Vol. 5, Pergamon Press, New York, 138-159 (1980).
3. Evans, G., "A Numerical Study of Three-Dimensional, Laminar, Mixed Convection", Ph.D. Thesis, College of Engineering, Washington State Univ. (1981).
4. Young, R. J., and Yang, K., "Effect of Small Cross Flow and Surface-Temperature Variation on Laminar Free Convection Along a Vertical Plate", *Journal of Applied Mechanics* 85E, 252-256 (1963).
5. Eichhorn, R. and Hasan, M. M., "Mixed Convection about a Vertical Surface in a Cross-Flow: a Similarity Solution", *Journal of Heat Transfer* 102, 775-777 (1980).
6. Plumb, O. A., "The Effect of Crossflow on Natural Convection from Vertical Heated Surfaces", ASME paper no. 80-HT-71.
7. Oosthuizen, P. H., and Leung, R. K., "Combined Convective Heat Transfer from Vertical Cylinders in a Horizontal Flow", ASME paper no. 78-WA/HT-45.
8. Oosthuizen, P. H., and Taralis, D. N., "Combined Convective Heat Transfer from Vertical Cylinders in a Horizontal Fluid Flow", ASME paper no. 76-HT-41.
9. Oosthuizen, P. H., "Numerical Study of Combined Convective Heat Transfer from a Vertical Cylinder in a Horizontal Flow", *Proceedings of the 6th International Heat Transfer Conference*, Toronto, Canada, MC-4, 19-24 (1978).
10. Yao, L. S., and Chen, F. M., "Analysis of Convective Heat Loss from the Receiver of Solar Power Plants", ASME paper no. 79-WA/HT-36.
11. Yao, L. S., Catton, I., and McDonough, J. M., "Free-Forced Convection from a Heated Longitudinal Horizontal Cylinder", *Numerical Heat Transfer* 1, 255-266 (1978).
12. Yao, L. S. and Catton, I., "Buoyancy Cross-Flow Effects on the Boundary Layer of a Heated Horizontal Cylinder", *Journal of Heat Transfer* 99, 122-124 (1977).
13. McAdams, W. H., Heat Transmission, 3rd ed, McGraw-Hill, New York, 258 (1954).
14. van der Hegge Zijnen, B. G., "Modified Correlation Formulae for the Heat Transfers by Natural and by Forced Convection from Horizontal Cylinders", *Applied Sci. Res., Sect. A* 6, 129-140 (1956).

15. Hatton, A. P., James, D. D., and Swire, H. W., "Combined Forced and Natural Convection with Low-Speed Air Flow over Horizontal Cylinders", *Journal of Fluid Mechanics* 42, 17-31 (1970).

16. Morgan, V. T., "The Overall Convective Heat Transfer from Smooth Circular Cylinders", Advances in Heat Transfer 11, 199-264 (1975).

17. Churchill, S. W., and Usagi, R., "A General Expression for the Correlation for Rates of Transfer and Other Phenomena", *AIChE* 18, no. 6, 1121-1128 (1972).

18. Sparrow, E. M., Discussion - Author's closure, *Journal of Heat Transfer* 103, 824-825 (1981).

19. Carey, V. P., and Mollendorf, J. C., "Variable Viscosity Effects in Several Natural Convection Flows", *IJHT* 23, 95-108 (1980).

20. Shaukatullah, H., and Gebhart, B., "The Effect of Variable Properties on Laminar Natural Convection Boundary-Layer Flow Over a Vertical Isothermal Surface in Water", *Numerical Heat Transfer* 2, 215-232 (1979).

21. Hara, T., "Heat Transfer by Laminar Free Convection About a Vertical Flat Plate with Large Temperature Difference", *Bull. JSME* 1, No. 3, 251-254 (1958).

22. Sparrow, E. M., and Gregg, J. L., "The Variable Fluid-Property Problem in Free Convection", *Trans. Am. Soc. Mech. Engrs.* 80, 879-886 (1958).

23. Pirovano, A., Viannay, S., and Jannot, M., "Convection Naturelle En Regime Turbulent Le Long D'Une Plaque Plane Verticale", *Proceeding of the 4th International Heat Transfer Conference*, Paris-Versailles, France, NC-1.8, 1-12 (1970).

24. Kays, W. M., and Crawford, M. E., Convective Heat and Mass Transfer, 2nd ed, McGraw-Hill Book Co. (1980).

25. Kraabel, J. S., "The Effect of Variable Fluid Properties on Scale Modeling", *ASME HTD* 13, 103-110 (1980)

26. Clausing, A. M. and Kempka, S. N., "The Influences of Property Variations on Natural Convection from Vertical Surfaces", *Journal of Heat Transfer* 103, 609-612 (1981).

27. Siebers, D. L., Schwind, R. G., and Moffat, R. J., "Mixed Convection Heat Transfer and Flow Measurements on a Large, Vertical, Hot Plate", SAND80-8184, Sandia National Laboratories, Livermore, CA (1980).

28. Eckert, W. J., Mort, K. W., and Piazza, J. E., "An Experimental Investigation of End Treatments for Non-Return Wind Tunnels", NASA TMX-3402, June, 1976.

29. Hornung, H. G. and Joubert, P. N., "The Mean Velocity Profile in Three-Dimensional Turbulent Boundary Layers", *Journal of Fluid Mechanics* 15, Part 3, 368-384 (1963).

30. Folsom, R. G., "Review of the Pitot Tube", *Trans. of ASME* 78, 1447-1460 (1956).

31. Thermocouple Reference Tables Based on the IPTS-68, NBS Monograph 125, Sect. A7, 351-384 (1974).

32. Eckert, R. G. and Goldstein, R. J., Measurements in Heat Transfer, 2nd ed., McGraw-Hill, New York, 18-22 (1976).

33. Haskell, K. H. and Vandevender, W. H., "Brief Instructuions for Using the Sandia Mathematical Subroutine Library", SAND79-2382, p. 4-4 (1979).

34. "Subroutine-IQHSCU", IMSL Reference Manual 2(1980).

35. Kiine, S. J. and McClintock, F. A., "Describing Uncertainties in Single Sample Experiments", *Mechanical Engineering* 75, 3-8 (1953).

36. Kays, W. M., Moffat, R. J., and Thielbahr, W. H., "Heat Transfer to the Highly Accelerated Turbulent Boundary Layer With and Without Mass Addition", *Journal of Heat Transfer* 92, 499-505 (1970).

37. Orlando, A. F., Moffat, R. J., and Kays, W. M., "Turbulent Transport of Heat and Momentum in a Boundary Layer Subject to Deceleration Suction and Variable Wall Temperature", HMT-17, Thermosciences Division, Mechanical Engrg. Dept., Stanford University (1974).

38. Blackwell, B. F., Kays, W. M., and Moffat, R. J., "The Turbulent Boundary Layer on a Porous Plate: An Experimental Study of the Heat Transfer Behavior with Adverse Pressure Gradients", HMT-16, Thermosciences Division, Mech. Engrg. Dept., Stanford University (1972).

39. Churchill, S. W. and Chu, H. H., "Correlating Equations for Laminar and Turbulent Free Convection From a Vertical Plate", *IJHT* 18, 1323-1329 (1975).

40. Gebhart, B., Heat Transfer, 2nd Ed, McGraw-Hill (1975).

41. Crawford, M. E. and Kays, W. M., "STAN5-A Program for Numerical Computation of Two-Dimensional Internal and External Boundary Layer Flows", NASA CR-2742 (1976).

42. Kraabel, J., McKillop, A. A., and Baughn, J. W., "Heat Transfer to Air from a Yawed Cylinder", *IJHT* 25, 409-418 (1982).

43. White, F., Viscous Fluid Flow, McGraw-Hill (1974).

44. Ashkenas, H. and Riddell, F. R., "Investigation of the Turbulent Boundary Layer on a Yawed Flat Plate", NACA TN 3383 (1955).

45. East, L. F. and Hoxey, R. P., "Low Speed Three-Dimensional Turbulent Boundary Layer Data", *Royal Aircraft Establishment*, No. 3653, Parts 1 and 2 (1969).

46. Johnston, J. P., "Measurements in a Three-Dimensional Turbulent Boundary Layer Induced by a Swept Forward-Facing Step", *JFM* 42, part 4, 823-844 (1970).

47. Zimmerman, D. R., "An Experimental Investigation of a Three-Dimensional Turbulent Boundary Layer", Ph.D. Thesis, Purdue University (1975).

48. van den Berg, B. and Elsenaar, A., "Measurements in a Three-Dimensional Incompressible Turbulent Boundary Layer in an Adverse Pressure Gradient Under Infinite Swept Wing Conditions", National Aerospace Laboratory, Amsterdam, TR72092U (1972).

49. Hebbar, K. S. and Melnik, W. L., "Measurements in the Near-Wall Region of a Relaxing Three-Dimensional Low Speed Turbulent Air Boundary Layer", Office of Naval Research, Technical Report No. AE-76-1 (1976).

50. Hoogendoorn, C. J. and Euser, H., "Velocity Profiles in the Turbulent Free Convection Boundary Layer", *Proceedings of the 6th Int. National Heat Transfer Conference*, Toronto, Canada, NC-2, 193-197 (1978).

51. Cheesewright, R., "Turbulent Natural Convection From a Vertical Plane Surface", *Journal of Heat Transfer* 90, 1-8 (1968).

Appendix A
PROPERTY RELATIONSHIPS

The following property relationships were used in the data reduction. (T is in degrees C in all the following relationships)

Air

$$k(W/mC) = 2.5 \times 10^{-3}\frac{(T+273.15)^{1.5}}{(T+467.594)} \qquad \text{Ref. A.1} \qquad \text{(A-1)}$$

$$\mu(kg/ms) = 1.458 \times 10^{-6}\frac{(T+273.15)^{1.5}}{(T+383.55)} \qquad \text{Ref. A.1} \qquad \text{(A-2)}$$

$$c_p(J/kgC) = 1004.0 + 0.1120(T-26.85) + 1.099 \times 10^{-4}(T-26.85)^2 \qquad \text{Curve fit of data in Ref. A.2} \qquad \text{(A-3)}$$

$$\rho(kg/m^3) = \frac{P}{R(T+273.15)} \qquad \text{Ideal gas} \qquad \text{(A-4)}$$

$$i(J/kg) = \text{Data table interpolation } (i \text{ vs } T) \qquad \text{Ref. A.2} \qquad \text{(A-5)}$$

Fiberfrax Insulation

$$\left.\begin{aligned}
&\text{Duraboard}\\
&k(W/mC) = 0.0525 + 9.669 \times 10^{-5}T + 6.502 \times 10^{-8}T^2 && \text{(A-6)}\\
&\text{Paper}\\
&k(W/mC) = 0.05118 - 1.3308 \times 10^{-5}T + 1.3267 \times 10^{-7}T^2 && \text{(A-7)}\\
&\text{Moldable}\\
&k(W/mC) = 0.0253 + 3.026 \times 10^{-4}T - 9.339 \times 10^{-8}T^2 && \text{(A-8)}\\
&c_p(J/kgC) = 1130.0\\
&\rho(kg/m^3) = 280.35
\end{aligned}\right\} \quad \text{Curve fit of data in Ref. A.3}$$

Stainless Steel

$$r(ohm\ m) = 71.4 \times 10^{-8} + 0.0830 \times 10^{-8}T - 21.53 \times 10^{-14}T^2 \qquad \text{Curve fit of data in Appendix C} \qquad \text{(A-9)}$$

$$\epsilon = 0.751\sqrt{100.0r(T+273.15)} - 0.396r(T+273.15) + 0.02 \qquad \text{See Appendix B} \qquad \text{(A-10)}$$

$$\alpha\left(\frac{m}{m}\right) = 1.866 \times 10^{-5}(T-20) \qquad \text{Curve fit of data in Ref. A.4} \qquad \text{(A-11)}$$

References

A.1. White, T. M., Viscous Fluid Flow, McGraw Hill, New York, 28-33 (1974).

A.2. Eckert, E. G. R. and Drake, R.M., Analysis of Heat and Mass Transfer, McGraw Hill, New York (1972).

A.3. Fiberfrax Product Sheets, Carboraundum Corporation, Forms C740-A, C737-A, C739-D (1980).

A.4. Thermophysical Properties of High Temperature Solid Materials, (Touloukian, Y. S., et al.) MacMillan Company, New York, 3, 211 (1967).

Appendix B

EMITTANCE MEASUREMENTS FOR WIND TUNNEL SURFACES

Radiation heat transfer accounted for 4 to 50% of the heat transfer from the test surface depending on the test conditions. This meant accurate knowledge of various surface emittances in the wind tunnel was important. Based on an uncertainty analysis, the most important emittance was the emittance of the stainless steel test surface. The emittance of samples of the stainless steel was determined as a function of the temperature of the stainless steel and oxidation level on the stainless steel that developed during testing. The other tunnel wall emittances were of secondary importance, since the tunnel wall was water-cooled to ambient temperature. The emittances of the other tunnel wall surfaces were measured at room temperature only.

Samples of 304 stainless steel shimstock in various states, virgin, mildly oxidized, and the most oxidized condition that occurred, were sent to the TRW Thermophysics Laboratory to have the surface emittance measured. The TRW Paraboloid Reflectometer [B.1] was used to measure spectral reflectance in the infrared region from 2.0 to 25.0 microns. The Paraboloid Reflectometer is based on the "reciprocal" method of reflectance measurement; i.e., the specimen is hemispherically irradiated with infrared energy, and that portion of the energy which is reflected at a near-normal angle ($\simeq 9^\circ$ from specimen normal) is analyzed by the spectrophotometer portion of the instrument. The instrument is calibrated at each wavelength band using a gold-plated reference specimen of known reflectance.

The spectral reflectance of the specimens were initially measured at room temperature, then at steady state temperatures of 550 K and 850 K. A small resistance heater was used to heat the samples.

The infrared reflectance data was integrated over the appropriate Planckian black body emission spectra to yield an "average" reflectance value. This reflectance value when subtracted from unity yields the normal emittance of the specimen. Hemispherical emittance was calculated from normal emittance values using the theoretically and empirically derived correlation between hemispherical and normal emissivity shown in Ref. B.2.

Room temperature measurements of the test surface samples were also made by TRW with a Gier Dunkle DB100 Infrared Reflectometer [B.3]. These same measurements along with measurements of the emissivity of the other tunnel wall materials were made with a second Gier Dunkle DB100 Infrared Reflectometer in the tunnel. The DB100's measured normal, total emittances. The total, hemispherical emittances were determined from the total, normal emittances as described in the previous paragraph.

The detailed normal, spectral reflectance measurements of the stainless steel samples are presented in Ref. B.4 as received from TRW [B.5]. The results for the virgin samples are very similar to the results for polished 303 stainless steel samples presented in Refs. B.6 and B.7. Table B-1 is a summary of the total, hemispherical emittances of the stainless steel samples and the tunnel wall surfaces. The values are accurate to ±0.01 emittance units. The average tunnel wall total, hemispherical emittance determined by averaging the wood wall, aluminum floor, and steel test section values is 0.8 ±0.1. This is the value used for the background emissivity in the radiation correction in the calculation of convection heat transfer.

For the stainless steel measurements, the initial measurement at room temperature of Sample 1 of the virgin material may contain a significant undetermined experimental error, or the specimen may have acted atypically on the initial measurement. At least this seems probable, since the specimen's room temperature emittance was out of line with all other measured emittance values and also those reported in Refs. B.6 and B.7. This possible explanation was reinforced by the second room temperature measurement of the virgin material. It was in line with other values, as shown in Table B-1.

The stainless steel total, hemispherical emissivity measurements are plotted versus temperature in Fig. B-1. They are compared to the theoretical emissivity-temperature relationship, the dashed line, for pure metals given in Ref. B.8. The figure shows that the mildly oxidized and the virgin samples of material have the same emittance within the uncertainty of the data and these emittances are about 0.02 emittance units above the pure metal curve given by the dashed line. The most heavily oxidized sample has a significantly higher emissivity at higher temperatures.

The heaviest oxidation occurred on the last few nights of testing mainly in the boundary layer zone just before the transition zone, where the heavily oxidized sample was taken from. During the last few nights, the test surface was maintained at the peak average temperature level of 560 *C* for at least 30 hours of testing. The region just before transition approached 630 *C*. These high temperatures for long periods of time caused the heaviest oxidation of the test surface. The oxidation was uniform in that hot zone and speckled, but uniformly distributed, over the rest of the surface.

The values used for surface emissivity in the data reduction were calculated from the pure metal theory with the addition of 0.02 units of emittance or:

$$\epsilon = 0.751\sqrt{100.0r(T+273.15)} - 0.396r(T+273.15) + 0.02 \qquad \text{(B-1)}$$

This was used for all tests except for the test conducted on the last night. For this test at 560 C (ID 648), an average of the most heavily oxidized and mildly oxidized emittances was used since about 50% of the surface was in each state. The value used for the total, hemispherical emittance was 0.25 for that one case.

References

B.1. Newman, B. E., "High Temperature Reflectance Measurements with Paraboloid Reflectometer", *J. Spacecraft Rockets* 6, 72-74 (1968).

B.2. Eckert, E. R. G., and Drake, R. M., Jr., Heat and Mass Transfer, 2nd ed, McGraw-Hill Book Company, New York (1972).

B.3. Pettit, R. B., "Optical Measurement Techniques Applied to Solar Selective Coatings", SAND-77-0421, Sandia National Laboratories, Livermore, CA (1977).

B.4. Siebers, D. L., Schwind, R. G., and Moffat, R. J., "Mixed Convection Heat Transfer and Flow Measurements on a Large, Vertical, Hot Plate", SAND80-8184, Sandia National Laboratories, Livermore, CA (1980).

B.5. Gilmore, M. R., "Emittance of Three Stainless Steel (304) Specimens from Sandia National Laboratories", TRW Report No. L015.16g-82-05 (1980).

B.6. Edwards, D. K., and Catton, I., "Radiation Characteristics of Rough and Oxidized Metals", Advances in Thermophysical Properties at Extreme Temperatures and Pressures (Serge Gratch, ed.), ASME, 189-199 (1965).

B.7. Edwards, D. K., and deVolo, N. B., "Useful Approximations for Spectral and Total Emissivity of Smooth Bare Metals", Advances in Thermophysical Properties at Extreme Temperatures and Pressures (Serge Gratch, ed.), ASME, 174-188 (1965).

B.8. Siegel, R., and Howell, J. R., Thermal Radiation Heat Transfer, McGraw-Hill, New York, 116 (1972).

TABLE B-1. Normal, Total and Hemispherical, Total Emissivities of the Various Wind Tunnel Surfaces

Description of Material:	$T(K)$	Paraboloid Reflectometer		Gier Dunkle DB100			
		TRW ϵ_n	TRW ϵ_h	TRW ϵ_n	Sandia ϵ_n	TRW ϵ_h	Sandia ϵ_h
SS304 (Highest oxidation)	300	0.12	0.14	0.09	0.10	0.11	0.12
	590	0.18	0.21	—	—	—	—
	850	0.27	0.29	—	—	—	—
SS304 (Mild oxidation)	300	0.11	0.13	0.08	0.09	0.10	0.11
	590	0.14	0.17	—	—	—	—
	850	0.18	0.21	—	—	—	—
SS304 (Re-run of mildly oxidized sample after high temperature run)	300	0.11	0.13	—	—	—	—
SS304 (Sample 1 of virgin material)	300	0.15	0.18	0.08	0.09	0.10	0.11
	590	0.15	0.18	—	—	—	—
	850	0.19	0.22	—	—	—	—
SS304 (Sample 2 of virgin material)	300	0.10	0.12	—	—	—	—
Painted Aluminum Floor	Ambient	—	—	—	0.86	—	0.81
Steel Test Section Walls (Oxidized and Rough)	Ambient	—	—	—	0.73	—	0.72
Wood Tunnel Walls	Ambient	—	—	—	0.90	—	0.86

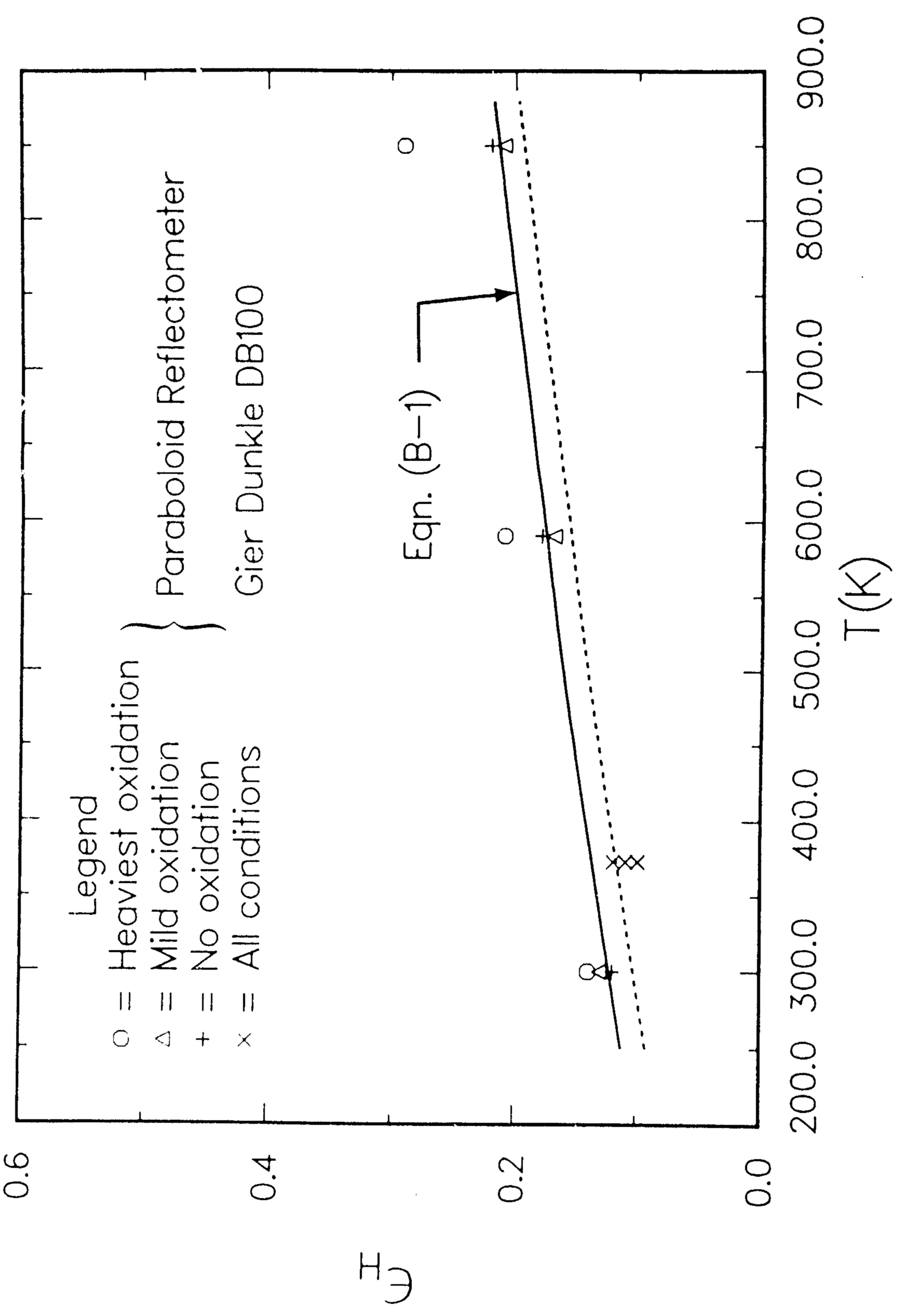

Fig. B-1 Total, Hemispherical Emittance of the Stainless Steel 304 Heating Strips versus Temperature.

Appendix C
SURFACE HEAT FLUX MEASUREMENT DETAILS

A primary measurement needed to determine the local heat transfer coefficient at a given point was the electric power dissipated per unit area by the stainless steel at that point. The electric power dissipated per unit area at a given point was affected by several factors: voltage, current, surface area, temperature, and non-uniformities in the stainless steel thickness. Of the last two factors, surface thickness variations were found not to be a problem. Thickness variations were measured to be less than $\pm 1\%$. The thickness variations were not random either. One side of the strips, across the width of the strip, was about 2% thinner than the other side. The nominal thickness of the heating strips was 0.127 mm. The temperature did, however, affect the local power release by causing variations in the resistivity along a heating strip as the temperature along a strip varied and by causing thermal expansion of the heating strips.

Since surface thickness variations are not important the electric power dissipated per unit area is given by:

$$q_{cle}(x,y) = \frac{EI}{A} A_c R_c \qquad \text{(C-1)}$$

The terms E and I are the measured RMS voltage drop and current for a given strip. The term A is the surface area between voltage leads on a strip when cold, including the folded under edges. The term A_c is a temperature related correction to the surface area, which accounts for thermal expansion of the strip when heated. The term R_c accounts for the variation in the electric power dissipated along a strip due to temperature variation (i.e., resistivity variation). It corrects the average power dissipated from a strip, EIA_c/A, giving the local power dissipated at a given point on a strip.

The area term A is simply the width times the length of the heating strip between the voltage measuring leads ($\approx 3.0m$). The term A_c is given by

$$A_c = \left[1 + a(\overline{T} - T_{cold})\right]^{-2} \qquad \text{(C-2)}$$

The temperature $\overline{T}$ in Eqn. (C-2) is the average strip temperature, and the temperature T_{cold} is a reference temperature for the thermal expansion data, 20 C.

The term a is equal to 1.866×10^{-5}. The values of a and T_{cold} are taken from Appendix A, Eqn. (A-11).

The resistance correction term is given by:

$$R_c = 1 + r'^{-1}[b(T - T') + c(T^2 - T'^2)] \tag{C-3}$$

The temperature T' is the temperature which gives the average strip resistivity. The term r' is the average strip resistivity for a given strip determined from the strip voltage, current, average temperature, and area measurements. The temperature T is the local temperature at the point where, $q_{ele}(x, y)$ is being calculated. Equation (C-3) is derived from a Taylor series expansion of Eqn. (A-9) about the average strip resistivity, r'. The term R_c is defined so that the average value of R_c for a strip is 1.0. The values of b and c are 0.0830×10^{-8} and -21.53×10^{-14}, respectively (from Eqn. (A-9)).

The corrections A_c and R_c range up to 1% and 3% of the average electric power dissipated on a strip, respectively, at the peak surface temperature of 580 C.

Besides the thickness measurements, the uniformity of power dissipated by a 30 cm long by 14.42 cm wide sample of stainless steel 304 was measured at low temperature. At low temperature thermal expansion and resistivity variations due to temperature variations were small and only thickness variations were important. The sample of the heating strip material was sandwiched between two postage stamp size heat flux gauges. The heat flux gauges could be moved around the sample to measure the uniformity of energy released by the sample. The standard deviation of the measured length-wise and width-wise variation in heat release were 0.5% and 0.9%, respectively, with no detectable trends in either direction.

As a check on the strip voltage and current measurements, the resistivity of the stainless steel was determined from the strip dimensions and strip voltage and current measurements made during various heat transfer tests. The resistivity as a function of temperature based on these calculations is plotted in Fig. C-1. Also shown are measurements for stainless steel 303 and 304 from Ref. C.1 and resistivity measurements made by this author on a 30 cm long by 0.3 cm wide sample of the stainless steel heating strip material placed in an oven. The resistivity for the 30 cm by 0.3 cm sample was determined from a direct measurement of resistance as a function of temperature. The agreement between the resistivity measurements for the small sample of stainless steel 304 and those determined from the strips during the heat transfer tests is within 1%. Both measurements are about 1-2% above the resistivity for stainless steel 304 reported in the literature, but below those for stainless steel 303 [C.1]. The figure gives an independent check on, and verification of, the voltage and current measurements made on each heating strip.

References

C.1. Thermophysical Properties of High Temperature Solid Materials, (Touloukian, Y. S., et al.) MacMillan Company, New York, 3, 151 (1967).

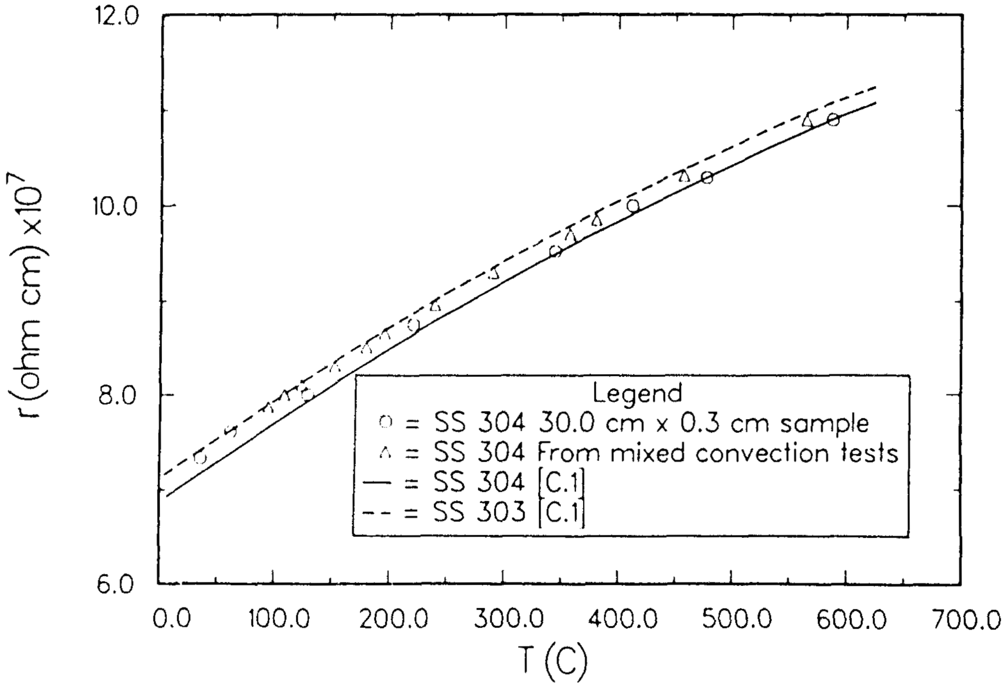

Fig. C-1 Resistivity of the Stainless Steel 304 Heating Strips versus Temperature.

Appendix D

LOWER LEADING EDGE OF THE TEST SURFACE

The lower leading edge of the test surface was described in Section 2.2 and is visible in Figs. 2-3 and 2-5. It consists of 6 *cm* of unheated insulation which forms a smooth extension of the heated surface. At the bottom edge of the insulation is step. The step height is equal to the amount the test surface protrudes into the test section, about 3 *cm*. Extending out of the unheated 6 *cm* of insulation are four support struts for the traverse.

The exact nature of the boundary layer starting condition on the lower leading edge could not be interpreted from the results of the experiment. It is complicated by the presence of the struts and the smooth unheated extension of the test surface. To alleviate problems with regard to starting conditions for numerical modeling of this mixed convection problem being conducted at Stanford University, boundary layer profiles were taken along the lower edge to supply starting conditions.

The extent of any possible strut effects and other effects of the lower leading edge starting condition on the flow and interpretation of results for regions away from the lower leading edge can be shown to be small. Smoke visualization showed some of the effects of the struts on the free-stream flow. Smoke was introduced into the flow ahead of the first strut. The smoke was visible in the free-stream in a cone shaped region extending from the first strut to the top, downstream end of the first heating strip. The cone shaped region was caused by the turbulent wake of the struts. This smoke flow visualization indicated that the effect of the struts on the free-stream flow is limited to a region over the first heating strip.

Heat transfer results which indicate the possible extent of effects of the lower leading edge starting condition are shown in Fig. D-1. Figure D-1 shows the strip average convection heat transfer coefficients for the 21 heating strips plotted versus the vertical location of the strip centerline. The heat transfer coefficient has been normalized by the overall average for the 21 heating strips. The figure shows that for the forced convection dominated flow, $Gr_H/Re_L^2=0.2$, the convection heat transfer on the bottom strip, the lower 5% of the test surface, is 30% higher than the rest. The second heating strip up from the bottom also shows slightly higher convection heat transfer. The increased convection heat transfer on the second strip is largely on the downstream end of that strip.

When Gr_H/Re_L^2 is increased to approximately 3.0 or 4.0, the middle of the average mixed convection heat transfer region, the region of high heat transfer on the bottom of the test surface extends one strip further up the test surface, covering the lower 10% of the test surface. The heat transfer on the bottom strip is 40% above the rest of the surface for these conditions. At a $Gr_H/Re_L^2 \approx 10.0$, dominant free convection, the region of high heat transfer relative to the rest of the surface occurs only on the first strip, the lower 5% of the surface, and the peak heat transfer on that strip is only 10% above the rest of the surface. The pure free convection case, $Gr_H/Re_L^2 = \infty$, shows no region of convection heat transfer on the bottom of the test surface similar to that seen in Fig. D-1. The convection heat transfer has normal laminar, transitional, and turbulent free convection regions.

Figure D-1 shows the effects of the lower leading starting condition are small. Based on the smoke visualization and heat transfer results, the region affected is a cone shaped region extending from near the upstream lower corner to the downstream end of the second or third heating strip up from the bottom of the test surface. Both the size of the region affected and the magnitude of the effect fade when Gr_H/Re_L^2 increases above 4.

The small effect of the lower leading edge starting condition for Gr_H/Re_L^2 less than 3 to 4 can be shown from the boundary layer measurements also. They show that no significant amount of boundary layer flow from the lower leading edge reaches more than 2 strips up on the test surface. This was confirmed in photographs of the hot surface, when glowing red. The streaks on the surface, streamlines of the constant angle region (see Section 4.2.3), showed very little flow from down stream of the first strut was carried more than two heating strips up on the test surface. The constant angle region has the greatest vertical rise of any flow in the boundary layer.

The statement that the influence of the lower leading edge starting condition declines rapidly in the vertical direction for high Gr_H/Re_L^2 was obtained by comparing the convection heat transfer results for high Gr_H/Re_L^2 to pure free convection heat transfer results. The pure free convection heat transfer results show fully turbulent free convection heat transfer (i.e., uniform h) by the third heating strip up for cases above 220 C. For cases with $Gr_H/Re_L^2 > 10$, all of which are above 200 C, the convection heat transfer looks like fully turbulent free convection by the second heat strip up. The difference between pure free convection and high

Gr_H/Re_L^2 cases is that pure free convection has laminar and transitional flow on the first two heating strips (and no forced convection on the vertical edge).

What is happening on the lower leading edge may just be the nature of the flow in that region or strut effects or a combination of both. The most likely explanation is a combination of events. The nature of the flow results in a thinner boundary layer along the lower leading edge (the effect of buoyancy). The thinner boundary layer coupled with the turbulent wake of the struts, which may trip the boundary layer, or at least make it more turbulent, causes higher heat transfer. The effects fade at high Gr_H/Re_L^2 because the flow is driven more by forces internal to the boundary layer, as opposed to the free-stream flow.

This appendix does not explain why the convection heat transfer is high along the lower leading edge relative to the rest of the test surface. The results presented do show that the region where the flow and heat transfer appear different than most of the rest of test surface is approximately the lower 10% of the test surface, from the first strut to the downstream end of the test surface. The higher heat transfer in the affected region for a given test has less than a 2% effect on the average heat transfer.

In addition to lower leading edge effects, Fig. D-1 shows that the struts on the top edge have little effect on the convection heat transfer. The average convection heat transfer is slightly higher on the top heating strip for low Gr_H/Re_L^2, but this is caused by earlier transition to turbulence as shown by the detailed heat transfer results. The individual regions of turbulent and laminar heat transfer on the top strip compare well with baseline correlations for turbulent and laminar flow. The effects of the top struts on the heat transfer the top heating strip disappear for higher Gr_H/Re_L^2.

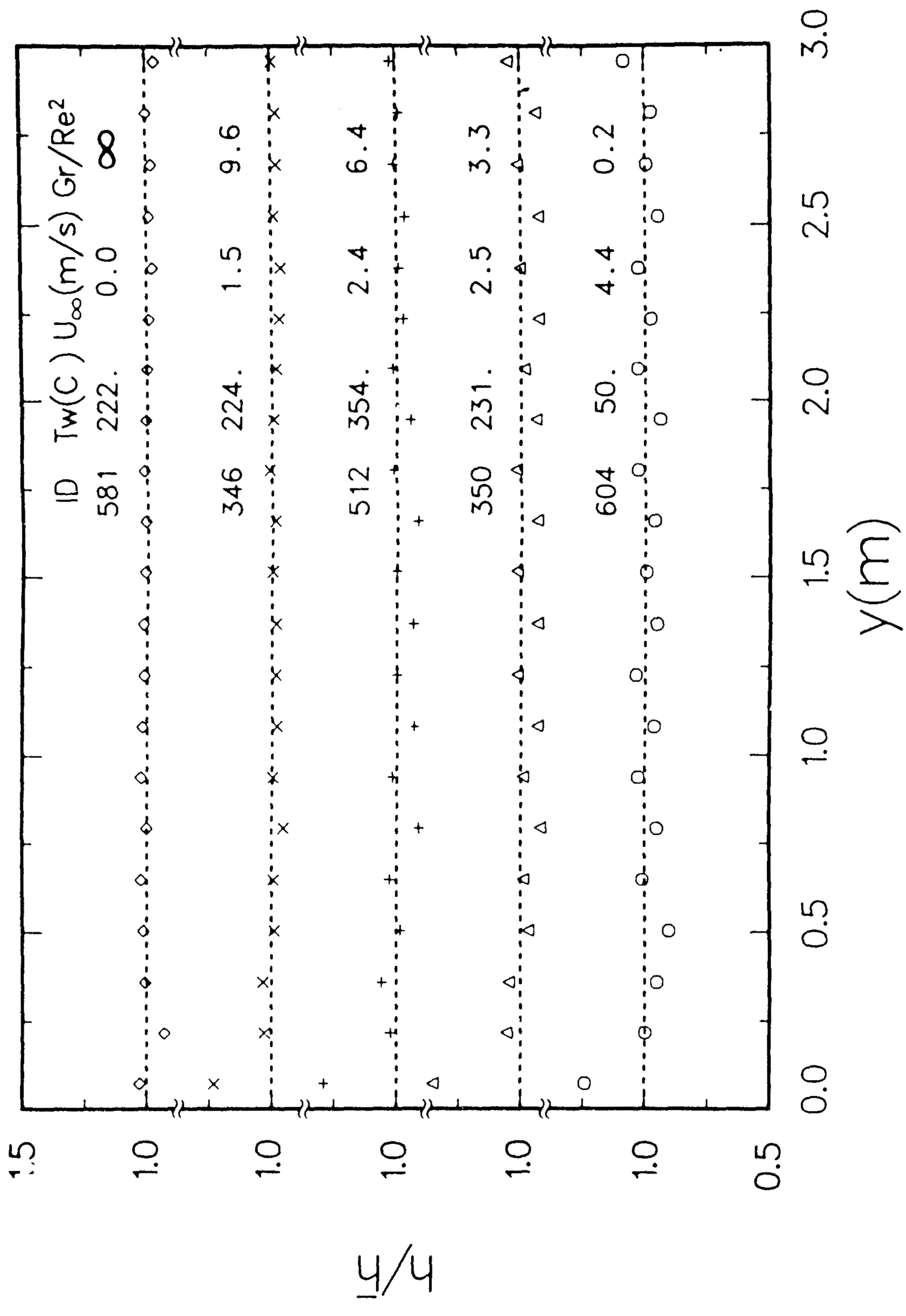

Fig. D-1 Vertical Variation of the Heat Transfer Coefficient on the Test Surface for $Gr_H/Re_L^2 \approx 0.2,\ 3.0,\ 10.0,\ \infty$.

Appendix E
HEAT TRANSFER DATA AND DATA REDUCTION CODES, "TEST" AND "REDUCE"

This appendix presents both the heat transfer results and the computer codes, "TEST" and "REDUCE", used to reduce the raw heat transfer data. Figure E-1 shows the locations where heat transfer data were taken in a T_w, U_∞ operating domain. Data were taken along lines of nominally constant T_w, nominally constant U_∞, or nominally constant Gr_H/Re_L^2. The numbers near each point in Fig. E-1 are the *ID* numbers of the tests conducted at that operating point. Table E-1 at the end of this appendix presents the average test conditions and heat transfer results for 46 of the tests run. The detailed heat transfer test conditions and results are presented for each test on the microfiche included with this appendix. The order of the data sets on the microfiche is the same as in Table E-1. Two pages of data are presented on the microfiche for each test condition. The first page contains the T_w, h, q_{conv}, and the normalized heat transfer coefficient for each of the 105 surface temperature measurement locations. The normalized heat transfer coefficient is the local value divided by the average value for that test, times 100. The normalized heat transfer coefficient more clearly shows the variation of the convection heat transfer coefficient over the test surface for each test condition. These four items are each presented in a box which represents a schematic of the surface. The location of a number in the box is the relative location on the test surface where that value for the parameter given on top of the box was measured. The buoyant force is in the upward direction and the forced flow is left to right for each box. Page two contains the Nu_x, Nu_y, $Re_{\Delta_{tz}}$, and the St based on U_∞. They are presented in the same box format. Both pages have the same information in the page heading.

The information in the heading above the boxes and on the left side of the boxes on each page are the following:

<u>Lines Above Boxes</u>

Line Number

1. Test *ID* number; file name; date and time of run; time to acquire data for the test
2. Wind tunnel conditions: U_Q; T_∞; inlet air stratification; barometric pressure; average wind tunnel wall temperature (non-test surface walls)

3. Test surface conditions: average T_w; average q_{conv}; stainless steel ϵ; *amps* through the three sets heating strips (7 strips in each set which are connected in series); and total flow through vertical leading edge suction slot
4. Misc. temperatures: air temperature in exhaust duct for air removed along top of test surface; air temperature for air removed at vertical leading edge suction slot; maximum temperature difference across the thermocouple zone box; inlet air temperature at the top of the tunnel inlet; inlet air temperature at the bottom of the tunnel inlet; reference bath temperature
5. Misc. temperatures: four temperatures measured by stratification probe at the elevations given - Environmental wind conditions: wind speed; RMS variation of the wind; wind direction (0° is approximately North)

6.-8. Average h; characteristic length, LH, used in average Nu; ratio of the average T_w and T_∞ (absolute temperatures); Re_L; Gr_H; Gr_H/Re_L^2; average Nu based on LH; percent of the total electric power dissipated lost by radiation from the front of the test surface; percent of the total electric power dissipated lost by conduction through the insulation on the back of the test surface; estimate of the percent of the total electric power dissipated being stored in the insulation

Line Below Boxes

1. Re_x divided by 1000 for column of data above it

Columns on Left Side of Boxes

Column Number

1. Gr_y for the center of each heating strip (Example 145 09=145 × 10^9)
2. Voltage drop across each heating strip
3. Electric power dissipated by each strip per unit area

Column Between Boxes

1. Strip Number

The following are some important points about the heat transfer data:

1. All properties are evaluated at the T_∞.
2. The stratification probe temperature at y=412 *cm* is zero because the thermocouple failed.
3. The leading edge suction rate is zero in cases where the suction rate was set based on suction fan RPM or pure free convection cases where it actually was zero.

4. The reference bath temperature is approximately 100 *C* for tests where it was placed in a boiling water bath, otherwise it was not used. The reference bath thermocouple was used to check the thermocouple data acquisition system periodically.
5. Tests with *ID*'s 456 and 604 have a vertical boundary trip wire at x=0.65 *m* which caused the flow to become turbulent at that location.
6. Tests with *ID*'s 553, 548, 543, and 566 have a vertical boundary trip wire at x=0.229 *m* which caused the flow to become turbulent at that location.
7. The test with *ID* 400, a forced convection baseline, has leading suction only over heating strips 11-21, the top 11 strips. Only data from these strips are used for *ID* 400.
8. The test with *ID* 585 has a transient correction made in the heat transfer coefficient calculation to account for energy storage in the insulation. The size of the correction in the energy balance is about 5% of the electric power dissipated and is given in the heading on that data set. This was done because the test was not yet at a fully steady state condition when it had to be stopped for safety reasons.
9. The tests with *ID*'s 390 and 406 are the free convection baseline heat transfer tests.
10. The tests with *ID*'s 376, 301, 382, 346, 400, and 553 are the forced convection baseline heat transfer tests.
11. The test with *ID* 648 has a slightly higher emissivity used in the data reduction (see Appendix B).
12. The x-coordinates in meters for columns of data 1 thru 10 are: 0.229, 0.510, 0.792, 1.073, 1.355, 1.673, 1.918, 2.200, 2.481, and 2.763, respectively.
13. The y-coordinates in meters heating strip centerlines are: 0.072, 0.216, 0.361, 0.505, 0.649, 0.793, 0.938, 1.082, 1.226, 1.371, 1.515, 1.659, 1.803, 1.948, 2.092, 2.236, 2.380, 2.525, 2.669, 2.813, and 2.958, respectively.

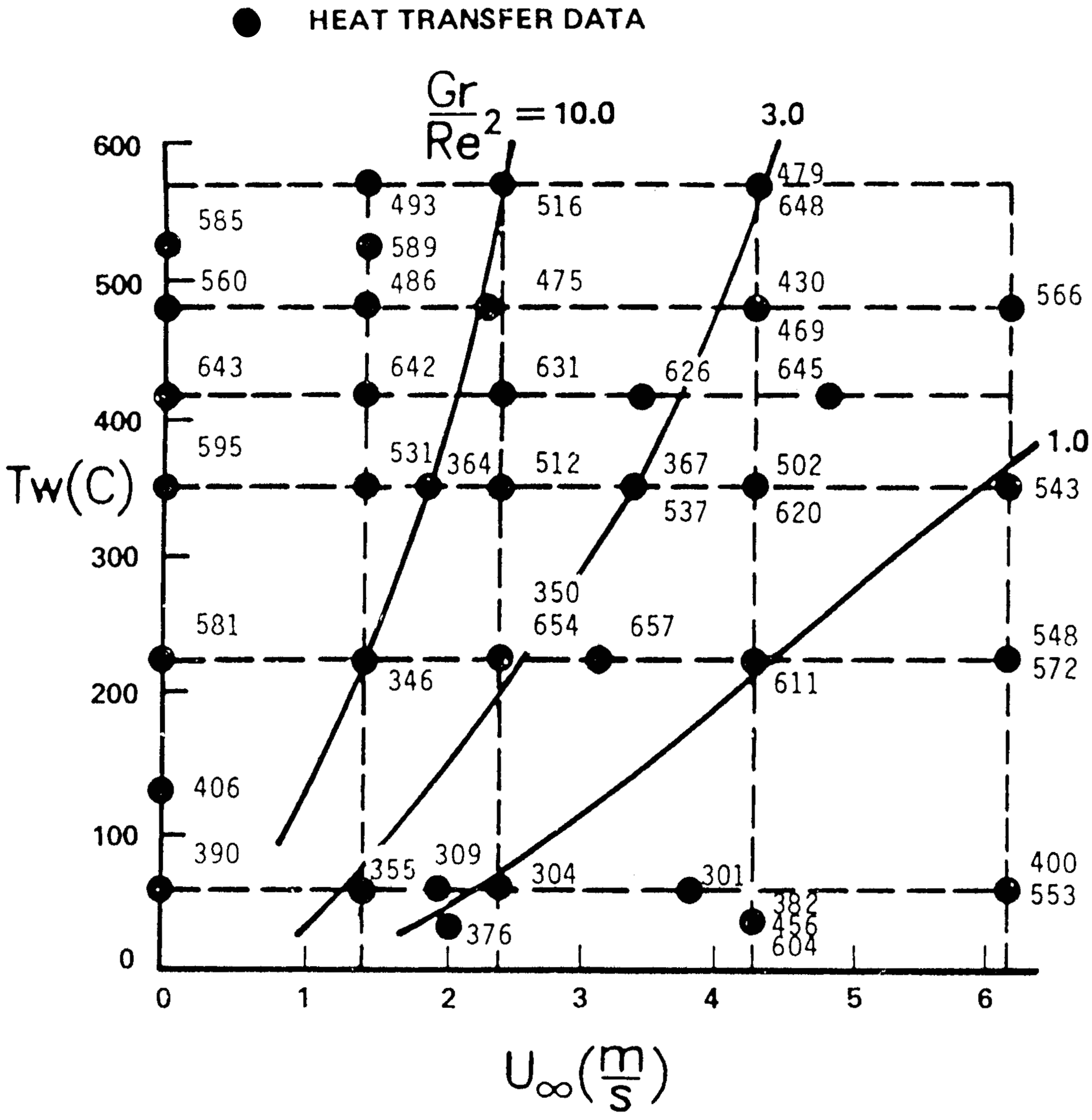

Fig. E-1 Locations of the Heat Transfer Data Sets in a Free-stream Velocity-Wall Temperature Operating Domain.

Table E-1
Heat Transfer Test Conditions and Average Heat Transfer Results

ID	U_∞ (m/s)	T_w (C)	$\frac{T_w}{T_\infty}$	q_w (W/m^2)	h (W/m^2C)	$\frac{Gr_H}{Re_L^2}$	LH (m)	Re_L $(\text{x}10^{-6})$	Gr_H $(\text{x}10^{-12})$	Nu_{LH}
390	0.0	60.	1.15	180.	4.3	3.03	0.00	0.17	∞	504.
355	1.3	62.	1.14	216.	5.4	2.96	0.25	0.16	2.49	615.
309	1.9	58.	1.12	215.	5.8	2.96	0.36	0.14	1.10	668.
376	2.0	46.	1.08	130.	5.3	2.95	0.39	0.10	0.64	602.
304	2.2	54.	1.12	233.	6.5	2.96	0.44	0.14	0.72	749.
301	3.8	60.	1.14	397.	9.6	2.95	0.75	0.14	0.26	1101.
456[1]	4.2	36.	1.06	218.	12.1	2.95	0.84	0.07	0.10	1397.
382	4.1	45.	1.08	239.	10.7	2.95	0.79	0.08	0.12	1219.
604[1]	4.4	50.	1.12	441.	12.8	2.95	0.89	0.14	0.18	1492.
400	6.2	60.	1.13	646.	15.5	2.95	1.21	0.16	0.11	1797.
553[2]	6.1	50.	1.13	581.	16.0	2.95	1.24	0.15	0.10	1876.
406	0.0	128.	1.39	688.	6.1	3.03	0.00	0.49	∞	728.
581	0.0	222.	1.72	1616.	7.8	3.03	0.00	0.89	∞	934.
346	1.5	224.	1.71	1591.	7.7	3.01	0.30	0.86	9.61	910.
350	2.5	231.	1.69	1749.	8.5	2.97	0.47	0.74	3.32	965.
654	2.4	220.	1.68	1712.	8.5	2.97	0.47	0.80	3.50	987.
657	3.0	231.	1.70	1943.	9.4	2.96	0.58	0.77	2.27	1068.
611	4.4	223.	1.71	2481.	12.0	2.96	0.87	0.85	1.12	1396.
548[2]	6.1	239.	1.77	3214.	14.5	2.95	1.22	0.92	0.62	1679.
572	6.1	234.	1.75	3340.	15.6	2.95	1.23	0.89	0.59	1807.
595	0.0	349.	2.14	2733.	8.3	3.03	0.00	1.30	∞	979.
531	1.4	350.	2.17	2871.	8.5	3.02	0.28	1.54	19.82	1021.
364	1.8	344.	2.09	2583.	8.0	3.01	0.35	1.30	10.87	934.
512	2.4	354.	2.18	3066.	9.0	2.99	0.48	1.50	6.40	1070.
367	3.4	353.	2.11	3111.	9.4	2.97	0.64	1.23	2.95	1076.
537	3.4	356.	2.19	3453.	10.1	2.97	0.68	1.50	3.25	1189.
502	4.3	360.	2.20	3888.	11.3	2.96	0.84	1.40	1.97	1318.
620	4.4	339.	2.09	3789.	11.8	2.96	0.86	1.27	1.71	1366.
543[2]	6.2	360.	2.20	4910.	14.2	2.96	1.25	1.47	0.93	1658.
643	0.0	424.	2.37	3539.	8.8	3.03	0.00	1.42	∞	1030.
642	1.4	417.	2.40	3648.	9.1	3.02	0.29	1.80	21.73	1084.
631	2.4	412.	2.37	3782.	9.5	3.00	0.49	1.73	7.36	1127.
626	3.5	416.	2.38	4176.	10.5	2.97	0.69	1.69	3.53	1219.
645	4.7	423.	2.37	4845.	12.1	2.96	0.91	1.57	1.89	1383.
560	0.0	477.	2.58	4078.	8.9	3.03	0.00	1.78	∞	1053.
486	1.4	477.	2.61	4006.	8.7	3.03	0.28	1.93	25.04	1036.
475	2.3	473.	2.59	4153.	9.1	3.01	0.47	2.01	9.17	1075.
430	4.0	507.	2.68	5105.	10.4	2.97	0.79	2.01	3.20	1214.
469	4.1	491.	2.65	5145.	10.8	2.97	0.83	2.07	3.04	1267.
566[2]	6.2	487.	2.65	6134.	13.0	2.96	1.25	2.02	1.29	1517.
585	0.0	520.	2.74	4339.	8.6	3.03	0.00	1.86	∞	1026.
589	1.5	534.	2.81	4757.	9.2	3.03	0.30	2.30	25.90	1094.
493	1.4	557.	2.89	4840.	8.9	3.03	0.27	2.28	30.23	1068.
516	2.5	588.	3.00	5343.	9.3	3.01	0.50	2.56	10.21	1110.
479	4.4	567.	2.90	6047.	11.0	2.97	0.87	2.32	3.07	1282.
648	4.3	556.	2.87	5616.	10.4	2.97	0.87	2.32	3.06	1216.

---

[1] Vertical boundary layer trip wire at x=0.65 m.

[2] Vertical boundary layer trip wire at x=0.229 m.

Appendix F

BOUNDARY LAYER DATA AND DATA REDUCTION CODE, "BLTEST"

This appendix presents both the boundary layer results and the computer code, "BLTEST", that was used to reduce the raw boundary layer data. The property routines used by "BLTEST" are the same as those in Appendix E.

The locations where boundary layer data were taken in a T_w, U_∞ operating domain are shown in Fig. F-1. Each point represents several boundary layer profiles (as indicated in the figure) taken at various x and y locations on the test surface at the given T_w, U_∞ test condition. The number near each point in Fig. F-1 is the *ID* number for the companion heat transfer data set taken along with the boundary layer data sets at that test condition. The companion heat transfer data set is in Appendix E.

Table F-1 presents identification information, the test conditions, and δ_t for each set of data (velocity, flow angle, and temperature profiles) taken at a given x and y location on the test surface. The detailed boundary layer results and test conditions are presented for each set of data at a given x and y location on the microfiche included with this appendix. The order of the data sets on the microfiche is the same as in Table F-1. The data sets are broken into groups of data taken at each T_w, U_∞ test condition. The groups are presented in order of increasing T_w. The individual data sets at a given T_w, U_∞ are presented first in order of increasing y and second in order of increasing x.

On the microfiche, one page of information is presented for each ID^* given in Table F-1, a total of 104 data sets. The information is divided into three groups for each set of data. The first group contains the test conditions and identification information. These are (in the order presented on each page on the microfiche): the companion heat transfer file name and *ID*; the ID^* of the data set; the x and y location of the data set (generally over a surface thermocouple location given in Fig. 2-11); the number of points in the data set temperature, velocity, and flow angle profiles; the test surface Gr_H/Re_L^2; Re_x; Gr_y; whether the flow was laminar, transitional, or turbulent; the barometric pressure; the tunnel-Q; U_∞, β_∞, and T_∞ at the x and y location of the profile; the mean value of $T_w - T_\infty$; T_w at the x and y location of the profile; the mean tunnel wall to free-stream temperature difference; the emissivity of the stainless steel; the environmental wind speed; the RMS variation of the wind speed; and the wind direction.

The properties in Re_x and Gr_y are evaluated at the free-stream condition. The nature of the flow, whether it was laminar, transitional, or turbulent, was determined from the heat transfer coefficient data as described in Section 4.3. The average T_w is an average of the 105 test surface temperature measurements taken at the locations shown in Fig. 2-11. The mean tunnel wall temperature is an average of the various measurements of tunnel wall temperature surrounding the test surface. These previous two mean quantities and the stainless steel emissivity are used in the data reduction of the boundary layer temperature measurement. The environmental wind conditions were used to determine when testing had to be stopped due to the adverse influence of winds on the tunnel performance.

The second group of information on each page is the boundary layer profiles. Presented are z, z/δ_t, Q, Q/U_∞, u, u/U_∞, v, v/U_∞, β, $tan(\beta)$, T, θ, i, θ_i, T_{b_1}, and T_{b_2} for each point in the boundary layer profile at a given location.

The third group of information on each page is integral parameters obtained from integrating the boundary layer profiles. The integral parameters presented are defined as follows:

$$mf_x = \int_o^\delta (\rho_\infty U_\infty - \rho u)dz \tag{F-1}$$

$$mf_y = \int_o^\delta (-\rho v)dz \tag{F-2}$$

$$Mf_{xx} = \int_o^\delta \rho u(U_\infty - u)dz \tag{F-3}$$

$$Mf_{xy} = \int_o^\delta \rho v(U_\infty - u)dz \tag{F-4}$$

$$Mf_{yx} = \int_o^\delta (-\rho uv)dz \tag{F-5}$$

$$Mf_{yy} = \int_o^\delta (-\rho v^2)dz \tag{F-6}$$

$$if_x = \int_o^\delta \rho u(i - i_\infty)dz \tag{F-7}$$

$$if_y = \int_o^\delta \rho v(i - i_\infty)dz \tag{F-8}$$

$$\delta_t = \int_o^\delta (i - i_\infty)/(i_w - i_\infty)dz \tag{F-9}$$

For the first 11 ID^*'s, which are for a cold test surface, and ID^*'s 115 and 116, which for the free convection tests, some of the above information is not given, since it is not appropriate for these two-dimensional cases.

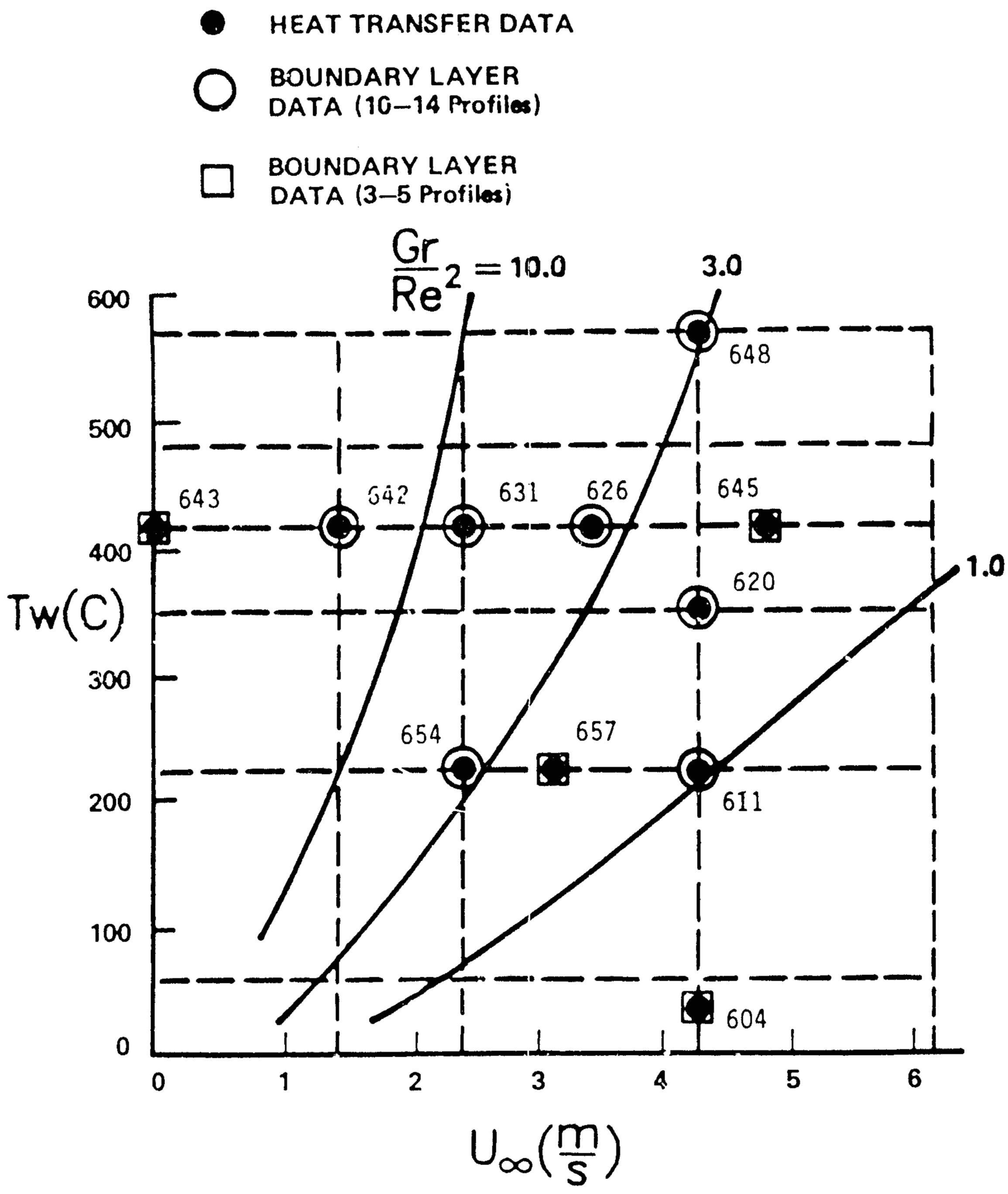

Fig. F-1 Locations of the Boundary Layer Profiles in a Free-stream Velocity-Wall Temperature Operating Domain.

Table F-1
Test Conditions and Thermal Boundary Layer Thicknesses for the Boundary Layer Profiles

ID^*	ID	*Flow*	T_w (C)	U_∞ (m/s)	T_∞ (C)	x (m)	y (m)	$\frac{Gr_H}{Re_L^2}$	NP	δ_t (cm)
39	cold	laminar	15.	4.4	15.	0.229	0.361		14	
38	cold	laminar	15.	4.3	14.	0.229	1.803		13	
40	cold	laminar	15.	4.3	15.	0.229	2.669		14	
37	cold	turbulent	15.	4.5	15.	1.637	1.947		18	
35	cold	turbulent	15.	4.4	15.	2.481	0.361		18	
33	cold	turbulent	16.	4.5	15.	2.481	1.803		18	
34	cold	turbulent	16.	4.5	15.	2.481	1.803		18	
105	cold	turbulent	29.	4.6	17.	2.481	1.803		18	
106	cold	turbulent	21.	4.6	19.	2.481	1.803		18	
36	cold	turbulent	15.	4.5	15.	2.481	2.669		18	
147	cold	turbulent	35.	4.4	25.	2.763	1.659		18	
46	604	laminar	46.	4.2	15.	0.229	1.803	0.18	15	0.12
45	604	laminar	47.	4.2	15.	0.229	1.947	0.18	15	0.12
42	604	turbulent	46.	4.4	16.	1.637	1.947	0.18	18	0.67
47	604	turbulent	47.	4.5	14.	2.418	1.803	0.18	19	0.69
30	604	turbulent	53.	4.5	16.	2.763	1.082	0.18	18	0.82
142	654	laminar	202.	2.5	19.	0.229	0.649	3.60	10	0.21
141	654	laminar	214.	2.4	19.	0.229	2.380	3.60	11	0.21
139	654	transitional	207.	2.5	17.	1.073	1.226	3.60	12	0.53
140	654	transitional	204.	2.5	18.	1.073	2.380	3.60	12	0.46
136	654	turbulent	211.	2.6	17.	1.918	2.380	3.60	18	0.72
133	654	turbulent	194.	2.3	17.	2.763	0.216	3.60	18	0.51
134	654	turbulent	211.	2.6	17.	2.763	0.793	3.60	19	0.91
143	654	turbulent	232.	2.6	20.	2.763	1.659	3.60	18	1.09
135	654	turbulent	221.	2.6	17.	2.763	2.524	3.60	20	1.12
145	657	turbulent	241.	3.2	23.	2.763	1.659	2.27	18	0.95
146	657	turbulent	235.	3.2	23.	2.763	2.524	2.27	18	1.00
61	611	laminar	204.	4.2	16.	0.229	1.082	1.12	17	0.13
59	611	transitional	196.	4.5	16.	1.073	0.216	1.12	12	0.43
60	611	transitional	207.	4.4	16.	1.073	1.082	1.12	15	0.46
58	611	turbulent	192.	4.5	16.	1.918	0.216	1.12	15	0.60
57	611	turbulent	216.	4.5	16.	1.918	1.803	1.12	18	0.65
56	611	turbulent	222.	4.6	16.	1.918	2.669	1.12	18	0.68
51	611	turbulent	226.	4.5	16.	2.481	1.803	1.12	22	0.83
52	611	turbulent	229.	4.5	17.	2.481	1.803	1.12	20	0.86
53	611	turbulent	227.	4.5	16.	2.763	0.505	1.12	20	0.87
54	611	turbulent	235.	4.6	16.	2.763	1.803	1.12	18	0.89
55	611	turbulent	235.	4.6	16.	2.763	2.669	1.12	18	0.94
75	620	laminar	329.	4.3	18.	0.229	0.649	1.71	11	0.19
74	620	laminar	337.	4.2	17.	0.229	2.092	1.71	14	0.18
71	620	transitional	310.	4.5	17.	1.073	0.216	1.71	12	0.43
72	620	transitional	319.	4.4	16.	1.073	1.370	1.71	12	0.36
73	620	transitional	319.	4.4	17.	1.073	2.669	1.71	10	0.41
70	620	turbulent	308.	4.5	17.	1.918	0.216	1.71	19	0.57

Table F-1 (cont.)

Test Conditions and Thermal Boundary Layer Thicknesses for the Boundary Layer Profiles

ID^*	ID	$Flow$	T_w (C)	U_∞ (m/s)	T_∞ (C)	x (m)	y (m)	$\frac{Gr_H}{Re_L^2}$	NP	δ_t (cm)
69	620	turbulent	347.	4.5	16.	1.918	1.082	1.71	20	0.71
68	620	turbulent	341.	4.5	16.	1.918	1.803	1.71	18	0.71
67	620	turbulent	336.	4.5	16.	1.918	2.669	1.71	19	0.68
64	620	turbulent	312.	4.2	16.	2.763	0.216	1.71	15	0.57
63	620	turbulent	343.	4.5	17.	2.763	0.505	1.71	18	0.77
65	620	turbulent	363.	4.5	16.	2.763	1.803	1.71	20	0.91
66	620	turbulent	354.	4.5	17.	2.763	2.669	1.71	19	1.04
115	643	turbulent	426.	0.7	28.	1.918	2.092	∞	19	1.20
116	643	turbulent	426.	0.7	37.	1.918	2.524	∞	21	1.37
112	642	laminar	446.	1.5	15.	0.229	0.361	21.73	11	0.40
113	642	laminar	451.	1.4	15.	0.229	1.370	21.73	12	0.30
114	642	laminar	445.	1.4	15.	0.229	2.669	21.73	13	0.34
111	642	transitional	406.	1.5	16.	1.073	0.216	21.73	11	0.49
110	642	transitional	414.	1.4	16.	1.073	1.370	21.73	13	0.69
109	642	transitional	418.	1.5	15.	1.073	2.669	21.73	18	0.92
103	642	turbulent	396.	1.5	17.	1.918	0.216	21.73	18	0.51
104	642	turbulent	408.	1.4	16.	1.918	1.371	21.73	19	1.15
107	642	turbulent	409.	1.4	17.	1.918	1.371	21.73	18	1.32
108	642	turbulent	408.	1.4	16.	1.918	2.669	21.73	20	1.61
102	642	turbulent	405.	1.4	16.	2.481	0.216	21.73	18	0.54
101	642	turbulent	402.	1.5	16.	2.481	0.938	21.73	20	1.04
100	642	turbulent	409.	1.5	16.	2.481	1.803	21.73	22	1.30
99	642	turbulent	406.	1.5	16.	2.481	2.669	21.73	24	1.67
98	631	laminar	422.	2.4	17.	0.229	1.226	7.36	10	0.25
97	631	laminar	418.	2.4	17.	0.229	2.669	7.36	11	0.25
95	631	transitional	389.	2.6	16.	1.073	0.216	7.36	14	0.47
96	631	transitional	401.	2.5	16.	1.073	2.669	7.36	14	0.61
94	631	turbulent	395.	2.5	16.	1.918	0.361	7.36	12	0.60
93	631	turbulent	410.	2.5	16.	1.918	1.515	7.36	18	0.82
92	631	turbulent	409.	2.6	16.	1.918	2.669	7.36	18	1.05
88	631	turbulent	394.	2.4	16.	2.763	0.216	7.36	26	0.56
89	631	turbulent	416.	2.6	17.	2.763	1.082	7.36	18	1.00
90	631	turbulent	417.	2.5	16.	2.763	1.947	7.36	19	1.31
91	631	turbulent	410.	2.6	16.	2.763	2.669	7.36	19	1.42
87	626	laminar	405.	3.4	17.	0.229	0.649	3.53	10	0.21
86	626	laminar	424.	3.3	17.	0.229	2.380	3.53	12	0.23
83	626	transitional	384.	3.5	17.	1.073	0.216	3.53	14	0.51
84	626	transitional	401.	3.5	17.	1.073	1.226	3.53	12	0.59
85	626	transitional	397.	3.5	17.	1.073	2.380	3.53	12	0.55
82	626	turbulent	375.	3.6	17.	1.918	0.216	3.53	21	0.58
81	626	turbulent	416.	3.5	17.	1.918	1.226	3.53	18	0.75
80	626	turbulent	419.	3.5	17.	1.918	2.380	3.53	18	0.79
76	626	turbulent	386.	3.2	18.	2.763	0.216	3.53	21	0.50
77	626	turbulent	411.	3.5	17.	2.763	0.793	3.53	21	1.01
78	626	turbulent	432.	3.6	18.	2.763	1.659	3.53	18	1.01
79	626	turbulent	423.	3.6	17.	2.763	2.524	3.53	18	1.14

Table F-1 (cont.)
Test Conditions and Thermal Boundary Layer Thicknesses for the Boundary Layer Profiles

ID^*	ID	$Flow$	T_w (C)	U_∞ (m/s)	T_∞ (C)	x (m)	y (m)	$\frac{Gr_H}{Re_L^2}$	NP	δ_t (cm)
119	645	turbulent	429.	4.8	21.	2.763	0.505	1.89	19	0.77
118	645	turbulent	447.	4.8	21.	2.763	1.803	1.89	18	0.94
117	645	turbulent	436.	4.9	20.	2.763	2.669	1.89	18	1.07
132	648	laminar	562.	4.3	18.	0.229	0.938	3.06	8	0.23
128	648	transitional	553.	4.5	17.	1.073	0.216	3.06	12	0.53
129	648	transitional	543.	4.5	17.	1.073	1.226	3.06	12	0.41
130	648	transitional	538.	4.4	17.	1.073	2.380	3.06	13	0.50
127	648	turbulent	530.	4.6	18.	1.918	0.216	3.06	19	0.59
126	648	turbulent	553.	4.5	17.	1.918	1.226	3.06	18	0.78
125	648	turbulent	554.	4.5	16.	1.918	2.380	3.06	18	0.87
122	648	turbulent	538.	4.3	17.	2.763	0.216	3.06	19	0.53
121	648	turbulent	553.	4.5	18.	2.763	0.793	3.06	19	1.05
123	648	turbulent	575.	4.5	17.	2.763	1.659	3.06	19	1.05
124	648	turbulent	548.	4.5	16.	2.763	2.524	3.06	19	1.08

UNLIMITED RELEASE

INITIAL DISTRIBUTION

U. S. Department of Energy
Forrestal Building
1000 Independence Avenue, S.W.
Washington, D.C. 20585
Attn: G. W. Braun
K. T. Cherian
C. B. McFarland
M. Scheve

U. S. Department of Energy
P. O. Box 5400
Albuquerque, NM 87115
Attn: J. E. Weisiger

U. S. Department of Energy
Solar One Field Office
P. O. Box 366
Daggett, CA 92327
Attn: S. D. Elliott

U. S. Department of Energy
1333 Broadway
Oakland, CA 94612
Attn: R. W. Hughey

University of California - Berkeley (6)
Department of Mechanical Engineering
Etcheverry Hall
Berkeley, CA 94720
Attn: K. S. Chen
R. Greif
J. A. C. Humphrey
P. Pagni
F. S. Sherman
W. M. To

University of California - Irvine
Department of Mechanical Engineering
Irvine, CA 92717
Attn: D. K. Edwards
M. Young

University of Cincinnati
Clifton Avenue
Cincinnati, OH 45221
Attn: R. T. Davis

Cornell University
289 Grumman Hall
Ithaca, NY 14850
Attn: K. Torrance

University of Delaware
Department of Mechanical
and Aerospace Engineering
Evans Hall
Newark, DE 19711
Attn: F. A. Kulacki

University of Houston (3)
Solar Energy Laboratory
4800 Calhoun
Houston, TX 77704
Attn: A. F. Hildebrandt
L. Vant-Hull
R. Eichhorn

University of Illinois
at Urbana-Champaign
2605 W. Green
Urbana, IL 61801
Attn: A. M. Clausing

University of Manchester (2)
Division of Thermodynamics &
Fluid Mechanics
Department of Mechanical Engineering
Institute of Science Technology
Manchester M60 1QD
England
Attn: B. Launder
D. B. Spalding

University of Michigan
Department of Mechanical Engineering
Ann Arbor, MI 48109
Attn: V. S. Arpaci

University of Minnesota (3)
Department of Mechanical Engineering
Minneapolis, MN 55455
Attn: R. J. Goldstein
E. Sparrow
T. Simon

University of Minnesota
Physics Department
116 Church Street, S.E.
Minneapolis, MN 55455
Attn: C. Jofeh

University of Pennsylvania
Department of Mechanical Engineering
212 Towne Building
Philadelphia, PA 19174
Attn: B. Gebhart

Purdue University (2)
School of Mechanical Engineering
W. Lafayette, IN 47907
Attn: R. Viskanta
F. P. Incropera

Rensselaer Polytechnic Institute
Troy, NY 12181
Attn: E. F. C. Somerscales

Rutgers State University of New Jersey
College of Engineering
P. O. Box 909
Piscataway, NJ 08854
Attn: Prof. V. Sernas

Stanford University (4)
Department of Mechanical Engineering
Stanford, CA 94305
Attn: B. Afshari
J. P. Johnston
R. J. Moffat
J. Ferziger

Washington State University
Department of Mechanical Engineering
Pullman, WA 99164
Attn: O. A. Plumb

University of N.S.W.
P. O. Box 1
Kensington, N.S.W. 2033
Attn: G. de Vahl Davis

AMFAC
P. O. Box 3230
Honolulu, HI 96801
Attn: G. E. St. John

ARCO Power Systems
7061 S. University, Suite 300
Littleton, CO 80122
Attn: F. A. Blake

ARCO Power Systems
302 Nichols Drive
Hutchins, TX 75141
Attn: R. L. Henry

Arizona Public Service Company
P. O. Box 21666
Phoenix, AZ 85036
Attn: B. Broussard
E. Weber

Babcock and Wilcox
91 Stirling Avenue
Barberton, OH 44203
Attn: G. Grant
I. Hicks
M. Wiener

Battelle Pacific Northwest Laboratories
Battelle Boulevard
P. O. Box 999
Richland, WA 99352
Attn: L. L. Eyler

Bechtel Group, Inc.
P. O. Box 3965
San Francisco, CA 94119
Attn: E. Y. Lam

Black and Veatch Consulting Engineering
P. O. Box 8405
Kansas City, MO 64114
Attn: J. C. Grosskreutz
S. L. Levy

Boeing Engineering and Construction Company
P. O. Box 3707
Seattle, WA 98124
Attn: J. R. Gintz
R. B. Gillette
R. C. Zenter

Center for Fire Research
National Bureau of Standards
Washington, D.C. 20585
Attn: J. G. Quintiere

Combustion Engineering, Inc.
1000 Prospect Hill Road
Winsor, CT 06095
Attn: C. R. Buzzuto

Dornier GmbH
P. O. Box 1360
Friedrichshafen
West Germany
Attn: M. Kuczera

Dynamic Technology, Inc.
22939 Hawthorne Boulevard
Torrance, CA 90505
Attn: R. C. Gran
T. Kubota

DFVLR
Linder Hohe
D-5000
Koln 90
West Germany
Attn: Manfred Becker

El Paso Electric Company
P. O. Box 982
El Paso, TX 79946
Attn: J. E. Brown

Electric Power Research Institute
P. O. Box 10412
Palo Alto, CA 94303
Attn: J. Bigger
E. DeMeo

Exxon Enterprises, Inc.
P. O. Box 592
Florham Park, NJ 07932
Attn: T. L. Guckes

Foster Wheeler Development Co.
12 Peach Tree Hill Road
Livingston, NJ 07039
Attn: R. J. Zoschak
S. F. Wu

General Electric
310 De Guigne Drive
Sunnyvale, CA 94086
Attn: S. Wolf

Georgia Institute of Technology
Atlanta, CA 30332
Attn: C. T. Brown

Jet Propulsion Laboratory
California Institute of Technology
4800 Oak Grove Drive
Pasadena, CA 91103
Attn: V. T. Truscello
E. J. Hanseth
W. Menard

Laboratorie D'Energetique Solaire
40 Avenue de Recteur Pineau
86022 Poitiers
France
Attn: F. Penot
P. LeQuere

Los Angeles Department of Water and Power
P. O. Box 111
111 North Hope Street
Los Angeles, CA 90051
Attn: Lyge Greene, Rm. 657

Martin Marietta Aerospace
P. O. Box 179, MS L0450
Denver, CO 80201
Attn: F. L. Oldham
H. C. Wroton
T. H. Oliver

McDonnell Douglas Astronautics Company
5301 Bolsa Avenue
Huntington Beach, CA 92647
Attn: R. L. Gervais
H. H. Dixon
G. F. Greenwald

Nielson Engineering and Research (2)
510 Clyde Avenue
Mountain View, CA 94043
Attn: R. G. Schwind
D. Spangler

Olin Chemical Company
Metals Research Laboratory
91 Shelton Avenue
New Haven, CT 06511
Attn: E. F. Smith
N. Christopher

Pacific Gas and Electric Company
77 Beale Street
San Francisco, CA 94105
Attn: R. E. Price

Pacific Gas and Electric Company
3400 Crow Canyon Road
San Ramon, CA 94526
Attn: H. E. Seielstad

Pioneer Mill Company (AMFAC)
P. O. Box 727
Lahaina, HI 96761
Attn: R. K. MacMillan

Rockwell International
Energy Systems Group
8900 De Soto Avenue
Canoga Park, CA 91304
Attn: T. Springer
W. B. Thomson

Rockwell International (3)
Rocketdyne Division
6633 Canoga Park, CA 91304
Attn: R. G. Surette
J. M. Friefeld
R. U. Morinishi

S. Levi, Incoropated
1999 S. Bascom
Campbell, CA 95008
Attn: J. C. Gillis

Solar Energy Research Institute (3)
1617 Cole Boulevard
Golden, CO 80401
Attn: B. Gupta
R. Hulstram
F. Kreith

Southern California Edison
P. O. Box 325
Daggett, CA 92327
Attn: P. Skvarna

Southern California Edison (2)
P. O. Box 800
Rosemead, CA 92807
Attn: J. N. Reeves

Spectron Development
3303 Harbor Boulevard
Suite G-3
Costa Mesa, CA 92626
Attn: C. F. Hess

SRI International
333 Ravenswood Avenue
Menlo Park, CA 94025
Attn: B. J. Grossi

Stearns-Roger
P. O. Box 5888
Denver, CO 80217
Attn: W. R. Lang

Stone and Webster Engineering Corporation
P. O. Box 1214
Boston, MA 02107
Attn: R. W. Kuhr

Westinghouse Electric Corporation
Advanced Energy Systems Division
P. O. Box 10864
Pittsburgh, PA 15236
Attn: J. R. Maxwell

D. B. Hayes, 1510; Attn: J. W. Nunziato, 1511
J. Cummings, 1512
D. W. Larson, 1513
R. S. Claassen, 8000; Attn: D. M. Olson, 8100
A. N. Blackwell, 8200
B. F. Murphey,8300
C. S. Selvage, 8000A
R. C. Wayne, 8110
L. D. Bertholf, 8120; Attn: G. A. Benedetti, 8121
C. S. Hoyle, 8122
W. D. Zinke, 8123
R. J. Gallagher, 8124 (10)
M. Abrams, 8125
M. J. Fish, 8125
S. Paolucci, 8125
J. S. Kraabel, 8132
W. E. Alzheimer, 8150
L. Gutierrez, 8400; Attn: R. A. Baroody, 8410
H. Hanser, 8440
J. F. Barham, 8460
J. B. Wright, 8450
A. F. Baker, 8452
J. J. Bartel, 8452 (2)
A. C. Skinrood, 8452 (10)
M. C. Stoddard, 8452
P. K. Falcone, 8453
W. G. Wilson, 8453
J. B. Woodard, 8454

D. L. Hartley, 8500 ; Attn: C. W. Robinson, 8520
T. M. Dyer, 8522
D. L. Siebers, 8522 (10)
D. G. Schueler, 9720
J. B. Otts, 9722
Publications Division 8265, for TIC (27)
Publications Division 8265/Technical Library Processes Division, 3141
Technical Library Processes Division, 3141 (3)
M. A. Pound, 8214, for Central Technical Files (3)